ISSN 2078-7405

МІНІСТЕРСТВО ОСВІТИ ТА НАУКИ УКРАЇНИ

РІЗАННЯ ТА ІНСТРУМЕНТИ

В ТЕХНОЛОГІЧНИХ СИСТЕМАХ

ЗБІРНИК НАКОВИХ ПРАЦЬ

104’2026

МІНІСТЕРСТВО ОСВІТИ ТА НАУКИ УКРАЇНИ

НАЦІОНАЛЬНИЙ ТЕХНІЧНИЙ УНІВЕРСИТЕТ
«ХАРКІВСЬКИЙ ПОЛІТЕХНІЧНИЙ ІНСТИТУТ»

Ministry of Education & Science of Ukraine
National Technical University
«Kharkiv Polytechnic Institute»

РІЗАННЯ ТА ІНСТРУМЕНТИ в технологічних системах

CUTTING & TOOLS IN TECHNOLOGICAL SYSTEMS

Збірник наукових праць
Collection of scientific papers

Заснований у 1966 р. М. Ф. Семко
Found by M. F. Semko in 1966

ВИПУСК № 104
Edition № 104

Харків НТУ «ХПІ» – 2026 – Kharkiv NTU «KhPI»

ISSN (print) 2078-7405
УДК 621.91

Ідентифікатор медіа R30-02559, згідно з рішенням Національної ради України з питань телебачення і радіомовлення від 27.07.2023 р. №598
Друкується за рішенням Вченої ради НТУ "ХПІ",
протокол № 5 від 28 квітня 2026 р.

У збірнику представлені наукові статті, в яких розглядаються актуальні питання в області механічної обробки різних сучасних матеріалів із застосуванням високопродуктивних технологій, нових методик, вимірювальних приладів для контролю якості оброблених поверхонь і високоефективних різальних інструментів. Розглядаються аспекти оптимізації та математичного моделювання на різних етапах технологічного процесу.

Для інженерів і наукових співробітників, що працюють в області технології машинобудування, різання матеріалів, проектування різальних інструментів в технологічних системах.

Збірник наукових праць «Різання та інструменти в технологічних системах» включений в Перелік фахових видань України категорії «Б», наказ МОН України від 17.03.2020 р., № 409

Різання та інструменти в технологічних системах/Cutting and Tools in Technological Systems: Збірник наукових праць. – Харків: НТУ «ХПІ», 2026. – Вип. 104. – 194 с.

Адреса редакційної колегії: вул. Кирпичова, 2, Харків, 61002, Національний технічний університет «Харківський політехнічний інститут», кафедра «Інтегровані технології машинобудування» ім. М.Ф. Семка, тел. +38 (057) 706-41-43.

УДК 621.91

UDC 621.923: **doi:10.20998/2078-7405.2026.104.01**

COATED DIAMONDS AND DIAMOND COATINGS (A REVIEW OF CURRENT DEVELOPMENTS)

Valerii **Lavrinenko** [1][0000-0003-2098-7992], Volodymyr **Solod** [2][0000-0002-7516-9535], Predrag **Dašić** [3][0000-0002-9242-274X]

[1]V. Bakul Institute for Superhard Materials NAS Ukraine, Kyiv, Ukraine
[2]Dniprovsk State Technical University, Kamianske, Ukraine
[3]Engineering Academy of Serbia (IAS), Belgrade, Serbia
lavrinenko@ism.kiev.ua

Received: 05 February 2026 / Revised: 16 February 2026 / Accepted: 01 April 2026 / Published: 15 May 2026

Abstract. *Recent studies have shown the effectiveness of coating diamond grains with thin layers of titanium and nickel to provide a tight interface with the nickel matrix. Wetting of diamond and nickel is improved by coating diamond particles with thin layers of titanium and nickel. Titanium carbide formed between Ti-coating and diamond provides stronger interfacial adhesion force compared to diamond micropowder with Ni-coating. To improve the thermal properties of diamond/metal composites, a metal carbide layer is needed that combines both the crystal structure and the heat transfer of heterogeneous interfaces. In modern research in coatings, in addition to TiC, attention is paid to other carbides: B_4C, V_2C and VC, as well as chromium carbides. A separate direction is oxide coatings on diamonds. The mechanism of diamond protection in this direction is the predominant oxide donor behavior of Mo–B–C coatings for the formation of a stable oxide layer on the diamond surface. Diamond films with three different grain sizes were grown on the surface of a titanium alloy by high-temperature chemical vapor deposition (HFCVD). The corrosion resistance of nanocrystalline diamond (NCD) films is clearly higher than that of microcrystalline diamond (MCD) films. But cutters with intact MCD coating demonstrate the longest service life. Attention has been paid to coatings applied to hard alloys and steels, with researchers mainly focusing on coatings containing titanium, namely TiAlN, TiN/CrN and Al_2O_3/TiO_2.*
Keywords: *coated diamonds; nickel coating; titanium coating; titanium carbide; boron carbide; vanadium carbide; oxide coating; nanocrystalline diamond films; microcrystalline diamond films.*

1. Introduction

The development of tool production necessitates the efficient processing of new, difficult-to-process materials. The search for ways to save energy dictates the need to obtain composite coatings on diamond grinding powder grains with new properties. Previous studies have established that the main factors that, for example, determine their diamond retention are the boundary chemical interaction with coating elements, for example, during high-temperature manufacturing of tools on

metal bonds, as well as diffusion interaction at the coating-bond interface. In diamond tools with polymer and metal-polymer bonds, chemical interaction occurs at the metal coating–polymer interface. The rougher the coating, the greater the grain surface area and the greater the efficiency of this interaction. In addition, research into coating both diamond grains of abrasive tools and diamond grains as components of diamond cutting composites and diamond-metal composites is relevant.

2. The state of the art in the field of diamond coating research

Researchers pay increased attention to the interface between diamond and matrix. Experimental results show [1] that a W-coating layer can effectively improve the wettability of the diamond surface and reduce the wetting angle from 108.6° to 13.2°. The W layer can also significantly prevent the graphitization of the diamond surface and improve the contact between diamond and copper matrix. Thus, the thermal conductivity of the W-coated composite with a diamond content of 18.4 vol.% increases and reaches 575 W/(m•K), which is 43.3% higher than that of pure Cu.

The introduction of an intermediate layer is an effective method to improve the interfacial thermal conductivity (G) of the Cu/diamond interface. In the paper [2], an amorphous carbon (a-C) layer was introduced at this interface by Ar ion bombardment, enriched with oxygen by Ar/O_2 ion bombardment, and the C-O bond was formed by acid treatment at the Cu/diamond interface. Compared to the pre-cleaned Cu/diamond interface, a 35% increase in G is achieved by obtaining a 4.5 nm thick a-C interlayer between Cu and diamond.

The low interfacial strength between the iron-based matrix and diamonds leads to premature detachment of diamond particles, which significantly affects the cutting efficiency of diamond composites. The work [3] aims to optimize the interfacial microstructure and mechanical properties of diamond/Fe-Ni-WC composites by depositing a Mo_2C layer on the diamond particles. Mo_2C-coated diamonds were prepared by the molten salt method. Diamond/Fe-Ni-WC composites were sintered by hot pressing under vacuum. Energy dispersive scanning spectroscopy showed that the Mo_2C coating layer changed the interfacial composition between the Fe–C alloy matrix and diamonds to Mo_2C, improving the interface strength. This change in interface composition results in an increase in interfacial strength, as evidenced by an increased flexural strength of 996 MPa, which is 24% higher than that of the uncoated diamond/Fe-Ni-WC composite. The increase in interfacial strength improves the holding capacity of the matrix on the diamond, which increases the height of the diamond protrusion, and the cutting efficiency of the Mo_2C-coated

diamond/Fe-Ni-WC composites increases. That is, the above indicates that the application of the effect of subsequent mechanochemical influence, both on the diamond-bond interface and on the contact of the diamond grain surface with the processed material, when coating diamond abrasives, allows to increase the efficiency of using a diamond abrasive tool.

3. Formulation of the purpose of the research

The coating of diamond grains is an important factor influencing the change in their properties and increasing their retention in the binding working layer of the grinding wheel. Considering that this area is actively developing, in this work we focus on modern developments that are in scientific publications over the past 5 years. Let us point out that here we were most interested in developments in the direction of applying coatings to diamond grains, which would be used in abrasive composites and composites for cutting tools, diamond-metal composites with increased thermal conductivity, as well as the features of applying and using diamond coatings on tool materials.

4. Presenting main material

Let us first consider developments in coating diamond grains for abrasive surface treatment of various difficult-to-machine materials.

Electroplated diamond wire saws are widely used in industry. The use of nickel (Ni) coated diamonds is a common approach to improve the efficiency of the electroplating process of composites in wire saw production. However, pure diamond does not chemically react with nickel, and the interfacial bond strength between the nickel coating and diamond is relatively weak. This often leads to separation of diamonds from the nickel coating during the cutting process. To solve this problem, titanium (Ti) coated diamonds have been used in the manufacture of wire saws. Specifically, in [4], a vacuum slow evaporation technology was developed to obtain diamond micropowder (8 μm) with uniform Ti coatings, firmly bonded to the diamond through the interfacial product TiC. Linear scanning voltammetry curves showed that the addition of Ti-coated diamond shifted the overvoltage of the composite electroplating in the positive direction, therefore it promoted the electrodeposition reaction more than diamond powder. Electrochemical impedance spectroscopy showed that Ti-coated diamond reduced the charge transfer resistance during composite electroplating. The Ti-coated diamond micropowder was completely covered with a Ni electroplated layer, and the TiC formed between the Ti-coating and diamond provided a stronger interfacial

adhesion force compared to that of the Ni-coated diamond micropowder (Fig. 1). The diamond ropes with titanium-coated diamond micropowder demonstrated excellent resistance to diamond grain shedding.

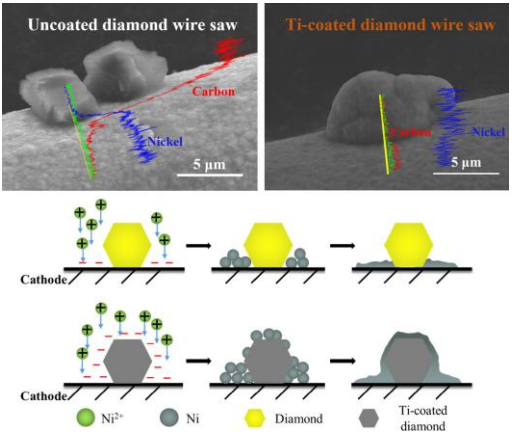

Fig. 1. Mechanism of improved retention of diamond particles with the presence of a titanium coating on them [4].

In the article [5], in order to effectively avoid thermal oxidation and thermal destruction of diamonds when working in a high-temperature aerobic environment, Mo–B–C coatings were developed and prepared to protect diamonds from oxidation. These coatings were synthesized on the diamond surface using Mo_2C-coated diamonds, boron powder, and boric acid. A two-step synthesis method was used to form coatings with different B contents on diamonds by controlling the reaction temperature, and the oxidation kinetics and oxidation mechanism of coated diamonds were investigated in the temperature range of 700–1200 °C. The mechanism of diamond protection in this study was the predominant oxidative donor behavior of Mo–B–C coatings to form a stable oxide layer on the diamond surface. For low-B coatings, four stages of coating oxidation were observed sequentially with increasing temperature, low-temperature MoO_3 evaporation, stable B_2O_3 protection, and rapid B_2O_3 evaporation. For high-B coatings, the predominant self-reducing flow of B_2O_3 not only suppressed the evaporation of MoO_3, but also provided a reducing environment for MoO_3 to form MoO_2 and Mo_2C with high melting point, which led to the formation of a double synergistic protective oxide layer and significantly improved the oxidation resistance of diamonds. Meanwhile, the oxide layer protection maintained the compressive strength of diamonds in high-

temperature oxidizing atmosphere, indicating its good applicability at high temperatures. The compressive strength of individual diamond grains is an important indicator of the quality of synthetic diamonds. The average compressive strength of uncoated diamonds was 80 N. The compressive strength of coated diamonds was significantly improved to 150 and 200 N. This means that the presence of the coating compensates for the defects of synthetic diamonds by filling gaps, repairing or encapsulating, which significantly seals cracks in diamonds and reduces the stress concentration of diamond particles when they are subjected to force [5].

B_4C coatings were successfully synthesized on the surface of faceted diamond crystals by the carbothermic reduction method using a system containing B_2O_3 and B [6]. The microstructure, chemical composition, and surface morphology of the B_4C coatings were studied. The growth mechanism of B_4C was explained using a new model [6], which accurately describes its formation on diamond surfaces and agrees well with experimental data. Thus, B_4C coatings are predominantly composed of rod-shaped crystals, which show preferential deposition on the (110) diamond surface compared to the (111) surface. Furthermore, the thickness of B_4C coatings increases with increasing temperature, reaching complete and uniform coverage of both (100) and (111) diamond faces at 1200 °C. This face-dependent selectivity is due to the different atomic arrangements and energetics of the diamond surface. The (100) surface provides a more ordered structural matrix for B_4C nucleation, a process that is additionally susceptible to the lower energy of boron (B) doping defect formation (ΔE = 4.49 eV) compared to the (111) surface. This thermodynamic susceptibility promotes the oriented attachment and lateral fusion of B_4C nuclei on the (100) surface, thereby accelerating the formation of the initial layer. Kinetic analysis shows that the growth of B_4C on the diamond (100) surface obeys a parabolic rate law with an activation energy of 124.7 kJ/mol in the temperature range from 1000 to 1300 °C. The growth of the B_4C coating is mainly determined by temperature and is kinetically limited by the diffusion of boron atoms, which leads to a gradual decrease in the deposition rate over a long processing time [6].

Diamond tools in the processing of ferrous metals have strong chemical wear, which makes their practical application difficult. To improve the wear resistance of diamond cutting tools in a strong covalent diamond-graphite structure obtained by laser-induced solid-state diffusion, it is possible to obtain carbon nanosheets (CNS) by electrochemically removing the graphite layer on the diamond matrix, which offers a new way to improve the limitations in the application of diamond tools [7]. After 14,400 cycles of reciprocating sliding on a GCr15 ball under a normal load of 2–8 N, the friction was reduced by 45.9–65.6% with high durability. During this process, the oxygen content is reduced by an order of magnitude, suggesting that CNS can prevent oxidative behavior at the sliding interface. The relative wear rate

of bare diamond was 4.1–15.4 times higher than that of CNS. This demonstrated competitive inhibition of mechanochemical wear.

In the next stage, we will consider developments in coating diamond grains for diamond composites for various purposes.

Thus, new composite materials using silicon nitride (Si_3N_4) as a substrate and diamond particles as a reinforcing phase were developed to improve both thermal conductivity and mechanical properties [8]. Such diamond composites provided a maximum thermal conductivity of 201.96 W•m, had high hardness (32.84 GPa) and low coefficient of thermal expansion (3.07×10^{-6}/K). The titanium coating on the surface of the diamond particles promoted the formation of a titanium carbonitride (TiC_iN_{1-i}) interface between the two components during sintering, creating a strong bond for high thermal conductivity at the diamond-Si_3N_4 interface. The titanium carbonitride formed at the interface creates a chemical bond and inhibits the graphitization of diamond (about 100 nm). In addition, a multilayer material design was developed in which layers of Si_3N_4-coated diamond and Si_3N_4/Ti were stacked alternately to give the composites a directional thermal conductivity characteristic. The multilayer designs gave the composites a directional heat transfer property, and the anisotropy increased by 66.67% compared to the few-layer structure. The thermal conductivity of the fabricated Si_3N_4/diamond composites increased by 272.87% compared to the thermal conductivity of commercially available Si_3N_4, making them excellent as thermal control materials [8].

Metal matrix composites (MMCs) have received increasing attention, and recently there has been growing interest in the additive manufacturing of complex-shaped MMCs. However, quality control of the composite powder for MMCs remains a challenge. In this study, diamond particles are first coated with thin layers of titanium and nickel to ensure a tight interface with the nickel matrix. Wetting of diamond and nickel is improved by applying thin layers of titanium and nickel to diamond particles. The effect of ball milling parameters on the preparation of diamond/N6 composite powder particles with Ni-Ti coating was analyzed, as well as the effect of processing parameters during laser powder bed melting (LPBF) on the densification and defectivity of the fabricated samples. The results show that at the ball mill stage, it is possible to obtain high-flowing composite powder particles for LPBF at a ball mill time of 4 hours, a speed of 250 rpm and a ball to powder ratio of 2:1. Using the optimized composite powder, a set of diamond MMCs with Ni-Ti/N6 coating is additionally fabricated at laser power of 150, 160 and 170 W and a scanning speed of 250 mm/s, the MMCs samples have a relative density of more than 99%. This study demonstrates the possibility of producing dense diamond/N6 and other similar MMCs with appropriate coating, ball milling parameters and LPBF [9].

Effective control of the diamond-metal interface is crucial for achieving optimal performance in metal-matrix/diamond composites. Here, Ti coatings prepared at different pressures were deposited on diamond particles by DC magnetron sputtering. Dia-1.0 was clean and homogeneous, without obvious defects, demonstrating optimal deposition quality and bond strength [10]. The results showed that the microstructure of Ti-coatings depends on the deposition pressure. All surfaces of the coatings had a granular morphology, and increasing the spraying pressure contributed to the grinding of the coating grains. The titanium coating obtained under a pressure of 1.0 Pa was thin and uniform, without obvious defects, demonstrating optimal deposition quality and adhesion density (Fig. 2). In addition, it was determined that the annealing temperature plays a key role in the reaction between Ti-coating and diamond. The TiC phase in Ti-coated diamond particles showed a gradual increase with increasing temperature, and the Ti-coated diamond underwent a complete transformation into TiC-coated diamond at 1000 °C. The experimental results and molecular dynamics simulations showed that the Ti-coating reacted more vigorously with the diamond (100) facet than with the diamond (111) facet at high temperature.

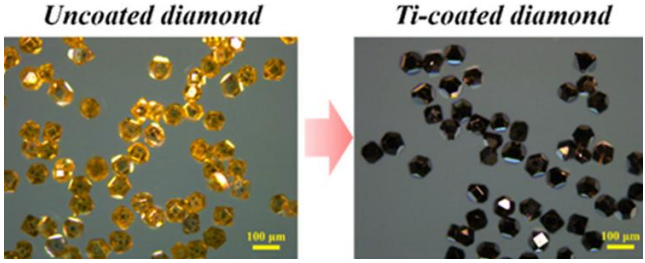

Fig. 2. Uncoated and coated diamonds with TiS [10].

In [11], the authors considered another carbide for coating, vanadium. Diamonds coated with vanadium carbide were produced by the molten salt method. The results showed that, compared to uncoated diamonds, the static compressive strength and oxidation resistance of coated diamonds increased by 42.27% and 158.82 °C, respectively. The vanadium carbide coatings were mainly composed of V_2C and VC. The thickness of the coatings increased with increasing temperature. With increasing relative vanadium content in the raw material, the crystal structure of the vanadium carbide coatings changed from microcrystalline to mesh, and vanadium carbide coatings with microcrystalline structure showed better performance.

To improve the thermal properties of diamond/metal composites, a metal carbide layer is required, which combines both the crystal structure and the heat transfer of heterogeneous interfaces. In [12], experiments were conducted with diamond/Cu–Cr composites to determine the effect of two important variables for thermal diffusion: temperature (800–1025 °C) and holding time (5–60 min), on the growth of chromium carbide interfaces and the resulting thermal conductivity, on the microstructural evolution (Fig. 3) and the corresponding thermal properties of diamond/Cu-0.8Cr composites. In the first stage, Cr dispersed in the Cu matrix diffused from Cu to the diamond surface. Fine flake Cr carbide was formed based on the Cr–C reaction. With increasing holding time or increasing temperature, the flake Cr carbide coalesced into an island structure under surface diffusion, which led to a surface energy difference between the {100} and {111} crystal faces of diamond. When the diffusion of Cr atoms gained further mobility, the "island" structure was finally transformed into a "porous" structure. However, due to the competition between Cr carbides (Cr_3C_2, Cr_7C_3, $Cr_{23}C_6$), cracks may occur between the Cr carbide layer and the diamond surface. When sintering at 900–950 °C for 60 s, Cr carbides are mainly prone to growth and transformed from a "convex" to a compacted structure. The main conclusion of the work [12] is that the optimal sintering condition for the studied diamond/Cu-0.8Cr composites is a temperature of 950 °C for 60 min, at which the sample can reach the maximum relative density (98.11%) and thermal conductivity (577 W/(m•K)).

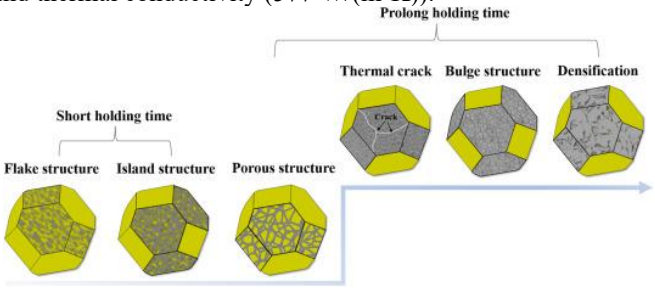

Fig. 3. Schematic diagram of the evolution of the interlayer structure on the surface of a diamond grain with a change in the carbide layer [12].

In the study [13], chemical deposition was used to deposit nickel on the diamond surface. The composite powder was prepared by ball milling, and then the diamond-copper composites were fabricated by rapid hot pressing. The results showed that at a diamond content of 30 vol. %, the composite achieved a thermal conductivity of 467 W/(m•K) with significantly improved interfacial bonding. The successful application of nickel coating by chemical deposition method provided

good thermal characteristics of diamond-copper composite. Copper powder with average particle size of 7 μm and nickel-coated diamond particles with average particle size of 120 μm were used as starting materials. These powders were homogenized by ball mill for 2 hours at 180 rpm, after which the uniformly mixed powder was loaded into a graphite mold. The consolidation process included cold pressing the powder compact at 50 MPa for 30 minutes, transferring the compact to a spark plasma sintering (SPS) furnace and vacuuming the chambers to 1.3×10^{-1} Pa. Subsequently, the pressure was applied at a rate of 10 MPa/min until 50 MPa was reached, while simultaneously heating to 800 °C at a rate of 100 °C/min. The temperature and pressure were maintained at 800 °C and 50 MPa for 10 minutes, after which the heating was stopped and natural cooling was carried out to room temperature. The corresponding surface condition of the nickel-coated diamond grain is shown in Fig. 3. Fig. 3 (g) and (h) show diamond particles coated with nickel by chemical deposition. The enlarged image of the nickel coating (h) confirms the formation of a homogeneous, dense and non-porous nickel layer. Based on the results obtained [13], it was found that an excessively long time of chemical nickel plating leads to the formation of a very thick coating, while an insufficient coating time can lead to excessive porosity at the interface between the coating and diamond. Therefore, a coating time of 5 minutes was chosen as the optimal conditions for this study.

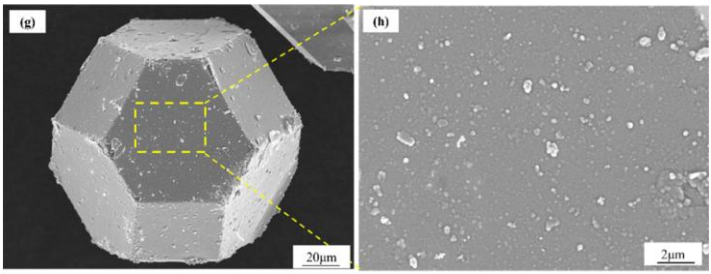

Fig. 3. g: Diamond grain with nickel coating; h: Enlarged image of the surface in Fig. (g) [13].

The above applies to the most common superhard material – diamond, but developments are also underway for a second superhard material – cubic boron nitride (cBN).

Thus, to improve the interfacial bonding between cBN and the SiAlON matrix, suppress the high-temperature phase transformation of cBN, and increase the synthesis density of SiAlON/cBN composites, the surface modification of cBN was carried out by the sol-gel method in this study. Using tetraethyl orthosilicate (TEOS) as a precursor and ammonia solution as a catalyst, a dense sintered SiO_2 coating was

deposited on cBN particles. Experimental results show that the sol-gel method successfully deposits a homogeneous, dense, and amorphous SiO_2 shell on cBN particles. The coating thickness shows precise controllability during the multi-cycle coating process (≈30 nm per cycle). For the SiAlON/20 wt.% cBN (coated) ceramic composite obtained using cBN particles after three coating cycles, the interfacial bonding between the cBN particles and the SiAlON matrix is significantly improved, demonstrating appreciable chemical bonding. The fracture mode transforms from intergranular to mixed transcrystalline-intergranular. Compared to the uncoated counterpart, its mechanical properties are significantly improved: the bulk density reaches 3.01 g/cm³, the Vickers hardness is 17.1 GPa, and the crack resistance reaches 4.76 MPa·m$^{1/2}$. This work demonstrates that the application of SiO_2 coating by the sol-gel method is an effective strategy for optimizing the characteristics of SiAlON/cBN ceramic composites [14].

We have already seen above that various coatings are applied to diamonds to protect them or improve their wettability, but diamond itself, in the form of films of microcrystalline or nanocrystalline diamond, is applied to various materials to improve their functional characteristics.

Thus, titanium alloys are widely used in the aerospace industry due to their good comprehensive properties. However, as the scope of application expands, higher requirements are placed on the corrosion resistance of titanium alloys. Due to its natural chemical stability, diamond is a good corrosion-resistant material. Diamond films with three different grain sizes were obtained on the surface of titanium alloys by the method of chemical vapor deposition (HFCVD). The efficiency of substrate protection by three types of films exceeds 90%. The corrosion resistance of nanocrystalline diamond (NCD) films is clearly higher than that of microcrystalline diamond (MCD) films. For NCD films, when the diamond grain size decreases, a cluster structure of particle stacking is formed, which prevents the ingress of aggressive substances to the substrate and additionally increases corrosion resistance [15].

Diamond-coated carbide (WC-Co) milling cutters are widely used for machining graphite or other difficult-to-machine materials. However, improvements in substrate adhesion and cutter life are urgent. In [16], a new electrostatic self-assembly method is demonstrated to solve this problem. The process involves immersing a two-step chemical pre-treated cutter in a specially prepared solution containing deionized water, nanodiamonds (NA) and trimethylammonium chloride. Compared to conventional pre-treatment by scratching or etching, this approach significantly increases the density and improves the uniformity of diamond grains during the nucleation process. As a result of this new approach, it is possible to achieve improvements in both the adhesion of the film to the substrate and the wear

resistance of the coated tools. The electrostatic self-assembly process enhances adhesion, which is reflected in the cooling phase. The electrostatic self-assembly etching has the unique ability to prevent direct delamination of the diamond film after growth at a substrate temperature of 920 °C. Cutters with intact MCD (microcrystalline diamond) coating (deposited at 860 °C) pretreated with this new pretreatment process show the longest service life [16].

Finally, let us pay attention to coatings that are applied to hard alloys and steels, and researchers here mainly pay attention to coatings with the presence of titanium, which, as we showed above, has shown its effectiveness in coatings on diamond.

In the study [17], a systematic analysis of the wear phenomenon of TiAlN-coated tools during dry milling of Ti-6Al-4V alloy was carried out. Additionally, the effect of tool wear on the morphology of the machined surface was studied. The results showed that diffusion wear of the tool is defined as the diffusion of Co and W elements outwards. Diffusion wear increases, with the diffusion of Co and W elements being the main cause of diffusion wear of the tool. The diffusion of Ti element is more sensitive to changes in temperature and pressure. During the tool wear process, a synergistic effect between diffusion and adhesive wear was observed. The combined effect of diffusion and oxidative wear weakened the strength of the tool. The main types of defects on the machined surface were grooves, pits, surface tears and sticking. In addition, as the tool wear increased, the chips transformed from conical spiral to arc-shaped, and the degree of sawtoothness of the chips increased [17].

Hard coatings are widely used in materials science as surface coatings to protect mechanical parts subject to friction. For the coating to be functionally successful, it must have high wear resistance. Experimental work was performed on multilayer TiN/CrN coatings with different modulated periods, deposited on XC48 steel substrates with two different surface roughnesses, by the direct current magnetron sputtering method. Their tribological characteristics were investigated after dry sliding wear tests using a tribometer with a “ball on flat surface” contact configuration. The wear mechanisms of TiN/CrN coatings are dominated by oxidation of wear residues and counter-transfer of material. Both decreasing the period thickness and increasing the substrate surface roughness significantly affect the wear rate. Coatings on rougher substrates showed improved wear resistance. However, changing the period thickness of the multilayer layer and increasing the substrate roughness did not lead to a significant improvement in wear resistance [18].

In wind power and other industries, Al_2O_3/TiO_2 coatings are prepared and ground on bearing rings to provide electrical erosion-resistant insulation for high-voltage motors. The wet chemical mechanical grinding (WCMG) process of the hard-brittle Al_2O_3/TiO_2 coating using a combination of a structured diamond

abrasive pad and NaOH solution has significant advantages in suppressing crack formation, reducing surface roughness, and improving surface integrity. It is assumed that the mechanism of material removal can be converted from mechanical brittle fracture to plastic removal caused by plastic deformation of the softened surface of the workpiece as a result of the chemical reaction between the NaOH solution and the Al_2O_3/TiO_2 composite. The surface roughness of the coating was reduced from an initial Sa of 3.293 μm to a final Sa of 0.049 μm in the WCMG process with a grain size of 3 μm and pH of 12.01, which is mainly attributed to the plastic removal of the chemically softened coating surface [19]. Fig. 4 illustrates the principle of the WCMG process of the Al_2O_3/TiO_2 composite coating on the bearing ring.

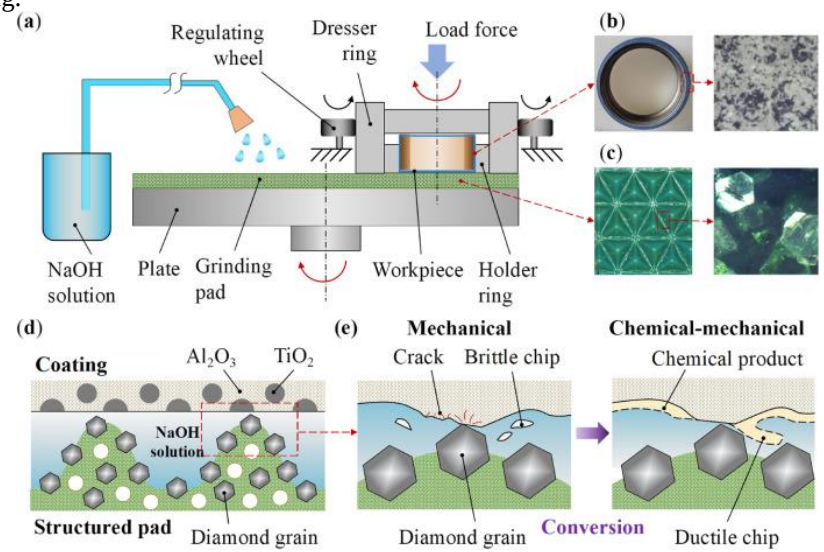

Fig. 4. Schematic diagram of the WCMG process on an Al_2O_3/TiO_2 coating of an insulated bearing, showing (a) the setup, (b) the workpiece, (c) the abrasive pad, (d) the cross-section of the grinding area, and (e) the chemical-mechanical removal of plastic material [19].

The end face of the workpiece is ground on a single-sided lapping and polishing machine using a combination of a structured diamond abrasive disc and NaOH solution. During the grinding process, as shown in Fig. 4(a), an abrasive pad is mounted on the rotating bottom plate of the machine, one end face of the workpiece is placed on the grinding pad, the geometric center of the circular workpiece is limited by the combination of the holder ring, the dressing ring and the position controller, and the workpiece rotates around its geometric center, while a loading force is applied to the other end face of the workpiece, and the NaOH solution is

pumped onto the surface of the grinding plate. In particular, there are two areas that appear white and black on the surface of the workpiece coating, containing Al_2O_3 and TiO_2 components, respectively, as shown in Fig. 1(b); in addition, an array structure of triangular pyramidal grooves is fabricated on the surface of the grinding plate, as shown in Fig. 4(c). During the grinding process, the NaOH solution is filled into the grooves of the grinding pad that contacts the surface of the workpiece coating, so that a chemical reaction can be initiated between the NaOH solution and the Al_2O_3/TiO_2 composite, resulting in two advantages as follows. The original hard brittle material on the surface of the workpiece can become softer and can be easily removed, contributing to the increase in the material removal rate. Many surface defects, especially cracks in the Al_2O_3 component area, can be significantly suppressed, explaining that the traditional mechanical removal, which causes brittle fracture caused by micro-cutting of abrasive grains, can be transformed into a term of plastic removal with elastoplastic deformation of softer chemical products under the synergistic effect of mechanical removal and chemical reaction.

Conclusions

Thus, it is possible to draw the following conclusions from the above.

1. In a number of studies, diamond particles are first coated with thin layers of titanium and nickel to ensure a tight interface with the nickel matrix. The wetting of diamond and nickel is improved by applying thin layers of titanium and nickel to the diamond particles.

2. The Ti-coated diamond micropowder was completely covered with a Ni electroplated layer, and the TiC formed between the Ti-coating and diamond provided a stronger interfacial adhesion force compared to that of the Ni-coated diamond micropowder. The titanium coating obtained under a pressure of 1.0 Pa was thin and uniform, without obvious defects, demonstrating optimal deposition quality and adhesion density. In addition, it was determined that the annealing temperature plays a key role in the reaction between Ti-coating and diamond. The TiC phase in Ti-coated diamond particles showed a gradual increase with increasing temperature, and the Ti-coated diamond underwent complete transformation into TiC-coated diamond at 1000 °C. That is, the production of titanium carbide is important.

3. In addition to titanium carbide, other carbides have been used by researchers. For example, B_4C coatings have been successfully synthesized on the surface of faceted diamond crystals by the carbothermic reduction method using a precursor system containing B_2O_3 and B. B_4C coatings consist mainly of rod-shaped crystals, which show preferential deposition on the (110) diamond surface compared to the (111) surface. Furthermore, the thickness of the B_4C coatings increases with

increasing temperature, reaching complete and uniform coverage of both (100) and (111) diamond faces at 1200 °C.

4. Vanadium carbide-coated diamonds were fabricated by the molten salt method. The results showed that compared to uncoated diamonds, the static compressive strength and oxidation resistance of coated diamonds were increased. The vanadium carbide coatings were mainly composed of V_2C and VC.

5. To improve the thermal properties of diamond/metal composites, a metal carbide layer is needed that combines both the crystal structure and the heat transfer of heterogeneous interfaces. Experiments have been conducted with diamond/Cu–Cr composites and the effectiveness of chromium carbides has been proven.

6. In addition to carbides, the effective action of oxides in diamond coatings has also been proven. The mechanism of diamond protection in this study was the predominant oxide donor behavior of Mo–B–C coatings to form a stable oxide layer on the diamond surface. For coatings with low B content, four stages of coating oxidation were observed sequentially with increasing temperature, low-temperature evaporation of MoO_3, stable protection of B_2O_3, and rapid evaporation of B_2O_3. For high-B coatings, the predominant self-reducing flux of B_2O_3 not only suppressed the evaporation of MoO_3, but also provided a reducing environment for MoO_3 to form MoO_2 and Mo_2C with high melting points, which led to the formation of a double synergistic protective oxide layer and significantly enhanced the oxidation resistance of diamonds.

7. Diamond films with three different grain sizes were obtained on the surface of a titanium alloy by the method of chemical vapor deposition (HFCVD). The efficiency of substrate protection by three types of films exceeds 90%. The corrosion resistance of nanocrystalline diamond (NCD) films is clearly higher than that of microcrystalline diamond (MCD) films. For NCD films, when the diamond grain size decreases, a cluster structure of particle stacking is formed, which prevents the ingress of aggressive substances to the substrate and additionally increases corrosion resistance. At the same time, cutters with an intact MCD coating (deposited at 860°C) demonstrate the longest service life.

8. Finally, let us pay attention to coatings applied to hard alloys and steels, and researchers here mainly pay attention to coatings with the presence of titanium, which, as we have shown above, has shown its effectiveness in coatings on diamond, namely TiAlN, TiN/CrN and Al_2O_3/TiO_2.

References: 1. Highly conductive diamond skeleton reinforced Cu-matrix composites for high-efficiency thermal management / *Zengkai Jiao, Long Zhang, Zejun Deng, Haichao li, Xiang Wang, Yuan Gang, Yijia Wang, Li Ma, Kechao Zhou, Qiuping Wei*. Applied Surface Science. Volume 645, 1 February 2024, 158829. https://doi.org/10.1016/j.apsusc.2023.158829. **2.** Amorphous carbon interlayer modulated interfacial thermal conductance between Cu and diamond / *Yongjian Zhang, Ziyang Wang, Ning Li,*

Fangyuan Sun, Jinpeng Hao, Haijun Wu, Hailong Zhang. Applied Surface Science. Volume 638, 30 November 2023, 158001. https://doi.org/10.1016/j.apsusc.2023.158001. **3.** Mo_2C interface layer: effect on the interface strength and cutting performance of diamond/Fe-Ni-WC composites / *Xinyue Mao, Qingnan Meng, Mu Yuan, Sifan Wang, Shiyin Huang, Baochang Liu*. Journal of Materials Research and Technology. Volume 25, July–August 2023, pp. 2029–2039. https://doi.org/10.1016/j.jmrt.2023.06.098. **4.** Ti-coated diamond micro-powder for the manufacture of the electroplated diamond wire saw / *Shengyao Su, Jianbing Zang, Yingke Zhou, Xinxin Zhang, Weifeng Liu, Zhenhao Wang, Menghui Zhao, Yanhui Wan.* Diamond and Related Materials. Volume 147, August 2024, 111273. https://doi.org/10.1016/j.diamond.2024.111273. **5.** Oxidation mechanism and high–temperature strength of Mo–B–C-coated diamonds in the 700°C–1200 °C temperature range / *Xinyue Mao, Qingnan Meng, Sifan Wang, Shiyin Huang, Mu Yuan, Yuting Qiu*. Journal of Materials Research and Technology. Volume 33, November–December 2024, pp. 7829–7841. **6.** Growth behavior of B_4C coatings on diamond faceted crystals via carbothermal reduction process / *Zhimin Chang, Yan Xiao, Zhenhui Chen, Meijun Yang, Song Zhang, Takashi Goto, Rong Tu*. Applied Surface Science. Volume 729, 30 May 2026, 166229. https://doi.org/10.1016/j.apsusc.2026.166229. **7.** Inhibition effect of covalent carbon nanosheets on mechanochemical wear of diamond / *Ni Chen, Junyi Zhao, Runkai Wang, Bo Yan, Yang Wu, Liang Li, Nan Yu, Ning He.* Materials & Design. Volume 237, January 2024, 112573. https://doi.org/10.1016/j.matdes.2023.112573. **8.** *Dandan Wu, Chengyong Wang, Xiaoyue Hu, Wanglin Chen*. Fabrication and characterization of highly thermal conductive Si_3N_4/diamond composite material. Materials & Design. Volume 225, January 2023, 111482. https://doi.org/10.1016/j.matdes.2022.111482. **9.** Laser powder bed fusion of diamond/N6 MMCs enabled by Ni-Ti coated diamond particles / *Sheng Zhang, Minglu Ding, Lu Wang, Wenjun Ge, Wentao Yan*. Materials & Design. Volume 217, May 2022, 110635. https://doi.org/10.1016/j.matdes.2022.110635. **10.** Reaction mechanisms for Ti coatings on diamond / *Xing Xu, Bingbing Wan, Wenfang Li, Fenghua Liu, Tongguang Zhai, Lijuan Zhang, Gongbin Tang*. Carbon. Volume 226, June 2024, 119206. https://doi.org/10.1016/j.carbon.2024.119206. **11.** *Xueqi Wang, Jianbo Tu, Baochang Liu*. Enhancement of mechanical and thermal properties of diamond particles via vanadium carbide coatings. Diamond and Related Materials. Volume 148, October 2024, 111510. https://doi.org/10.1016/j.diamond.2024.111510. **12.** Quantitative control of interfacial structure and thermal conductivity between diamond and copper via thermal diffusion of alloying element / *Yizhe Cao, Bo Li, Lei Liu, Shaolong Li, Dongxu Hui, Shaodi Wang, Huiying Liu, Xin Li, Xin Zhang, Shengyin Zhou, Shufeng Li*. Journal of Materials Research and Technology. Volume 33, November–December 2024, pp. 6641–6655. https://doi.org/10.1016/j.jmrt.2024.10.250. **13.** Effect of nickel-coated diamond on the thermal conductivity of copper matrix composites / *Yi Sun, Haohao Zou, Huadong Ye, Weiwei Zhu, Ying Han, Zhenxin Duan, Suqiu Jia, Xu Ran*. Journal of Materials Research and Technology. Volume 41, March–April 2026, pp. 2583–2592. https://doi.org/10.1016/j.jmrt.2026.01.112. **14.** *Xiuyi Chen, Kanglei Cao, Hanze Liang, Xinyan Yue*. Study on coating process and properties of SiAlON/cBN composites prepared by SiO_2-coated cBN particles. Ceramics International. Volume 52, Issue 7, March 2026, pp. 8633–8646. https://doi.org/10.1016/j.ceramint.2026.01.061. **15.** Corrosion resistance of diamond films with different grain sizes / *Zekai Liu, Zesen Zhuang, Xi Chen, Qiang Lin, Bin Shen, Sulin Chen*. Diamond and Related Materials. Volume 146, June 2024, 111162. https://doi.org/10.1016/j.diamond.2024.111162. **16.** Performance evaluation of diamond coated milling cutter fabricated based on electrostatic self-assembly seeding / *Enzhi Liu, Yu Qiao, ShiFei Chen, Yongkun Li, Da Shu, Xinchang Wang*. Diamond and Related Materials. Volume 148, October 2024, 111374. https://doi.org/10.1016/j.diamond.2024.111374. **17.** Analysis of tool wear of TiAlN coated tool, machined surface morphology and chip during titanium alloy milling / *Guanghui Fan, Jingjie Zhang, Hui Chen, Guangchun Xiao, Zhaoqiang Chen, Mingdong Yi, Chonghai Xu, Lili Fan, Guangqiang Li*. Tribology International. Volume 197, September 2024, 109751. https://doi.org/10.1016/j.triboint.2024.109751. **18.** Improvement of the tribological behavior of TiN/CrN

multilayer coatings by modulation wavelength variation / *Taous Doria Atmani, Mohammed-Said Bouamerene, Mohammed Gaceb, Corinne Nouveau, Hamid Aknouche*. Tribology International. Volume 192, April 2024, 109226. https://doi.org/10.1016/j.triboint.2023.109226. **19.** Surface roughness and fracture cracks of Al_2O_3/TiO_2 composite coating by wet chemical mechanical grinding with structured abrasives pad / *Weifeng Yao, Zhan Chen, Jianguo Yang, Fenfen Zhou, Tianqi Zhang, Jian Dong, Yuhui Zhang*. Journal of Materials Research and Technology. Volume 33, November–December 2024, pp. 361–375. https://doi.org/10.1016/j.jmrt.2024.09.058.

.

Валерій Лавріненко, Київ, Україна, Володимир Солод, Кам'янське, Україна, Предраг Дашич, Бєлград, Сербія

АЛМАЗИ З ПОКРИТТЯМИ ТА АЛМАЗНІ ПОКРИТТЯ (ОГЛЯД СУЧАСНИХ РОЗРОБОК)

Анотація. *Покриття зерен алмазів є важливим фактором впливу на зміну їх властивостей та підвищення утримання у зв'язуючому робочого шару шліфувального кругу. Враховуючи, що цей напрямок активно розвивається, в даній роботі нами зупинена увага саме на сучасних напрацюваннях, які є у наукових публікаціях за останні 5 років. Вкажемо, що тут нас найбільше цікавили розробки у напрямку нанесення покриттів на алмазні зерна, які би застосовувалися у абразивних композитах та композитах для різального інструменту, композитах алмаз-метал із підвищеною теплопровідністю, а також особливості нанесення та застосування алмазних покриттів на інструментальних матеріалах. Сучасні дослідження свідчать про ефективність застосування в покриттях на алмазних зернах тонких шарів титана і нікелю, щоби забезпечити щільне поєднання інтерфейсу з нікелевою матрицею. Змочування алмаза і нікелю поліпшується за рахунок нанесення тонких шарів титана і нікелю на частинки алмаза. Карбід титану, що утворюється між Ti-покриттям і алмазом, забезпечує більш сильну силу міжфазного зчеплення у порівнянні з силою алмазного мікропорошку з Ni-покриттям. Для поліпшення теплових властивостей композитів алмаз/метал потрібен шар металічного карбіду, який поєднує як кристалічну структуру, так і тепловий переніс гетерогенних інтерфейсів. У сучасних дослідженнях в покриттях окрім TiC, звертається увага і на інші карбіди: B_4C, V_2C та VC, а також на карбіди хрому. Окремим напрямком є оксидні покриття на алмазах. Механізм захисту алмазів в цьому напрямку уявляє собою переважну окисну донорну поведінку покриттів Mo–B–C для формування стабільного оксидного шару на поверхні алмаза. Алмазні плівки з трьома різними розмірами зерен були отримані на поверхні титанового сплаву методом хімічного осадження з парової фази (HFCVD). Корозійна стійкість плівок нанокристалічного алмаза (NCD) явно вище, аніж у плівок мікрокристалічного алмаза (MCD). Але фрези з непошкодженим покриттям MCD демонструють найбільш довгий термін служби. Звернено увагу на покриття, які наносяться на тверді сплави та сталі, причому переважно дослідники тут надають увагу саме покриттям з наявністю титану, а саме TiAlN, TiN/CrN та Al_2O_3/TiO_2.*

Ключові слова: *алмази з покриттями; покриття нікелем; покриття титаном; карбід титану; карбід бору; карбід ванадію; оксидне покриття; плівки з нанокристалічного алмазу; плівки з мікрокристалічного алмазу.*

UDC 658.511 **doi: 10.20998/2078-7405.2026.104.02**

SUPPLIER SEGMENTATION BASED ON PERFORMANCE DATA USING HIERARCHICAL CLUSTERING

Ágota **Bányai** [0000-0002-2537-7301]

University of Miskolc, 3515 Miskolc-Egyetemváros, Hungary
agota.banyaine@uni-miskolc.hu

Received: 25 March 2026 / Revised: 27 April 2026 / Accepted: 10 May 2026 / Published: 15 May 2026

Abstract. *In many manufacturing environments, procurement managers must regularly compare suppliers with significantly different performance profiles, which makes structured evaluation essential. Grouping suppliers with similar performance characteristics can make procurement decisions more transparent and easier to justify in practice. However, supplier performance is typically described by multiple evaluation criteria measured on different scales, and these performance characteristics may change over time. For this reason, analytical approaches are required that can handle both the multidimensional nature of the data and the changes in supplier performance over time. In this paper, an adaptive supplier segmentation approach is developed based on hierarchical clustering techniques. Supplier performance is evaluated using multiple operational criteria, including quality rate, on-time delivery, unit price, lead time, complaint frequency, and operational flexibility. After applying min–max normalization and weighted performance evaluation, supplier similarities are calculated using Euclidean distance, and hierarchical clustering methods are applied to identify homogeneous supplier groups. Several linkage strategies are compared, and the clustering quality is assessed using internal validation indices such as the Silhouette, Davies–Bouldin, Calinski–Harabasz, and Dunn indices. The empirical analysis is conducted on a dataset containing 15 suppliers observed in two consecutive evaluation periods. The results indicate that hierarchical clustering can reveal interpretable supplier groups with clearly distinguishable performance profiles. A comparison of clustering structures across consecutive periods also shows that supplier segmentation evolves as new performance data become available.*
Keywords: *adaptive supplier segmentation; hierarchical clustering; supplier evaluation; cluster validation; supply chain management; multi-criteria decision analysis; performance-based clustering; supplier performance analysis.*

1. Introduction

In industrial practice, procurement managers often deal with dozens of suppliers whose performance differs not only in cost but also in reliability and flexibility. Some suppliers consistently deliver high-quality products and meet delivery deadlines, while others may offer lower prices but struggle with reliability or flexibility. In such environments, evaluating and managing the supplier base becomes a complex task. In most real-world cases, procurement decisions rely on multiple performance indicators rather than a single metric [1,2].

In practice, organizations often monitor supplier performance using indicators

such as product quality, delivery reliability, procurement cost, lead time, or the frequency of service-related issues. These indicators provide valuable information about the operational capabilities of suppliers. However, when several suppliers are evaluated simultaneously across multiple criteria, interpreting the results becomes increasingly difficult. Even experienced managers may find it challenging to identify patterns in the data or determine which suppliers exhibit similar performance profiles.

Another important challenge is that supplier performance is not static [3]. Over time, suppliers may improve their processes, introduce technological innovations, or adjust their pricing strategies. Conversely, operational disruptions, capacity constraints, or logistical challenges may temporarily reduce supplier performance. As a result, the structure of the supplier base can change continuously. A supplier that was previously considered reliable may gradually lose its competitive position, while another supplier may become more attractive due to improvements in quality or delivery performance. This dynamic nature of supplier performance suggests that supplier evaluation should not be treated as a one-time classification problem but rather as an ongoing analytical process.

Data-driven analytical methods can support this process by revealing patterns in multidimensional performance data. Among these methods, clustering techniques have gained increasing attention in supply chain analytics [4,5]. Clustering methods group entities according to similarity, allowing analysts to identify homogeneous groups within complex datasets. When applied to supplier performance data, clustering techniques can reveal groups of suppliers with similar operational characteristics, thereby supporting more structured procurement strategies.

Despite the growing use of data analytics in supply chain management, many supplier evaluation approaches still focus on static analyses. In practice, however, supplier performance data are updated periodically, and analytical tools should be able to incorporate these changes. This highlights the importance of adaptive analytical frameworks that allow supplier segmentation to evolve when new performance information becomes available.

Motivated by these considerations, this study proposes an adaptive supplier segmentation framework based on hierarchical clustering techniques. The proposed approach evaluates suppliers using multiple operational performance criteria and groups them according to their performance characteristics. In addition, the framework allows the clustering structure to be updated when new data become available, enabling the analysis of how supplier groups evolve over time.

The empirical analysis is conducted using a dataset containing fifteen suppliers evaluated across six performance indicators. Several hierarchical clustering methods are examined and compared using multiple cluster validation indices. By analysing supplier clusters across two consecutive evaluation periods, the study demonstrates

how adaptive clustering can capture structural changes in supplier performance and provide valuable insights for procurement decision-making.

2. Problem description

Supplier evaluation and segmentation represent a critical task in modern supply chain management. Organizations typically cooperate with multiple suppliers whose performance may differ significantly in terms of quality, delivery reliability, procurement cost, operational lead time, and service flexibility. Effective supplier management therefore requires analytical tools capable of identifying homogeneous groups of suppliers based on their operational characteristics.

In many practical situations, supplier performance is evaluated using several criteria measured on different scales. These criteria may include both benefit-type indicators, where higher values indicate better performance (e.g., quality rate or delivery reliability), and cost-type indicators, where lower values are preferable (e.g., procurement cost or lead time). Because of this multidimensional structure, it is often difficult for procurement managers to directly identify patterns in supplier performance.

Another important challenge arises from the dynamic nature of supplier performance. Operational conditions, production efficiency, logistics processes, and service quality may change over time. As a result, supplier performance data must be periodically re-evaluated, which may lead to changes in the segmentation structure of the supplier base.

The objective of the present study is therefore to develop a data-driven framework capable of grouping suppliers according to their performance characteristics while also allowing the segmentation structure to adapt when updated performance data become available. The proposed approach applies hierarchical clustering techniques combined with multiple cluster validation measures in order to identify meaningful supplier groups and evaluate the stability of the segmentation over time.

Figure 1 illustrates the conceptual structure of the proposed supplier segmentation problem. Supplier performance data are collected for multiple evaluation criteria, normalized to ensure comparability, and then processed using hierarchical clustering. The resulting clusters represent groups of suppliers with similar performance characteristics. When new performance data become available in a subsequent evaluation period, the clustering process is repeated, enabling the identification of structural changes in supplier segmentation.

3. Mathematical Model of Adaptive Supplier Segmentation

The proposed adaptive supplier segmentation model is based on hierarchical clustering techniques applied to supplier performance indicators. The objective of the model is to identify homogeneous groups of suppliers according to their

operational performance while allowing the segmentation structure to be updated dynamically as new data become available.

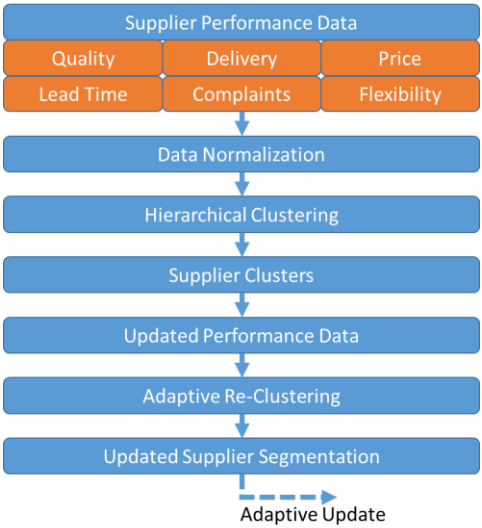

Figure 1 – Conceptual framework of adaptive supplier segmentation with feedback loop [own elaboration].

Let $S = \{s_1, s_2, \dots, s_n\}$ denote the set of suppliers where n represents the total number of suppliers considered in the evaluation process.

Supplier performance is described using a set of evaluation criteria $K = \{k_1, k_2, \dots, k_m\}$, where m denotes the number of performance indicators. These criteria typically represent key operational indicators such as quality level, delivery reliability, procurement cost, complaint rate or lead time.

The performance of suppliers with respect to the defined criteria can be represented in the form of a decision matrix $X = [x_{ij}]$, where x_{ij} denotes the performance value of supplier s_i with respect to criterion k_j. The matrix can therefore be written as

$$X = \begin{bmatrix} x_{11} & x_{12} & \cdots & x_{1m} \\ x_{21} & x_{22} & \cdots & x_{2m} \\ \vdots & \vdots & \ddots & \vdots \\ x_{n1} & x_{n2} & \dots & x_{nm} \end{bmatrix}.$$

Because the criteria are measured on different scales, normalization is required before further analysis. The normalized performance value is calculated using min–max normalization

$$z_{ij} = \frac{x_{ij} - min\ (x_j)}{max(x_j) - min\ (x_j)},$$

where z_{ij} represents the normalized value of criterion j for supplier i. The normalized matrix can be expressed as $Z = [z_{ij}]$.

In order to incorporate the relative importance of evaluation criteria, a weight vector $W = \{w_1, w_2, \dots, w_m\}$ is defined where

$$\sum_{j=1}^{m} w_j = 1.$$

For cost criteria higher normalized values represent higher cost levels. The weighted normalized matrix can therefore be calculated as $v_{ij} = w_j \cdot z_{ij}$.

The similarity between suppliers is determined by calculating the distance between supplier vectors in the multidimensional performance space. In this study the Euclidean distance is applied

$$d_{ik} = \sqrt{\sum_{j=1}^{m} (v_{ij} - v_{kj})^2},$$

where d_{ik} denotes the distance between suppliers s_i and s_k. The resulting distance matrix is defined as $D = [d_{ik}]$.

Based on the distance matrix, hierarchical clustering is performed in order to identify homogeneous supplier groups. In hierarchical clustering the algorithm starts with n individual clusters and iteratively merges the closest clusters until a hierarchical structure is formed.

Let $C = \{c_1, c_2, \dots, c_k\}$ denote the set of clusters obtained during the clustering process. Different linkage strategies can be applied to determine the distance between clusters.

In the case of single linkage, the distance between two clusters is defined as the minimum pairwise distance between their elements

$$d(C_a, C_b) = \min_{i \in C_a, j \in C_b} d_{ij}.$$

For complete linkage, the distance is determined by the farthest pair of elements

$$d(C_a, C_b) = \max_{i \in C_a, j \in C_b} d_{ij}.$$

The average linkage method calculates the mean distance between all elements of the two clusters

$$d(C_a, C_b) = \frac{1}{|C_a| \cdot |C_b|} \cdot \sum_{i \in C_a} \sum_{j \in C_b} d_{ij}.$$

Finally, the Ward method merges clusters based on the minimum increase of within-cluster variance [6]. The merging criterion is defined as

$$\Delta(C_a, C_b) = \frac{n_a \cdot n_b}{n_a + n_b} \cdot \|\mu_a - \mu_b\|^2,$$

where n_a and n_b denote the sizes of clusters C_a and C_b, while μ_a and μ_b represent their centroids.

The hierarchical clustering process results in a dendrogram that represents the nested grouping of suppliers.

Since different clustering strategies may produce different segmentation results, cluster validation techniques are required in order to evaluate the quality of the clustering structure.

One of the most widely used validation measures is the Silhouette index, which evaluates how well each supplier fits within its assigned cluster. For each supplier i, the average intra-cluster distance is defined as

$$a_i = \frac{1}{|C_i| - 1} \cdot \sum_{j \in C_i, j \neq i} d_{ij}.$$

The distance to the nearest neighbouring cluster is

$$b_i = \min_{C_k \neq C_i} \left(\frac{1}{|C_k|} \cdot \sum_{j \in C_k} d_{ij} \right).$$

The silhouette value is therefore

$$S_i = \frac{b_i - a_i}{\max(a_i, b_i)}.$$

The overall clustering quality is obtained by averaging over all suppliers

$$S = \frac{1}{\mathrm{n}} \cdot \sum_{i=1}^{n} S_i.$$

Another important validation measure is the Davies–Bouldin index [7], which evaluates the ratio between intra-cluster dispersion and inter-cluster separation

$$DB = \frac{1}{\mathrm{k}} \cdot \sum_{i=1}^{k} \max_{j \neq i} \left(\frac{\sigma_i + \sigma_j}{d(\mu_i, \mu_j)} \right),$$

where σ_i denotes the dispersion of cluster i.

The Calinski–Harabasz index [8] measures the ratio between between-cluster and within-cluster variance

$$CH = \frac{Tr(B_k)}{Tr(W_k)} \cdot \frac{n-k}{k-1},$$

where B_k and W_k represent the between-cluster and within-cluster dispersion matrices.

The Dunn index [9] evaluates cluster compactness and separation

$$D = \frac{\min\limits_{i \neq j} d(C_i, C_j)}{\max\limits_{k} diam(C_k)},$$

where $d(C_i, C_j)$ is the distance between clusters and $diam(C_k)$ is the diameter of cluster k.

In the proposed adaptive framework supplier performance data may change over time. Let $X^{(t)}$ represent the decision matrix observed in period t. The clustering structure is therefore defined as

$$C^{(t)} = HC\left(X^{(t)}\right),$$

where HC denotes the hierarchical clustering operator.

The stability of supplier segmentation across consecutive periods can be evaluated using the Jaccard similarity index [10,11]

$$J = \frac{\left|C^{(t)} \cap C^{(t+1)}\right|}{\left|C^{(t)} \cup C^{(t+1)}\right|}.$$

Higher values of J indicate greater stability of supplier segmentation over time.

The proposed mathematical framework therefore enables adaptive supplier segmentation by combining hierarchical clustering with multiple cluster validation metrics and temporal stability analysis.

4. Numerical Results

4.1. Description of the Dataset

The empirical analysis was conducted using a dataset containing 15 suppliers evaluated according to six performance criteria. Each supplier represents one row of the decision matrix, while each column corresponds to an evaluation criterion. The

suppliers are identified as $S_1, S_2, \ldots, S_{15}$. The selected criteria represent key operational and economic aspects of supplier performance, including product quality, delivery reliability, procurement cost, operational lead time, service reliability, and operational flexibility. Since these criteria are expressed in different measurement units and value ranges, normalization is required before applying the clustering procedure.

The criteria used in the evaluation process are summarized in Table 1.

Table 1 – Supplier evaluation criteria [own elaboration]

Criterion	Type	Measurement unit	Weight
Quality Rate	Benefit	%	0.25
On-Time Delivery	Benefit	%	0.20
Unit Price	Cost	numeric value	0.20
Lead Time	Cost	days	0.15
Complaints	Cost	number of cases	0.10
Flexibility	Benefit	rating (1–10)	0.10

Quality Rate, On-Time Delivery and Flexibility are treated as benefit criteria, where higher values indicate better supplier performance. In contrast, Unit Price, Lead Time and Complaints are considered cost criteria, where lower values are preferred. The weights assigned to the criteria reflect their relative importance in supplier evaluation and sum to one.

The supplier performance data used in the analysis are presented in Tables 2 and 3. Table 2 shows the evaluation values in period t, while Table 3 contains the updated performance values in period $t + 1$. The second dataset represents changes in supplier performance over time and enables the demonstration of the adaptive behaviour of the proposed clustering model.

Table 2 – Supplier performance data in period t [own elaboration]

Supplier	Quality	On-time delivery	Unit price	Lead time	Complaints	Flexibility
S1	96	95	110	8	1	9
S2	92	91	104	10	2	8
S3	88	87	99	13	3	7
S4	84	82	96	14	4	6
S5	79	80	92	16	5	5
S6	98	97	118	7	1	9
S7	90	89	102	11	2	7
S8	76	78	89	18	6	5
S9	81	83	95	15	4	6
S10	94	92	108	9	2	8
S11	87	86	101	12	3	7

S12	73	75	88	19	7	4
S13	85	84	97	14	4	6
S14	91	90	103	10	2	8
S15	78	79	91	17	5	5

Table 3 – Supplier performance data in period $t + 1$ [own elaboration]

Supplier	**Quality**	**On-time delivery**	**Unit price**	**Lead time**	**Complaints**	**Flexibility**
S1	97	96	111	8	1	9
S2	90	89	105	11	3	7
S3	89	88	100	12	3	7
S4	82	80	95	15	5	6
S5	77	78	91	17	6	5
S6	99	98	119	7	1	10
S7	91	90	101	10	2	8
S8	74	76	87	19	7	4
S9	83	84	94	14	4	6
S10	95	93	107	9	2	8
S11	86	85	100	13	4	7
S12	71	73	86	20	8	4
S13	84	83	96	15	5	6
S14	92	91	104	10	2	8
S15	80	81	92	16	5	5

The presence of two consecutive datasets allows the evaluation of how supplier clusters evolve when new performance information becomes available, thereby supporting the adaptive nature of the proposed supplier segmentation framework.

4.2. Hierarchical Clustering Results

Hierarchical clustering was applied to identify groups of suppliers with similar performance characteristics. Four linkage methods were tested in the analysis, namely single, complete, average, and Ward linkage. The number of clusters was fixed at $k = 3$, which provided an interpretable segmentation of the supplier base.

To determine the most appropriate clustering method, several internal validation indices were calculated, including the Silhouette index, Davies–Bouldin index, Calinski–Harabasz index, and the Dunn index. The results for period t are summarized in Table 4.

Table 4 – Validation indices for different linkage methods [own elaboration]

Method	Silhouette	Davies-Bouldin	Calinski-Harabasz	Dunn
Single	0.483	0.448	23.77	0.285
Complete	0.435	0.547	29.77	0.221
Average	0.435	0.547	29.77	0.221
Ward	0.462	0.562	30.93	0.203

The single linkage method achieved the highest Silhouette value (0.483) and the lowest Davies–Bouldin index (0.448), indicating the best balance between cluster cohesion and separation. The Dunn index also reached its highest value (0.285) for the single linkage solution. Although the Ward method produced the largest Calinski–Harabasz value (30.93), its Davies–Bouldin index was higher, indicating slightly weaker cluster separation. Based on the combined evaluation of the indices, the single linkage method was selected as the primary clustering approach.

The dendrograms obtained using the four linkage methods are shown in Figure 2. The graphical representation illustrates how suppliers are gradually merged during the hierarchical clustering process. Despite differences in merging distances and cluster compactness, the examined linkage methods consistently suggest the presence of three main supplier groups.

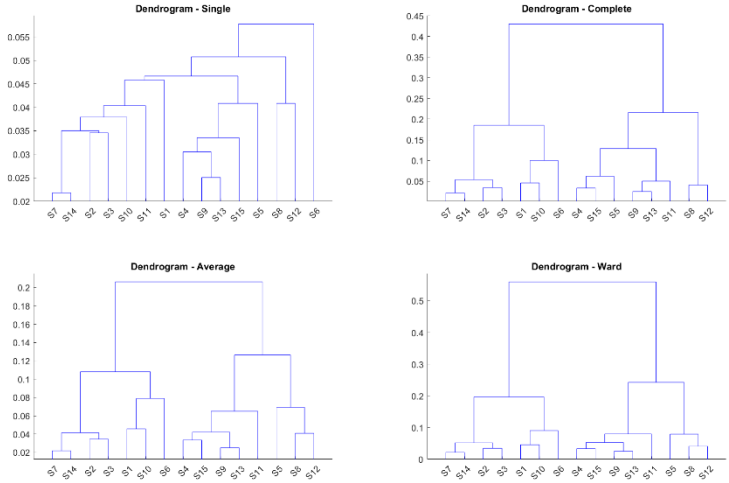

Figure 2 – The dendrograms obtained using the four linkage methods [own elaboration].

In the single linkage dendrogram, several suppliers form compact subclusters at low linkage distances. For example, suppliers S7 and S14 merge at very low

distances, indicating highly similar performance profiles. Similarly, suppliers S4 and S9, and S9 and S13, form closely connected subgroups within the second cluster. In contrast, supplier S6 joins the clustering structure only at a much higher linkage distance, indicating a significantly different performance profile compared to the rest of the supplier base.

Using the selected clustering configuration, suppliers were grouped into three clusters in period t. The resulting cluster composition was as follows: Cluster 1: S1, S2, S3, S7, S10, S11, S14; Cluster 2: S4, S5, S8, S9, S12, S13, S15; Cluster 3: S6.

Clusters 1 and 2 each contain seven suppliers, while Cluster 3 consists of a single supplier. The presence of a single-member cluster indicates that supplier S6 represents a distinct performance profile that differs substantially from the other suppliers.

The cluster mean profiles provide further insight into the differences between supplier groups. In period t, the normalized cluster averages show clear performance differences. Cluster 1 exhibits relatively high values for key benefit criteria, including Quality Rate (0.73), On-Time Delivery (0.68), and Flexibility (0.74). These values suggest that suppliers in this group demonstrate generally strong operational performance.

In contrast, Cluster 2 shows significantly lower performance levels in the benefit criteria, with average normalized values of 0.26 for Quality Rate and 0.23 for On-Time Delivery. At the same time, the normalized value of Unit Price reaches 0.85, indicating higher cost levels compared to the suppliers in Cluster 1. Consequently, Cluster 2 represents a group of suppliers with weaker overall performance.

Cluster 3, consisting solely of supplier S6, demonstrates extreme values across several criteria. The normalized performance values reach 1.0 for Quality Rate, On-Time Delivery, Lead Time, Complaints, and Flexibility, while the normalized Unit Price value equals 0, indicating the highest price level in the dataset. These results indicate that supplier S6 represents a supplier with excellent operational performance but relatively high procurement cost.

The clustering structure changed in the second evaluation period $(t + 1)$, reflecting changes in supplier performance values. In this period, the clusters were formed as follows: Cluster 1: S8, S12; Cluster 2: S1, S2, S3, S4, S5, S7, S9, S10, S11, S13, S14, S15; Cluster 3: S6.

Compared with period t, the cluster structure became more concentrated. Cluster 2 expanded to 12 suppliers, while Cluster 1 decreased to two suppliers. Supplier S6 remained isolated in Cluster 3 in both periods, confirming the stability of its distinct performance profile.

A comparison of cluster memberships across the two periods reveals that 9 out of 15 suppliers changed their cluster assignment, indicating substantial changes in supplier performance patterns. In particular, several suppliers originally belonging to Cluster 1 moved to Cluster 2 in the second period. Meanwhile, suppliers S8 and

S12 formed a separate cluster, indicating that their performance profiles became more distinct from the rest of the supplier base.

The clustering results reveal clearly distinguishable supplier groups that differ in both performance and cost structure.

4.3 Cluster Validation

To evaluate the quality of the clustering solutions obtained using different linkage methods, several internal validation indices were calculated. The analysis included four widely used cluster validity measures: the Silhouette index, the Davies–Bouldin index, the Calinski–Harabasz index, and the Dunn index. Each of these indices captures a different aspect of clustering quality, including cluster cohesion, cluster separation, and overall cluster structure.

The comparison of the validation indices for the examined hierarchical clustering methods in period $t$is illustrated in Figure 3.

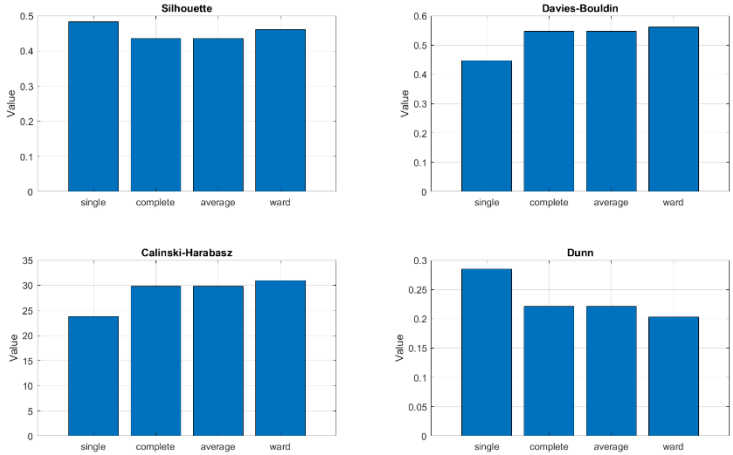

Figure 3 – Comparison of clustering validation indices for different linkage methods in period t [own elaboration].

The Silhouette index measures how well each observation fits within its assigned cluster compared with neighboring clusters. Higher values indicate better-defined clusters. As shown in Figure 3, the single linkage method achieved the highest Silhouette value (0.483) among the examined methods, suggesting the strongest overall cluster cohesion and separation. The Ward method produced a slightly lower value (0.462), while the complete and average linkage methods resulted in similar values of approximately 0.435.

The Davies–Bouldin index evaluates the average similarity between clusters, where lower values indicate better clustering performance. According to the results, the single linkage method again achieved the most favorable value (0.448),

indicating the best separation between supplier groups. The other methods produced noticeably higher values, ranging between 0.547 and 0.562, which suggests weaker cluster separation compared with the single linkage solution.

The Calinski–Harabasz index measures the ratio of between-cluster dispersion to within-cluster dispersion. In this case, the Ward linkage method achieved the highest value (30.93), followed by the complete and average linkage methods (approximately 29.77). The single linkage method produced a lower value (23.77), which can be explained by the presence of a small cluster consisting of a single supplier. Such cluster structures often reduce the between-cluster variance measured by this index.

Finally, the Dunn index, which evaluates the ratio between the minimum inter-cluster distance and the maximum intra-cluster diameter, also supports the effectiveness of the single linkage solution. The highest Dunn value (0.285) was obtained using the single linkage method, indicating stronger cluster separation compared with the other methods. The remaining methods produced lower values, ranging between 0.203 and 0.221.

Considering all four validation indices together, most validation indices favour the single linkage method for the examined supplier dataset. Although the Ward method performs well according to the Calinski–Harabasz index, the single linkage method consistently achieves better results in terms of Silhouette, Davies–Bouldin, and Dunn indices. Therefore, the single linkage method was selected as the most appropriate clustering approach for the subsequent supplier segmentation analysis.

4.4 Cluster Profile Analysis

The characteristics of the identified supplier clusters can be further examined through the analysis of cluster mean profiles. Figure 4 illustrates the average normalized performance values of the three clusters obtained using the single linkage method in period t.

The cluster profiles reveal substantial differences among the supplier groups across the six evaluation criteria: Quality Rate, On-Time Delivery, Unit Price, Lead Time, Complaints, and Flexibility.

Cluster 1 represents a group of suppliers with relatively strong overall performance. The average normalized value of Quality Rate reaches approximately 0.73, while On-Time Delivery equals 0.68, indicating a high level of product quality and delivery reliability. Similarly, the normalized values of Lead Time (0.71) and Flexibility (0.74) suggest that these suppliers are able to maintain efficient operational processes.

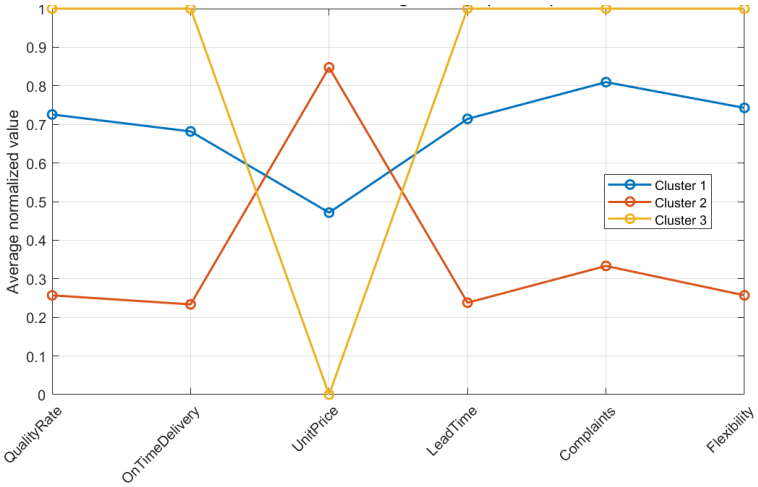

Figure 4 – Cluster profiles based on normalized supplier performance criteria [own elaboration].

The value of Unit Price (0.47) is moderate compared with the other clusters, indicating balanced cost performance. Additionally, the normalized value for Complaints reaches approximately 0.81, which indicates a relatively higher complaint frequency compared with the suppliers in Cluster 1.

Cluster 1 can be interpreted as a group of high-performing and reliable suppliers, representing the core supplier base with stable operational performance.

Cluster 2 shows considerably weaker performance across most evaluation criteria. The normalized value of Quality Rate decreases to approximately 0.26, while On-Time Delivery reaches only 0.23, indicating significantly lower reliability compared with Cluster 1. Similarly, the values for Flexibility (0.26) and Lead Time (0.24) suggest less efficient operational performance.

At the same time, the normalized Unit Price value reaches 0.85, indicating that suppliers in this cluster tend to have higher procurement costs. This combination of lower operational performance and higher cost values suggests that the suppliers in Cluster 2 represent a less competitive supplier group.

The cluster therefore can be interpreted as a group of average or potentially underperforming suppliers, which may require performance improvement initiatives or closer monitoring by procurement managers.

Cluster 3 contains a single supplier (S6) whose performance profile differs significantly from the rest of the supplier base. The normalized values reach 1.0 for Quality Rate, On-Time Delivery, Lead Time, Complaints, and Flexibility, indicating the best observed performance for these criteria in the dataset. At the same time the

normalized value of Unit Price equals 0, indicating the highest price level among the examined suppliers.

Such extreme values indicate that supplier S6 exhibits a distinct performance profile compared with the other suppliers. Consequently, Cluster 3 represents a supplier with a unique performance structure characterized by excellent operational indicators but relatively high procurement cost.

The comparison of the cluster profiles highlights clear structural differences between the supplier groups. Cluster 1 demonstrates strong operational performance with balanced cost levels, Cluster 2 exhibits lower quality and delivery performance combined with relatively higher costs, while Cluster 3 represents a distinct supplier with outstanding operational performance but unfavourable procurement cost.

These findings suggest that the clustering approach provides a useful, although not exhaustive, representation of supplier performance patterns. Such segmentation can provide valuable support for procurement decision-making, enabling managers to distinguish between strategic suppliers, standard suppliers, and exceptional high-performing suppliers within the supplier base.

4.5 Adaptive Supplier Segmentation

One of the key objectives of the proposed model is to demonstrate the adaptive nature of supplier segmentation, meaning that supplier groups can change when new performance data become available. To analyze these changes, the clustering results obtained in periods $t$and $t+1$were compared.

Table 5 summarizes the cluster memberships of suppliers in both periods. The results reveal that several suppliers changed their cluster assignment when the updated performance data were introduced.

Table 5 – Cluster memberships [own elaboration]

	1	**2**	**3**	**4**	**5**	**6**	**7**	**8**	**9**	**10**	**11**	**12**	**13**	**14**	**15**
Cluster *t*	1	1	1	2	2	3	1	2	2	1	1	2	2	1	2
Cluster *t+1*	2	2	2	2	2	3	2	1	2	2	2	1	2	2	2

A detailed examination of the results shows that 9 out of the 15 suppliers changed their cluster membership between the two evaluation periods. Specifically, suppliers S1, S2, S3, S7, S10, S11, and S14 moved from Cluster 1 to Cluster 2, while suppliers S8 and S12 moved from Cluster 2 to Cluster 1. These changes indicate that supplier performance patterns evolved between the two evaluation periods, leading to a different clustering structure.

In contrast, several suppliers remained stable in their cluster assignments. Suppliers S4, S5, S9, S13, and S15 remained in Cluster 2, while supplier S6 remained in Cluster 3 in both periods. The stability of supplier S6 confirms the

earlier observation that this supplier represents a distinct performance profile that differs significantly from the rest of the supplier base.

The cluster size distribution also changed considerably between the two periods. In period t, the clustering structure was relatively balanced, with Cluster 1 and Cluster 2 each containing 7 suppliers, while Cluster 3 contained a single supplier. However, in period $t + 1$the cluster structure became more concentrated. Cluster 2 expanded to 12 suppliers, while Cluster 1 decreased to only 2 suppliers, consisting of suppliers S8 and S12. Cluster 3 remained unchanged with a single supplier (S6).

These results indicate that the relative performance of suppliers changed over time. Several suppliers that previously belonged to the higher-performing cluster moved to a larger cluster representing average performance levels, suggesting a relative deterioration in their competitive position. Conversely, the formation of a small cluster containing suppliers S8 and S12 suggests that these suppliers became more distinct in terms of their performance characteristics.

The results confirm that the proposed clustering framework is capable of capturing dynamic changes in supplier performance. The adaptive clustering mechanism allows procurement managers to continuously reassess supplier groups as new performance information becomes available. Such dynamic segmentation provides valuable decision support in supplier relationship management, enabling organizations to identify stable strategic suppliers, suppliers with declining performance, and suppliers whose performance is evolving over time.

5. Discussion

The results demonstrate that hierarchical clustering can effectively support supplier segmentation based on multiple performance indicators. The applied methodology successfully identified meaningful groups of suppliers with clearly different operational characteristics. In particular, the clustering results revealed three distinct supplier categories, reflecting differences in quality performance, delivery reliability, procurement cost, and operational flexibility.

The comparison of clustering methods indicated that the single linkage approach provided the most suitable solution for the examined dataset. This result was supported by several internal validation indices, including the Silhouette, Davies–Bouldin, and Dunn indices, which collectively indicated better cluster cohesion and separation compared with the other linkage methods. Although the Ward method achieved the highest Calinski–Harabasz value, the overall evaluation of the indices favoured the single linkage solution.

The analysis of cluster profiles further highlighted the practical relevance of the segmentation results. Cluster 1 represents suppliers with relatively strong operational performance and balanced cost levels, while Cluster 2 contains suppliers with lower reliability and higher procurement costs. Cluster 3 consists of a supplier with a distinct performance profile characterized by excellent operational indicators

but relatively high procurement cost. These findings demonstrate that clustering can reveal complex performance patterns that may not be immediately visible in the raw data.

An important contribution of the proposed framework is its adaptive nature. The comparison of clustering results between periods t and $t+1$ showed that supplier groups may change as new performance information becomes available. In the presented case, nine out of fifteen suppliers changed their cluster membership, indicating that supplier performance is dynamic and requires continuous monitoring. Such adaptive segmentation enables procurement managers to periodically reassess supplier relationships and identify changes in supplier competitiveness. One limitation of the analysis is the relatively small sample size, which may influence the stability of the clustering results. From a managerial perspective, the identified clusters may support differentiated supplier management strategies, such as performance monitoring or contract renegotiation.

The results confirm that hierarchical clustering combined with performance-based evaluation criteria can provide a useful analytical tool for supplier segmentation and decision support in supply chain management. Future research may apply stability indices such as the Jaccard coefficient to further examine the temporal stability of supplier clusters.

References: 1. *Siino M., Iezzi S., Gara M.* Corruption risk indicators in public procurement: Definition and evaluation with organised crime data. Socio-Economic Planning Sciences. 2026, № 105, 102429. https://doi.org/10.1016/j.seps.2026.102429 **2**. *Ghyas Q.M., Akter T.* Critical Evaluation of Key Performance Indicators (KPI) in Procurement Management Information System (PROMIS): The Case of Bangladesh. ACM International Conference Proceeding Series. 2024, pp. 405 – 409. https://doi.org/10.1145/3670013.3670014 **3**. *Hoque I., Sumi R.S.* Buyer-supplier relational dynamics and supplier dynamic capabilities for improving environmental sustainability mitigating climate change vulnerabilities. Climatic Change. 2026, № 179, 8. https://doi.org/10.1007/s10584-025-04096-y **4**. *Keskin G.A.* A Novel Perspective to Sustainable Supplier Performance Evaluation Problem: A Case Study Based on Determining the Optimum Number of Clusters. International Journal of Information Technology and Decision Making. 2022, № 21, pp. 1349 – 1379. https://doi.org/10.1142/S0219622022500195 **5**. *Rahiminia M., Razmi J., Shahrabi Farahani S., Sabbaghnia A.* Cluster-based supplier segmentation: a sustainable data-driven approach. Modern Supply Chain Research and Applications. 2023, № 5, pp. 209 - 228. https://doi.org/10.1108/MSCRA-05-2023-0017 **6**. *Ogasawara, Y., Kon, M.* Two clustering methods based on the Ward's method and dendrograms with interval-valued dissimilarities for interval-valued data. International Journal of Approximate Reasoning. 2021, № 129, pp. 103 – 121. https://doi.org/10.1016/j.ijar.2020.11.001 **7**. *Ros, F., Riad, R., Guillaume, S.* PDBI: A partitioning Davies-Bouldin index for clustering evaluation. *Neurocomputing*. 2023, № 528, pp. 178 – 199. https://doi.org/10.1016/j.neucom.2023.01.043 **8**. *Preedasawakul, O., Wiroonsri, N.* A Bayesian cluster validity index. Computational Statistics & Data Analysis. 2025, № 202, 108053. https://doi.org/10.1016/j.csda.2024.108053 **9**. *Ncir, C.E.B., Hamza, A., Bouaguel, W.* Parallel and scalable Dunn Index for the validation of big data clusters. Parallel Computing. 2021, № 102, 102751. https://doi.org/10.1016/j.parco.2021.102751 **10**. *Krasnodębska, K., Goch, W., Uhl, J.H., Verstegen, J.A., Pesaresi, M.* Advancing Precision, Recall, F-score, and Jaccard index: An approach for continuous, ratio-scale measurements. Environmental Modelling & Software 2025. № 193, 106614. https://doi.org/10.1016/j.envsoft.2025.106614 **11**. *Chen, J., Qi, S., Wang, F., Xing, L., Chen, Y.* An Jaccard similarity coefficient-based evolutionary algorithm for sparse large-scale multi-objective

optimization problems. Swarm and Evolutionary Computation. 2026. № 100, 102269. https://doi.org/10.1016/j.swevo.2025.102269

Агота Баньяї, Мішкольц, Угорщина

СЕГМЕНТАЦІЯ ПОСТАЧАЛЬНИКІВ НА ОСНОВІ ДАНИХ ПРО ПРОДУКТИВНІСТЬ ЗА ДОПОМОГОЮ ІЄРАРХІЧНОЇ КЛАСТЕРИЗАЦІЇ

Анотація. *У багатьох машинобудівних виробничих середовищах менеджери з закупівель повинні регулярно порівнювати постачальників із суттєво різними профілями ефективності, що робить структуровану оцінку необхідною. Об'єднання постачальників із подібними характеристиками продуктивності може зробити рішення щодо закупівель більш прозорими та легшими для обґрунтування на практиці. Однак ефективність постачальника зазвичай описується кількома критеріями оцінки, виміряними на різних шкалах, і ці характеристики можуть змінюватися з часом. З цієї причини потрібні аналітичні підходи, здатні опрацьовувати як багатовимірний характер даних, так і зміни продуктивності постачальників з часом. У цій статті розроблено адаптивний підхід сегментації постачальників на основі ієрархічних методів кластеризації. Ефективність постачальника оцінюється за кількома операційними критеріями, включно з рівнем якості, своєчасною доставкою, ціною за одиницею, терміном виконання, частотою скарг та операційною гнучкістю. Після застосування мінімально-максимальної нормалізації та зваженої оцінки продуктивності подібності постачальників розраховуються за допомогою евклідової відстані, а для ідентифікації однорідних груп постачальників застосовуються ієрархічні методи кластеризації. Порівнюються кілька стратегій зв'язку, а якість кластеризації оцінюється за допомогою внутрішніх валідаційних індексів, таких як індекси Silhouette, Davies–Bouldin, Calinski–Harabasz та Dunn. Емпіричний аналіз проводиться на наборі даних, що містить 15 постачальників, які спостерігались у двох послідовних періодах оцінки. Результати свідчать, що ієрархічна кластеризація може виявити інтерпретовані групи постачальників із чітко розрізняючими профілями ефективності. Порівняння структур кластеризації протягом послідовних періодів також показує, що сегментація постачальників змінюється з появою нових даних про продуктивність.*

Ключові слова: *адаптивна сегментація постачальників; ієрархічна кластеризація; оцінка постачальників; валідація кластерів; управління ланцюгом постачання; аналіз рішень за мультикритеріями; кластеризація на основі ефективності; аналіз ефективності постачальників.*

UDC 658.511 **doi: 10.20998/2078-7405.2026.104.03**

INVENTORY PLANNING FOR 3D-PRINTED SPARE PARTS UNDER UNCERTAIN DEMAND

Tamás **Bányai** [0000-0002-0229-4781]

University of Miskolc, 3515 Miskolc-Egyetemváros, Hungary
tamas.banyai@uni-miskolc.hu

Received: 25 March 2026 / Revised: 10 April 2026 / Accepted: 25 April 2026 / Published: 15 May 2026

Abstract. *In recent years, additive manufacturing technologies have increasingly appeared in industrial spare parts logistics systems. Instead of maintaining large inventories of finished components, companies can increasingly rely on digital inventories and produce spare parts on demand using 3D printing. This shift creates new decision-making challenges related to the management of raw printing materials and the planning of production under uncertain demand. This paper proposes a two-echelon newsvendor model for inventory planning in additive manufacturing-based spare parts supply systems. In the proposed framework, the first decision stage determines the quantity of raw printing material to be stocked before demand realization, while the second stage determines the number of spare parts produced in response to stochastic customer demand. The model captures the trade-offs between material procurement cost, inventory holding cost, and shortage penalties. The mathematical formulation is developed as a two-stage stochastic optimization problem. Numerical experiments are conducted to analyze the relationship between raw material inventory levels and expected system cost. The results show that the cost function exhibits a well-defined minimum and that the optimal material inventory level strongly depends on shortage cost parameters. Sensitivity analysis further demonstrates how shortage penalties influence optimal inventory decisions. The findings highlight the strategic role of raw material inventory in additive manufacturing supply systems and provide practical insights for companies adopting 3D printing technologies in spare parts logistics.*
Keywords: *additive manufacturing; spare parts logistics; two-echelon newsvendor model; inventory planning; stochastic demand; supply chain optimization.*

1. Introduction

Efficient spare parts management is a critical component of modern industrial logistics. Industries such as aerospace, automotive manufacturing, and heavy machinery rely heavily on the availability of spare parts to maintain system reliability and minimize downtime. However, spare parts demand is often highly uncertain and intermittent, which makes traditional inventory management approaches costly and inefficient. Maintaining large inventories to ensure availability can lead to high holding costs, while insufficient stock may result in service delays or production disruptions.

For several decades, the Institute of Logistics at the University of Miskolc has

been actively engaged in the analysis and design of logistics systems [1–4]. This research direction has played an important role not only in education but also in industrial research and development activities. One of the strategic objectives of this research field is to continuously explore new application areas where modern optimization methods can support practical logistics decision-making. In this context, additive manufacturing and the supply chains associated with 3D printing represent a promising and emerging field of application [5, 6].

In several industrial projects related to spare parts logistics, it can be observed that many companies still rely primarily on traditional stocking strategies, even when new manufacturing technologies could offer alternative solutions. This practical observation highlights that the integration of new technologies into logistics decision-making frameworks often lags behind technological development itself.

From the author's perspective, additive manufacturing may fundamentally reshape the traditional logic of spare parts logistics. While classical supply chains were designed around centralized production and long-term storage of physical products, 3D printing enables a more flexible, decentralized, and demand-driven production approach. Instead of storing large quantities of finished products, companies may increasingly rely on digital inventories and produce components only when they are required.

Although additive manufacturing is frequently described as a disruptive technology, its practical integration into analytical logistics models remains relatively limited. In particular, the interaction between raw material stocking decisions and on-demand production planning has received only limited attention in the operations research literature. This raises an interesting research question: how can classical stochastic inventory models [7,8] be adapted to capture the decision-making challenges arising in additive manufacturing environments?

This observation motivates the development of analytical models that combine established inventory theory with emerging manufacturing technologies. One of the most widely used stochastic inventory models is the newsvendor model, which determines the optimal order quantity for a single period under uncertain demand. While the classical newsvendor model considers only a single decision point, many real-world supply systems involve multiple sequential decision stages.

In additive manufacturing-based spare parts logistics, two key decision stages can be identified. The first stage corresponds to the stocking of printing materials, while the second stage represents the production of spare parts in response to uncertain customer demand. These two stages are inherently connected, since the number of parts that can be produced is limited by the available raw material.

In the author's view, the integration of additive manufacturing technologies with established operations research models offers an interesting opportunity to bridge theoretical modeling and practical industrial challenges. Exploring such hybrid manufacturing–logistics systems may contribute both to the academic literature and to practical decision support in modern supply chains.

This paper therefore proposes a two-echelon newsvendor framework for modeling inventory decisions in a 3D printing-based spare parts supply system. In the proposed system, the first stage represents the stocking decision for printing material, while the second stage determines the number of parts produced to meet uncertain customer demand. The model captures the trade-offs between material procurement costs, inventory holding costs, and shortage penalties resulting from unmet demand.

The main objective of this study is to develop a stochastic optimization model that supports decision-making in additive manufacturing spare parts logistics under demand uncertainty. By integrating raw material inventory decisions with production planning, the proposed model provides a structured approach to balancing supply chain costs and service levels in additive manufacturing environments.

The remainder of the paper is organized as follows. Section 2 describes the problem setting and system structure. Section 3 presents the mathematical formulation of the proposed model. Section 4 discusses the numerical analysis. Finally, Section 5 concludes the paper and outlines potential directions for future research.

2. Problem description

This study considers a spare parts supply system supported by additive manufacturing technology. The system is designed to provide spare components under uncertain demand conditions while maintaining a balance between inventory costs and service level requirements. In contrast to traditional spare parts logistics, where finished products are stored in advance, the considered system relies on the storage of printing materials and the possibility of producing parts on demand using 3D printing technology (see Figure 1).

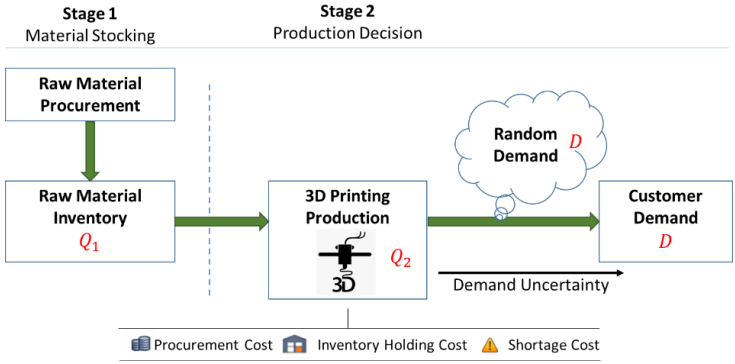

Figure 1 – Two-stage structure of additive manufacturing spare parts supply system [own elaboration].

The proposed system consists of two sequential decision stages. The first stage corresponds to the inventory decision related to the raw material required for additive manufacturing. The second stage represents the production decision, where spare parts are produced in response to realized demand. These two stages form a two-echelon decision structure, since the production of spare parts is directly constrained by the availability of printing material.

At the beginning of the planning period, the decision-maker determines the quantity of raw material to be stocked. This decision must be made before the actual demand for spare parts becomes known. The stocked material represents the available capacity for future production, and therefore it plays a critical role in determining the responsiveness of the system.

After the demand for spare parts is realized, the second decision stage takes place. At this point, the decision-maker determines how many spare parts should be produced using the available material. Since the production quantity cannot exceed the available raw material, the production decision is constrained by the initial stocking decision. If the produced quantity is insufficient to meet demand, shortage costs may occur, representing lost sales, delayed service, or other operational penalties.

The demand for spare parts is assumed to be stochastic and is represented by a random variable. This reflects the typical characteristics of spare parts demand, which is often irregular and difficult to predict. The objective of the decision-maker is to determine the optimal raw material stocking level and production quantity that minimize the expected total cost of the system.

The total cost of the system may include several components. First, there is a procurement cost associated with purchasing the raw printing material. Second, inventory holding costs may arise if part of the material remains unused after the production decision. Third, holding costs may also occur if produced spare parts exceed realized demand. Finally, shortage costs are incurred when the realized demand exceeds the available produced quantity.

The decision structure of the system can therefore be interpreted as a two-stage stochastic decision problem. The first-stage decision determines the raw material inventory level, while the second-stage decision determines the production quantity after the uncertainty in demand has been revealed. This structure naturally leads to a two-echelon newsvendor-type model, where the first echelon represents material stocking and the second echelon represents spare part production.

From a practical standpoint, such a system can be observed in modern spare parts supply chains where additive manufacturing technologies are used to complement or partially replace traditional inventory-based strategies. Instead of storing large numbers of finished components, companies may maintain a stock of printing material and produce parts only when they are required.

The decision process considered in this study can be conceptually illustrated as a two-stage supply chain structure. In the first stage, printing material is procured and stored, while in the second stage spare parts are produced using the available material to satisfy uncertain customer demand.

To formally describe the decision problem, several key elements are considered in the model. Let Q_1 denote the quantity of printing material stocked at the beginning of the planning period, and let Q_2 denote the number of spare parts produced after demand realization. The demand for spare parts is represented by a random variable D. The model considers material procurement cost, inventory holding costs, and shortage penalties associated with unmet demand. The following section presents the mathematical formulation of the proposed optimization model.

3. Mathematical Model of the Two-Echelon Inventory System

This section presents the mathematical formulation of the proposed two-echelon newsvendor model for additive manufacturing-based spare parts supply under demand uncertainty. The model describes the sequential relationship between raw material stocking and spare part production while capturing the main cost components of the system.

The planning horizon is assumed to consist of a single decision period. During this period the demand for spare parts is uncertain and is represented by a random variable. The decision process therefore takes place in two stages. In the first stage the decision-maker determines the quantity of raw material required for additive manufacturing. This decision must be made before the actual demand becomes known. After the realization of demand, the second stage begins, where the number of spare parts to be produced is determined based on the available raw material.

Let D denote the stochastic demand for spare parts. The first-stage decision variable is Q_1 which represents the quantity of raw printing material stocked before demand realization. After demand becomes known, the second-stage decision variable $Q_2(D)$ determines the number of spare parts produced in response to the realized demand. Since spare parts can only be produced from available material, the production quantity cannot exceed the available raw material inventory.

The cost structure of the system includes several components. First, a procurement cost arises when raw printing material is purchased. In addition, holding costs may occur if part of the raw material remains unused after the production decision. Further holding costs may also appear when the produced number of spare parts exceeds the realized demand.

Finally, shortage costs are incurred if demand exceeds the available production quantity. In order to describe the inventory dynamics of the system, three quantities are introduced. The first quantity corresponds to the unused raw material that remains after production.

This quantity can be written as

$$I_1 = Q_1 - Q_2(D)$$

where I_1 denotes the remaining raw material inventory.

The second quantity represents the surplus finished spare parts that remain after demand has been satisfied. This situation occurs when the production quantity exceeds the realized demand. The surplus inventory can therefore be expressed as

$$I_2 = (Q_2(D) - D)^+$$

where the operator $(x)^+ = \max(x, 0)$ denotes the positive part of a value.

The third quantity corresponds to the shortage that occurs when the realized demand exceeds the produced quantity. The shortage amount can therefore be written as

$$B = (D - Q_2(D))^+$$

These expressions allow both surplus inventory and unmet demand to be represented in a compact mathematical form.

Based on these quantities, the total cost of the system can be defined. The overall cost consists of four components: the procurement cost of raw material, the holding cost of unused material, the holding cost of surplus finished spare parts, and the shortage cost resulting from unmet demand. The objective of the decision-maker is therefore to determine the decision variables that minimize the expected total cost of the system. The expected cost function of the system can be written as

$$\min_{Q_1, Q_2(D)} \left[c \cdot Q_1 + \mathbb{E}(h_1 \cdot \left(Q_1 - Q_2(D)\right) + h_2 \cdot (Q_2(D) - D)^+ + p \cdot (D - Q_2(D))^+) \right]$$

subject to the material availability constraint

$$0 \leq Q_2(D) \leq Q_1$$

and the non-negativity condition

$$Q_1 \geq 0.$$

The operator $\mathbb{E}(\cdot)$ denotes the expected value with respect to the stochastic demand. The first term of the objective function represents the procurement cost of raw material. The remaining terms describe the expected holding costs of unused material, the holding costs of surplus finished spare parts, and the penalty associated with unmet demand.

The structure of the model can also be interpreted within the framework of two-stage stochastic programming. In this interpretation the first-stage decision determines the raw material inventory level, while the second-stage decision determines the production quantity after the realization of demand. This structure reflects the operational flexibility offered by additive manufacturing systems, where production decisions can adapt to realized demand within the limits imposed by the available raw material.

4. Numerical results and sensitivity analysis

This section presents the numerical results obtained for the proposed model in the context of additive manufacturing-based spare parts supply. The objective of the analysis is to illustrate how the raw material inventory level influences the expected

operational cost of a spare parts system where components are produced on demand using 3D printing technology.

The numerical experiments also reflect the two-stage decision structure introduced in the mathematical model. In the first stage, the decision-maker determines the raw material inventory level Q_1, representing the available printing material. In the second stage, after the realization of demand D, spare parts are produced using additive manufacturing technology up to the limit imposed by the available material inventory.

Numerical Input Data

For the numerical experiments, the model parameters were specified based on a simplified spare parts demand scenario. The demand for the considered spare part was represented by three discrete demand scenarios in order to illustrate the stochastic nature of spare parts demand. The demand levels were assumed to be $d_1 = 80, d_2 = 100, d_3 = 120$ units with corresponding probabilities 0.30, 0.50, and 0.20 respectively.

The cost parameters of the system were defined as follows. The procurement cost of raw printing material was set to $c = 5$ cost units per unit. The holding cost of unused raw material was assumed to be $h_1 = 1$ cost unit per unit, while the holding cost of surplus finished spare parts was $h_2 = 2$ cost units per unit. The shortage cost associated with unmet demand was assumed to be $p = 10$ cost units per unit.

In the numerical analysis, the candidate raw material inventory level Q_1 was evaluated within the interval $0 \leq Q_1 \leq 160$. For each possible value of Q_1, the production decision was determined according to the available raw material and the realized demand scenario. Accordingly, the production quantity in scenario s was defined as

$$Q_{2s} = min(Q_1, d_s),$$

which reflects the assumption that spare parts are produced on demand, but the production quantity cannot exceed the available raw material inventory.

Based on these parameters, the expected total cost of the system was calculated for each inventory level, and the optimal raw material inventory level was determined. The numerical calculations and graphical illustrations presented in this section were generated using MATLAB.

Expected Total Cost and Optimal Inventory Level

Figure 2 illustrates the relationship between the raw material inventory level Q_1 and the expected total cost of the system. When the available material inventory is very low, the system frequently experiences shortages because insufficient printing material is available to produce the required spare parts. For example, when

$Q_1 = 0$, the expected total cost is approximately 980 cost units, mainly driven by shortage penalties.

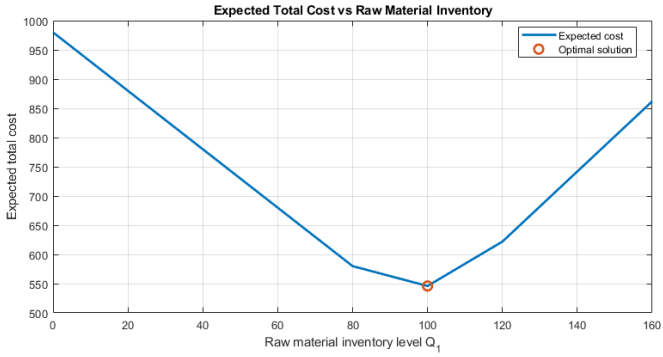

Figure 2 – Expected total cost vs. raw material inventory [own elaboration].

As the inventory level increases, the expected cost decreases significantly because the system gains greater production flexibility. When the inventory level reaches $Q_1 = 80$ units, the expected cost decreases to 580 cost units.

The minimum expected cost occurs at $Q_1^* = 100$, where the expected total cost is approximately $C(Q_1^*) = 550$.

This value represents the optimal balance between shortage costs and inventory-related costs. If the material inventory increases further, the expected cost begins to rise again. For example, at $Q_1 = 160$ the expected cost increases to 860 cost units, mainly due to increasing procurement and holding costs.

Analysis of Cost Components

Figure 3 decomposes the total cost into procurement cost, raw material holding cost, finished goods holding cost, and shortage cost.

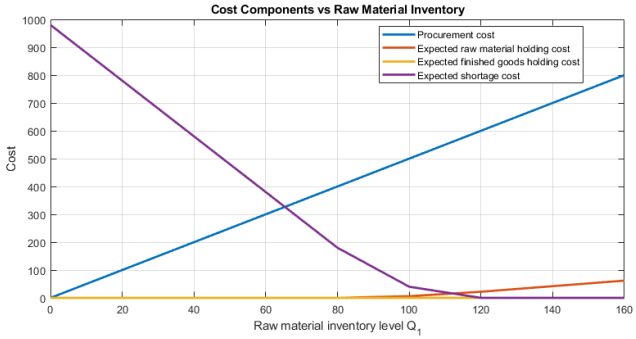

Figure 3 – Cost components vs. raw material inventory [own elaboration].

The procurement cost increases linearly with the inventory level according to $c \cdot Q_1$, which reflects the cost of acquiring printing material used in the additive manufacturing process.

In contrast, the expected shortage cost decreases rapidly as the inventory level increases. When no printing material is available, the system cannot produce spare parts and shortages occur in every demand scenario, resulting in an expected shortage cost of 980 cost units. As the inventory level increases, the additive manufacturing system becomes capable of responding to demand more effectively, significantly reducing shortage penalties. Around $Q_1 = 100$ the expected shortage cost becomes very small and above 120 units it is almost negligible.

The expected holding cost of raw material gradually increases as the inventory level grows, because larger inventories increase the probability that part of the material remains unused during the planning period. At $Q_1 = 160$ the expected raw material holding cost reaches 60 cost units.

The holding cost of finished spare parts remains minimal across most of the examined range. This reflects one of the main advantages of additive manufacturing: spare parts are produced only when demand occurs, reducing the need for storing finished goods.

Sensitivity Analysis with Respect to Shortage Cost

Figure 4 presents the sensitivity of the optimal raw material inventory level to changes in the shortage cost parameter p.

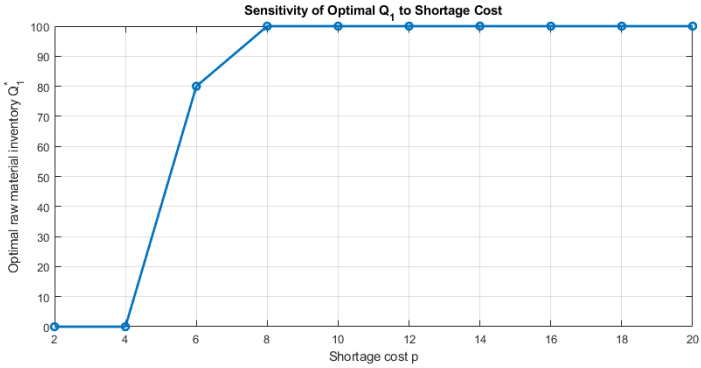

Figure 4 – Sensitivity of optimal Q_1 to shortage cost [own elaboration].

When shortage costs are very low ($p = 2$ or $p = 4$), the optimal inventory level is essentially zero, indicating that maintaining raw material inventory is not

economically justified. When the shortage cost increases to $p = 6$, the optimal inventory level rises sharply to $Q_1 = 80$ units.

For shortage cost values above $p = 8$, the optimal inventory level stabilizes around $Q_1^* = 100$, which approximately corresponds to the most probable demand level.

Sensitivity of the Minimum Expected Cost

Figure 5 illustrates how the minimum expected total cost changes as a function of the shortage cost parameter. As expected, higher shortage penalties increase the overall expected system cost.

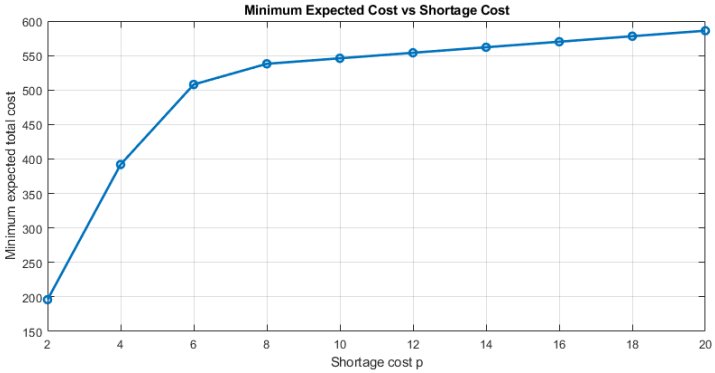

Figure 5 – Minimum expected cost vs. shortage cost [own elaboration].

When $p = 2$, the minimum expected cost is approximately 200 cost units. When the shortage cost increases to $p = 10$, the minimum expected cost rises to 550 cost units. For higher shortage cost values the expected cost increases gradually, reaching 590 cost units when $p = 20$.

Managerial Implications

The numerical results provide several insights for supply chain managers implementing additive manufacturing technologies. First, raw printing material inventory plays a critical role in ensuring the responsiveness of 3D printing-based spare parts supply systems. Maintaining an adequate level of printing material allows companies to exploit the flexibility of additive manufacturing and produce spare parts on demand.

Second, the optimal inventory level strongly depends on the economic consequences of shortages. In industries where equipment downtime is costly,

maintaining higher levels of printing material inventory becomes economically justified.

Finally, the analysis demonstrates that additive manufacturing can reduce the need for storing finished spare parts. Instead of maintaining large finished goods inventories, companies may rely on raw material inventory combined with digital spare parts models, producing components only when actual demand occurs.

5. Discussion and Conclusions

The results of this study demonstrate how classical inventory theory can be adapted to emerging manufacturing technologies such as additive manufacturing. By extending the traditional newsvendor framework to a two-echelon decision structure, the proposed model captures the interaction betwee n raw material stocking decisions and on-demand production enabled by 3D printing. The numerical analysis confirms that the optimal raw material inventory level is determined by a trade-off between shortage penalties and inventory-related costs. When raw material inventory is insufficient, the system experiences frequent shortages, leading to high penalty costs. Conversely, excessive material inventory increases procurement and holding costs. The optimal solution therefore emerges at the point where these opposing cost components are balanced.

An important insight of the study is the strategic role of raw material inventory in additive manufacturing environments. Unlike traditional spare parts supply chains that rely on storing finished products, additive manufacturing enables a more flexible production approach where raw material inventory effectively represents production capacity. Maintaining an appropriate level of printing material allows companies to respond to uncertain demand while avoiding excessive finished goods inventory. The sensitivity analysis also highlights the strong influence of shortage cost parameters on the optimal inventory decision. In industries where equipment downtime is costly, maintaining higher levels of printing material inventory may be economically justified in order to ensure service availability.

From a practical perspective, the proposed model provides a structured analytical framework for supporting inventory decisions in additive manufacturing-based spare parts logistics. The model can assist decision-makers in determining appropriate raw material stocking levels while considering demand uncertainty and cost trade-offs. Future research may extend the proposed framework in several directions. Possible extensions include multi-period decision models, multiple spare parts types, capacity constraints of additive manufacturing systems, and the integration of distributed 3D printing networks within spare parts supply chains.

References: 1. *Cselényi J., Gubenko, V.K., Bányai, Á., Bányai T.* Logistics System of a Seaport and Some of Its Theoretical Problems (in Hungarian). Logistics Yearbook 1996. pp. 137-153. **2.** *Illés, B., Németh, J.* Sensitivity analysis of road transport by sensibility of production-function. Key Engineering Materials. 2014. № 581. pp. 539 – 546. https://doi.org/10.4028/www.scientific.net/KEM.581.539 **3.** *Lukács, B.L.,*

Verees, P. Innovative techniques for the storage and transportation of hazardous materials. Advanced Logistic Systems: Theory and Practice. Miskolc. 2024. № 18. pp. 120 – 128. https://doi.org/10.32971/als.2024.023 **4.** *Veres, P., Bósa, F., Kydykov, A.* The Usability of Craft Layout Design Method with the Examination of Simplifications. Advanced Logistic Systems: Theory and Practice. Miskolc. 2022. № 16. pp. 54 – 59. **5.** *Sonar H., Khanzode V., Akarte M.* Additive Manufacturing Enabled Supply Chain Management: A Review and Research Directions. Vision. 2022. № 26. pp. 147 – 162. https://doi.org/10.1177/09722629221087308 **6.** *Bouchenine A., Abdel-Aal M.A.M.* Towards supply chain resilience with additive manufacturing: A bibliometric survey. Supply Chain Analytics. 2023. № 2. 100014, https://doi.org/10.1016/j.sca.2023.100014 **7.** *Dhaiban A.K.* A comparative study of stochastic quadratic programming and optimal control model in production-inventory system with stochastic demand. Pesquisa Operacional. 2017. № 37. pp. 193 – 208. https://doi.org/10.1590/0101-7438.2017.037.01.0193 **8.** *Vidal G.H.* Deterministic and Stochastic İnventory Models in Production Systems: a Review of the Literature. Process Integration and Optimization for Sustainability. 2023. № 7, pp. 29 – 50. https://doi.org/10.1007/s41660-022-00299-3

Тамаш Баньяї, Мішкольц, Угорщина

ПЛАНУВАННЯ ЗАПАСІВ 3D-ДРУКОВАНИХ ЗАПЧАСТИН ЗА НЕВИЗНАЧЕНОГО ПОПИТУ

Анотація. *Останніми роками технології адитивного виробництва дедалі частіше з'являються в логістичних системах промислових запасних частин. Замість того, щоб підтримувати великі запаси готових компонентів, компанії дедалі більше покладаються на цифрові запаси та виготовляють запчастини за запитом за допомогою 3D-друку. Ця зміна створює нові виклики для прийняття рішень, пов'язані з управлінням сировиною для друку та плануванням виробництва за умов невизначеного попиту. У цій статті пропонується модель продавця новин на два рівні для планування запасів у системах постачання запасних частин на основі адитивного виробництва. У запропонованій структурі перший етап прийняття рішення визначає кількість сировини для друку до реалізації попиту, тоді як другий етап визначає кількість запасних частин, виготовлених у відповідь на стохастичний попит клієнтів. Модель відображає компроміси між витратами на закупівлю матеріалів, витратами на зберігання запасів і штрафами за дефіцит. Математичне формулювання розроблено як двоетапна задача стохастичної оптимізації. Проводяться чисельні експерименти для аналізу взаємозв'язку між рівнем запасів сировини та очікуваною вартістю системи. Результати показують, що функція витрат має чітко визначений мінімум, а оптимальний рівень запасів матеріалів значною мірою залежить від параметрів дефіциту витрат. Аналіз чутливості додатково демонструє, як штрафи за дефіцит впливають на оптимальні рішення щодо запасів. Результати підкреслюють стратегічну роль запасів сировини в системах постачання адитивного виробництва та дають практичні інсайти для компаній, які впроваджують технології 3D-друку в логістиці запасних частин.*

Ключові слова: *адитивне виробництво; логістика запасних частин; модель продавця газет, яка має дворівневу структуру; планування запасів; стохастичний попит; оптимізація ланцюга постачання.*

UDC 621.922 **doi: 10.20998/2078-7405.2026.104.04**

ANALYSIS OF THE INFLUENCE OF TECHNOLOGICAL PARAMETERS ON THE PROPERTIES OF DIAMOND-BEARING COMPOSITES USING 3D MODELING

Vladimir **Fedorovich** [0000-0001-7015-8653], Natalia **Kozakova** [0000-0002-1891-4615]

National Technical University «Kharkiv Polytechnic Institute», Kharkiv, Ukraine
Volodymyr.Fedorovych@khpi.edu.ua

Received: 29 March 2026 / Revised: 19 April 2026 / Accepted: 10 May 2026 / Published: 15 May 2026

Abstract. *This paper presents a methodology for 3D simulation of the thermo-forced deflected mode in the sintering zone of diamond composite materials (DCM) and the grinding area, considering them as a unified system: "material to be machined – grain – metallphase – bond." The approach includes experimental studies of the 3D topography of interacting surfaces using laser scanning. A simulated 3D model of the system "diamond crystallites – metallphase – grain – bond" enables analysis of its behavior under various sintering and machining conditions, wheel performance parameters, grain anisotropy, and the presence or absence of cutting fluid. This methodology supports the development of an expert system for designing efficient, resource-saving combined processes for precision machining of superhard composite materials, with full consideration of their anisotropy.*
Keywords: *Diamond composite materials (DCM); single point diamond tools; simulation; expert systems.*

1. Introduction

Currently, in world practice, the methods of three-dimensional modeling are most often used, which is due to the need to increase the adequacy and information sufficiency of models. The prerequisite for such a transition is the development of the finite element method (FEM), hardware and software [1]. A review of the relevant publications shows that there is currently no complex three-dimensional methodology for studying the processes of processing diamond-abrasive tools, but there is a real prospect of its development. The creation of such a methodology will significantly reduce the volume of experimental studies to determine the best design data of diamond-abrasive tools, optimal conditions for their production and application.

The unique, potentially high properties of DCMs can only be fully realized if

their type, grain, and concentration are used rationally, which is optimal for the given bond and the specified material to be processed (MM). To increase the efficiency of diamond grinding, it is necessary to solve the problems of the optimal combination of physical and mechanical properties of diamond grains, their granularity and concentration depending on the physical and mechanical properties of MM. These issues should be explored throughout the DCM lifecycle, including design, manufacturing, and application processes. Realization of the proposed methodology by experiment is very labour-intensive and expensive process.

The main stages of finite element analysis: 1. synthesis of system functional; 2. partitions of system on finite elements and selection of coordinate functions; 3. constructions of stiffness matrixes and reduction of load to vector of nodal loads; 4. synthesis of canonical equations; 5. solutions of a system of canonical equations and definition of values of degree of freedoms of a system; 6. definitions of DM of system under consideration [2].

2. Simulation of DCM sintering process

Operating efficiency of tools from diamond-composite materials is stimulated by a series of reasons, including structural defects connected with destruction of a portion of grains during tool manufacturing process. It was demonstrated at the Bakul Institute of Superhard Materials of National Academy of Sciences of Ukraine under the direction of academician N.V. Novikov, that up to 90% of diamond grains fail at sintering of composite diamond-containing materials such as "twesal" [2]. A similarity of sintering processes of diamond-containing composite materials such as "twesal" type and diamond-bearing layer of diamond wheels on metallic and ceramic bonds, and also measurement of grain size of diamond dust extracted from a fragment of diamond-bearing layer of a non-operated wheel, is evidence of breaking of diamond grains during the wheel manufacturing process [3]. Bond composition, mark of diamond grain, its graininess and concentration in cake, and also technological features of DCM manufacture are the factors which essentially influence the grain integrity.

The task, solved in the process of 3D simulation of DM of sintering zone of DCM is the determination of optimal combination of strength properties of bond and diamond grains, their graininess and concentration, at which integrity retention of diamond grains is provided during the DCM sintering process.

At simulation of the sintering process, the fragment of diamond-bearing layer of the wheel was presented as a cube of bond dimensioned 300x300x300 μm, in midpoint of which a diamond grain as an ellipsoid dimensioned 120x100 μm was placed, that corresponds to 100 % concentration of diamond wheel. The metallic

phase in diamond grain was simulated as an interlayer of 5–10 μm in thickness and of various form and length. The schematic diagram and the FEM model of DCM sintering process are shown in Fig.1.

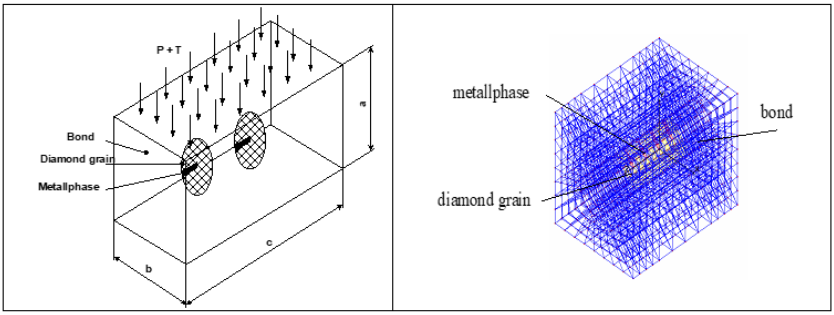

Fig. 1 (a) A schematic diagram and (b) the FEM model of "Bond - metallphase - grain" system

The calculations based on FEM in application package "Cosmos" and "Ansys" allow to obtain computerized quantitative assessment of principal and reduced stress, strain energy and density of strain energy in the elements to be sintered, depending on their sizes, physical-mechanical properties and conditions of sintering (temperature, pressure). The volumes of materials were considered as broken down, if reduced stress and/or density of strain energy in them exceeds the appropriate limiting values [2].

The sintering process of DCM of various concentrations on various metallic, ceramic and organic bonds with diamond grains of various strength from AC2 up to AC160T was modeled. The model was loaded by pressure and temperature conforming to an actual sintering process of DCM.

At the first stage the calculations were carried out for a fragment of diamond-bearing layer which includes a single diamond grain, surrounded by solid metal bond. Thus grain size, corresponding to the grain size of 50/40 up to 500/400, temperature and pressure of sintering, and also physical-mechanical properties of examined components of the cake were varied. At the second stage the fragment of diamond-bearing layer, which includes some diamond grains, integrated by means of bond, see Fig.1a, was considered. In this series the size ratio of the diamond grains and solid bond surrounding these grains was to varied that corresponded to various values of grain size and concentration (from 5 up to 200 %) of diamonds in the layer to be sintered. Grain and bond were considered as elastic solid bodies in the model.

Diamond grains were modeled as ellipsoids dimensioned from 50x30 up to 500x300 µm, depending on the grain size under consideration. Presence of metallic phase in diamond grains was modeled as interlayers oriented at random, the volumetric contents of which is 0,1–10 % depending on the marks of a grain [2,4]. The bond is considered as prismatic fragment dimensioned from 0,5x0,5x1,1 up to 3x3x6, depending on marks, size and grain concentration. The model is loaded by static monoaxial evenly distributed load by means of applied pressure and temperature. Theoretical research of sintering process of DCM on various bonds is carried out with the purpose to determine the conditions, under which the integrity of diamond grains in a material is ensured.

It is established that stresses exceeding the ultimate stress limit of diamond grains and placed along the metallphase interlayers results in the development in a grain. The stresses on the periphery of the grain being sintered are distributed in such a manner that can result in shearing grain submicroedges. As a result, the cutting edges are circularized, that can subsequently lead to the negative influence on cutting capacity of grains in diamond wheel. The outcomes of the 3D simulation of the DM of sintering zone of DCM are shown in Fig. 2.

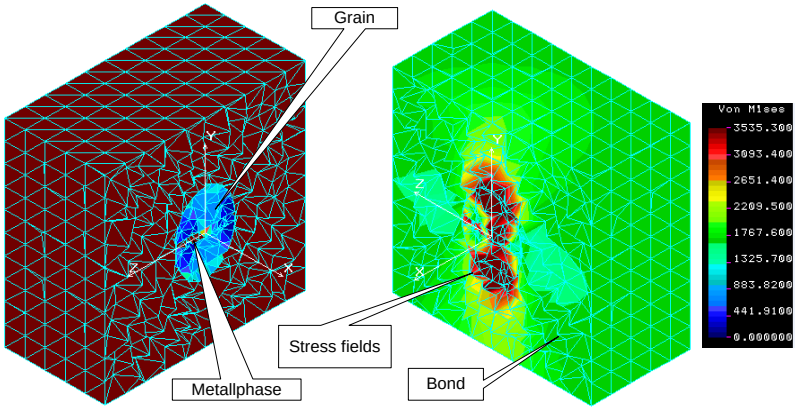

Fig. 2 (a) Section of 3D model "Grain – metallphase - bond" (b) and fields of reduced stress in the system at DCM sintering

By varying the combination of diamond grain strength and grain concentration in the wheel for various bonds, one can determine such combinations, at which retention of diamond grain integrity was provided. It is established, that not all of the commercial wheels with usable combination of brand of diamond grains and brand

of metal and ceramic bonds can be manufactured with standard concentration of diamond grains without failure of their integrity. So, for example, at sintering of wheel on bond M6-14 with diamond grains of brand AC6, the grain concentration in the wheel should not exceed 7 %, otherwise grains will be fracture as early as wheel sintering. It is shown, that for guaranteed retention of diamond grain integrity practically in all commercial wheels, their concentration should be much less than the applied one. Such tendency coordinates perform well with possibility and necessity of lowering the diamond grain concentration for the wheel up to the level of 10–15 % at grinding of superhard materials [2,5].

Optimum combinations of properties of bond and diamond grains with maximum allowable concentration of them in DCM, which ensure retention of their integrity during the manufacturing process, are established due to the carried out calculations. The optimum ratio of strength of bond, diamond grains and their concentration in diamond-abrasive tool, obtained at the first stage, are only limiting parameters and should be determine more exactly for the process of diamond grinding depending on the strength properties of material to be machined [6].

3. Simulation of process of diamond-abrasive machining of DCM

The reduced modulus of elasticity of the eutectic, see Table 1, and its thermal-expansion coefficient differ essentially, about 4 times, i.e. the diamond $\alpha_1=3.7\text{x}10^{-6}$ and the metallphase $\alpha_1=3.7\text{x}10^{-6}$, from the corresponding properties of diamond, at heating (up to the temperature of the inclusion), this eutectic extends, creating, therefore, an internal pressure which may result to uncontrolled macrodestruction of the diamond grains, to the occurrence of grids of microcracks and the migration of the metallphase on a surface. The level of the pressure on a plane can be estimated from the ratio [2,7],

$$q = \bar{K}_2(\alpha_2 - \alpha_1)(T_1 - T_0) \tag{1}$$

where K_2, α_2, – are the reduced compression modulus and thermal-expansion coefficient of the metallphase nickel-manganese, respectively, being in an equal proportion K_2=150.77 GPa, $\alpha_2=14.1\text{x}10^{-6}$; T_1 is the temperature at which there is an output of the metallphase drops on the surface of the diamond accompanied with formation of cracks. According to Ref. [8], this temperature corresponds to 973 K.

The thermal-expansion coefficient of diamond is in the range up to 750 K, $\alpha_1=3.7\text{x}10^{-6}$ K. The value of the thermal pressure in a cavity with metallphase according to equations (1) will be equal to q=144.5 MPa. However, the given analytical

sequence does not take into account the influence of the force factor on the stress level in diamond grains and is solved in conditions of 2D simulation.

In our case three possible variants of orientation of a grain relative to polycrystal in 3D modeling are considered: the contact of a grain to a polycrystal on the tip of a grain (point contact); an edge (linear contact) and a face (flat contact – imitation of wear platform on a grain). Various combinations of these variants were considered when studying the combined action of the grains.

The loading of the models was associated by: specifying (α) the displacement U_y of the top plane of a bond (kinematic influence – imitation of cross-feed S_{tran}) and (b) the imposition of the pressure of the top plane of a bond (force impact of normal and tangential components of cutting force – imitation of the elastic grinding pattern). The advantage of such an approach is the possibility to study the 3D DM, both at the elastic grinding pattern and on the rigid one, allowing for the comparison of results of these investigations.

The characteristic model parameters may be listed: the displacement of the average node of the top surface of a bond (value of cross-feed), U_y^{CB}; the displacement of the top node of a grain (embedding of grains in a bond), U_y^3; the displacement of node of contact of a grain with a polycrystal (elastic embedding of grains in workpiece material), U_y^{PK}; the reduced stresses (according to Mises criterion) in the top node of the contact of a grain with a bond, σ_{CB}; the reduced stresses in node of contact of a grain with a polycrystal, σ_{PK}.

At temperature as early as 700–1000ºC thermal stresses, which valued as commensurable ones with the bending strength and the tensile strength of diamond grains, can occur in microzones of several crystallites. Given technique allows to estimate the "contribution" of the force and temperature factors to the DM of system.

From the analysis of the results presented in Table 1, it may be concluded that the higher the temperature of grinding the more essential is the role of thermostress.

Table 1 – Dependence of intercrystallite thermal and thermo-forced stresses on temperature

Value, MPa	Temperature, $^{\circ}C$							
	500	600	700	800	900	1000	1100	1200
Maximal	24,04 / 28.2	28,85 / 29,56	33,65 / 34,12	38,46 / 40,17	43.27 / 44,27	48,08 / 51,11	52,88 / 53,34	57,69 / 60,45

Minimal	9,55 10,11	11,46 13,34	13,37 15,21	15,28 17,54	17.19 19,98	19,10 21,56	21,01 23,57	22,92 25,12

Numerator – reduced thermostresses without taking into account force factor.
Denominator – the reduced thermo-forced stresses.

Note that, at temperatures of the order 700–800°C tensile stresses, exceeding the corresponding ultimate stress limit of diamond, occur in diamond matrix due to the anisotropy of thermal expansion of diamond and the difference in coefficients of thermal expansion of the diamond and the metals-catalysts.

If these stresses can initiate intercrystallite destructions in the areas adjacent to non-oriented metal inclusions, then intracrystallite brittle fracture will be initiated in the field of diamond, covering the oriented metal inclusions. Note, also, that, due to these stresses the sites of flat compression of diamond appear where a crystal is subjected by local destruction, if the stresses reach critical values and a grid of microcracks appear on the surface of diamond grains. Thus, thermally activated processes can intensity microdestruction (self-sharpening) of diamond grains at grinding.

Finite element modeling using the FEM package "COSMOS" was carried out for the validation of the proposed hypothesis. The FE model and results of computation of the deflected mode of system "bond – grain – metallphase – workpiece material" are presented in Fig. 3 (a) and (b), respectively.

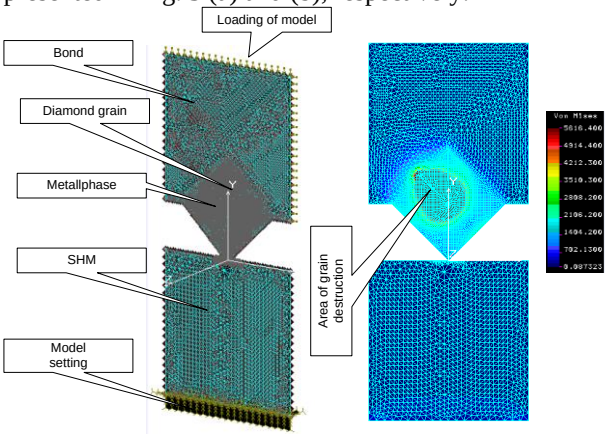

Fig. 3 (a) FEM model of system "bond – grain – metallphase – workpiece material" and (b) results of computation of deflected

Since in the real process of diamond grinding the considered technical system is loaded not only by force impacts, but also temperature ones, it is necessary to determine the values of principal and reduced stresses and also the values of deformations, strain energy and density of strain energy in each element of the system "workpiece material – grain – bond" caused by force, temperature and total (thermo-forced) loading. For this purpose the values of the contact temperature and the temperature of lubricant-cooling agent input in the grinding area were specified, too, in addition to the value of normal pressure or cross-feed.

The temperature in the grinding area predetermines the process of self-sharpening of diamond grains in many respects. The FE simulation results reveal that the value of the thermo-forced stresses in diamond grains and, consequently, the probability of their macrodestruction are reduced considerably, due to the presence of lubricant-cooling agent in the grinding area, see Fig. 3.

Subsequently, affects the temperature factor essentially the efficiency of the process of self-sharpening of diamond wheels. Both force (reduced stress exceeds the tensile strength of the workpiece material) and power (strain energy in an element exceeds the limiting value) criteria of destruction were used to determine the amount of damage workpiece material and diamond grains. The package allows to calculating the values of strain energy and density of strain energy in each element of the system. Thus, it is possible to determine the amount of elements with supercritical values of reduced stress or supercritical strain energy. In order to obtain the most reliable computing results of amount of destroyed workpiece materials and diamond grains, the FEM grid of elements of the system "workpiece material – grain – metallphase – bond" was thickened when approaching the contact area (to damage zone) up to the sizes of element volume not exceeding $10^{-4}\mu m^3$, i.e. much less than the really damage amount obtained once by a diamond grain during grinding.

Using the 3D simulation of DM of system "workpiece material – grain – metallphase – bond" and the specially developed program for computing the amount of destroyed and dropped out (loss) grains and the amount of damage workpiece materials, it is possible to theoretically estimate the major parameters of the self-sharpening process at diamond grinding of superhard materials, namely the specific consumption and the specific wear of diamond grains. Numerical results regarding the amount of destroyed grains, V_d and dropped out from a bondgrains, V_{loss}, depending on the working height of grains and the critical size of their embedding, $h_{cr.}$

The specific wear is defined as

$$q_w = \frac{V_d}{V_{SHM}}$$

and the specific consumption

$$q = \frac{V_d + V_{loss}}{V_{SHM}}$$

where V_{SHM} is the volume of the damaged workpiece material. Calculation, of these values, depending on the physical-mechanical properties of the workpiece material, grains, modulus of elasticity of bond, cross-feed, grinding speed and normal pressure.

It is possible to re-distribute the energy input in grinding area between the system elements owing to control of the contact parameters (value of relative actual area) and dynamics of interaction of the elements of the system "workpiece material – grain – bond" (speed, feed, normal pressure, introduction of energy of ultrasonic vibrations in the area).

The technique of 3D simulation of DM of system "workpiece material – grain – metallphase – bond" allows to determine the conditions under which the maximal part of energy input in grinding area will be directed to microdestruction of the workpiece material, minimizing microdestruction – self-sharpening of diamond grains, eliminating their loss from a bond.

Investigations of the effect of the wheel working surface (WWS) topography parameters on 3D DM of the system have shown, that if the diamond grain even insignificantly projects from a bond ($h_p \neq 0$), i.e. the bond does not contact to workpiece material, so the stress occurs in the diamond grain, which is sufficient for the process of self-sharpening (microdestruction). If the grain is completely embedded in a bond ($h_p=0$), it is not self-sharpened due to the volumetric "crimping" by a bond and the absence of free boundaries. In this connection productive process of workpiece material grinding should be put into practice only under condition of realization of interaction of the first type in system "WWS – workpiece material" i.e. without a contact of bond to workpiece material.

The time history of changing parameters of the topography of wheel working surface (WWS) during self-sharpening was experimentally verified employing the technique of laser scanning and electronic data processing the changes of 3D parameters of the WWS, sub-microrelief of separate diamond grains, were investigated in order to estimate the relative reference area of the surface topography, t_{ps} [2,8]. Thus, it is possible to determine the value t_{ps} both at macrolevel (WWS), and at microlevel, i.e. a microrelief of separate diamond grains. The value of sub-microrelief of separate diamond grains is the important parameter at definition of the actual contact area in the system "DCM-grain", which is difficult to obtain by other ways, since the sub-microrelief of diamond grains determines the efficiency of self-sharpening of diamond grains.

The experimental result reveal that, when grinding superhard materials by wheels on an organic bond under theoretically determined conditions of wheel self-

sharpening parameters, its relief remains practically constant for a long time, see Fig. 4.

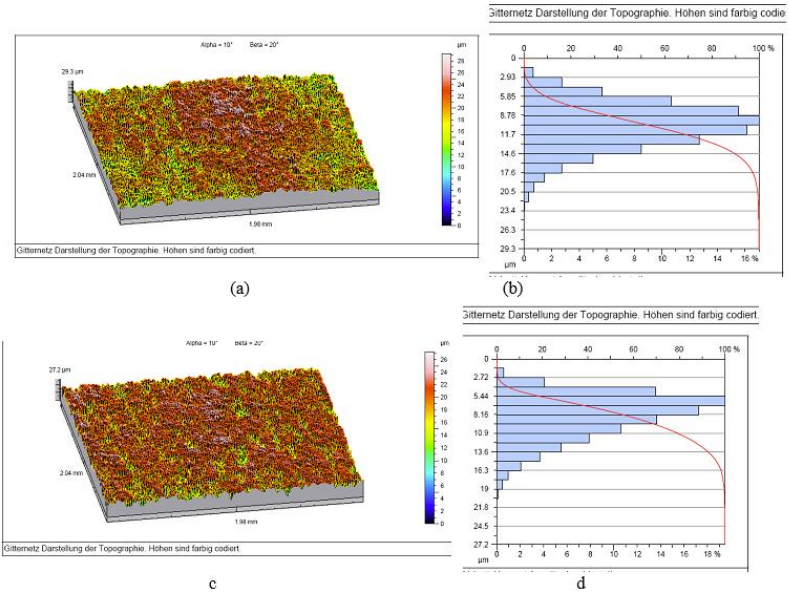

Fig. 4 (a, c) 3D topography of WWS and (b,d) relative distribution function of relative reference area of WWS; a,b – after 30 s of grinding c,d – after 5 min of grinding

4. Conclusions:

Summarizing the main features of the numerical and experimental results reported pertaining to 3D simulation of diamond composite materials, the following conclusions may be drawn:

1. The methodology of 3D simulation of processes of manufacturing, machining and exploiting of DCM is developed and found as a result of use of CIT.

2. The methodology of 3D simulation of thermo-forced deflected mode of the sintering zone of DCM and grinding area as the unified system "material to be machined - grain - metallphase - bond", which includes experimental study of 3D topography of interacting surfaces by laser scanning is proposed. Simulated 3D model of the deflected mode of the system "diamond crystallites – metallphase - grain - bond", which allows to analyze its behaviour depending on modes and conditions of

sintering and machining, wheel performances taking into account anisotropy of grains, and availability or absence of cutting fluid is developed on this basis.

3. For the first time the rational compositions of type, graininess and concentration of diamond grains with marks of metallic, ceramic and organic bond, which ensure the integrity of grains in DCM are defined on the basis of 3D simulation of deflected mode of DCM, originating in the sintering process of its components. It is established that, decrease of diamonds concentration in the wheel up to 5–40 % allows to ensure minimum defectiveness of wheel grains at optimum selection of their marks, graininess and bond type. Recommendations on optimum diamond-metallic and ceramic compositions for the manufacture of grinding wheels are provides.

4. Based on the worked out methodology it is possible to create the expert system for development of effective technological resource-saving combined processes of precision machining of superhard composite materials, taking into account their anisotropy. The proposed methodology allows to elaborating high-effective technological processes of preliminary and precision machining of various DCM, that permits an increase of productivity about 1,5–2 times, a reduce of the expenditure of expensive diamond grains on 30–40 % and increasing reliability of single-point tool from superhard materials by 20–40 %, that is very important in CAM. The developed expert system for prediction and optimization of processes of manufacturing and exploiting of diamond-abrasive tool will essentially promote tool production.

References: 1. *Mamalis, A.G., Fedorovich, V.A., Romashov, D.V., Ostroverkh, Y.V.* Algorithmic Foundations of Optimization using Finite Element Modeling of High-Speed Grinding Technology in Application to 3D Micro-Level Models//Nanotechnology Perceptions, 2024, 20(1), pp. 80–91 **2**. Modeling the diamond grinding process using the finite element method [Electronic resource]: monograph / *Fedorovich, V.A., Fedorenko D.O., Romashov, D.V., Ostroverkh, Y.V., Pupan L.I.*; National Technical University "Kharkiv Polytechnic Institute". – Electronic text data. – Kharkiv, [In Ukrainian] 2023. – 257 p. – URI: https://repository.kpi.kharkov.ua/handle/KhPI-Press/64334 **3**. Optimization of functionally graded polycrystalline diamond compact based on residual stress: Numerical simulation and experimental verification. *Linglong Rong, Shaohe Zhang, Dongyu Wu, Jingjing Wu, Xiangwang Kong, Tao He*. International Journal of Refractory Metals and Hard Materials. Volume 117, December 2023, 106414. https://www.sciencedirect.com/science/article/abs/pii/S0263436823003141 **4.** Residual stress and stress gradients in polycrystalline diamond compacts. *J.W Paggett, E.F Drake, A.D Krawitz, R.A Winholtz, N.D Griffin.* International Journal of Refractory Metals and Hard Materials. Volume 20, Issue 3, May 2002, pp. 187–194. https://www.sciencedirect.com/science/article/abs/pii/S0263436801000774 **5**. Effect of interlayers on thermal residual stresses in diamond/MPEA composites predicted by finite element method. *Xuemei Liu, Changyong Yue, Yang Gao, Zhi Zhao, Wei Zhang, Yong Liu, Xiaoyan Song.* https://www.sciencedirect.com/science/article/abs/pii/S0263436823003141 **6**. Optimization of functionally graded polycrystalline diamond compact based on residual stress: Numerical simulation and experimental verification. *Linglong Rong, Shaohe Zhang , Dongyu Wu, Jingjing Wu, Xiangwang Kong, Tao He.* International Journal of Refractory Metals and Hard Materials Volume 117, December 2023, 106414. https://www.sciencedirect.com/science/article/abs/pii/S0263436823003141 **7**.*Tian, C.; Li, X.; Li, H.; Guo, G.; Wang, L.; Rong, Y.* Study on process and manufacturability of metal-bonded diamond grinding wheel fabricated by selective

laser melting (SLM). J. Phys. Conf. Ser. 2019, *1303*, 012144. https://iopscience.iop.org/article/10.1088/1742-6596/1303/1/012144 **8.** *Tian, C.; Li, X.; Chen, Z.; Guo, G.; Wang, L.; Rong, Y.* Study on formability, mechanical property and finite element modeling of 3D-printed composite for metal-bonded diamond grinding wheel application. J. Manuf. Process. 2020, *54*, pp. 38–47. https://www.sciencedirect.com/science/article/abs/pii/S1526612520301080?via%3Dihub

Володимир Федорович, Наталія Козакова, Харків, Україна

АНАЛІЗ ВПЛИВУ ТЕХНОЛОГІЧНИХ ПАРАМЕТРІВ НА ВЛАСТИВОСТІ АЛМАЗОВМІСНИХ КОМПОЗИТІВ ЗА ДОПОМОГОЮ 3D-МОДЕЛЮВАННЯ

Анотація. *У цій роботі запропоновано методологію 3D-моделювання термовимушеного деформованого режиму зони спікання АКМ та зони шліфування як єдиної системи "матеріал, що обробляється - зерно - металофаза - пов'язок", яка включає експериментальне дослідження 3D-топографії взаємодіючих поверхонь за допомогою лазерного сканування. На цій основі розроблено імітаційну 3D-модель деформованого режиму системи "алмазні кристаліти - металофаза - зерно - пов'язок", яка дозволяє аналізувати її поведінку залежно від режимів та умов спікання та обробки, характеристик круга з урахуванням анізотропії зерен, а також наявності або відсутності рідини для різання. Вперше раціональні склади типу, зернистості та концентрації алмазних зерен із ознаками металевого, керамічного та органічного пов'язку, які забезпечують цілісність зерен у АКМ, визначені на основі 3D-моделювання відхиленого режиму АКМ, що виникає в процесі запікання його компонентів. Встановлено, що зниження концентрації алмазних зерен у крузі до 5-40 % дозволяє забезпечити мінімальну дефектність зерен круга при оптимальному виборі їхніх позначок, зернистості та типу пов'язку. Надаються рекомендації щодо оптимального алмазно-металевого та керамічного складу для виготовлення шліфувальних кругів. На основі розробленої методології можливо створити експертну систему для розробки ефективних технологічних ресурсозберігаючих комбінованих процесів прецизійної обробки надтвердих композитних матеріалів з урахуванням їх анізотропії. Запропонована методологія дозволяє розробити високоефективні технологічні процеси попередньої та точної обробки різних АКМ, що дозволяє збільшити продуктивність приблизно в 1,5-2 рази, зменшити витрати на дорогі алмазні зерна на 30-40 % і підвищити надійність одноточкового інструмента з надтвердих матеріалів на 20-40 %, що є дуже важливим у АКМ. Розроблена експертна система для прогнозування та оптимізації процесів виробництва та експлуатації алмазно-абразивного інструменту фактично сприятиме виробництву інструментів.*

Ключові слова: *алмазні композитні матеріали (АКМ); одноточкові алмазні інструменти; моделювання; експертні системи.*

UDC 621.922.025 **doi: 10.20998/2078-7405.2026.104.05**

IMPROVING THE EFFICIENCY OF USING DIAMOND GRINDING WHEELS ON THE ORGANIC BINDER BY CALCULATING THE RATIONAL STRUCTURE AND INTRODUCTION OF ULTRADISPERSED DIAMOND

Yevgeniy **Ostroverkh** [0000-0002-8926-1324]

National Technical University «Kharkiv Polytechnic Institute», Kharkiv, Ukraine
Yevgeniy.Ostroverkh@khpi.edu.ua

Received: 29 March 2026 / Revised: 15 April 2026 / Accepted: 26 April 2026 / Published: 15 May 2026

Abstract. *The article presents one of the options for developing scientifically based recommendations for choosing a rational combination of the strength of the binder, the size of the diamond grain, the concentration of diamond grains with the physical and mechanical properties of different types of binders in the manufacture of diamond grinding wheels. The conducted studies have shown the feasibility of using detonation nanodiamond powders as a modifier of the polymer binder. The introduction of nanopowder into the polymer leads to an increase in microhardness by 23%, and the recommended mass fraction of nanodiamond should be about 1% of the weight of the binder. It is possible to use such polymer compositions in the diamond layer of standard grades, which theoretically will increase their hardness due to constant thermal conductivity.*
Keywords: *diamond grinding wheels; organic binder; nanodiamond.*

1. Problem statement

At present the process of manufacturing of diamond wheels on the organic binder is characterized by high labor intensiveness and low productivity, high consumption of expensive diamond grains and, as a consequence, the high cost of the process of further exploitation of diamond wheels. It is necessary to increase the reliability and quality in the manufacture of diamond-abrasive tools, which is indispensable to its effective use in production. Manufacturing of diamond-abrasive tools is based on the establishment of physical laws and technological patterns of grinding process, as well as a comprehensive understanding of the diamond layer destruction process. Up to now there are no scientifically grounded recommendations for choosing the rational combination of the binder strength, grain grade, concentration with the physical-mechanical properties of different types of binders. Available recommendations for the use of diamond wheels on various bonds

are general in nature. Therefore, nonrational choice of component properties causes damage to diamond grains during sintering and excessive wear of the wheel in the operational phase of diamond tools [1, 2].

2. Analysis of recent research and publications

Analysis of recent research and publications showed that the problem of increase of diamond grinding efficiency is still relevant and modern methods of mathematical modeling can bring significant results. The studies of wear of diamond grinding wheels showed that more than half of diamonds loss occurs due to falling out grains from the binder. Therefore the study of the role of binders in the process of grinding is an important and necessary task. Despite the fact that the wear of binder depends on and is determined by the wear of abrasive grains, the binder has a very significant impact on the process of grinding the details. Optimal characteristic of the binder depends on many factors: chemical interaction of the binder with the metal to be processed, thermal effect of chip on the binder, etc. Problem of increase of binder efficiency is particularly relevant in view of the fact that in recent few years it is possible to improve significantly the available binders, despite the fact that they permit to use potential properties of abrasives by no more than 20% [3].

In international practice, simulation of technological processes has proved to be a great tool for the evaluation and optimization of cutting and grinding processes. Information about the interaction between the elements of the "tool – workpiece" system at grinding permits to choose selectively the process parameters in order to achieve the best quality of the workpiece, minimum cutting time or high economic indexes of grinding. Being based on an inclusive interaction between the system parameters, processing parameters and results of grinding, the simulation of grinding processes is widely used in theoretical and practical study of abrasive processes. [4]. Using modern software tools of computer modeling for grinding process it is possible to implement the numerous empirical experiments in virtual space and the search of the rational properties of the "binder – grain – workpiece" system as far back as the design phase of diamond-abrasive tools.

The aim of the study. The aim is to develop a methodology for determining the optimal combination of strength properties of the elements of the grinding wheel, which will ensure the integrity of diamond grains in the manufacture and operation of the diamond grinding wheel on an organic binder.

Basic research results. During the study the original techniques for calculating the optimal properties of diamond grinding wheel for processing of different groups

of materials (superhard materials, hard metals, ceramics, and so on) have been developed.

In particular, the method of three-dimensional dynamic simulation of the deflected mode of diamond grinding area has been developed. For the first time the software package LS-DYNA has been applied in regard to grinding process, that allowed to follow step by step the dynamic change of equivalent stresses, temperature, strain and so on of the system «binder – grain – material-to-be-processed» [5].

The algorithm for grinding process simulation and the creation of three-dimensional model can be represented as a sequence: the creation of three-dimensional geometry of the object of research, the creation of the finite element mesh of the object components, parameterization of the mesh, parameter assignment of the material behavior patterns, determining the properties of the contact interaction, assignment of the loads on the components of the system, analysis of the results.

A wide range of materials behavior is realized in LS-DYNA. To implement the grinding process simulation a few models that correspond to the plastic or elastic behavior of the material was used. For simulation of organic binder the solid body model (initial mechanical properties of the material: elastic modulus *E*, shear modulus *G*, Poisson's ratio μ, mass density of material ρ) was used. Metal-catalyst in the diamond grain, metal coating and workpiece were described by the model of plastic material behavior, which implements the basic Hooke's law up to the conditions of von Mises plasticity, ie the fourth criterion of strength. Series of computational experiments allows to obtain the dependence of limit equivalent stress in the system on the compound alloy content in the grain, its brand or the concentration of grains in the diamond-bearing layer (Figure 1., Figure .2)

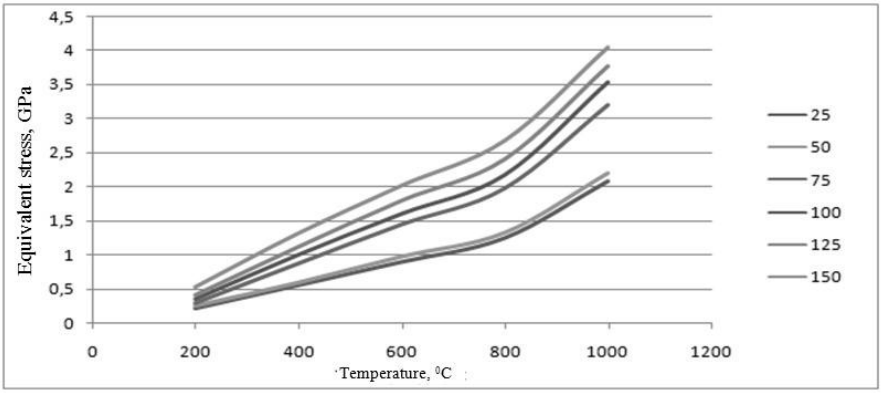

Fig. 1 – Dynamics of change of stress in the system «diamond – binder» in granularity of grains 63/50 on the temperature in the grinding area.

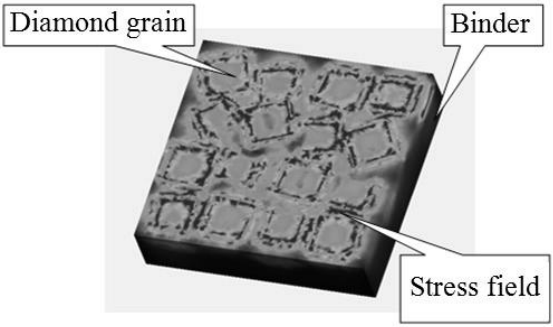

Fig. 2 – Distribution of stresses in the system «binder – grain – metal phase» with grain concentration of 150%.

In the operating phase of diamond grinding wheel of various grit sizes, concentration and grain drade, the modification of the standard nickel coating of synthetic diamond using ultradispersed diamond is proposed. In addition, ultradispersed diamond was also added to the resinbinder during sintering, which allowed to improve the adhesion between diamonds and organic binder of the wheel. Recently information about the possibility of further improvement of the properties of metal, in particular nickel coatings is available. This can be achieved owing to addition agents and obtaining new composite coatings that compare favorably with pure nickel coatings because of their physical and mechanical properties [6]. Special attention should be paid to the chemical reduction of nickel coatings with the inclusion of nano (ultradispersed) diamonds. Such composite coatings significantly improve the characteristics of conventional nickel coatings: increase strength, improve wear resistance, increase microhardness, anti-adhesion and anti-friction properties, reduce friction coefficient, increase the load carrying capacity, thermal stability, etc.

To get in practice the composite coatings based on chemically deposited nickel and nanodiamonds, the previously known technique to obtain nickel-plated synthetic diamonds has been modified. The technique includes the following stages (Figure 3):

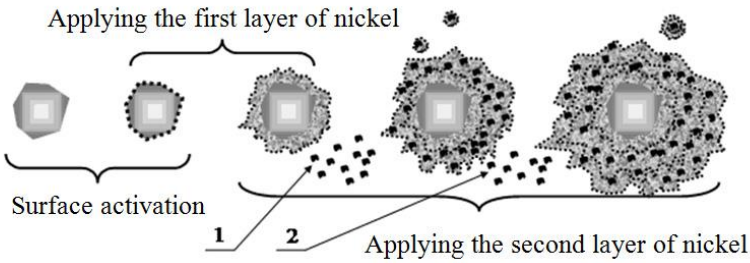

Fig. 3 – The sequence of chemical deposition of nickel coating with inclusions of nanodiamonds (1 – adding nanodiamond suspension during deposition of the second layer of nickel, 2 – adding nanodiamond suspension during deposition of subsequent layers of nickel).

Carried out tests of the resultant coatings have confirmed the theoretical backgrounds and composite coating with the addition ultradispersed diamond allowed to increase the performance of the diamond wheel by 27% compared with the wheel, which uses conventional nickel.

3. Modification of the polymer bond by the introduction of a detonation nanodiamond.

The bond, along with the grade, grain and concentration of the diamond grains, is the most important characteristic of the diamond grinding wheel. The quality of the bond determines the utilization rate of the potential of the diamond, the scope of application and performance of the diamond tool, productivity, economic efficiency and quality of grinding. More than 55% of the total range of produced binders is occupied by bonds on an organic binder, which is explained by the ease of manufacture and low cost of such diamond tools. At the same time, the problem of excessive wear of the organic (polymer) diamondiferous layer remains relevant. The standard modifier of the mechanical and chemical properties of the bond is the filler, the percentage of which varies along with the concentration of diamond grains. The properties of the filler may not be affected by thermal conductivity, hardness, coefficient of friction or ductility of the bond. For example, dispersed graphite, the content of which in the B2-01 bond is contained in the amount of 0.8% of the volume of the diamondiferous layer and significantly increases its antifriction properties. However, the most effective means of increasing diamond retention is the introduction of components that chemically interact with diamond into the bind. In this case, the strength of diamond retention depends on the adhesion activity of the

bond components to the diamond surface and increases with increasing adhesion work. Given the linear dependence of the amount of filler and diamonds in the diamondiferous layer, there is a need to search for new modifying components that will allow changing the mechanical properties of the bond with a constant ratio of filler and diamond grains [11].

Studies conducted by foreign and domestic scientists have shown that one of the applications of ultrafine diamond is its use as a polymer modifier. Filling the aromatic polyamide phenylon C-2 with nanodiamonds makes it possible to increase the abrasive wear resistance of samples by 3.5 times, increase the modulus of elasticity by 104.5 MPa, and the compression yield strength by 6.5 MPa (Table 5.1) [99,107].

Detonation nanodiamond can be successfully used as an additive to such polymers as fluoroelastomers, polysilicones, isoprene rubbers (Table 5.1). When creating a composition from such polymers and nanodiamonds, the elastic modulus of the nanodiamond composite can be increased by 10 times, and the tensile strength is increased by 1.3 to 11 times [99].

Table 5.1 – Strength characteristics of phenyl and phenyl-based nanocomposites.

Polymer Grade	Modulus of Elasticity (MPa)	Tensile Strength (MPa)
Fluoroelastomer	8.5	15.7
Nanodiamond Composite	92	173
Polysilicon	19	52
Nanodiamond Composite	53	154
Isoprene rubber	7.7	20.5
Nanodiamond Composite	12.3	28.2

As you know, the binding element of bakelite bonds is a polymer - phenolic binder SFP-012A. The binder is a mixture of pillow-case phenol-formaldehyde oligomer SF-012 with a curing agent - hexamethylenetetramine. Taking into account the positive effect of nanodiamond on the mechanical properties of polymers, it is suggested that the addition of nanodiamond can change the physical and mechanical properties of standard polymer bond grades, increasing their hardness, modulus of elasticity, and at the same time reduce the temperature in the microcutting zone due to changes in the frictional properties of the diamondiferous layer [3].

To confirm the hypothesis, samples of the diamondiferous layer were jointly created, in which a modifying component in the form of a nanodiamond was introduced. To avoid nanodiamond agglomeration and uniform distribution of nanopowder particles in the polymer binder SFP-012A, pulverbakelite was mixed with an aqueous suspension of nanodiamond and evenly dispersed in the resulting

emulsion. Next, the emulsion was completely dried with subsequent mixing using ultrasonic vibrations. The resulting composite was further sintered using the standard technology for manufacturing diamond wheels on a polymer bond.

The effect of the presence of nanodiamond particles on the hardness of bakelite was studied on two types of samples. The first is a B2-01 bundle based on the binder SFP-012A and the content of urotropin (hexamethylenetetramine) is equal to 6% by weight, the second is a similar composition of the polymer SFP-012A, filler and 6% wt. GMTA with the addition of 0.5%, 1% and 2% wt. nanodiamond. The composition of two types was made by sintering rings with a size of 125x3x3 mm (Fig. 5.5).

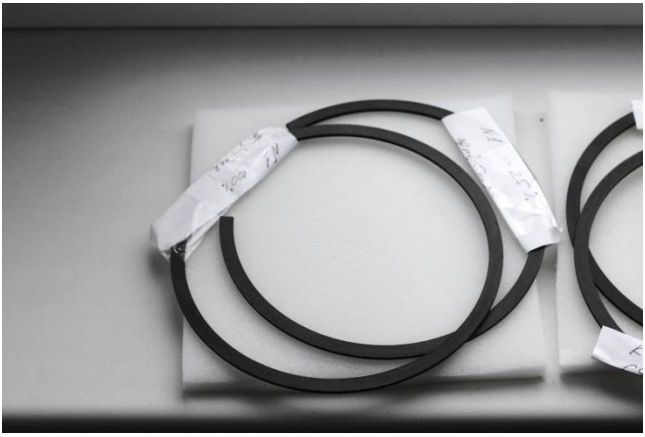

Figure 5.5 – Prototypes of a polymer diamondiferous layer with a size of 125x3x3 mm.

Hardness measurement on the PMT-3 device at a load of P = 50 g with a diamond pyramid with an angle at the apex of 136° showed that the introduction of nanodiamond particles into the polymer binder leads to an increase in the Vickers microhardness by 16 to 23%. Thus, the hardness of the bond sample without the presence of nanodiamond was 78 HV. When ultrafine diamond with a mass fraction of 0.5% was introduced into the composite, the hardness of the composition increased by 16% and amounted to 91 HV. The largest increase in hardness was observed on a sample with a 1% nanodiamond content (96 HV). With a nanodiamond content of 1.5% by weight. the hardness was 93 HV.

Thus, the studies carried out have shown the expediency of using detonation nanodiamond powders as a modifier of a polymer binder. The introduction of nanopowder into the polymer composition leads to an increase in microhardness by 23%, and the recommended mass fraction of nanodiamond should be about 1% of

the bond weight. It is possible to use such polymer compositions in the diamondiferous layer of standard grades, which will theoretically increase their hardness with constant thermal conductivity.

4. Conclusions and prospects for development.

1. The physical nature of the synthetic diamond destruction, where the decisive factor is the temperature at the microcutting area is established. It is need to control this factor, along with force.

2. It is established that metal phase material and its percentage of the volume of the diamond influences significantly on the diamond grains efficiency. For example, the replacement of compound alloy with prevailing Mn content by the compound alloy with Ni reduces the probability of failure under conditions of force and thermal load by 27%.

3. From the calculations one can see that the concentration of diamond grains in diamond-bearing layer of the wheels can be significantly reduced compared to conventional values used in serial production.

4. As a result of the investigations it is determined that in contrast to the conventional thickness of the metal coating on the diamond surface within 56 – 100%% wt., the thickness of the coating should be recommended specifically for each graininess. For example, 50/40 – 80/63 from 175 to 200%, 100/80 – 160/125 from 150 to 175%, 200/160 – 400/315 125% wt.

References: 1. Grinding wheels of superhard materials for diamond-abrasive processing: new in the famous. *Lavrinenko V.I.*, Kyiv, PH "Akademperiodyka", 2019, 200 p. http://doi.org/10.15407/akademperiodyka.388.190 **2**. *Mamalis, A.G., Grabchenko, A.I., Romashov, D.V., Fedorenko, D.O., Lagoudas, D., Fedorovich, V.A.and Kundrak, J.* Determination of the diamond wheel structure in high-speed grinding usingnanoindentation techniques: experimental and numerical simulation. Nanotechnol. Perceptions9(2013) 187–197. **3**. *Li, J.; Niu, G.; Mu, P.; Yan, B.; Liu, F.; Zhao, S.; Fang, L.; Gou, H.* Amorphous diamond embedded in dense boron nitride with excellent mechanical properties. Microstructures 2024, *4*, 2024010. http://dx.doi.org/10.20517/microstructures.2023.54 **4.** *Kundrák, J., Fedorovich,V., Markopoulos, A. P., Ostroverkh Y., Pyzhov, I.* Theoretical Assessment of the Role of Bond Material during Grinding of Superhard Materials with Diamond Wheels. Machines, 2022, 10(7), 543 https://www.mdpi.com/2075-1702/10/7/543 **5**. *Kunpeng Zhang*, Research on the Polishing Technology of Diamond Semiconductor Substrate Material. Proceedings of the 2025 International Conference on Electronics, Electrical and Grid Technology (ICEEGT 2025), Advances in Engineering Research, 2026, https://doi.org/10.2991/978-94-6463-986-5_20 **6.** *Krajnik, P., Wegener, K., Bergs, T. et al* (2024). Advances in modeling of fixed-abrasive processes. CIRP Annals - Manufacturing Technology, 73(2): 589-614. http://dx.doi.org/10.1016/j.cirp.2024.05.001 **7.** *Wiederkehr P, Grimmert A, Heining I, Siebrecht T and Wöste F* (2023) Potentials of grinding process simulations for the analysis of individual grain engagement and complete grinding processes. Front. Manuf. Technol. 2:1102140. doi: 10.3389/fmtec.2022.1102140

8. *Wiesener, F., Freudenberg, T., Bergmann, B. et al.* A multiscale simulation approach for grinding processes: grain engagement, heat generation, and coolant interaction. Prod. Eng. Res. Devel. 20, 31 (2026). https://doi.org/10.1007/s11740-025-01389-0 **9**. Knowledge-Based Adaptive Design of Experiments (KADoE) for Grinding Process Optimization Using an Expert System in the Context of Industry 4.0. S Fattahi, B Azarhoushang, H *Kitzig-Frank J*. Manuf. Mater. Process. 2025, *9*(2), 62; https://doi.org/10.3390/jmmp9020062 **10.** Modelling the Bond Behavior and Tool Wear of Metal-Bonded Microfinishing Tools considering the Run-In Phase. *Ines Heining, Tailaiti Taiwupike, Petra Wiederkehr*, Procedia CIRP Volume 133, 2025, pp. 621–626, https://doi.org/10.1016/j.procir.2025.02.106

Євгеній Островерх, Харків, Україна

ПІДВИЩЕННЯ ЕФЕКТИВНОСТІ ВИКОРИСТАННЯ АЛМАЗНИХ ШЛІФУВАЛЬНИХ КРУГІВ НА ОРГАНІЧНОМУ ЗВ'ЯЗУЮЧОМУ МАТЕРІАЛІ ШЛЯХОМ РОЗРАХУНКУ РАЦІОНАЛЬНОЇ СТРУКТУРИ ТА ВИКОРИСТАННЯ УЛЬТРАДИСПЕРСНОГО АЛМАЗУ

Анотація. *У статті представлено один із варіантів розробки науково обґрунтованих рекомендацій щодо вибору раціонального поєднання міцності зв'язуючої речовини, розміру алмазного зерна, концентрації алмазних зерен із фізичними та механічними властивостями різних типів зв'язуючих матеріалів у виробництві алмазних шліфувальних кругів. Проведені дослідження показали доцільність використання детонаторних наноалмазних порошків як модифікатора полімерної зв'язуючої речовини. Щоб уникнути агломерації наноалмазів і рівномірного розподілу нанопорошкових частинок у полімерній зв'язуючій речовині SFP-012A, пульвербакеліт змішували з водною суспензією наноалмазу та рівномірно дисперсували в отриманій емульсії. Далі емульсія повністю висушувалася з подальшим змішуванням за допомогою ультразвукових вібрацій. Отриманий композит додатково спікався за стандартною технологією виготовлення алмазних кругів на полімерному пов'язку. Вплив наявності частинок наноалмазу на твердість бакеліту вивчався на двох типах зразків. Перший — це зразок B2-01, заснований на зв'язуючій речовині SFP-012A, вміст уротропіну (гексаметиленетераміну) становить 6% за вагою, другий — схожий склад полімеру SFP-012A, наповнювача і 6% ваги GMTA з додаванням 0,5%, 1% і 2% ваги наноалмаза. Композиція з двох типів здійснювалася шляхом спікання кілець розміром 125x3x3 мм. Додавання наноалмазу у полімерний зв'язувач призводить до збільшення мікротвердості по Вікерсу на 16–23%. Таким чином, твердість зразка пов'язку без наявності нанодіаманта становила 78 HV. Коли в композит додавали ультрадрібний алмаз з масовою часткою 0,5%, твердість складу збільшувалася на 16% і становила 91 HV. Найбільше зростання твердості було зафіксовано на зразку з вмістом наноалмазу 1% (96 HV). Вміст нанодіаманту становить 1,5% за вагою, твердість становила 93 HV. Введення нанопорошку в полімер призводить до збільшення мікротвердості на 23%, а рекомендована масова частка наноалмазу має становити близько 1% від ваги зв'язуючої речовини. Можливо використовувати такі полімерні композиції в алмазному шарі стандартних сортів, що теоретично підвищує їхню твердість через більш високу та постійну теплопровідність.*

Ключові слова: *алмазні шліфувальні круги; органічний зв'язуючий матеріал; нанодіамант.*

UDC 519.711, 621.923.6 **doi: 10.20998/2078-7405.2026.104.06**

THE EFFECT OF MECHANICAL AND GEOMETRIC CHARACTERISTICS OF INHOMOGENEOUS REGIONS ON THE INTENSITY OF CRACK FORMATION DURING THE GRINDING OF PARTS MADE OF FUNCTIONALLY-GRADIENT MATERIALS

Anatoliy **Usov** [0000-0002-3965-7611], Maksym **Kunitsyn** [0000-0003-1764-8922], Yuliia **Sikirash** [0000-0003-0853-582X], Valeriy **Davydiuk** [0000-0002-9460-9129]

National University "Odessa Polytechnic", Odessa, Ukraine
m.v.kunitsyn@op.edu.ua

Received: 02 April 2026/ Revised: 18 April 2026/ Accepted: 28 April 2026 / Published: 15 May 2026

Abstract. *The lack of research on the specifics of the initiation of grinding cracks and their development into main cracks depending on the design, technological, and structural inhomogeneities of the material of the products does not allow for the unambiguous application of existing recommendations for eliminating the defects in question. This work is devoted to investigating the influence of inherent inhomogeneities in the surface layer, their geometry, and mechanical characteristics in products made of functionally graded materials on the selection of technological conditions for defect-free machining of parts. It has been established that the magnitude of the stress intensity factors for inherent inhomogeneities formed in the surface layer of products made of functionally graded materials is influenced by the size and orientation of these defects, their depth of occurrence and mutual arrangement, and the magnitude of the heat flux during grinding. The geometry and properties of inclusions formed by previous operations in the surface layer can create conditions for both the inhibition and the development of grinding cracks. If the heat flux is directed parallel to the inclusion axis and a straight, thermally isolated crack, then when the linear thermal expansion coefficient of the inclusion is greater than that of the matrix, an increase in the stiffness of the inclusion leads to an increase in the stress intensity factors K_I ($K_{II} = 0$) for various ratios of the thermal conductivity coefficients of the material components. This leads to the propagation of microcracks. Conversely, if the thermal expansion coefficient of the inclusion is lower than that of the matrix, a decrease in the stiffness of the inclusion leads to a decrease in the stress intensity factors K_I ($K_{II} = 0$) for the same ratios of thermal conductivity coefficients, i.e., conditions favorable for the non-propagation of microcracks are present. Therefore, when determining defect-free grinding parameters, it is necessary, first and foremost, to establish the maximum permissible cutting depths. In doing so, it is also important to have information not only on the thermophysical and mechanical properties of the material and the presence of inhomogeneities in the surface layer, but also on its processing conditions.*

Keywords: *functionally graded materials; inhomogeneities; grinding; crack formation.*

1. Introduction

Establishing relationships between the most important operational properties

of parts (wear resistance, fatigue and long-term strength, contact stiffness, magnetic properties, etc.) and the technological parameters of grinding—the micro-relief of the machined surface, microhardness, the presence of microcracks and chips, and the depth of the hardened layer—is one of the most important tasks in mechanical engineering technology.

The works [1], [2] are devoted to the study of thermophysical phenomena accompanying the finishing operation and determining the quality of the surface layer of products made of functionally graded materials, as well as to establishing their influence on crack and burn formation based on a quantitative analysis of the thermal stress state.

However, the problem of ensuring the required quality of the working surface of products made of functionally graded materials during finishing operations cannot be solved by thermal criteria alone. Given that the materials used to manufacture parts exhibit a high degree of heterogeneity, significant changes in the distribution of temperatures and deformations should be expected in areas where heterogeneities accumulate, as well as in their geometry; this, in turn, can lead to the formation of local deformations and the appearance of cracks on the working surfaces of ground products.

2. Analysis of sources and problem description

Stresses in workpieces during grinding typically propagate through a very thin layer several hundredths of a millimeter thick. The counteracting compensating stresses, on the other hand, are distributed over a significantly larger volume but have a negligible absolute magnitude, so their influence on the part's operational properties can be disregarded. Maximum stresses thus occur near the machined surface, at a shallow depth.

A number of studies [3] have proposed a method for calculating the maximum thermoelastic stresses functionally related to the processing conditions. The resulting relationships were used as criteria for defect-free processing based on the absence of crack formation.

In cases where the workpieces being processed are homogeneous pieces (coated workpieces), their stress-strain state depends on the properties of their constituent materials. Taking into account their physical and mechanical properties, as well as the coating thickness, allowed the author of [4], [5] to determine, based on the solution to the problem [6], the stress state resulting from grinding temperatures at the coating-matrix interface and to develop limit defect-free grinding cycles for coated parts.

The studies of the causes of grinding cracks presented in the works [7], [8] from the perspective of structural and phase transformations that generate corresponding structural stresses— $\sigma_{\text{str}}(M, \tau)$ —are also of a specific nature and do not allow for

a comprehensive understanding of the true picture of crack-type defect formation on the machined surface. The fact is that both structural and phase transformations (in volumes sufficient to generate destructive structural stresses) must occur at relatively low rates of heating (or cooling) and over a significant period of time. Meanwhile, grinding is characterized by short durations, high heating rates of the order of 3,000–50,000 °C/s, and approximately the same cooling rates [9]. These, in turn, are conditions close to thermal shock [10], [11], during which thermal stresses reach very high values.

The known functional relationships between process parameters and grinding temperature [2], [12] make it possible, using appropriate techniques, to eliminate burn marks on the machined surfaces of products made from functionally graded materials that do not contain design- or process-related inhomogeneities and whose material does not contain significant inhomogeneities. Studies of the conditions for improving the quality of machined surfaces by eliminating defects such as cracks were conducted primarily at the level of identifying qualitative relationships between process parameters and the physical and mechanical properties of the materials being ground [13]. The quantitative relationships between stresses and processing conditions obtained in a number of studies [14] are of a specific nature and do not reflect the general patterns of the stress-strain state of the surface layer depending on technological conditions and the properties of the materials being processed. In later studies [15], [16], the stress state of ground surfaces was evaluated using numerical methods.

However, the lack of studies on the specifics of the initiation of grinding cracks and their development into main cracks depending on the design, technological, and structural inhomogeneities of the material of the products does not allow for the unambiguous application of existing recommendations for eliminating the defects in question.

3. Research objectives

Therefore, the objective of this work is to investigate the influence of inherent inhomogeneities in the surface layer, their geometry, and mechanical characteristics in products made of functionally graded materials on the selection of technological conditions for defect-free machining of parts.

This objective can be achieved by solving the following tasks:

1. Create a mathematical model describing the thermomechanical processes in the surface layer during the grinding of products made of functionally graded materials, taking into account the inhomogeneities and their geometry formed during previous operations, starting from the production of the blank.

2. Select criteria for crack and burn formation on the machined surfaces and establish their relationship with the investigated technological parameters of the grinding process.

3. Develop the prerequisites for optimizing the thermomechanical state of the surface layer of products made of functionally graded materials during the grinding process, thereby preventing the occurrence of grinding defects such as cracks and burn marks.

4. Determine the technological capabilities for controlling the quality of the surface layer of parts using the established relationships between the physical and mechanical properties of functionally graded materials, the inhomogeneities and their geometry within the machined layer, and the technological parameters of the grinding process.

4. Research methods

The grinding process of machine parts is accompanied by both thermal and mechanical phenomena, which, interacting with each other, determine the quality of the surface layer. A quantitative description of these phenomena requires the selection of specific models. Due to the interconnection and interdependence of phenomena and processes during metal grinding, it becomes evident that the stress-strain state of the surface layer is determined primarily by the grinding temperature. If we use a thermoelastic body model that reflects the interrelationship between mechanical and thermal phenomena under finite heat fluxes, we can make significant progress in research on the influence of thermomechanical phenomena accompanying the grinding process on the quality characteristics of the machined surfaces of parts

For further studies of the kinetics of thermomechanical processes, we will use the following system of differential equations [17] as the main theoretical framework, which describes the interaction between the strain field and the temperature field:

$$\begin{gathered} G\Delta\vec{U}_j + (\lambda_t + G)\ grad\ div\ \vec{U}_j - \rho\frac{\partial^2\vec{U}_j}{\partial\tau^2} + P_j = \alpha_t\beta_t\ grad\ T \\ \Delta T - \frac{1}{a}\frac{\partial T}{\partial\tau} - \eta l\frac{\partial}{\partial\tau}\ div\ \vec{U}_j = -\frac{W}{\lambda} + C_q^{-2}\frac{\partial^2 T}{\partial t^2} \end{gathered} \quad (1)$$

where λ_t, G are Lamé constants; $\beta_t = 3\lambda_t + 2G$; ρ is the density of the processed material; α_t is the thermal coefficient of linear expansion of the metal; $a = \lambda/C_v$ is the thermal conductivity; λ is the thermal conductivity; C_v is the specific heat capacity; $\vec{U}(\Phi, t)$ is the total displacement vector of the internal point $\Phi\ (x, y, z)$ of the surface layer under the action of thermomechanical phenomena accompanying the grinding process: $l = 1 + \tau r\ \delta/\delta$ (τ is the relaxation time); $\eta =$

$\alpha t \beta t T(\Phi, \tau) \,/\, \lambda$; W is the power of the heat source; C_q is the heat diffusion coefficient in the workpiece material; τ is the time; P_j are cutting forces;

$$grad\, T(x,y,z) = \frac{\partial T}{\partial x}\vec{\imath} + \frac{\partial T}{\partial y}\vec{\jmath} + \frac{\partial T}{\partial z}\vec{k}$$

$$div\, \vec{U}_j = \frac{\partial U}{\partial x} + \frac{\partial U_y}{\partial y} + \frac{\partial U_z}{\partial z}, \qquad j \rightleftarrows x, y, z$$

Since thermal phenomena prevail over mechanical forces during grinding, the term accounting for the conversion of mechanical energy into heat can be neglected in the heat conduction equation, and we arrive at a parabolic-type heat conduction equation. To solve the given system (1) in explicit form, we will neglect the influence of inertial terms and the finiteness of the heat propagation speed. Furthermore, to overcome the analytical difficulties associated with solving spatial thermoelasticity problems, we will consider a plane problem. This transition is justified by the fact that, for investigating the thermomechanical state of ground surfaces, information regarding the propagation of temperatures and deformations with depth and in the direction of the tool's movement is crucial.

An analysis of large-scale interaction schemes between the wheel and the workpiece surface has shown [18], [19] that the curvature of the wheel and the workpiece within the contact zone has a negligible effect on the geometric interaction scheme between the wheel and the workpiece. Therefore, when formulating the computational model, we assume that the workpiece is a half-plane whose surface layer contains inhomogeneities of inherent origin. This allows us to study thermomechanical processes during the grinding of workpieces with inhomogeneities Δa_K having different geometries and locations within the matrix—the material of the workpiece. This scheme determines the thermal and deformation coupling conditions at their boundaries - a_K.

We will account for the influence of structural inhomogeneities in the machined surface in the model by the presence of inclusions and defects such as cracks.

The equation of transient heat conduction:

$$\frac{\partial T}{\partial \tau} = a^2 \left(\frac{\partial^2 T}{\partial x^2} + \frac{\partial^2 T}{\partial y^2} \right) \tag{2}$$

b) Lame's elasticity equations in displacements:

$$\begin{aligned} &\frac{\partial \theta}{\partial x} \cdot \frac{1}{1-2\mu} + \Delta \vec{U} = b^T \frac{\partial T}{\partial x}, \qquad \vec{U} = \frac{U}{2G}, \qquad \vec{\mathrm{V}} = \frac{\mathrm{V}}{2\mathrm{G}}; \\ &\frac{\partial \theta}{\partial y} \cdot \frac{1}{1-2\mu} + \Delta \vec{U} = b^T \frac{\partial T}{\partial y}, \qquad b^T = \frac{4G(1+\mu)}{1-2\mu}\alpha t \end{aligned} \tag{3}$$

c) Initial conditions:

$$T(x, y, o) = 0 \tag{4}$$

d) boundary conditions for the temperature and strain fields:

$$\frac{\partial T}{\partial x} = -\frac{q(y,t)}{\lambda}, \qquad |y| < a, \qquad -\frac{\partial T}{\partial x} + jT = 0, \qquad |y| > a;$$
$$(\sigma_x(x,y,t)|_{x=0} = \tau_{xy}((x,y,t)\big|_{x=0} = 0 \tag{5}$$

e) Coupling conditions between the boundaries of the inhomogeneities and the base material:

for temperature fields	for strain fields
$\overset{k-1}{T}(a_k - 0, y, \tau) = \overset{k}{T}(a_k + 0, y, \tau)$	$\overset{k-1}{V_j}(a_k - 0, y) = \overset{k}{V_j}(a_k + 0, y)$
$\lambda_{k-1}\frac{\partial \overset{k-1}{T}}{\partial x}(a_k - 0, y, \tau) = \lambda_k \frac{\partial \overset{k}{T}}{\partial x}(a_k + 0, y, \tau)$	$\overset{k-1}{\sigma}_x(a_k - 0, y) = \overset{k}{\sigma_x}(a_k + 0, y)\ \overset{k-1}{\tau}_{xy}(a_k - 0, y) = \overset{k}{\tau_{xy}}(a_k + 0, y)$

(6)

e) Discontinuity conditions of the solution:

at inclusions:	at crack-like defects:
$< \tilde{u} >= 0, \quad < \sigma_x > \neq 0$	$< \sigma_x >= 0, \quad < \tilde{u} > \neq 0$
$< v >= 0, \quad < \tau_{xy} > \neq 0$	$< \tau_{xy} >= 0, \quad < \tilde{v} > \neq 0$

The conditions for the discontinuity of solution (6) at inhomogeneities such as inclusions and crack-like defects should be understood as follows [2], [20]:

$$< \tilde{u} \geq \tilde{u}(-0, y) - \tilde{u}(+0, y), \qquad < \sigma_x \geq \sigma_x(-0, y) - \sigma_x(+0, y)$$
$$< v >= \hat{v}(-0, y) - \hat{v}(+0, y), \qquad < \tau_{xy} >= \tau_{xy}(-0, y) - \tau_{xy}(+0, y)$$

5. Research results

The presence of stress concentrators in the surface layer of ground products—which include various types of defects introduced during the production of the blank and subsequent processing steps—significantly complicates the investigation of the causes of crack formation. Therefore, when determining the limit equilibrium state of the deformable surface layer, the values of the stress and strain components at the tip of the stress concentrator must be substituted into the classical strength criteria. This approach is used in fracture mechanics [21], where new strength criteria are formulated as specific invariants, both in models of continuum mechanics and in models that account for micro-inhomogeneities in the material being processed. Of the criteria available in fracture mechanics, which are divided into energy, force, and deformation criteria [22], [23], the most suitable for our case are the force-based criteria associated with the use of the stress intensity factor (SIF) [23], [24]. In the most general case, the distribution of strains in the vicinity of the crack-like defect is represented as a superposition of three partial strains corresponding to the three main types of crack surface displacement: normal separation, transverse, and longitudinal shear.

The stress intensity factors K_I, K_{II}, and K_{III} serve as a measure of stress singularity near the tip of a crack-like defect. The critical stress intensity, K_C, is a material property. When loading causes the stress intensity to reach the critical value,

the crack-like defect transforms into a main crack. The critical stress is inversely proportional to the square root of the initial length of the crack-like defect [25]:

$$\sigma_C = \frac{K_{1C}}{\sqrt{\pi l}}$$

where $2l$ is the initial length of the crack-like defect, and the subscript 1 denotes the first type of fracture.

The thermally stressed grinding process generates thermomechanical stresses in the surface layer, which, in the presence of inhomogeneous defects, can lead to their propagation in the form of chips and a network of cracks even in the absence of external mechanical loads.

Let there be defects in an elastic half-plane on the lines a_1, a_2, ..., a_k has $|\tilde{y}_1| < l_1$, $|\tilde{y}_2| < l_2, \ldots, |\tilde{y}_K| < l_K$, across which the displacement and stress fields undergo discontinuities. Hereinafter, we will consider a system of defects consisting of two cracks ($k = 1, 2$) located in local coordinates at $\tilde{x}_1 o_1 \tilde{y}_1$ ($k = 1$) and $\tilde{x}_2 o_2 \tilde{y}_2$ ($k = 2$), respectively. Fig. 1 shows a computational scheme for determining the influence of defects on crack initiation under thermal loading.

Let us consider the jumps in displacements and stresses at the defects:

$$\langle \tilde{V}_k(\tilde{y}) \rangle = \tilde{V}_k(-0, \tilde{y}) - \tilde{V}_k(+0, \tilde{y}), \qquad \left\langle \overset{k}{\sigma}_x(\tilde{y}) \right\rangle = \overset{k}{\sigma}_x(-0, \tilde{y}) - \overset{k}{\sigma}_x(+0, \tilde{y})$$

$$\langle \tilde{U}_k(\tilde{y}) \rangle = \tilde{U}_k(-0, \tilde{y}) - \tilde{U}_k(+0, \tilde{y}), \qquad \left\langle \overset{k}{\tau}_{xy}(\tilde{y}) \right\rangle = \overset{k}{\tau}_{xy}(-0, \tilde{y}) - \overset{k}{\tau}_{xy}(+0, \tilde{y})$$

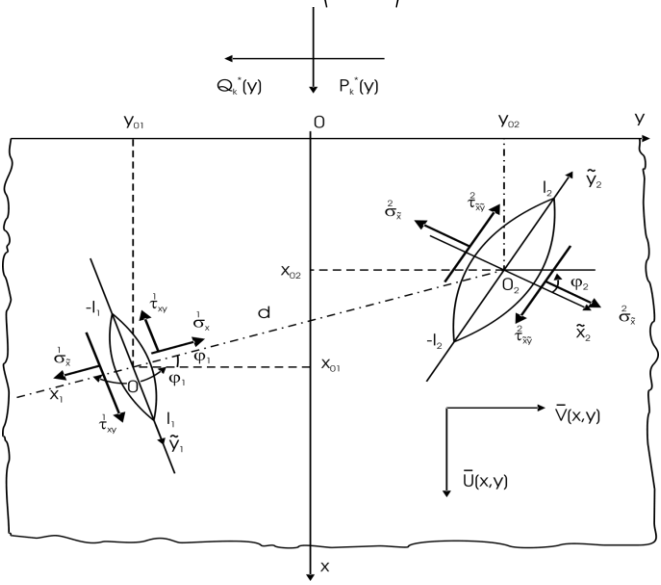

Fig. 1. Calculation scheme for determining the influence of defects on the intensity of crack formation under thermal loading.

According to conditions (6), at crack-type defects, the jumps in normal and tangential stresses are zero, i.e., $< \overset{K}{\sigma_r}(y) \geq 0,\ < \overset{K}{T_{xy}}(y) \geq 0$. The displacements $\widetilde{U}_K(\tilde{x},\tilde{y}), V_K(\tilde{x},\tilde{y}), \theta_K(\tilde{x},\tilde{y})$ must satisfy the Lamé equations:

$$\frac{\tilde{\Theta}'}{1-2\mu} + \Delta\widetilde{U}_k = b^T T', \qquad \frac{\tilde{\Theta}`}{1-2\mu} + \Delta\tilde{V}_k = b^T T`, \qquad \tilde{\Theta}_k = \widetilde{U}_k' + \tilde{V}`_k \qquad b^T = \frac{4G(1+\mu)dt}{1-2\mu}$$

Using Treffz's representations [2], [26], [27] in the Fourier transformants with respect to the variable y, one can determine the displacements $\widetilde{U}_{\beta K}(\tilde{x})$, $\tilde{V}_{\beta K}(\tilde{x})$ and the stresses $\overset{k}{\sigma}_{\tilde{x}\beta}(\tilde{x})\overset{k}{\tau}_{\tilde{x}\beta}(\tilde{x})$, $\overset{k}{\sigma}_{\tilde{x}\beta}(\tilde{x}) = \overset{k}{\sigma}_{y\beta}(\tilde{x})\tilde{y}$.

Returning to the original discontinuous solutions for the stress in local coordinates $\tilde{x}_K o_K \tilde{\tilde{y}}_K$, via the derivatives of the displacement jumps $< \widetilde{U}_K'(\tilde{y}) >, < V_K'(\tilde{y}) >$ are expressed as:

$$\overset{kI}{\sigma}_{\tilde{x}}(\tilde{x},\tilde{y}) = \frac{1}{4\pi(1-\mu)} \int_{-e_k}^{e_k} \langle \widetilde{U}_k'(r) \rangle \frac{(\tilde{y}-r)[(4\mu-3)(((\tilde{y}-r)^2+\tilde{x}^2)-\tilde{x}^2]}{[(\tilde{y}-r)^2+\tilde{x}^2]^2}\, dr - \\ - \frac{\tilde{x}}{4\pi(1-\mu)} \int_{-e_k}^{e_k} \langle \tilde{V}_k'(r) \rangle \frac{((\tilde{y}-r)^2-\tilde{x}^2)}{[(\tilde{y}-r)^2+\tilde{x}^2]^2} dr \tag{7}$$

$$\overset{kI}{\tau}_{\tilde{x}}(\tilde{x},\tilde{y}) = \frac{-\tilde{x}}{4\pi(1-\mu)} \int_{-e_k}^{e_2} \left\langle \widetilde{U_k'}(r) \right\rangle \frac{\left((\tilde{y}-r)^2-\widetilde{x^2}\right)}{\left[(\tilde{y}-r)^2+\widetilde{x^2}\right]^2} dr \\ - \frac{1}{4\pi(1-\mu)} \int_{-e_k}^{e_2} \left\langle \widetilde{V_k'}(r) \right\rangle \frac{(\tilde{y}-r)^2}{\left[(\tilde{y}-r)^2+\widetilde{x^2}\right]^2} dr \tag{8}$$

$$\overset{k'}{\sigma}_y(\tilde{x},\tilde{y}) = \int_{-e_k}^{e_k} \langle \widetilde{U}_k'(r) \rangle \left\{ \frac{(\tilde{y}-r)}{4\pi[(\tilde{y}-r)^2+\tilde{x}^2]^2} \left(1 + \frac{\tilde{x}^2}{(1-\mu)[(\tilde{y}-r)^2+\tilde{x}^2]^2}\right)\right\} dr + \\ + \frac{1}{2\pi(1-\mu)} \int_{-e_k}^{e_k} \langle \tilde{V}_k'(r) \rangle \left\{ (1+\mu)\tilde{x} l_n[(\tilde{y}-r)^2+\tilde{x}^2] + \frac{\tilde{x}[\tilde{x}^2+(\tilde{y}-r)^2]^2}{2[\tilde{x}^2+(\tilde{y}-r)^2]^2} \right\} dr \tag{9}$$

We find the compensating stresses as follows. We express the discontinuous solutions (7) – (9) in global coordinates and, setting $x = 0$, find the stresses at the boundary.

They will be equal to:

$$\overset{kI}{\sigma}_x(0,y) = \int_{-e_k}^{e_k} \left[\langle \widetilde{U}_k'(r) \rangle \overset{k}{R}_1(y,r) + \langle \tilde{V}_k'(r) \rangle \overset{k}{N}_1(y,r) \right] dr = P_k^*(y) \tag{10}$$

$$\overset{k}{\tau}_{xy}(0,y) = \int_{-e_k}^{e_k} \left[\langle \widetilde{U}_k'(r) \rangle \overset{k}{R}_2(y,r) + \langle \tilde{V}_k'(r) \rangle \overset{k}{N}_2(y,r) \right] dr = q_k^*(y) \tag{11}$$

Here, $\overset{K}{R}_j(x,y)$, $\overset{K}{N}_j(y,z)$ are the kernels ($k = 1,2$); characterizing the coordinate transformation (local $\tilde{x}_K o_K \tilde{y}_K$ to global XOY and the expressions of stress components in global coordinates. Taking as boundary conditions ($x = 0$):

$$\sum_{k=1}^{2} \overset{k}{\sigma}_x(0,y) = -P_k^*(y) = \sigma_x(0,y) \tag{12}$$

$$\sum_{k=1}^{2} \overset{k}{\tau}_{xy}(0,y) = -q_k^*(y) = \tau_{xy}(0,y) \tag{13}$$

we find the stress state of the surface layer:

$$\begin{aligned}\sigma_y^{II}(x,y) = {} & \frac{-\alpha_1 x\mu^*}{\pi}\sum_{k=1}^{2}\int_{-e_k}^{e_k}\left[\langle\tilde{U}_k'(r)\rangle\overset{k}{R}_1(y,r) + \langle\tilde{V}_k'(r)\rangle\overset{k}{N}_1(y,r)\right]\frac{dr}{x^2+(y-r)^2} + \\ & + \frac{\alpha_2 x}{\pi}\sum_{k=1}^{2}\int_{-e_k}^{e_k}\left[\langle\tilde{U}_k'(r)\rangle\overset{k}{R}_1(y,r) + \langle\tilde{V}_k'(r)\rangle\overset{k}{N}_1(y,r)\right]\frac{[x^2+(y-r)^2]dr}{[x^2+(y-r)^2]^2} + \\ & + \frac{\alpha_3+\mu^*}{2\pi}\sum_{k=1}^{2}\int_{-e_k}^{e_k}\left[\langle\tilde{U}_k'(r)\rangle\overset{k}{R}_1(y,r) + \langle\tilde{V}_k'(r)\rangle\overset{k}{N}_1(y,r)\right]\frac{(y-r)dr}{x^2+(y-r)^2} - \\ & - \frac{2\alpha_4 x}{\pi}\sum_{k=1}^{2}\int_{-e_k}^{e_k}\left[\langle\tilde{U}_k'(r)\rangle\overset{k}{R}_1(y,r) + \langle\tilde{V}_k'(r)\rangle\overset{k}{N}_1(y,r)\right]\frac{(y-r)dr}{[x^2+(y-r)^2]^2}\end{aligned} \tag{14}$$

$$\begin{aligned}\tau_{xy}^{II}(x,y) = {} & \frac{1}{2\pi}\left(\nu + \frac{\tilde{\mu}_1^*}{1-\mu}\right)\sum_{k=1}^{2}\int_{-e_k}^{e_k}\left[\langle\tilde{U}_k'(r)\rangle\overset{k}{R}_1(y,r) + \langle\tilde{V}_k'(r)\rangle\overset{k}{N}_1(y,r)\right]\frac{(y-r)dr}{x^2+(y-r)^2} \\ & + \\ & + \frac{-x\tilde{\mu}_1^*}{2\pi(1-\mu)}\sum_{k=1}^{2}\int_{-e_k}^{e_k}\left[\langle\tilde{U}_k'(r)\rangle\overset{k}{R}_1(y,r) + \langle\tilde{V}_k'(r)\rangle\overset{k}{N}_1(y,r)\right]arctg\frac{(y-r)dr}{|x|} - \\ & - \frac{x\nu^*}{2\pi}\sum_{k=1}^{2}\int_{-e_k}^{e_k}\left[\langle\tilde{U}_k'(r)\rangle\overset{k}{R}_1(y,r) + \langle\tilde{V}_k'(r)\rangle\overset{k}{N}_1(y,r)\right]ln\frac{1}{\sqrt{x^2+(y-r)^2}}dr - \\ & - \frac{x^2(1+\nu^*)}{2\pi(1-\mu)}\sum_{k=1}^{2}\int_{-e_k}^{e_k}\left[\langle\tilde{U}_k'(r)\rangle\overset{k}{R}_1(y,r) + \langle\tilde{V}_k'(r)\rangle\overset{k}{N}_1(y,r)\right]\frac{(y-r)dr}{[x^2+(y-r)^2]^2} - \\ & - \frac{x\tilde{\mu}_1^*}{4\pi(1-\mu)}\sum_{k=1}^{2}\int_{-e_k}^{e_k}\left[\langle\tilde{U}_k'(r)\rangle\overset{k}{R}_1(y,r) + \langle\tilde{V}_k'(r)\rangle\overset{k}{N}_1(y,r)\right]\frac{x^2+(y-r)^2}{[x^2+(y-r)^2]^2}dr + \\ & + \frac{x}{4\pi(1-\mu)}\sum_{k=1}^{2}\int_{-e_k}^{e_k}\left[\langle\tilde{U}_k'(r)\rangle\overset{k}{R}_1(y,r) + \langle\tilde{V}_k'(r)\rangle\overset{k}{N}_1(y,r)\right]\frac{(y-r)(3x^2+(y-r)^2)}{[x^2+(y-r)^2]^3}dr - \\ & + \frac{x}{4\pi(1-\mu)}\sum_{k=1}^{2}\int_{-e_k}^{e_k}\left[\langle\tilde{U}_k'(r)\rangle\overset{k}{R}_1(y,r) + \langle\tilde{V}_k'(r)\rangle\overset{k}{N}_1(y,r)\right]\frac{(y-r)(3x^2+(y-r)^2)}{[x^2+(y-r)^2]^3}dr -\end{aligned} \tag{15}$$

$$-\frac{x(1+\nu^*)}{\pi}\sum_{k=1}^{2}\int_{-e_k}^{e_k}\left[\left\langle\tilde{U}_k'(r)\right\rangle\overset{k}{R}_1(y,r)+\left\langle\tilde{V}_k'(r)\right\rangle\overset{k}{N}_1(y,r)\right]\frac{dr}{x^2+(y-r)^2}$$

$$\begin{aligned}\sigma_x^{II}(x,y)=\gamma_1\sum_{k=1}^{2}\int_{-e_k}^{e_k}\left[\left\langle\tilde{U}_k'(r)\right\rangle\overset{k}{R}_1(y,r)+\left\langle\tilde{V}_k'(r)\right\rangle\overset{k}{N}_1(y,r)\right]\frac{2xdr}{x^2+(y-r)^2}-\\ -x\gamma_2\sum_{k=1}^{2}\int_{-e_k}^{e_k}\left[\left\langle\tilde{U}_k'(r)\right\rangle\overset{k}{R}_1(y,r)+\left\langle\tilde{V}_k'(r)\right\rangle\overset{k}{N}_1(y,r)\right]\frac{2[x^2+(y-r)^2]dr}{[x^2+(y-r)^2]^2}+\\ +2\gamma_3\sum_{k=1}^{2}\int_{-e_k}^{e_k}\left[\left\langle\tilde{U}_k'(r)\right\rangle\overset{k}{R}_1(y,r)+\left\langle\tilde{V}_k'(r)\right\rangle\overset{k}{N}_1(y,r)\right]\frac{(y-r)dr}{x^2+(y-r)^2}-\\ -4x^2\gamma_4\sum_{k=1}^{2}\int_{-e_k}^{e_k}\left[\left\langle\tilde{U}_k'(r)\right\rangle\overset{k}{R}_1(y,r)+\left\langle\tilde{V}_k'(r)\right\rangle\overset{k}{N}_1(y,r)\right]\frac{(y-r)dr}{[x^2+(y-r)^2]^2}\end{aligned} \tag{16}$$

In equations (14) – (16), the following notation is used:

$$\bar{\mu}_1^*=\frac{(3-4\mu)(1-2\mu)}{4\mu(1-2\mu)},\bar{\mu}_2^*=\frac{3-4\mu}{2\mu};\nu=\frac{1-2\mu}{2(1-2\mu)};\nu^*=\frac{3-4\mu}{4\mu(1-2\mu)}$$

$$\mu_1^*=\frac{1-2\mu}{2(1-\mu)}\bar{\mu}_1^*;\quad \mu_2^*=\frac{1-2\mu}{2(1-\mu)}\bar{\mu}_2^*;\quad \mu^*=\frac{1}{4\pi(1-\mu)}$$

$$\alpha_1=\frac{1+\bar{\mu}_2^*+\mu_2^*}{2};\quad \alpha_2=\frac{\mu_1^*-1-\bar{\mu}_2^*}{4\pi(1-\mu)};\quad \alpha_3=\mu_1^*+\nu;\quad \alpha_4=\frac{\mu_2^*-\bar{\mu}_1^*+1}{4\pi(1-\mu)}$$

$$\gamma_1=\frac{\mu(\bar{\mu}_1^*-\bar{\mu}_2^*)-(\mu+\bar{\mu}_2^*-2\mu\bar{\mu}_2^*)}{4\pi(1-\mu)};\quad \gamma_2=\frac{\bar{\mu}_1^*-1-\bar{\mu}_2^*}{8\pi(1-\mu)}$$

$$\gamma_3=\frac{2(\mu\bar{\mu}_1^*-\mu\bar{\mu}_2^*-\mu)-(3-4\mu)+(1-2\mu)\bar{\mu}_1^*-2(1-\mu)\bar{\mu}_2^*}{8\pi(1-\mu)};\quad \gamma_4=\frac{\bar{\mu}_1^*-\bar{\mu}_2^*-1}{8\pi(1-\mu)}$$

The thermoelastic stresses generated by the heat flux $q(y,t)$ acting at the boundary $x=0$, in the contact zone $|y|<a$, and by heat transfer according to Newton-Richman's law $\lambda\delta T/\delta x+\gamma T=0$ [28], outside this zone, i.e., $|y|>a$, we obtain from the solution of problem (2)–(6) (the special case $k=0$, $0\le x<\Delta$). In global coordinates, these stresses are expressed as:

$$\begin{aligned}\sigma_x^{III}(x,y)=\frac{2\alpha_1(x^2-y^2)}{\pi[x^2+y^2]^2}-\frac{2\alpha_2 y(3x^2-y^2)}{\pi[x^2+y^2]^3}+\frac{(\alpha_3-x\alpha_4)}{\pi}\frac{2x(x^2-3y^2)}{[x^2+y^2]^3}-\\ -\frac{x\alpha_5}{\pi}\frac{\Gamma(4)\cos(\frac{4x}{\sqrt{x^2+y^2}})}{[x^2+y^2]^2}+\frac{b^T}{2\pi}\int_{-\infty}^{\infty}\int_{0}^{\infty}e^{-i\beta y}\left[T_\beta''(\xi)\Phi_\beta(x-\xi)+\right.\\ \left.+T_\beta'(\xi)\Phi_\beta'(x-\xi)-\lambda^2\beta^2T_\beta(\xi)\Phi_\beta(x-\xi)\right]d\xi d\beta\end{aligned} \tag{17}$$

$$\tau_{xy}^{III}(x,y)=\frac{\gamma_1 2xy}{\pi[x^2+y^2]^2}-\frac{\gamma_2 x(x^2-3y^2)}{\pi[x^2+y^2]^3}+ \tag{18}$$

$$+\frac{\gamma_3}{\pi}\frac{y(3x^2-y^2)}{[x^2+y^2]^3}-\frac{\gamma_4 x}{\pi}\frac{\Gamma(4)\,sin(\frac{4x}{\sqrt{x^2+y^2}})}{[x^2+y^2]^2}-$$
$$-\frac{b^T}{2\pi}\int_{-\infty}^{\infty}\int_0^{\infty}e^{-i\beta y}\left[2T_\beta^{'}(\xi)\Phi_\beta(x-\xi)+T_\beta(\xi)\Phi_\beta^{'}(x-\xi)\right]d\xi d\beta$$

$$\sigma_y^{III}(x,y)=\frac{b_1}{\pi}\frac{x^2-y^2}{[x^2+y^2]^2}-\frac{b_2+b_3x}{\pi}\frac{x(x^2-3y^2)}{[x^2+y^2]^3}+$$
$$+\frac{b_4 x\Gamma(4)\,cos(\frac{4x}{\sqrt{x^2+y^2}})}{[x^2+y^2]^2}- \qquad (19)$$
$$-\frac{b^T}{2\pi}\int_{-\infty}^{\infty}\int_0^{\infty}\beta^2 e^{-i\beta y}\,T_\beta(\xi)\Phi_\beta(x-\xi)d\xi d\beta$$

Returning to the solutions found for the normal $\sigma_x^{II}(x,y)$, $\sigma_x^{III}(x,y)$, and tangent $\tau_{xy}^{II}(x,y)$, $\tau_{xy}^{III}(x,y)$ stresses in local coordinates and using the obvious conditions:

$$\lim_{\tilde{x}\to 0}\left[\overset{k}{\sigma}_{\tilde{x}}^{I}(\tilde{x},\tilde{y})+\overset{k}{\sigma}_{x}^{II}(\tilde{x},\tilde{y})+\overset{k}{\sigma}_{x}^{III}(\tilde{x},\tilde{y})\right]=0$$
$$\lim_{\tilde{x}\to 0}\left[\overset{k}{\tau}_{xy}^{I}(\tilde{x},\tilde{y})+\overset{k}{\tau}_{xy}^{II}(\tilde{x},\tilde{y})+\overset{k}{\tau}_{xy}^{III}(\tilde{x},\tilde{y})\right]=0 \qquad (20)$$

We finally arrive at a system of 4 singular integral equations with respect to the sought-after derivatives of the displacement jumps $<\tilde{U}_K^{'}(y)>,<\tilde{V}_K^{'}(y)>(K=1,2)$ [29], [30]:

Of greatest interest is the behavior of the stresses $\sigma_x(o,y)+iT_{xy}(o,y)$ for $y\to lK\pm o$. These stresses determine the nature of the stress intensity factors—SIFs: K_I and iK_{II}.

Consider the case of a crack-type defect of length $2l$, located in a surface layer of thickness $2h$ and arbitrarily oriented. The stress state of the surface layer is determined by the disturbance near the crack of a given temperature field $T_q(x,y,\tau)$. If the temperature field is described by the function $\mathrm{T}_o(x,y,\tau)=q(\tau)(ycos\beta+xsin\beta)$, then to determine the stress intensity factors, we have the formula:

$$K_I^{\pm}-iK_{II}^{\pm}=\mp i\frac{\sqrt{\pi l}Hql}{\lambda}sin(\beta-\phi)\times$$
$$\times\left\{1-\frac{\delta^2}{2}(\alpha_1-N_{11})-\frac{\delta^4}{4}\left[d_2+\frac{3}{2}d_3-d_1N_{11}-N_{11}^2+N_{31}\right]+0(\delta^6)\right\} \qquad (21)$$

where β is the angle between the direction of the heat flux and the Oy axis; ϕ is the angle between the defect axis and the Ox axis; $\delta=l/h$ is the dimensionless width of the band:

$$d_1=-\left(i\,sin\,2\,\phi+e^{-4i\phi}\right)I_1-\frac{1}{2}e^{-2i\phi}\Im_1-\left(1-2e^{-2i\phi}-e^{-4i\phi}\right)A_2-4e^{-4i\phi}E_4$$

$$d_3 = \frac{1}{6}\left[\left(\sin 4\phi - 2e^{-4i\phi} + 2e^{-6i\phi}\right)I_3 + \frac{1}{2}e^{-4i\phi}\Im_3 + \left(4e^{-2i\phi} - e^{-4i\phi} - 4e^{-4i\phi} - e^{-6i\phi}\right)\right]A_4 - 4e^{-6i\phi}E_6$$

$$d_2 = \frac{1}{8}\left[1 - \cos 4\phi + 8\sin^2\phi + 5i\sin\phi\left(e^{-5i\phi} - 2e^{-i\phi}\right)\right]\Im_1 + \frac{1}{2}\left(\cos 4\phi - 5i\sin\phi\, e^{-5i\phi}\right)I_3 + \Im_{3/4} + 2e^{-i\phi}E_6 +$$

$$+\left[i\sin\phi\left(3e^{-i\phi} - 2e^{-i\phi}\right) - e^{-2i\phi}\right] + \frac{1}{2}\left[2i\left(3e^{i\phi} - 3e^{-i\phi} - 2e^{-i\phi} + e^{3i\phi}\right)\sin\phi + e^{2i\phi} - 2e^{-2i\phi} - 16\sin^2\phi\, e^{-4i\phi}\right]E_4$$

$$\Im_n = 4\int_0^\infty y^{n+2} sh2y e(y)dy; \quad I_n = \int_0^\infty y^n[(1 - e^{-2y})sh2y - 4y^2]e(y)dy$$

$$A_n = \int_0^\infty y^n(ch2y - 1)e(y)dy;$$

$$E_n = \int_0^\infty y^n e(y)dy\,; e(y) = \frac{1}{4y^2 - sh^2 2y}$$

$$N_{11} = \frac{\pi^2}{48}(\cos 2\phi \pm 3); \quad N_{31} = \frac{\pi^4}{256}(\cos 4\phi/15 \pm \cos 2\phi); \quad N_{33} = \frac{N_{31}}{3}$$

Here and hereafter, the upper index corresponds to the right end of the defect, and the lower index to the left end.

Figures 2 and 3 show the relationships between $K_I^* = \lambda K_I/\sqrt{\pi l}Hql$ and $K_{II}^* = \lambda K_I/\sqrt{\pi l}Hql$ as a function of the crack rotation angle φ for $l/h = d = 0.1$ (Curves 1 and 2 correspond to the boundary conditions of the heat conduction problem: if the boundary temperature is specified as -1, or if the heat flux and heat transfer conditions are specified as 2), when the heat flux is perpendicular to the OY axis; solid lines correspond to the right end of the crack, dashed lines to the left; $H = \alpha t^{\circ}E/2$.

The figures show that the values of K_I and K_{II} in the absence of heat transfer (curves 2) are greater in absolute magnitude than when the boundary outside the contact zone is thermally insulated.

The value of K_{II} reaches its maximum when the heat flux is perpendicular to the crack.

The normal stress intensity factors K_I, which take on negative values, have no independent significance, since in this case it is necessary to solve the problem in a formulation that accounts for contact between the crack walls.

We investigate the stress intensity at the tips of a crack located at a depth of $\delta*$, when a temperature T_0 is maintained at its edges, and a heat flux $q(T, y)$ directed perpendicular ($\beta = 0$ —the angle between the flux direction and the Ox axis) to this surface is applied at the part's surface ($x = 0$). The thermoelastic state

of the machined surface will be determined solely by the disturbed temperature field. Given that along the line of a crack-like defect $T0 = 2q0 * \delta *$ from equations (17) – (19) and (21), we find:

$$K_I^{*\pm} = \mp q_0^* Hl\sqrt{\pi l}; \quad K_{II}^{*\pm} = \pm 2HT_0\sqrt{\frac{l}{\pi}} \tag{22}$$

If we introduce the quantity $P\eta = q0 * Hl\delta *$, where P is the tensile stress formed under the action of temperatures, andh is a parameter, then the following important characteristics for the behavior of defects can be established. If the values of the stress intensity factors are known, then the initial crack propagation angle $\theta *$ and the limiting value of the heat flux for it are determined from the relations [31], [32], [33]:

$$\theta_* = 2arctgD, \quad D = \frac{K_I - \sqrt{K_I^2 + 8K_{II}^2}}{4K_{II}} \tag{23}$$

$$q_{0*} = \frac{\sqrt{3}\lambda K_{1C}}{Hl\sqrt{\pi l}\delta^*} \tag{24}$$

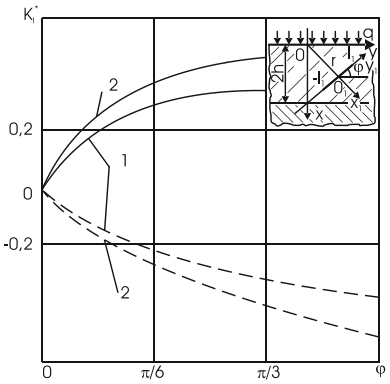

Fig. 2. Dependence of $K_I^* = \lambda K_I / \sqrt{\pi l} Hql = f(\phi)$ on the crack rotation angle φ at $\delta = l/h = 0.1$; 1 – when the boundary temperature is specified; 2 – when the heat flux and heat transfer conditions are specified; solid lines 1 and 2 represent the right end of the crack, and dashed lines represent the left end.

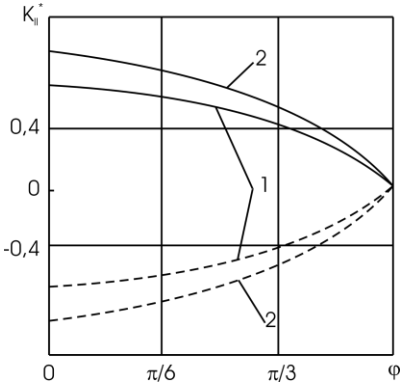

Fig. 3. Dependence of $K_{II}^* = \lambda K_I / \sqrt{\pi l} Hql = f(\phi)$ on the crack rotation angle φ at $\delta = l/h = 0.1$; 1 - Type I stress state; 2 - heat flux and heat transfer conditions are specified; solid lines 1, 2 - right, dashed lines - left ends of the crack.

Figs. 2 and 3 show the dependencies of the angle θ and the reduced tensile stress $\bar{P}_* = \sqrt{\pi l} \cdot P/K_{1C}$ at the right end of the crack on the angle α and various values of $\eta = q_o^* H l^*/p$.

Under the action of the heat flux, the thermally insulated crack begins to grow from both ends simultaneously. As shown in Fig. 2, with an increase in the heat flux, the ultimate stresses decrease, i.e., a disturbance of equilibrium is possible in the region of the defect under consideration, and a microcrack forms.

Let us consider the mutual influence of defects on stress intensity using the example of two arbitrarily oriented inhomogeneities. We will choose the origin on one of the inhomogeneities, and the second can move arbitrarily relative to the first. From equations (21) – (24), with $l_K = l$, $a_{ij} = a$, $\varphi_1 = 0$, $\varphi_2 = \varphi$, and $\delta = l/d$, after calculations accurate to δ^7,the SIF expression for the upper crack takes the form:

$$K_I^{\pm} = \frac{1}{\sqrt{\pi l} H q l}[0{,}5\delta - 0{,}25\delta^3 + 0{,}207\delta^5 - 0{,}0371\delta^7] \qquad (25)$$

$$K_{II}^{\pm} = \frac{1}{\sqrt{\pi l} H q l}[1 - 0{,}25\delta^2 + 0{,}195\delta^4 - 0{,}1787\delta^8] \qquad (26)$$

Fig. 4 shows the dependence of the values of K_s ($S = I$ – solid line, $S = II$ – dashed line) on the dimensionless distance between cracks $\alpha = a/2l$, calculated numerically using equations (25) and (26). When $\delta < 0.5$, the presence of the second defect has little effect on the value of K_{II}, whereas the coefficient K_I still depends significantly on the distance between the cracks. Fig. 5–10 shows the dependence of SIF on the angle φ (the angle of rotation of the second crack relative to the first) for $\delta = 1/3$ ($a = 3l$) when $\psi = 0, \pi/6, \pi/3, \pi/2$ (the curves are labeled with numbers 1–4 for the moving crack and 1′–4′ for the stationary crack; solid lines correspond to SIF at the right vertices of the crack (K_j^+), dashed lines at the left vertices (K_j^-).

The figures show that, for certain crack configurations, the coefficient K_I at one end may be negative (this means that the crack edges come into contact in the vicinity of that end). In this case, the SIF values in the vicinity of the other end of the macrocrack remain practically unchanged and can be used to determine the critical force at which the crack reaches a state of limit equilibrium.

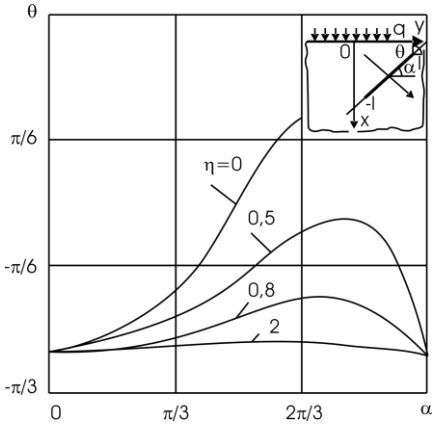

Fig. 4. Dependence of the initial crack propagation angle $\theta*$ on the angle α for various values of $\eta = q_0^* Hl\delta^*/P$.

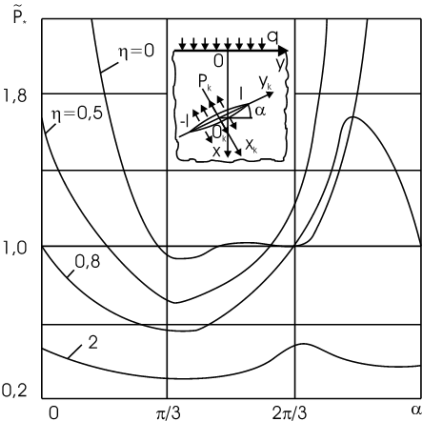

Fig. 5. Dependence of the reduced value of on tensile stresses $\tilde{P}_* = \sqrt{\pi l} \cdot P_*/K_{1C}$

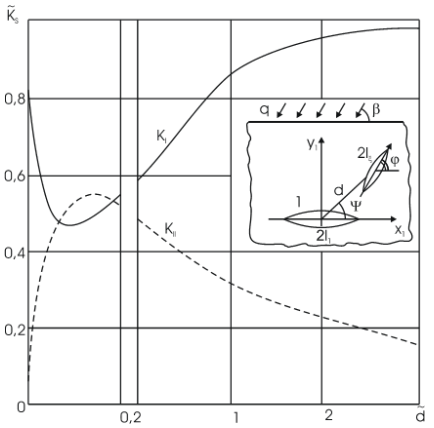

Fig. 6. Dependence of the value of K_s ($S = I$ – solid line, $S = II$ – dashed line) on the dimensionless crack spacing $\tilde{\alpha} = \alpha/2l$.

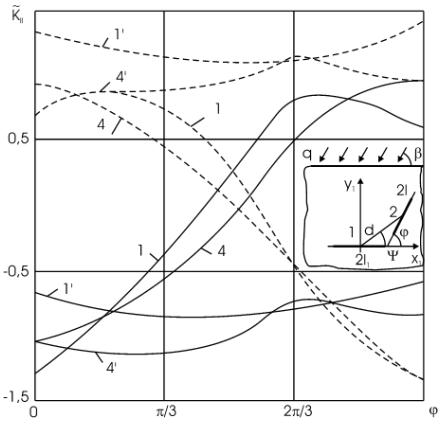

Fig. 7. Dependence of the value $\tilde{K}_{II}$ on the angle φ—the rotation of the second crack relative to the first—when $\delta = 1/3$, $\psi = 0$, $\psi = \pi/2$.

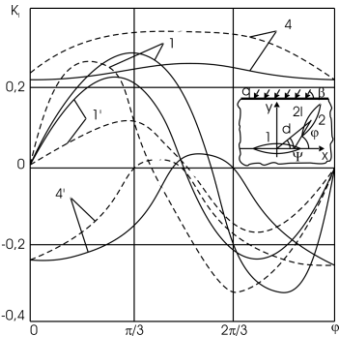

Fig. 8. Dependence of K_I on the angle φ of rotation of the second crack relative to the first at $\delta = 1/3$, when $\psi_1 = 0$, $\psi_4 = \pi/2$.

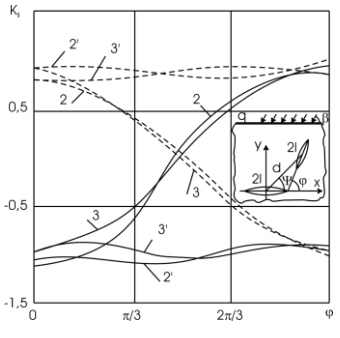

Fig. 9. Dependence of $K_{II} = f(\varphi)$ for $\delta = 1/3$, when $\psi_2 = \pi/6$, $\psi_3 = \pi/3$; solid lines—at the right vertices of the crack, dashed lines—at the left vertices.

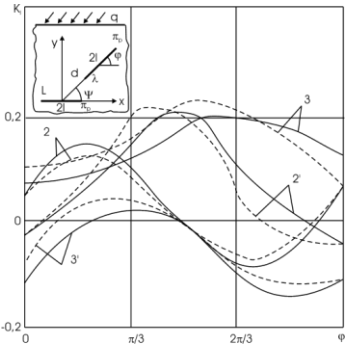

Fig. 10. Dependence of $K_I = f(\varphi)$ for $\delta = 1/3$ when $\psi_2 = \pi/6$, $\psi_3 = \pi/3$; solid lines—at the right vertices of the cracks, dashed lines—at the left vertices.

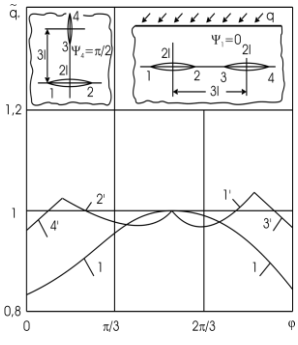

Fig. 11. Dependence of the critical heat flux value $\tilde{q}^* = q_0 l\sqrt{\pi l}/\sqrt{3}K_{1C}\lambda$ on the angle φ when $\delta = l/a = 1/3$.

For the values of SIF obtained from equations (7), (8), (17), and (19), the critical heat flux q^* is determined. The dependence of the reduced values $\tilde{q}^* = q^*/q_1$ ($q_1 = \sqrt{3}K_{1C}\lambda/(Hl\sqrt{\pi l})$ —corresponds to the value of the critical heat flux in a plane with a single crack) on the angle φ at $\delta = = l/a = 1/3$ is shown in Fig. 11. The curves labeled 1–4 correspond to the minimum value of $\tilde{q}^*$ at which crack propagation will begin from the corresponding vertex; the initial numbering of the crack vertices is chosen when $\varphi = 0$. Fig. 12 shows curves of the values $\tilde{q}^*$ for $\psi_1 = 0$ and $\psi_4 = \pi/2$ — for $\psi_2 = \pi/6$, $\psi_3 = \pi/3$ (the dashed curves correspond to the values $\psi_2 = \pi/2$ and $\psi_3 = \pi/3$).

It follows from the figures shown that when $0 \le \psi \le \pi/6$, a stationary crack begins to propagate first, and for all values of φ (with the exception of a certain region in the vicinity of $\varphi = \pi/2$) at vertex I. The critical heat flux has the smallest value for $\psi = 0$ and $\varphi = 0$ and for $\psi = \pi/6$ when $\varphi = \pi/2$. If $\psi = \pi/3$, then crack propagation begins from the bridge side, and the minimum value of $\tilde{q}^*$ is achieved when $\varphi = \pi/4$. In the case where $\pi/2 \le \varphi \le 5\pi/6$, the cracks mutually reinforce each other, i.e., the strength of the body in this case is higher than when there is only one crack. When $\psi = \pi/2$ and $\delta = 1/3$, the cracks practically do not interact.

Analysis of equations (16), which describe the thermally stressed state of the treated surface layer containing inclusions, allows us to determine the influence of the mechanical and thermophysical properties of these inclusions on the nature of their interaction with crack-like defects.

As an example, let us examine the stress state of a surface layer containing an inclusion with a crack (Fig. 13). We will present the solution to the heat conduction problem in the form:

$$T(S) = \frac{2q_0 l \sin\beta_0}{\lambda_{12}}\sqrt{1-S^2}\left[1 - \lambda_* \frac{\delta^2}{2} + \lambda_*^2 \frac{\delta^4}{4} - \lambda_* \left(S^2 + \lambda_*^2 + \frac{1}{2}\right)\frac{\delta^6}{8}\right] \qquad (27)$$

where $\lambda_{12} = \lambda_1 + \lambda_2$, $S = T/l$, $\delta = l/R$, $\lambda_* = \lambda_1/\lambda_2$. The stresses along the crack line are determined by the formulas:

$$\begin{gathered} -\sigma_x(S) = -A_0 - 3A_1 S\cos\beta_0 \\ \tau_{xy}(S) = -A_1 S \sin\beta_0 \end{gathered} \qquad (28)$$

where $A_0 = -\frac{4G_1(\alpha_2-\alpha_1)T_0}{2G+x_1-1}$; $A_0 = -\frac{2q_0 l G_1 \alpha_2 D_2^*}{\alpha_2(\hat{G}+x_1)}$; $D_2^* = \frac{2\lambda_2\alpha}{\lambda_{12}}$, a_1, a_2 are the linear thermal expansion coefficients of the insert and the matrix, respectively, $\tilde{\alpha} = a_1/a_2$

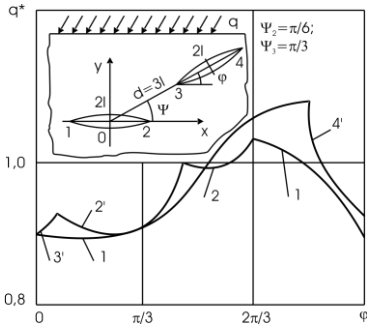

Fig. 12. Dependence of the critical heat flux value $\tilde{q}^* = q_0 l\sqrt{\pi l}/\sqrt{3}K_{1C}\lambda$ on the rotation angle φ of the crack-like defect of the second crack at $\delta = l/a = 1/3$.

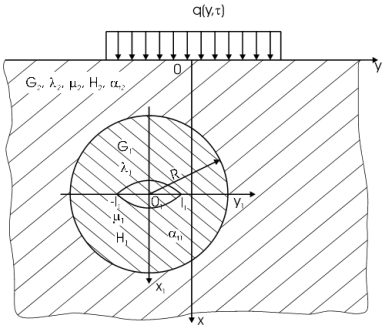

Fig. 13. Calculation scheme for determining the thermal stress state of a surface layer with an inclusion containing a crack-like defect.

G_1, G_2 - shear moduli of the inclusion and the matrix; $\tilde{G} = \mathrm{G}_1/\mathrm{G}_2$ - relative shear stiffness $H_{1(2)} = (3 - 4V_{1(2)})/(1 + V_{1(2)})$, $V_{1(2)}$ - Poisson's ratio of the inclusion (matrix): λ_1 , λ_2 - thermal conductivities of the inclusion and the matrix, respectively; q_o - heat flux acting on the boundary of the half-plane.

Substituting (28) into the formula:

$$K_j^{\pm} = C_j + \int_{-l}^{l} K_j^{\pm}(S)\sigma_x(S)dS \tag{29}$$

we find:

$$\begin{gathered} K_I^{\pm} = \sqrt{\pi l}\left[A_0\left(1 + \frac{1}{2}B_{10} + \frac{1}{8}B_{12} + \frac{1}{16}B_{14}\right) + \frac{3}{2}A_1 \cos\beta_0\left(\pm 1 + \frac{1}{4}B_{11} + \frac{1}{8}B_{13}\right)\right] \\ K_{II}^{\pm} = \sqrt{\pi l}\left[A_1 \sin\beta_0\left(\pm 1 + \frac{1}{4}B_{21} + \frac{1}{8}B_{23}\right) + \frac{q_0 H_1 \delta l}{\lambda_{12}}\sin\beta_0\left(\pm f_1 \pm 3f_2\frac{\delta^4}{4} + \frac{1}{4}f_1 B_{21}\right)\right] \pm \\ \pm \frac{H_1\sqrt{\pi l}}{4}\left[T_0 - \frac{l f_1 \lambda_*}{2\lambda_1}(2 - \lambda_*\delta^2)\frac{\delta^6}{32}\right]\left\{1 - B_1\frac{\delta^2}{2} + (9B_1 + C_1)\frac{\delta^4}{8} + (18 + 9B_1 + C_1)\frac{\delta^6}{32}\right\} \end{gathered} \tag{30}$$

where

$$B_1 = \frac{(x_1 + 1)}{(x_1 + \bar{G})}; \quad C_1 = -\frac{(x_1 + 1)}{(Gx_2 + 1)}$$

Analysis of the results shows that the presence of a hard switch ($V_1 > V_2$) leads to an increase in the value of K_I under mechanical loading and to a decrease under thermal loading. The thermal linear expansion coefficients of the composite have a significant influence on the nature of the change in SIF. For example, when $\alpha_{t1} < \alpha_{t2}$, $K_I > 0$, and when $\alpha_{t1} > \alpha_{t2}$, $K_I < 0$. The thermal conductivity coefficients λ_1 and λ_2 do not qualitatively affect K_I and K_{II}, but only alter them quantitatively. Thus, when $\tilde{\lambda} = 4$, the absolute value of SIF is greater than when $\tilde{\lambda} = 0.5$.

If the inclusion is considered as an ellipse, then when $\beta = 0$, the heat flux is directed parallel to the major axis; an increase in the stiffness of the inclusion ($V_1 > V_2$) according to the works [34], [35], [36], [37] leads to an increase in the stress intensity factors K_I ($K_{II} = 0$) for various composite $\tilde{\lambda}$.

The examples discussed above demonstrate the interaction between cracks and inclusions, as well as the stress state of a material containing these inhomogeneities. It has been shown that under certain conditions, stiffer inclusions strengthen the material, while softer structural components help inhibit the development of microcracks into main cracks. By appropriately selecting the material of the inclusions, the stress concentration in crack-like defects can be reduced.

Thus, for defect-free machining of workpieces made of functionally graded materials, their structural heterogeneity must be taken into account. The presence of crack-like defects and inclusions means that when selecting machining parameters and tool characteristics, one should be guided by the limiting values of the resulting heat flux.

To study the influence of the tool's design parameters on the part's temperature field, we will use the following discrete model. In the contact zone of length $2a$ between the wheel and the part, a heat flux $q(y,T)$ is formed due to the superposition of temperature pulses from individual grains of the wheel, equal to [38]:

$$q(y,\tau) = +\frac{C\sqrt{\tau_k}}{\lambda}[H(y) - H(y-2a)]\sum_{k=0}^{n}\delta\left(y + kl^* - V_{kp}\tau_k\right) \quad (31)$$

here $H(y)$ is the Heaviside function; $\delta(y)$ is the Dirac delta function; k is the number of grains passing through the contact zone during the time interval $\tau_k = \frac{\sqrt{D_{cr}t_{gr}}}{V_{cr}}$; a, λ are the thermal diffusivity and thermal conductivity of the workpiece material; $C\sqrt{\tau}$ is the heat flux from a single grain; V_g, V_{cr}, $\mathrm{t_{grind}}$ are the grinding conditions.

The fundamental solution to problems (2), (4), and (5) is known [39]:

$$G(x-x', y-y', \tau-\tau') = \frac{1}{4\pi a(\tau-\tau')}e^{-\frac{(x-x')^2+(y-y')^2}{4a(\tau-\tau')}}$$

Therefore, using Duamel's principle [40], the solution to problems (2), (4), and (5), taking (31) into account, can be expressed as:

$$T(x,y,\tau) = \frac{C}{2\pi\lambda}\int_0^{\tau}\frac{d\tau'}{\sqrt{\tau-\tau'}}\int_{-\infty}^{\infty}[H(y) - H(y-2a^*)]\,e^{\frac{2V_g y' + V_g^2\tau}{4a} + \frac{(y-y')^2+x^2}{4a(\tau-\tau')}}\sum_{k=1}^{n}\delta(y' + kl - V_{kp}\tau')\,dy' K_j^{\pm} = C_j + \int_{-l}^{l}K_j^{\pm}(S)\sigma_x(S)dS \quad (32)$$

or, moving to the desired function and applying the properties of the function $H(y)$, we obtain:

$$T(x,y,\tau) = \frac{C}{2\pi\lambda}\int_0^{\tau}\frac{d\tau'}{\sqrt{\tau-\tau'}}\int_0^{L}e^{-\frac{V_\partial(y-y')}{2a} - \frac{V_\partial^2(\tau-\tau')}{4a} - \frac{(y-y')^2+x^2}{4a(\tau-\tau')}}\sum_{k=0}^{\infty}\delta(y' + kl - V_{kp}\tau')\,dy' \quad (33)$$

This expression is already a solution to the problem, but it is inconvenient for practical calculations and research.

Using well-known transformations [41] and applying the properties of the delta function, we reduce the solution to a simpler form.

Due to the uniform convergence of the series under the integral, it can be integrated term by term, i.e.,

$$T(x,y,\tau) = \frac{C}{2\pi\lambda}\sum_{k=0}^{\infty}\int_0^{\tau}\frac{d\tau'}{\sqrt{\tau-\tau'}}\int_0^{L}e^{-\frac{V_\partial(y-y')}{2a} - \frac{V_\partial^2(\tau-\tau')}{4a} - \frac{(y-y')^2+x^2}{4a(\tau-\tau')}}\delta(y' + kl - V_{kp}\tau')dy' \quad (34)$$

Expression (34) can be simplified by using the definition of the delta function and the obvious inequality for the source coordinate y': $0 \le y' \le L = a*$; $K_l/V_{\text{кр}} \le \tau' \le (L+K_l)/V_{\text{кр}}$

$$\Im_k = \int_0^{L} exp\left[-\frac{V_\partial(y-y')}{2a} - \frac{V_\partial^2(\tau-\tau')}{4a} - \frac{(y-y')^2+x^2}{4a(\tau-\tau')}\right]\delta(y' + kl - V_{kp}\tau')dy' = \quad (35)$$

$$= exp\left[-\frac{V_\partial(y-y')}{2a} - \frac{{V_\partial}^2(\tau-\tau')}{4a} - \frac{(y-y')^2+x^2}{4a(\tau-\tau')}\right]$$

For $\tau' \overline{\in} \left[\frac{kl}{V_{kp}}; \frac{L+kl}{V_{kp}}\right]$, the integral $I_K = 0$. Applying the Heaviside function, this can be expressed as follows:

$$\Im_k = \left[H(\tau' - \frac{kl}{V_{kp}}) - H(\tau' - \frac{L+kl}{V_{kp}})\right] e^{-\frac{V_\partial(y+kl-V_{kp}\tau')}{2a} - \frac{{V_\partial}^2(\tau-\tau')}{4a} - \frac{(y+kl-V_{kp}\tau')^2+x^2}{4a(\tau-\tau')}}$$

The integral solution to (34) then takes the form:

$$T(x,y,\tau) = \frac{C}{2\pi\lambda}\sum_{k=0}^{\infty}\left[H(\tau' - \frac{kl}{V_{kp}}) - H(\tau' - \frac{L+kl}{V_{kp}})\right] exp\left[-\frac{V_\partial(y+kl-V_{kp}\tau')}{2a} - \frac{{V_\partial}^2(\tau-\tau')}{4a} - \frac{(y+kl-V_{kp}\tau')^2+x^2}{4a(\tau-\tau')}\right]\frac{d\tau'}{\sqrt{\tau-\tau'}} \quad (36)$$

This expression contains a Heaviside function under the integral. Using its properties, as before, we can determine the actual limits of integration. Solution (36) can be written in a form convenient for calculation:

$$\int_0^{\tau}\left[H(\tau' - \frac{kl}{V_{kp}}) - H(\tau' - \frac{L+kl}{V_{kp}})\right] f(\tau,\tau')d\tau' = H(\tau - \frac{kl}{V_{kp}}) - H(\tau - \frac{L+kl}{V_{kp}})\int_{\gamma_1}^{\gamma_2} f(\tau,\tau')d\tau' \quad (37)$$

where

$$\gamma_1 = \frac{kl}{V_{kp}}\left[H\left(\frac{kl}{V_{kp}}\right) - H\left(\frac{kl}{V_{kp}} - \tau\right)\right];$$

$$\gamma_2 = \frac{L+kl}{V_{kp}}H(\frac{L+kl}{V_{kp}}) - \left(\frac{L+kl}{V_{kp}} - \tau\right)H(\frac{kl}{V_{kp}} - \tau); \quad (38)$$

$$f(\tau,\tau') = exp\left[-\frac{V_\partial(y+kl-V_{kp}\tau')}{2a} - \frac{{V_\partial}^2(\tau-\tau')}{4a} - \frac{(y+kl-V_{kp}\tau')^2+x^2}{4a(\tau-\tau')}\right]\frac{1}{\sqrt{\tau-\tau'}}$$

And solution (36) takes the following form:

$$T(x,y,\tau) = \frac{C}{2\pi\lambda}\sum_{k=0}^{\infty} H(\tau - \frac{kl}{V_{kp}})H(\frac{L+kl}{V_{kp}})\int_{\gamma_1}^{\gamma_2} f(\tau,\tau')d\tau' \quad (39)$$

The initial conditions (4) imply that for all $K < 0$, expression (39) vanishes, and in fact the solution is constructed for $K \geq 0$.

The terms are the values of the function:

$$\Psi = \int_{\gamma_1}^{\gamma_2} e^{-\frac{V_\partial(y+kl-V_{kp}\tau')}{2a} - \frac{{V_\partial}^2(\tau-\tau')}{4a} - \frac{(y+kl-V_{kp}\tau')^2+x^2}{4a(\tau-\tau')}}\frac{d\tau'}{\sqrt{\tau-\tau'}} \quad (40)$$

This solution converges rapidly and thus reflects the actual grinding conditions. Indeed, the number of grains on the wheel passing along the contact arc at specific values of V_{kr} and V_g is limited. Therefore, the transition in expression (39) to a finite sum is justified, i.e., the temperature distribution of the part can be represented as:

$$T(x,y,\tau)=\frac{C}{2\pi\lambda}\sum_{k=0}^{\infty}H(\tau-\frac{kl}{V_{kp}})H(\frac{L+kl}{V_{kp}})\int_{\gamma_1}^{\gamma_2}f(\tau,\tau')d\tau' \quad (41)$$

Calculations in MathCAD for specific grinding conditions of magnetically hard alloys make it possible to trace the process of temperature field formation in the workpiece at the contact zone4 and study its kinetics.

The steady-state component of the temperature field, which does not depend on time, can be isolated from the general solution (41) as follows. Let us represent the intensity of the total heat flux as a time-periodic function with period $T = 2l$. We expand the delta function into a Fourier series over the interval $(-l/2V_{cr}; l/2V_{cr})$ [42]:

$$\delta\left(\tau-\frac{y}{V_{kp}}\right)=\frac{V_{kp}}{l}\sum_{-\infty}^{\infty}e^{ik\frac{\pi V_{kp}}{l}\left(\tau-\frac{y}{V_{kp}}\right)}$$

Taking this into account, the boundary condition (31) takes the following form:

$$\frac{\partial T}{\partial x}(0,y,\tau)=-\frac{C\sqrt{\tau}}{\lambda l}V_{kp}[H(y)-H(y-L)]\sum_{k=-\infty}^{\infty}e^{ik\frac{\pi V_{kp}}{l}\left(\tau-\frac{y}{V_{kp}}\right)}$$

The integral solution (3.2.3) in this case takes the form:

$$T(x,y,\tau)=\frac{CV_{kp}}{2\pi\lambda l}\int_0^{\tau}-\frac{d\tau'}{\sqrt{\tau-\tau'}}\int_0^{L}e^{-\frac{V_\partial(y-y')}{2a}-\frac{V_\partial{}^2(\tau-\tau')}{4a}-\frac{(y-y')^2+x^2}{4a(\tau-\tau')}}\sum_{k=0}^{\infty}exp\left[ik\frac{\pi V_{kp}}{l}\left(\tau'-\frac{y'}{V_{kp}}\right)\right]dy'$$

Let us make the following variable substitutions: $\tau-\tau'=Z;\ d\tau'=-dZt-t'=Z$ we obtain:

$$T(x,y,z)=\frac{CV_{kp}}{2\pi\lambda l}\int_0^{\infty}\frac{dz}{\sqrt{z}}\int_0^{L}e^{-\frac{V_\partial(y-y')}{2a}-\frac{V_\partial{}^2z}{4a}-\frac{(y-y')^2+x^2}{4az}}\sum_{k=0}^{\infty}exp\left[ik\frac{\pi V_{kp}}{l}\left(\tau-\frac{y'}{V_{kp}}-z\right)\right]dy' \quad (42)$$

If we set $K = 0$, then this expression does not depend on time and numerically characterizes the regular part of the part's temperature field:

$$T(x,y)=\frac{CV_{kp}}{2\pi\lambda l}\int_0^{\infty}\int_0^{L}e^{-\frac{V_\partial(y-y')}{2a}-\frac{V_\partial{}^2z}{4a}-\frac{(y-y')^2+x^2}{4az}}\frac{dz}{\sqrt{z}}dy' \quad (43)$$

Using the known relations [43], [44], we can rewrite (43) in a simpler form:

$$T(x,y,\tau)=\frac{CV_{kp}}{2\pi\lambda l\sqrt{V_g}}\int_0^{L}\sqrt[4]{(y-y')^2+x^2}e^{-\frac{V_\partial(y-y')}{2a}}K_{1/2}\left(\frac{V_\partial}{2a}\sqrt{(y-y')^2+x^2}\right)dy' \quad (44)$$

The impulsive component of the temperature field is expressed as:

$$T(x,y,\tau)=\frac{CV_{kp}}{2\pi\lambda l}\int_0^{\infty}\frac{dz}{\sqrt{z}}\int_0^{L}exp\left[-\frac{V_\partial(y-y')}{2a}-\frac{V_\partial{}^2z}{4a}-\frac{(y-y')^2+x^2}{4az}\right]\sum_{k=0}^{\infty}cos\frac{k\pi V_{kp}}{l}\left(\tau-\frac{y'}{V_{kp}}-z\right)dy' \quad (45)$$

On the surface (at $X = 0$), the expression for the steady-state component of the part's temperature field can be represented in terms of elementary functions. To

do this, we will use the well-known asymptotic representation of the Macdonald function for large values of the argument [45], [46]:

$$K_{1/2}(z) = \sqrt{\frac{\pi}{2z}} e^{-z} \tag{46}$$

Taking this into account, expression (44) takes the form:

$$T_k(0, y, \tau) = \frac{CV_{kp}a}{\lambda l V_g^2} \sqrt{\frac{\pi}{a}} \left\{ exp\left[\frac{(L-y)V_g}{a}\right] - exp\left[-\frac{V_g y}{a}\right] \right\} \tag{47}$$

In [45], [47], it is shown that when $U_{gl}/(2a) \geq 10$, the maximum of the temperature curve occurs at the point where the section of the machined surface exits the heating zone. In our case, this will be the point $y = L$. Then, considering that $L = \sqrt{Dt}$ [47], [48] from (3.2.18), we will have:

$$T_{kmax}(L, 0, \tau) = \frac{CV_{kp}a}{\lambda l V_g^2} \sqrt{\frac{\pi}{a}} \left[1 - exp\left(-\frac{V_\partial \sqrt{D_t}}{a} \right) \right]_{kmax} \tag{48}$$

The resulting expression (48) allows us to calculate the maximum contact temperature of the workpiece, which forms at the boundary between the contact zone and the zone of intense cooling, depending on the processing conditions, the characteristics of the grinding wheels used, and the thermophysical properties of the material being ground.

It is interesting to note that when calculating the maximum values of the steady-state component (T_K) and the instantaneous temperature of individual grains (T_M) for a specific material, and when experimentally evaluating the highest values of contact and instantaneous temperatures, a fairly good agreement between theoretical and experimental results was obtained.

The derived expressions for the instantaneous and contact grinding temperatures, as seen in equations (44) and (47), (48), depend on many technological parameters—grinding depth (t_{gr}), wheel speed (V_w) and workpiece speed (V_w), the grit size of the wheels used, the bond characteristics μ, the distance between cutting grains l and their number, as well as the thermophysical and mechanical properties of functionally graded materials.

In this regard, it appears possible to use these expressions as criteria for predicting the conditions under which defects such as burn marks form and the depth of their occurrence.

As for the study of the causes of grinding cracks, the micro-discontinuity of temperature fields, which is a consequence of the cutting process by individual grains, has a negligible effect on the nature and intensity of crack formation. The magnitude of the heat flux plays a greater role here.

Qualitatively new phenomena in the behavior of crack-like defects occur during macro-intermittent grinding, i.e., when wheels with an intermittent working surface are used [37], [49], [50].

Of interest is the behavior of the stress intensity factor K_I in the case of a non-stationary temperature field formed in the surface layer during grinding with intermittent wheels. To this end, let us consider the following problem.

In the contact zone $[-a*, a*]$, between the circle and the workpiece, there is a linear defect of length $2l$, part of which is located beneath the recess, while the remaining portion $2l - d$ is beneath the cutting edge. The heat conduction equation for this case takes the form:

$$a\left(\frac{\partial^2 T}{\partial x^2}+\frac{\partial^2 T}{\partial y^2}\right)=\frac{\partial T}{\partial \tau}-q\frac{(r)}{2\pi r}\delta(\tau), \quad r=\sqrt{(x-\xi)^2+(y-r)^2} \tag{49}$$

ξ, η — coordinates of the heat source; $\delta(r)$ —delta function. The boundary conditions will be, respectively,

$$\begin{aligned} &T(0,y,\tau)=T_k, \quad at \quad d<y<a, \tau>0 \\ &\frac{\partial T}{\partial x}(0,y,\tau)=T_k, \quad at \quad 0<y<d, \tau>0 \end{aligned} \tag{50}$$

The initial conditions coincide with (4).

The problem is solved using the Laplace integral transform [51] with respect to τ and the Hankel transform [47], [51] with respect to the variable r:

$$T_p(x,y)=\int_0^\infty T(x,y,\tau)e^{-p\tau}d\tau; \quad T_{p\alpha}(x)=\int_0^\infty T_p(r)\Im_0(\alpha r)\,dr$$

Performing the inverse Laplace transforms, we find

$$T_p(x,y,\tau)=\frac{q}{2\pi a}\int_0^\infty e^{-\alpha^2 a\tau}\alpha\,\Im_0(\alpha r)d\alpha=\frac{qe^{-\frac{r^2}{4a\tau}}}{2\pi a\tau} \tag{51}$$

We determine the thermal stresses by solving the Lamé equations (3) with boundary conditions (5).

We are interested in the case where an instantaneous heat source with intensity $q* = 1$ acts at the point $X = \xi_1 = 0, Y = \xi_2$. In this case, the solution takes the form:

$$\begin{aligned} \sigma_y(x,y,\tau)&=-\frac{\mu m}{\pi r^2}\left\{\left(1-e^{-\frac{r^2}{4a\tau}}\right)\left(1-\frac{2y^2}{r^2}\right)+\frac{(y-\xi)^2}{2a\tau}e^{-\frac{r^2}{4a\tau}}\right\} \\ \tilde{\sigma}_x(x,y,\tau)&=-\frac{\mu m}{\pi r^2}\left\{\left(1-e^{-\frac{r^2}{4a\tau}}\right)\left(1-\frac{2x^2}{r^2}\right)+\frac{x^2}{2a\tau}e^{-\frac{r^2}{4a\tau}}\right\} \\ \tilde{\tau}_{xy}(x,y,\tau)&=-\frac{r\mu m}{\pi r^2}(y-\xi)x\left\{\frac{e^{-\frac{r^2}{4a\tau}}}{4a\tau}-\frac{\left(1-e^{-\frac{r^2}{4a\tau}}\right)}{r^2}\right\} \end{aligned} \tag{52}$$

Using expressions (51)–(52), we can determine the temperature and stresses for heat sources $q(x,t)$ distributed along the axis $X = 0, Y > d$, with time-varying intensity. We previously established that the heat flux intensity is not

constant over time. Therefore, determining the thermal stresses for this case is of interest.

The temperature distribution in the part under these conditions will be:

$$T(x,y,\tau)=\int_0^{\infty}d\xi\int_0^{\tau}\left\{\frac{q(\varepsilon,\tau')}{4\pi a(\tau-\tau')}e^{-\frac{(y-d-\xi)^2+x^2}{4a(\tau-\tau')}}\right\}d\tau' \quad (53)$$

Then, the stress components can be found using the following formulas:

$$\begin{aligned}\sigma_y^{'}&=\int_0^{\infty}d\xi\int_0^{\tau}q\left(\varepsilon,\tau^{'}\right)\bar{\sigma}_y\left(y-d-\xi,x,\tau-\tau^{'}\right)d\tau^{'}\\ \sigma_x^{'}&=\int_0^{\infty}d\xi\int_0^{\tau}q\left(\varepsilon,\tau^{'}\right)\bar{\sigma}_x\left(y-d-\xi,x,\tau-\tau^{'}\right)d\tau^{'}\\ \tau_{xy}^{'}&=\int_0^{\infty}d\xi\int_0^{\tau}q(\varepsilon,\tau')\bar{\tau}_{xy}(y-d-\xi,x,\tau-\tau')d\tau'\end{aligned} \quad (54)$$

The stress state of the surface layer will not change if we replace the temperature function $T(x,y,\tau)$ with the expression $T(x,y,\tau)-TK$, since the stress components corresponding to uniform heating of the surface layer of the parts and vanishing at infinity are identically equal to zero. Therefore, equation (54) can be written as follows:

$$\sigma_x^{'}(0,y,\tau)=\mu xT_k+\mu x\int_0^1 T(0,y,\frac{\tau}{\alpha})d\alpha-2\mu xT(0,y,\tau) \quad (55)$$

Substituting the expression for the temperature distribution in item (53) into formula (55), we obtain the following expression for determining the stress state components on the surface $X=0$ in the form:

$$\begin{aligned}\sigma_x^{'}(0,y,\tau)\big|_{y<d}&=\mu xT_k+\frac{\mu xT_k}{\pi}\int_0^{\infty}\frac{1}{\tau^{'}\sqrt{\tau^{'}-1}}erfc\left[\frac{(d-y)\tau^{'}}{2\sqrt{a\tau^{'}}}\right]d\tau^{'}+\\ &+\frac{2}{\sqrt{\pi}}\frac{\sqrt{a\tau^{'}}}{(d-y)\tau^{'}}e^{-\frac{(d-y)^2\tau^{'2}}{4a\tau^{'}}}-\frac{2a\tau^{'}}{(d-y)^2\tau^{'2}}erf\left[\frac{(d-y)\tau^{'}}{2\sqrt{a\tau^{'}}}\right]\\ \sigma_x^{'}(0,y,\tau)\big|_{y>d}&=0\end{aligned} \quad (56)$$

To ensure that the edges of crack-like defects are stress-free at $y>0$, consider a stress state with components $\sigma_x^{''}$, $\sigma_y^{''}$, $\sigma_z^{''}$, chosen such that the following conditions are satisfied:

$$\tau_{xy}^{''}(0,y,\tau)=0;\quad \sigma_x^{'}(0,y,\tau)+\sigma^{'x} \quad (57)$$

For the normal stress $\sigma_x^{''}$ along the crack path, we obtain the expression:

$$\sigma_x^{''}(0,y,\tau)=\frac{1}{\pi\sqrt{|y|}}\int_0^{\infty}\frac{\sqrt{u}\sigma_x^{'}(o,u,\tau)}{u-y}du \quad (58)$$

Based on (53), (58), and (30), we find the stress intensity factor for the crack in the case of continuous contact, i.e., when the machined surface with a defect in the contact zone with the tool is subjected to continuous heating:

$$K = \lim_{y\to 0}\left[\sqrt{2\pi y}\sigma_x(0,y,\tau)\right] = 2\sqrt{\frac{2}{\pi}}\mu x T_k\sqrt{d} - \sqrt{\frac{2}{\pi}}\mu x T_k\sqrt{d}\frac{1}{\pi}\int_1^\infty \frac{d\tau'}{\sqrt{1-\xi}}\times$$
$$\times\left\{\int_0^1 erfc\left(\frac{\tau'}{\tau^*}\xi\right)\frac{d\xi}{\xi\sqrt{1-\xi}} + \frac{1}{\sqrt{\pi}}\frac{\tau'}{\tau^*}\int_0^1\left[e^{-\frac{\tau'^2\xi^2}{\tau^{*2}}} - \frac{\sqrt{\pi}}{2}\frac{\tau'}{\tau^*\xi}erf\left(\frac{\tau'}{\tau^*}\xi\right)\right]\frac{d\xi}{\xi\sqrt{1-\xi}}\right\} \quad (59)$$

here

$$\tau^* = \frac{2\sqrt{a\tau}}{d}, \quad \sigma_x(0,y,\tau) = \sigma'_x(0,y,\tau) + \sigma''_x(0,y,\tau)$$

Fig. 14 shows a graph of the dependence of the value.

$$K^* = \frac{K}{2\sqrt{2}\mu}\frac{\sqrt{\pi}}{xT_k\sqrt{a}}a\tau^*$$

As can be seen from the graph, the initial moments of time are the most dangerous in terms of crack propagation.

Consider the case where the surface layer with a defect at $X = 0, y > 0$ is subjected to a temperature field satisfying the following conditions on the $X = 0$ axis:

$$\begin{aligned} T(0,y,\tau) &= T_k, \quad at \quad d < y < d+l \\ T(0,y,\tau) &= 0, \quad at \quad y > d+l \\ \left.\frac{\partial T}{\partial x}\right|_{x=0} &= 0, \quad at \quad y < d \end{aligned} \quad (60)$$

In this case, the expression for the temperature on the $X = 0$ axis takes the form:

$$T(0,y,\tau) = \begin{cases} 1, & d < y < d+l \\ \frac{1}{\pi}\int_1^\infty\left\{erfc\left[\frac{|y-d|\tau'}{2\sqrt{a\tau}}\right] - erfc\left[\frac{|y-d-l|\tau'}{2\sqrt{a\tau}}\right]\right\}\frac{d\tau'}{\tau'\sqrt{\tau'-1}}, & y < d \end{cases} \quad (61)$$

For the stress intensity factor corresponding to this temperature field, we obtain the expression:

$$K = \sqrt{\frac{2}{\pi}}2\mu x T_k\sqrt{d}\left[1 - \sqrt{1+S} + F(\tau^*,S) - F(\tau^*,0)\right] \quad (62)$$

here

$$S = l/d, \quad F(\tau^*,S) = \frac{1}{2\pi}\int_1^\infty\left\{\int_0^1 erfc\left(\frac{\tau'}{\tau^*}(S+\xi)\right)\frac{d\xi}{\sqrt{1-\xi}} + \right.$$
$$\left.\frac{1}{\sqrt{\pi}}\frac{\tau_1^*}{\tau'}\int_0^1\left\{e^{-\frac{(S+\xi)^2\tau'^2}{\tau^{*2}}} - \frac{\sqrt{\pi}\tau^*}{2\tau'(S+\xi)}erf\left(\frac{\tau'}{\tau^*}(S+\xi)\right)\right\}\frac{d\xi}{(S+\xi)\sqrt{1-\xi}}\right\}\frac{d\tau'}{\tau'\sqrt{\tau'-1}}$$

The dependence of $K^* = \frac{K}{2\sqrt{2}\mu}\frac{\sqrt{\pi}}{xT_k\sqrt{a}}$ on τ^* is shown in Fig. 14.

The temperature field, in the case of intermittent contact between the tool and the workpiece with a crack-like defect in the machined layer (Fig. 15), leads to the emergence of compressive normal stresses along the defect, which helps to inhibit fracture propagation.

Thus, it appears possible to use local thermoelastic fields as a tool capable of controlling the trajectory and rate of defect propagation into cracks.

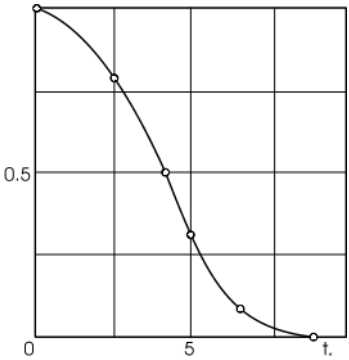

Fig. 14 Dependence of the stress intensity factor on time when the heat source is in full contact with the defect.

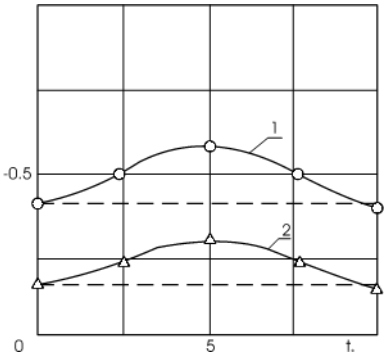

Fig. 15 Dependence of the stress intensity factor with time for intermittent contact between the heat source with the defect $1 - \lambda = 0.5; 2 - \lambda = 1 (l_{bc} = l_{bn})$.

The cutting depth t_{grind} is a determining factor in the formation of grinding cracks. The tensile transient stresses forming in the processing zone, which contribute to crack formation, are proportional to t_{grind}, since $T_K(O, y, \tau) \sim t_{grind}$.

$$\sigma_{\rho}^{max \frac{1+v}{1-v} t_k \left(\frac{x}{2\sqrt{a\tau}}\right)}$$

Therefore, when determining defect-free grinding parameters, it is necessary, first and foremost, to establish the maximum permissible cutting depths. In doing so, it is also important to have information not only on the thermophysical and mechanical properties of the material and the presence of inhomogeneities in the surface layer, but also on its processing conditions.

As heat transfer increases, high tensile stresses arise, contributing to the formation of grinding cracks on the machined surface.

Since the stress intensity factor for an isolated defect is determined by the formula [52], [53]:

$$K_1 = -\frac{1}{\sqrt{\pi l}} \int_{-l}^{l} \sigma_y(x, 0, \tau) \sqrt{\frac{l+x}{l-x}} dx$$

then, finally, p we obtain:

$$K_1 = \frac{GT_k(1+\nu)\alpha_t}{\sqrt{\pi l}}\left\{\pi l + \frac{2}{\pi}\int_{-l}^{l}\left[arctg\left(\frac{\sqrt{Dh}}{2(\xi+b)}\right) + arctg\left(\frac{\sqrt{Dh}}{2(b-\xi)}\right)\right]\sqrt{\frac{l+\xi}{l-\xi}}d\xi - \right.$$
$$\left. - \frac{1}{2\sqrt{\pi}}\int_{-l}^{l}\int_{0}^{\tau_k}\frac{1}{\tau\sqrt{a\tau}}\left[(\xi+b)e^{-\frac{(\xi+b)^2}{4a\tau}} + (b-\xi)e^{-\frac{(b-\xi)^2}{4a\tau}}\right]erf\left(\frac{\sqrt{Dh}}{4\sqrt{a\tau}}\right)\sqrt{\frac{l+\xi}{l-\xi}}d\tau d\xi\right\} \quad (63)$$

In the case where the stress intensity factor approaches the local failure criterion K_C in magnitude, the crack-like defect begins to develop into a crack. Thus, from the last relation, we obtain the equilibrium conditions for defects of length $2l$ in the form:

$$l_0 < \frac{K_C^2}{\pi[GT_k(1+\nu)\alpha_t]^2} \quad (64)$$

In this formula, the contact temperature T_K in the grinding zone depends on the process parameters and properties of the material being machined and can be determined by the formula:

$$T_k = \frac{CV_{kp}}{\lambda\sqrt{Dh}V_g^2}\sqrt{\frac{\pi}{a_n}}\left[1 - e^{-\frac{V_0\sqrt{Dh}}{a\tau}}\right]$$

where V_{cr}, V_g, h are machining conditions; D, C are tool parameters; λ, a_n — thermophysical characteristics of the workpiece material.

6. Conclusions

1. The values of the stress intensity factors for inherent inhomogeneities formed in the surface layer of products made of functionally graded materials are influenced by the size and orientation of these defects, their depth, their relative arrangement, and the magnitude of the heat flux during grinding.

2. For any values of the thermal conductivity, linear thermal expansion coefficient, and shear modulus of the material of the product and the inclusions located in the surface layer, when the stress intensity factors $K_I = 0$, $K_{II} \neq 0$ if the heat flux is directed perpendicular to the inhomogeneity within the inclusion, and conversely, if parallel to the crack, then $K_I \neq 0$, $K_{II} = 0$.

3. The geometry and properties of inclusions formed by previous operations in the surface layer can create conditions for both the inhibition and the propagation of grinding cracks. If the heat flux is directed parallel to the inclusion axis and a straight thermally isolated crack, then when the linear thermal expansion coefficient of the inclusion is greater than that of the matrix, the increase in the stiffness of the inclusion leads to an increase in the stress intensity factors K_I ($K_{II} = 0$) for various ratios of the thermal conductivity coefficients of the material components. This leads to the propagation of microcracks. Conversely, if the thermal expansion coefficient

of the inclusion is lower than that of the matrix material, a decrease in the stiffness of the inclusion leads to a decrease in the stress intensity factors K_I ($K_{II} = 0$) for the same ratios of thermal conductivity coefficients, i.e., conditions favorable for the non-propagation of microcracks are present.

4. For crack-like inhomogeneities located in a layer with a lower thermal conductivity coefficient a_t, the orientation of the microdefect strongly influences the value of SIF. When a microcrack located in a stiffer layer of the material being processed is significantly distant, the stress intensity factor K_I reaches its maximum values when the microdefect is oriented parallel to this line, and as the inhomogeneities approach, the maximum K_I is achieved when they are oriented perpendicular to the direction of the heat flux

5. The presence of a hard inclusion leads to an increase in K_I under mechanical loading and to a decrease under thermal loading. In this case, the thermal conductivity (TLCR) a_t has a significant influence on the nature of the stress intensity factor (SIF) variation. When the inclusion's $a_t < a_1$ of the matrix, $K_I > 0$, and when $\alpha_t^{incl} > \alpha_t^{(M)}$, $K_I < 0$. In a soft inclusion, a microcrack will begin to propagate at a lower heat flux than in a hard inclusion; that is, the strength of a body with a hard inclusion is higher than that with a soft inclusion

6. The micro-intermittent nature of the grinding process generates compressive stresses in the machined zone, which help reduce the incidence of grinding cracks. The stress intensity factor reaches its lowest values when the lengths of the cutting ridges and grooves of the intermittent grinding wheels are equal.

References: 1. A. A. Ferreira, 'Effects of Processing Parameters on Functionally Graded Materials for Industrial Components Repair', *MCMS*, vol. 4, no. 2, Sep. 2021, doi: 10.33552/MCMS.2021.04.000585. **2**. A. Usov, M. Kunitsyn, D. Klymenko, and V. Davydiuk, 'Modeling the effect of stochastic defects formed in products during machining on the loss of their functional dependencies', *Pratsi OPU*, vol. 1, no. 65, pp. 16–29, 2022, doi: 10.15276/opu.1.65.2022.02. **3.** F. Wöste, J. Kimm, J. A. Bergmann, W. Theisen, and P. Wiederkehr, 'Investigation of the effect of residual stresses in the subsurface on process forces for consecutive orthogonal cuts', *Production Engineering*, vol. 15, no. 6, pp. 873–883, Dec. 2021, doi: 10.1007/S11740-021-01058-Y. **4.** L. Jakubovičová, M. Vaško, and F. Synák, 'Evaluation of Load-Bearing Performance and Cost Efficiency in Steel-Welded and Modular Aluminum Rack Structures', *Machines*, vol. 13, no. 6, Jun. 2025, doi: 10.3390/MACHINES13060506. **5.** A. S. Kairov, V. Y. Oshovsky, and V. A. Kairov, 'INVESTIGATION OF THE EFFECT OF NANOCOATINGS ON THE WEAR-RESISTANCE OF SOCKET CARBIDE MILLS', Problems of computational mechanics and structural strength (in Ukrainian), no. 35, pp. 104–114, Dec. 2022, doi: 10.15421/4222220. **6**. V. Greshta, A. Yershov, V. Hrabovskyi, V. Vinichenko, and S. Seidametov, 'PHYSICAL-MECHANICAL CHARACTERISTICS AND THERMAL STRESS OF PLASMA COVERING', *New Materials and Technologies in Metallurgy and Mechanical Engineering*, no. 3, pp. 27–33, Oct. 2023, doi: 10.15588/1607-6885-2023-3-4. **7.** K. Osička, Z. Fišerová, J. Otoupalík, and J. Chladil, 'Tension of the Surface Layer in Machining Hardened Steels', *Manufacturing Technology*, vol. 17, no. 1, pp. 22–23, 2017, doi: 10.21062/UJEP/X.2017/A/1213-2489/MT/17/1/72. **8.** A. Salenko *et al.*, 'Forming a defective surface layer when cutting parts made from Carbon-carbon and carbon-polymeric composites', *Eastern-European Journal of Enterprise Technologies*, vol. 4, no. 1–94, pp. 61–72, 2018, doi: 10.15587/1729-

4061.2018.139556. **9.** G. Sun and Z. Ding, 'Effects of Heating Rate and Strain Rate on Phase Transformation in Micro-Grinding', *EPJ Web of Conferences*, vol. 224, pp. 05003–05003, 2019, doi: 10.1051/EPJCONF/201922405003. **10.** S. J. Eder *et al.*, 'Experimentally validated atomistic simulation of the effect of relevant grinding parameters on work piece topography, internal stresses, and microstructure', *Friction*, vol. 10, no. 4, pp. 608–629, Apr. 2022, doi: 10.1007/S40544-021-0523-3. **11.** A. Rajaei, B. Hallstedt, C. Broeckmann, S. Barth, D. Trauth, and T. Bergs, 'Numerical Prediction of the Microstructure and Stress Evolution During Surface Grinding of AISI 52100 (DIN 100Cr6)', *Integr Mater Manuf Innov*, vol. 7, no. 4, pp. 202–213, Dec. 2018, doi: 10.1007/s40192-018-0122-y. **12.** E. Sauter, E. Sarikaya, M. Winter, and K. Wegener, 'In-process detection of grinding burn using machine learning', *International Journal of Advanced Manufacturing Technology*, vol. 115, no. 7–8, pp. 2281–2297, Aug. 2021, doi: 10.1007/S00170-021-06896-9. **13.** I. Pavlenko *et al.*, 'Parameter identification of cutting forces in crankshaft grinding using artificial neural networks', *Materials*, vol. 13, no. 23, pp. 1–12, Dec. 2020, doi: 10.3390/MA13235357. **14.** P. Krajnik, K. Wegener, T. Bergs, and A. J. Shih, 'Advances in modeling of fixed-abrasive processes', *CIRP Annals*, vol. 73, no. 2, pp. 589–614, Jan. 2024, doi: 10.1016/J.CIRP.2024.05.001. **15.** R. Strunk, F. Borchers, B. Clausen, and C. Heinzel, 'Influence of subsequently applied mechanical and thermal loads on surfaces ground with mechanical main impact', *Materials*, vol. 14, no. 9, May 2021, doi: 10.3390/MA14092386. **16.** V. Stupnytskyy, E. Dragašius, S. Baskutis, and S. Xianning, 'Modeling and simulation of machined surface layer microgeometry parameters', *Ukrainian Journal of Mechanical Engineering and Materials Science*, vol. 8, no. 1, pp. 1–11, 2022, doi: 10.23939/UJMEMS2022.01.001. **17.** L. Urgoiti, D. Barrenetxea, J. A. Sánchez, and J. L. Lanzagorta, 'Detailed thermo-kinematic analysis of face grinding operations with straight wheels', *Metals*, vol. 10, no. 4, Apr. 2020, doi: 10.3390/MET10040524. **18.** A. A. Dyakonov and L. V. Shipulin, 'Geometric Model of the Interaction of the Grinding Wheel and Workpiece during Surface Grinding with the Periphery of a Straight Wheel', *Applied Mechanics and Materials*, vol. 756, pp. 41–46, Apr. 2015, doi: 10.4028/WWW.SCIENTIFIC.NET/AMM.756.41. **19.** W. Graham and A. T. Abdullahi, 'The nature of wheel-workpiece contact in surface grinding', *International Journal of Machine Tool Design and Research*, vol. 15, no. 3, pp. 153–160, 1975, doi: 10.1016/0020-7357(75)90017-7. **20.** C. F. Tiffany and J. N. Masters, 'APPLIED FRACTURE MECHANICS', *ASTM Special Technical Publication*, vol. STP 381, pp. 249–277, 1965, doi: 10.1520/STP26592S. **21.** G. I. Barenblatt, 'The Mathematical Theory of Equilibrium Cracks in Brittle Fracture', in *Advances in Applied Mechanics*, vol. 7, H. L. Dryden, Th. von Kármán, G. Kuerti, F. H. van den Dungen, and L. Howarth, Eds, Elsevier, 1962, pp. 55–129. doi: 10.1016/S0065-2156(08)70121-2. **22.** B. Skjetne and A. Hansen, 'Implications of realistic fracture criteria on crack morphology', *Frontiers in Physics*, vol. 7, no. APR, 2019, doi: 10.3389/FPHY.2019.00050. **23.** 'Fracture mechanics criteria and applications', *Choice Reviews Online*, vol. 29, no. 03, pp. 29–1536, Nov. 1991, doi: 10.5860/CHOICE.29-1536. **24.** P. Cornetti, N. Pugno, A. Carpinteri, and D. Taylor, 'Finite fracture mechanics: A coupled stress and energy failure criterion', *Engineering Fracture Mechanics*, vol. 73, no. 14, pp. 2021–2033, Sep. 2006, doi: 10.1016/J.ENGFRACMECH.2006.03.010. **25.** M. Kunitsyn, A. Usov, and Y. Zaychyk, 'The Influence of Cutting Forces on Cracks Formation During the Grinding of Products from Materials Prone to Defect Formation', in *Advances in Design, Simulation and Manufacturing VII*, V. Ivanov, J. Trojanowska, I. Pavlenko, E. Rauch, and J. Piteľ, Eds, in Lecture Notes in Mechanical Engineering. , Cham: Springer Nature Switzerland, 2024, pp. 240–250. doi: 10.1007/978-3-031-61797-3_20. **26.** Q. H. Qin, 'Trefftz finite element method and its applications', *Applied Mechanics Reviews*, vol. 58, no. 1–6, pp. 316–337, 2005, doi: 10.1115/1.1995716. **27.** F. L. de Silva Bussamra, E. L. Neto, and M. A. C. Rodrigues, 'Simulation of stress concentration problems in laminated plates by quasi-Trefftz finite element models', *Latin American Journal of Solids and Structures*, vol. 13, no. 9, pp. 1677–1694, 2016, doi: 10.1590/1679-78252698. **28.** A. Mioduchowski and Z. Płochocki, 'Thermal stresses in a coating layer. I. General theoretical scheme', *Acta Mech*, vol. 215, no. 1–4, pp. 319–333, Dec. 2010, doi: 10.1007/s00707-010-0345-2. **29.** W. T. Ang, 'A boundary integral equation for deformations of an elastic body with an arc crack', *Quarterly of Applied Mathematics*, vol. 45, no. 1, pp. 131–139, Apr. 1987, doi: 10.1090/QAM/885175. **30.** O. Maksymovych and A. Podhorecki, 'Determination of Stresses in

Composite Plates with Holes and Cracks Based on Singular Integral Equations', *Dynamical Systems Theory*, Mar. 2020, doi: 10.5772/INTECHOPEN.87718. **31.** P. S. Theocaris and G. A. Papadopoulos, 'Crack-propagation trajectories under biaxial loading, based on fracture criteria', *Journal of the Franklin Institute*, vol. 319, no. 4, pp. 443–456, 1985, doi: 10.1016/0016-0032(85)90013-4. **32.** D. Leguillon, E. Martin, O. Sevecek, and R. Bermejo, 'What is the tensile strength of a ceramic to be used in numerical models for predicting crack initiation?', *Int J Fract*, vol. 212, no. 1, pp. 89–103, Jul. 2018, doi: 10.1007/s10704-018-0294-7. **33.** H. F. Li, P. Zhang, B. Wang, and Z. F. Zhang, 'Predictive fatigue crack growth law of high-strength steels', *Journal of Materials Science & Technology*, vol. 100, pp. 46–50, Feb. 2022, doi: 10.1016/j.jmst.2021.04.042. **34.** F. Erdogan, 'Fracture problems in composite materials', *Engineering Fracture Mechanics*, vol. 4, no. 4, pp. 811–840, 1972, doi: 10.1016/0013-7944(72)90018-5. **35.** F. Erdogan, G. D. Gupta, and M. Ratwani, 'Interaction between a circular inclusion and an arbitrarily oriented crack', *Journal of Applied Mechanics, Transactions ASME*, vol. 41, no. 4, pp. 1007–1013, 1974, doi: 10.1115/1.3423424. **36.** H. Shen, P. Schiavone, C. Q. Ru, and A. Mioduchowski, 'Interfacial thermal stress analysis of an elliptic inclusion with a compliant interphase layer in plane elasticity', *International Journal of Solids and Structures*, vol. 38, no. 42–43, pp. 7587–7606, Sep. 2001, doi: 10.1016/S0020-7683(01)00033-6. **37.** J. Lee, S. Oh, and A. Mal, 'Calculation of interfacial stresses in composites containing elliptical inclusions of various types', *European Journal of Mechanics, A/Solids*, vol. 44, pp. 17–40, 2014, doi: 10.1016/J.EUROMECHSOL.2013.09.008. **38.** B. Gao, W. Bao, T. Jin, C. Chen, M. Qu, and A. Lu, 'Variation of wheel-work contact geometry and temperature responses: Thermal modeling of cup wheel grinding', *International Journal of Mechanical Sciences*, vol. 196, Apr. 2021, doi: 10.1016/J.IJMECSCI.2021.106305. **39.** V. N. Burlayenko, H. Altenbach, T. Sadowski, S. D. Dimitrova, and A. Bhaskar, 'Modelling functionally graded materials in heat transfer and thermal stress analysis by means of graded finite elements', *Applied Mathematical Modelling*, vol. 45, pp. 422–438, May 2017, doi: 10.1016/j.apm.2017.01.005. **40.** K. Topczewska and P. Zamojski, 'Effect of Pressure Fluctuations on the Temperature during Braking', *Acta Mechanica et Automatica*, vol. 14, no. 2, pp. 103–107, Jun. 2020, doi: 10.2478/AMA-2020-0015. **41.** P. Oza, K. Agarwal, and J. Tyagi, 'Fundamental solutions: a brief review', *Differential Equations & Applications*, no. 1, pp. 39–70, 2024, doi: 10.7153/DEA-2024-16-03. **42.** X. Xu, G. Li, Y. Zhao, and T. Liu, 'Analytical solutions for heat conduction problems with three kinds of periodic boundary conditions and their applications', *Applied Mathematics and Computation*, vol. 442, Apr. 2023, doi: 10.1016/J.AMC.2022.127735. **43.** A. A. Snarskii and I. V. Bezsudnov, 'Rotating thermoelectric device in periodic steady state', *Energy Conversion and Management*, vol. 94, pp. 103–111, 2015, doi: 10.1016/J.ENCONMAN.2015.01.058. **44.** M. Bayram, T. Partal, and G. Orucova Buyukoz, 'Numerical methods for simulation of stochastic differential equations', *Adv Differ Equ*, vol. 2018, no. 1, p. 17, Dec. 2018, doi: 10.1186/s13662-018-1466-5. **45.** S. C. Gupta, 'Temperature and moving boundary in two-phase freezing due to an axisymmetric cold spot', *Quarterly of Applied Mathematics*, vol. 45, no. 2, pp. 205–222, Jul. 1987, doi: 10.1090/QAM/895094. **46.** J. J. Shu and K. K. Shastri, 'Basic Properties of Incomplete Macdonald Function with Applications', *Journal of Function Spaces*, vol. 2020, 2020, doi: 10.1155/2020/6548298. **47.** J. L. González-Santander, 'Analytic solution for maximum temperature during cut in and cut out in surface dry grinding', *Applied Mathematical Modelling*, vol. 40, no. 3, pp. 2356–2367, Feb. 2016, doi: 10.1016/J.APM.2015.09.031. **48.** C. Salame and A. Malakizadi, 'An enhanced semi-analytical estimation of tool-chip interface temperature in metal cutting', *Journal of Manufacturing Processes*, vol. 105, pp. 407–430, Nov. 2023, doi: 10.1016/J.JMAPRO.2023.09.015. **49.** G. Anlas, M. H. Santare, and J. Lambros, 'Numerical Calculation of Stress Intensity Factors in Functionally Graded Materials', *International Journal of Fracture*, vol. 104, no. 2, pp. 131–143, Jul. 2000, doi: 10.1023/A:1007652711735. **50.** A. Fesenko, F. Yevsiukova, and O. Naboka, 'Development of a tool module for external intermittent grinding with the activation of the cutting fluid', *Mechanics and Advanced Technologies*, vol. 5, no. 2, Dec. 2021, doi: 10.20535/2521-1943.2021.5.2.234543. **51.** J. Pérez *et al.*, 'Heat transfer analysis of intermittent grinding processes', *International Journal of Heat and Mass Transfer*, vol. 51, no. 15–16, pp. 4132–4138, Jul. 2008, doi: 10.1016/J.IJHEATMASSTRANSFER.2007.11.043. **52.** E. Asadi, S. Fariborz, and M. Ayatollahi, 'Analysis of multiple axisymmetric annular cracks', *Journal of Mechanics of Materials and Structures*,

vol. 4, no. 1, pp. 1–11, Jan. 2009, doi: 10.2140/JOMMS.2009.4.1. **53.** J. Tweed, S. C. Das, D. P. Rooke, and D. P. Rooke, 'The stress intensity factors of a radial crack in a finite elastic disc', *International Journal of Engineering Science*, vol. 10, no. 3, pp. 323–335, 1972, doi: 10.1016/0020-7225(72)90047-X.

Анатолій Усов, Максим Куніцин, Юлія Сікіраш, Валерій Давидюк
Одеса, Україна,

ВПЛИВ МЕХАНІЧНИХ ТА ГЕОМЕТРИЧНИХ ХАРАКТЕРИСТИК НЕОДНОРІДНИХ ДІЛЯНОК НА ІНТЕНСИВНІСТЬ УТВОРЕННЯ ТРІЩИН ПІД ЧАС ШЛІФУВАННЯ ДЕТАЛЕЙ, ВИГОТОВЛЕНИХ ІЗ МАТЕРІАЛІВ З ФУНКЦІОНАЛЬНИМ ГРАДІЄНТОМ

Анотація. *Відсутність досліджень щодо особливостей виникнення шліфувальних тріщин та їх переростання в основні тріщини залежно від конструктивних, технологічних та структурних неоднорідностей матеріалу виробів не дозволяє однозначно застосовувати існуючі рекомендації щодо усунення зазначених дефектів. Ця робота присвячена дослідженню впливу внутрішніх неоднорідностей у поверхневому шарі, їх геометрії, та механічних характеристик виробів з функціонально-градієнтних матеріалів на вибір технологічних умов для бездефектної обробки деталей. Встановлено, що на величину коефіцієнтів інтенсивності напружень для внутрішніх неоднорідностей, що утворюються в поверхневому шарі виробів з функціонально-градієнтних матеріалів, впливають розмір і орієнтація цих дефектів, глибина їхнього залягання та взаємне розташування, а також величина теплового потоку під час шліфування. Геометрія та властивості включень, що утворилися в результаті попередніх операцій у поверхневому шарі, можуть створювати умови як для гальмування, так і для розвитку шліфувальних тріщин. Якщо тепловий потік спрямований паралельно осі включення і утворюється пряма, термічно ізольована тріщина, то коли коефіцієнт лінійного теплового розширення включення більший за коефіцієнт матриці, збільшення жорсткості включення призводить до збільшення коефіцієнтів інтенсивності напружень K_I ($K_{II} = 0$) для різних співвідношень коефіцієнтів теплопровідності компонентів матеріалу. Це призводить до поширення мікротріщин. І навпаки, якщо коефіцієнт теплового розширення включення нижчий за коефіцієнт матриці, то зменшення жорсткості включення призводить до зменшення коефіцієнтів інтенсивності напружень K_I ($K_{II} = 0$) при тих самих співвідношеннях коефіцієнтів теплопровідності, тобто створюються умови, сприятливі для нерозповсюдження мікротріщин. Тому при визначенні параметрів шліфування без дефектів необхідно, перш за все, встановити максимально допустимі глибини різання. При цьому важливо мати інформацію не тільки про теплофізичні та механічні властивості матеріалу та наявність неоднорідностей у поверхневому шарі, а й про умови його обробки.*

Ключові слова*: матеріали з функціональним градієнтом; неоднорідності; шліфування; утворення тріщин.*

UDC 621.91.01 **doi: 10.20998/2078-7405.2026.104.07**

EFFECT OF THE TURNING INSERT SHAPE AND FEED ON THE SURFACE PROFILE

Suratjon **Nuriddinov** [0009-0009-6932-4234], Balázs **Mikó** [0000-0003-3609-0290]

Óbuda University, Budapest, Hungary
miko.balazs@bgk.uni-obuda.hu

Received: 09 April 2026/ Revised: 19 April 2026/ Accepted: 29 April 2026 / Published: 15 May 2026

Abstract. *This study investigates the combined effect of cutting insert geometry and feed rate on surface roughness in turning of 42CrMo4 alloy steel. Controlled experiments were conducted on a CNC lathe using three insert geometries (C, D, and V types) and three feed rates (0.15, 0.25, and 0.35 mm/rev), while maintaining constant cutting speed and depth of cut. Surface characteristics were evaluated through quantitative roughness measurements and qualitative microscopic analysis. The results demonstrate that feed rate is the dominant factor influencing surface roughness, with increasing feed leading to a significant deterioration in surface quality, as reflected by higher R_z and Rt values. Insert geometry also plays a critical role: C and D inserts produce consistently lower roughness values, whereas the V insert results in inferior surface quality under identical cutting conditions. Notably, despite identical nose radii, substantial differences were observed between C and V inserts, highlighting the pronounced influence of edge geometry, particularly the end cutting edge angle. The findings indicate that conventional geometric models based solely on feed and nose radius are insufficient to accurately predict surface roughness. Instead, insert shape parameters must also be considered. This study contributes to improved understanding of the interaction between tool geometry and machining parameters and provides practical guidance for optimizing surface quality in turning operations.*
Keywords: *surface profile; turning; insert shape; feed; surface roughness; main effect plot.*

1. Introduction

Machining is a process used to create a part or shape with precise dimensions and tolerances [1]. Surface roughness plays a crucial role in determining the quality of the product [2], as it directly impacts the product's performance during use. The quality of the surface significantly enhances properties such as fatigue strength, corrosion resistance, and creep life [3]. With the increasing demand for improved surface quality, especially in industries like automotive, aerospace, and die and mould manufacturing, achieving a smooth surface finish is essential. Surface roughness is typically measured by a specific value, where a higher value indicates a rougher surface and a shorter fatigue life. Therefore, it's important to clearly specify the required surface roughness in designs to ensure the machining process is appropriately adjusted to meet these standards [4].

Achieving an ideal surface finish in machining remains a significant challenge due to the complex and interdependent interactions between the cutting tool, the workpiece material, and the machining environment. Several factors contribute to surface imperfections, including the formation of a built-up edge (BUE) [5], which alters the effective geometry of the cutting tool; surface damage caused by chips curling back and impacting the freshly machined surface; tearing during chip formation in ductile materials; and surface cracks resulting from discontinuous chip formation in brittle materials [8]. Friction between the tool's flank and the workpiece further degrades the surface finish. Beyond these, key machining parameters - such as feed rate, cutting speed, and depth of cut - along with the process kinematics, cutting tool geometry and material, mechanical properties of the workpiece, and dynamic issues like machine vibrations and tool deflection, play crucial roles. The precision, rigidity, and overall condition of the machine tool itself also significantly influence surface quality [6,7].

Surface roughness measurement is essential for evaluating the quality and performance of machined components, as it directly affects factors like friction, wear, fatigue strength, and sealing capability [8]. Depending on the required accuracy, surface type, and application, different measurement techniques are used. Contact methods, such as stylus profilometers, are widely adopted for their reliability and standardized outputs, while non-contact optical methods, like interferometry and confocal microscopy, offer high-resolution analysis without risking surface damage. Advanced techniques like atomic force microscopy enable nanoscale assessments, although they are limited to small areas and specialized applications. Selecting the appropriate method depends on balancing precision needs, surface characteristics, and practical constraints such as speed and cost [9,10].

Predicting surface roughness in machining is critical for ensuring product quality and process optimization. Multiple approaches have been developed, each leveraging different principles, tools, and technologies. Below are five key approaches to surface roughness prediction, along with expanded explanations [11,12]:

- Approaches that are based on machining theory to develop analytical models and computer algorithms to represent the machined surface,
- Approaches that examine the effects of various factors through the execution of experiments and the analysis of the results,
- Approaches that use designed experiments,
- Artificial intelligence (AI) approaches,
- Surface roughness characterization by using image processing.

Numerous roughness parameters have been developed to describe surface textures. These parameters describe different characteristics of surface roughness, so

we can choose the parameter most suitable for describing the surface, knowing the purpose under investigation [13]. Whitehouse proposed an approximation technique to estimate the maximum peak-to-valley roughness (R_t) and the arithmetic average roughness (R_a) for surfaces generated using a circular tool nose. Similarly, Vajpayee provided an approximation for estimating R_t for surfaces created with a circular tool nose. Qu and Shih formulated mathematical models to predict R_t, R_a, and root-mean-square roughness (R_q) for ideal tool nose shapes composed of elliptical and circular arcs, using both implicit and approximation methods. Their work is further analysed and compared to the digital simulation method introduced in this study [14].

The aim of this research is to investigate the influence of insert geometry and feed rate on surface roughness during the turning process. The study focuses on analysing how different insert shapes affect the quality of the machined surface under three different feed conditions.

2. Material and methods

The experiment was carried out using a CNC turning on a Euroturn 12B CNC turning machine. The workpiece material used was 42CrMo4 (1.7225) alloy steel, which is commonly used for high-strength mechanical components and an often used reference test material in cutting experiments.

Each test was performed under the same machining conditions except for the feed rate, allowing a comparison of the machining behaviour and surface characteristics produced during the CNC turning process. Three specimens were machined with three tools, and each test part contain 3 separate surfaces (Figure 1). The cylindrical workpiece had a diameter (D) of 34 mm and a length (L) of 30 mm. During the turning operation, a constant cutting speed (v_c) of 120 m/min and a depth of cut (a_p) of 0.5 mm were maintained throughout the experiment. To investigate the influence of feed rate on the machining process, three different feed values were applied: 0.15 mm/rev, 0.25 mm/rev, and 0.35 mm/rev.

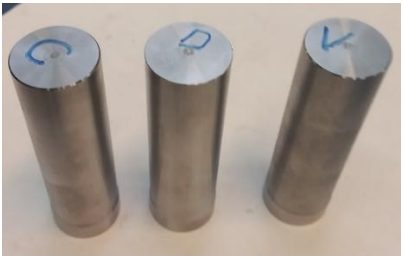

Figure 1 - Turned specimens.

Three different cutting insert and tool-holder combinations were used during the CNC turning experiments to evaluate their influence on the machining

performance and surface quality of the workpiece. The inserts were manufactured by Sandvik Coromant and TaeguTec (Table 1, Figure 1), which are widely recognized suppliers of cutting tools for metal machining applications.

Table 1. Data of three turning tools.

Insert	KAPR	SIG	ECEA	RE
CCMT 09T304-PM4225 (Sandvik)	95	80	5	0.4
DCMT 11T308 FG TT8125 (TaeguTec)	93	55	32	0.8
VBMT 110204-UF4315 (Sandvik)	93	35	52	0.4

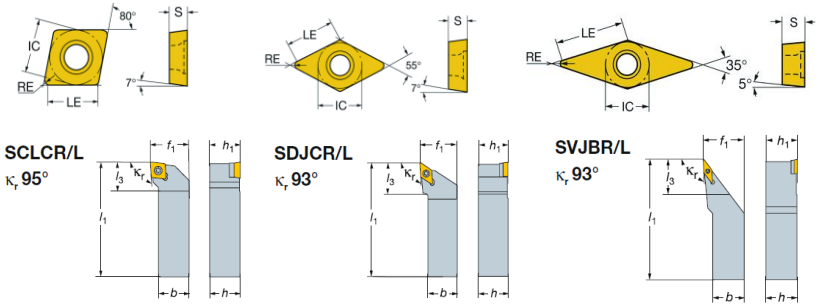

Figure 2 - Cutting insert geometries and tool holder configurations.

The first cutting tool used was the CCMT 09T304-PM4225 insert mounted on an SCLCR 1616 H9 tool holder (Figure 2). This tool configuration has a tool cutting edge angle (KAPR) of 95°, a clearance angle (SIG) of 80°, an end cutting edge angle (ECEA) of 5°, and a nose radius (RE) of 0.4 mm. This geometry is typically used for stable turning operations and is suitable for medium machining conditions due to its balanced cutting forces and good chip control.

The second tool consisted of a DCMT 11T308 FG TT8125 insert mounted on an SDJCR 1616 H11 tool holder, produced by TaeguTec. This configuration has a KAPR of 93°**,** SIG of 55°, ECEA of 32°, and a nose radius of 0.8 mm. The larger nose radius can improve surface finish and distribute cutting loads more evenly, which may reduce tool wear during machining.

The third tool used in the experiment was the VBMT 110204-UF4315 insert mounted on an SVJBR 1616 H11 tool holder, produced by Sandvik. This tool also has a KAPR of 93°, but with SIG of 35°**,** ECEA of 52°, and a nose radius of 0.4 mm. The sharper geometry and smaller nose radius make this insert suitable for finishing operations and precision machining where lower cutting forces and improved surface quality are required. The larger end cutting edge angle (ECEA) ensures turning a steep undercutted feature.

The use of these three different tool geometries allowed the investigation of how insert shape, cutting edge angle, and nose radius affect the machining process, tool performance, and the resulting surface characteristics of the turned specimen.

Surface roughness of the machined surfaces were measured after the turning process. Surface roughness measurements were carried out using a Mitutoyo SJ-301 Surface Rroughness Tester (Figure 3). The instrument was used to determine the roughness parameters of the machined surfaces. Each surface was measured ten times, so the analysis was performed based on 90 data sets.

Three surface roughness parameters were analysed:

- R_z – Average Maximum Height of the Profile is the average of the successive values of R_{ti}.
- R_t – Maximum Height of the Profile is the vertical distance between the highest and lowest points of the profile.
- R_{sm} - Mean Spacing of Profile Irregularities is the mean value of the spacing between profile irregularities.

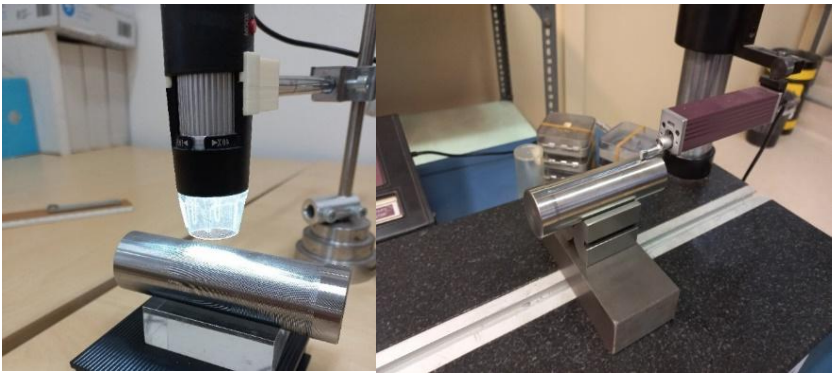

Figure 3 - Measurement and testing of the three machined specimens for surface roughness analysis: a) Digital microscope b) Mitutoyo SJ-301.

For the qualitative roughness measurements, the surface topography of the specimens was examined using a digital microscope (Figure 3). The microscope images allowed a detailed observation of the surface texture, feed marks, and machining patterns generated during the turning operation. The combination of the roughness measurements obtained from the surface tester and the visual analysis from the digital microscope provided a more precise evaluation of the surface quality of the machined specimens.

The data analysis was performed with Jamovi v2.6.44 and Minitab v22 software.

3. Results

The most significant results of the surface roughness measurements under different machining conditions are presented below. Figure 4 shows that at a feed rate of 0.15 mm/rev, the surface profiles exhibit low amplitude with shallow valleys, indicating smoother surfaces. At 0.25 mm/rev feed rate, the peaks become more noticeable and regularly spaced, showing a moderate increase in roughness. At 0.35 mm/rev feed rate, the profiles display high, sharp peaks and deeper valleys, indicating a significantly rougher surface. It can be observed that the surface profile produced with inserts C and D is similar for all three feeds.

This similarity can also be seen in the microscopic images (Figure 5). However, the V insert shows a significantly different profile and image. In case of small feed, the V insert produced more regular profile, than C and D.

Table 2 shows the mean values of the measured R_z, R_t and R_{Sm} values as a function of the insert shape and feed. The values of R_z and R_t are almost the same. The V insert shows a substantially stronger sensitivity to feed rate, with R_z increasing by up to 254%, compared to 159–168% for C and D inserts. The values of R_{Sm} increased by 99%, 53% and 116% for the feed. The R_{Sm} mean value is highly correlated with the feed, no clear dependence on insert geometry can be identified.

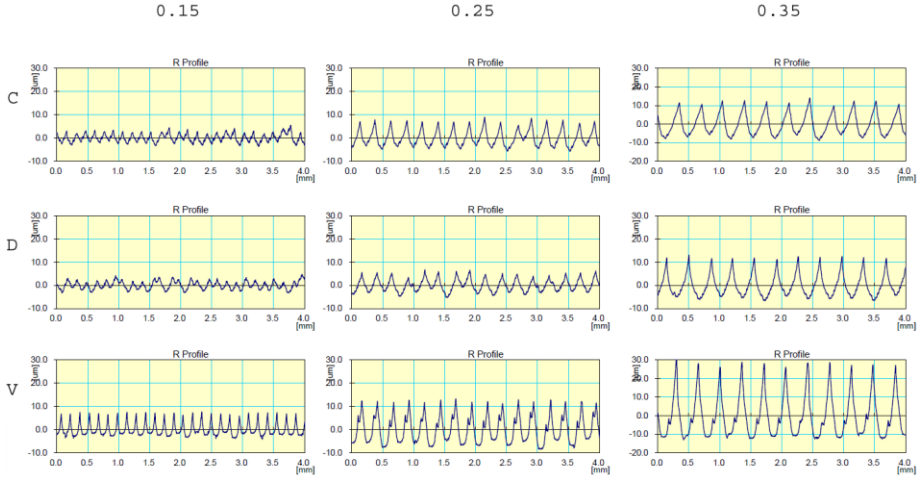

Figure 4 - One measurement results of surface profile.

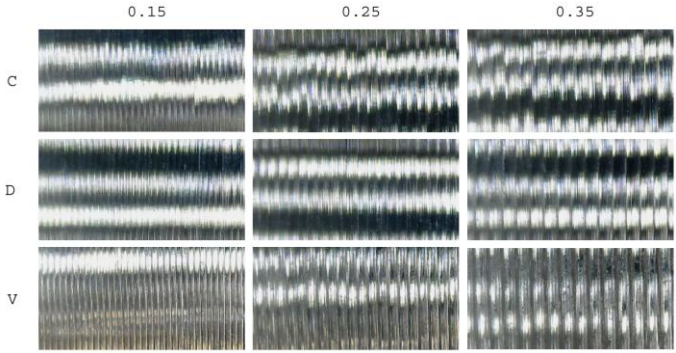

Figure 5 - Images of three inserts taken with a digital microscope.

Table 2. Mean value of R_z, R_t and R_{Sm} parameters.

Insert	***f***	$\boldsymbol{R_z}$	$\boldsymbol{R_t}$	$\boldsymbol{R_{Sm}}$
C	0.15	7.57	9.16	0.175
	0.25	14.20	15.60	0.269
	0.35	20.30	21.70	0.349
D	0.15	7.06	8.16	0.228
	0.25	10.50	11.70	0.277
	0.35	18.30	19.30	0.348
V	0.15	11.60	12.90	0.164
	0.25	21.00	22.90	0.262
	0.35	41.10	42.80	0.355

4. Discussion

Three surface roughness parameters were selected from the results, because several of the parameters show high correlation. Based on the measured results presented in Figure 6, it can be concluded that both insert geometry and feed rate have influence on surface roughness parameters (R_z, R_t, and R_{sm}) during the turning process. The distributions clearly demonstrate that variations in feed rate (0.15, 0.25, and 0.35 mm/rev) lead to noticeable changes in roughness values across all insert types (C, D, and V).

As the feed rate increases, there is a general trend of increasing roughness values, particularly evident in R_z and R_t parameters, indicating a deterioration in surface quality. Lower feed rates produce more concentrated and stable distributions with smaller roughness values, which suggests better surface finish. In contrast, higher feed rates result in wider distributions and higher peaks, reflecting increased variability and roughness.

The effect of insert shape is also prominent. The V insert geometry tends to produce higher roughness values under similar cutting conditions, while C and D demonstrate more stable and lower roughness profiles. This indicates that insert geometry plays a crucial role in controlling surface characteristics.

Additionally, the R_{sm} parameter shows sensitivity to both feed rate and insert type, reflecting changes in the spacing of surface irregularities. This suggests that not only the height but also the pattern of surface texture is influenced by machining conditions.

Based on the geometric model of the theoretical surface roughness of the turning, the nose radius (RE) and the feed (*f*) have influence on the surface roughness. Based on it, the C and V insert should be produces similar profile and surface roughness parameters because of the same RE. However, the more favorable ECEA angle of insert C in terms of surface roughness compensates for the unfavorable nose radius. Thus, the roughness of the surfaces created by inserts C and D is similar, while insert V with a large ECEA angle and a small tip radius shows much higher roughness results.

The statistical analyses of the measured data by Main Effect Plot (Figure 7) shows that feed rate has the strongest influence on surface roughness, which meet with the theory. As the feed rate increases, R_z and R_t values rise, leading to poorer surface quality, while lower feed rates ensure a smoother finish.

Insert geometry also plays an important role: C and D inserts produce lower roughness, whereas the V insert results in higher values. The analysis confirms the effect of the insert shape on the surface roughness, the average roughnesses for inserts C and D are almost the same, while the values for insert V are significantly higher. It can also be observed that the effect of the shape of insert C does not completely eliminate the difference, insert D with a larger nose radius provides better surface roughness.

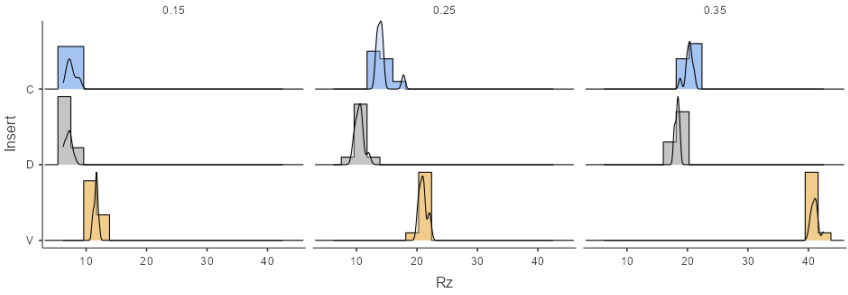

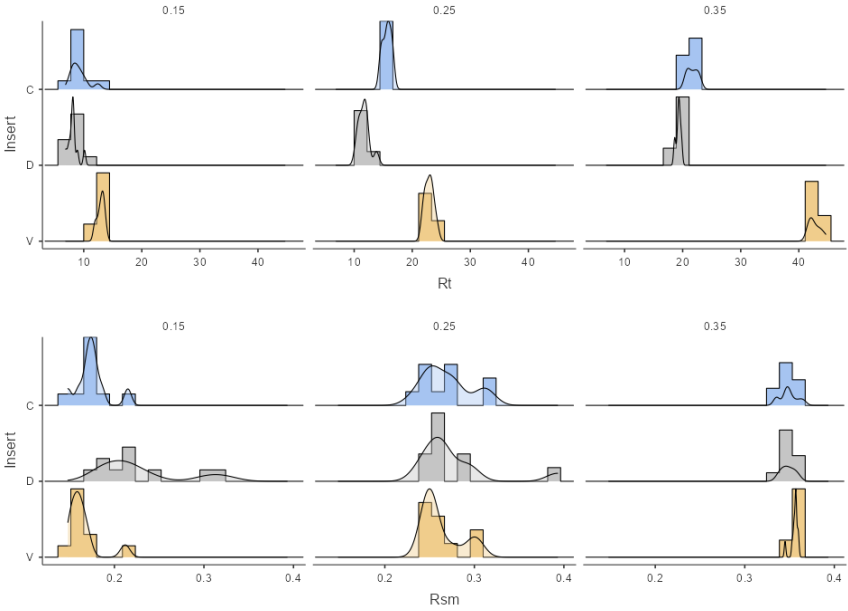

Figure 6 - The results of the measure.

The R_{sm} parameter in the feed direction shows a different pattern. Based on the measured data (Figure 6), the C and V inserts show a similar pattern, while the D insert has a significantly higher variance, especially at low feed rates.

The main effects plot shows the ratio of R_{sm} to feed, which is ideally 1. At higher feed rates, the R_{sm} parameter approaches the feed rate value. As can be seen, the C and V inserts with the same radius resulted in almost the same average value, which is also shown by the radius effect. In this case, the shape of the C insert has no compensating effect.

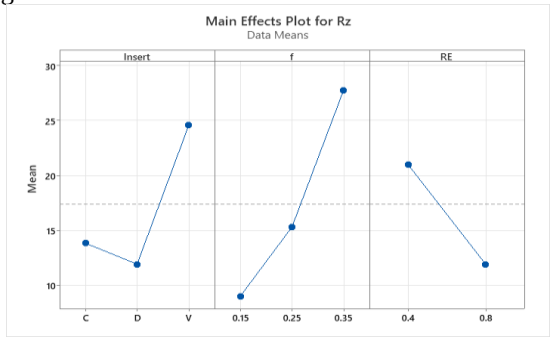

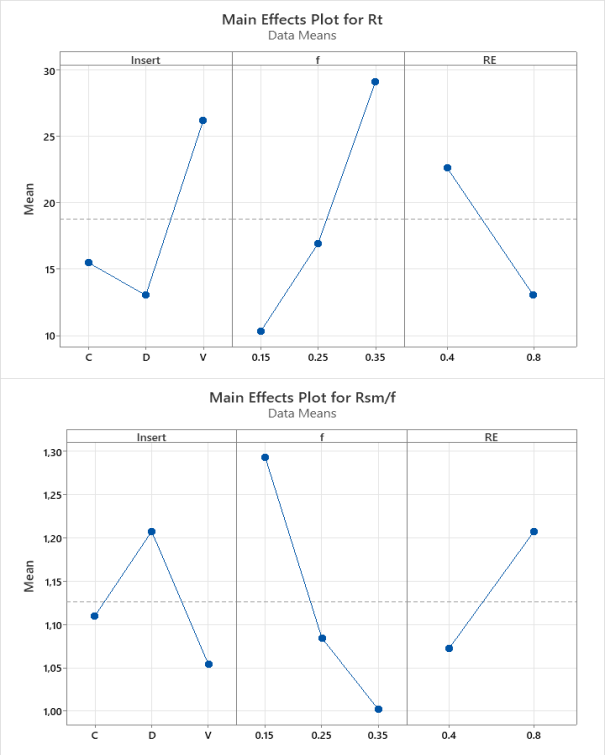

Figure 7 – Main effects plots for R_z, R_t and R_{sm}.

Overall, the results confirm that optimal surface quality can be achieved by selecting appropriate insert geometry and maintaining lower feed rates. These findings provide a useful basis for improving machining performance, enhancing product quality, and optimizing cutting parameters in turning operations.

5. Summary

This study investigates the surface profile and roughness values of turned surfaces as a function of feed and insert geometry for 42CrMo4 steel alloy. Three insert geometries (C, D, V) were compared. Feed rate was found to be the dominant factor in terms of surface roughness of the turned surface, but edge geometry variations resulting from insert shape have significant secondary influence on surface roughness.

The future work of the research is to develop a roughness prediction model based on a geometric-kinematic model. The model, supplemented with statistical

elements, creates an equivalent replacement profile (ERP), which allows for the joint estimation of several roughness parameters. Based on the current results presented in the article, when designing the statistical model, not only the classical feed and nose radius parameters should be taken into account, but also the shape of the insert.

References: 1. J. Schmidt, B. Thorenz, F. Schreiner, F. Döpper, Comparison of areal and profile surface measurement methods for evaluating surface properties of machined components, Procedia CIRP 2021 102:459–464 https://doi.org/10.1016/j.procir.2021.09.078 **2.** Abellán-Nebot J.V., Pastor C.V., Siller H.R.: A Review of the Factors Influencing Surface Roughness in Machining and Their Impact on Sustainability. Sustainability 2024 16(5):1917 https://doi.org/10.3390/su16051917 **3.** Wang, Z. et al. Built-up-edge effects on surface deterioration in micromilling processes. Journal of Manufacturing Processes. 2016 24(2):321–327 https://doi.org/10.1016/j.jmapro.2016.03.016 **4.** Tseng, T. L.: *Novel approach to predict surface roughness in end-milling* (Journal of Computational Design & Engineering. 2016 3(1):1–13, https://doi.org/10.1016/j.jcde.2015.04.002 **5.** Segebade E, Zanger F, Schulze V. Influence of Different Asymmetrical Cutting Edge Microgeometries on Surface Integrity. Procedia CIRP, 2016. 45:11–14 https://doi.org/10.1016/j.procir.2016.02.070 **6.** Tomov, M., Prangoski, B., Karolczak, P.: Mathematical modelling and correlation between the primary waviness and roughness profiles during hard turning. Jordan Journal of Mechanical and Industrial Engineering, 2021 15(3):243–249 **7.** M. Liu, J. I. Takagi and A. Tsukuda, Effect of tool nose radius and tool wear on residual stress distribution in hard turning of bearing steel, J. Material Processing Technology. 2004 150(3):234–241 **8.** M. Dogra, V. S. Sharmab and J. Durejac, Effect of tool geometry variation on finish turning–A review, Journal of Engineering Science and Technology Review. 2011 4(1):1–13 **9.** Puertas Arbizu, I., Perez Luis, C.J.,: Surface roughness prediction by factorial design of experiments in turning processes. Journal of Materials Processing Technology, 2003 143–144:390-396. https://doi.org/10.1016/S0924-0136(03)00407-2 **10.** de Souza A.M. et al.: Performance of single Si3N4 and mixed Si3N4+PCBN wiper cutting tools applied to high speed face milling of cast iron. International Journal of Machine Tools and Manufacture 2005 45(3):335–344 https://doi.org/10.1016/j.ijmachtools.2004.08.006 **11.** Abellán-Nebot, J. V., Vila Pastor, C., Siller, H. R.A review of the factors influencing surface roughness in machining and their impact on sustainability. Sustainability. 2024. vol. 16(5). p. 1917. **12.** Bhirud, N. L., Dube, A. S., Patil, A. S., Bhole, K. S.Multi-objective optimization of cutting parameters and helix angle for temperature rise and surface roughness using response surface methodology and desirability approach for Al 7075.International Journal on Interactive Design and Manufacturing (IJIDeM). 2024. vol. 18(10). pp. 7095–7114. **13.** Chowdary, B. V., Sookhansingh, O.Tool geometry and machining variables influence on the surface roughness of end-milling process: a comparative study with application of RSM and GA tools and techniques.International Journal of Process Management and Benchmarking. 2024.vol. 16(1). pp.1–18. **14.** Molnar, V., Szabo, G.:Designation of minimum measurement area for the evaluation of 3D surface texture, Journal of Manufacturing Processes 83, pp. 40–48, 2022.

Суратжон Нуріддінов, Балаш Міко, Будапешт, Угорщина

ВПЛИВ ФОРМИ РІЗАЛЬНОЇ ВСТАВКИ ТА ПОДАЧІ НА ПРОФІЛЬ ОБРОБЛЕНОЇ ПОВЕРХНІ

Анотація. *Це дослідження вивчає сукупний вплив геометрії різальної вставки та величини подачі на шорсткість поверхні при токарній обробці легованої сталі 42CrMo4. Контрольовані експерименти проводилися на верстаті з ЧПУ з використанням трьох геометрій вставок (типи C, D і V) і трьох швидкостей подачі (0,15, 0,25 і 0,35 мм/оберт), зберігаючи постійну швидкість*

різання та глибину різу. Характеристики поверхні оцінювалися за допомогою кількісних вимірювань шорсткості та якісного мікроскопічного аналізу. Результати показують, що швидкість подачі є домінуючим фактором, що впливає на шорсткість поверхні, а збільшення подачі призводить до значного погіршення якості поверхні, що відображається у вищих значеннях R_z і R_t. Геометрія вставки також відіграє критичну роль: вставки C і D дають стабільно нижчі значення шорсткості, тоді як V-вставка призводить до гіршої якості поверхні за однакових умов різання. Варто зазначити, що, незважаючи на ідентичні радіуси вершини, спостерігалися суттєві відмінності між вставками C і V, що підкреслює виражений вплив геометрії країв, особливо кута ріжучої крайки вершини. Результати свідчать, що звичайні геометричні моделі, засновані виключно на подачі та радіусі при вершині, недостатні для точного прогнозування шорсткості поверхні. Натомість слід враховувати параметри форми вставки. Це дослідження сприяє кращому розумінню взаємодії між геометрією інструмента та параметрами обробки та надає практичні рекомендації для оптимізації якості поверхні в токарних операціях. Майбутня робота дослідження полягає у розробці моделі прогнозування шорсткості на основі геометрично-кінематичної моделі. Модель, доповнена статистичними елементами, створює еквівалентний профіль заміни (ERP), що дозволяє спільно оцінювати кілька параметрів шорсткості. Виходячи з поточних результатів, представлених у статті, при розробці статистичної моделі слід враховувати не лише класичні параметри подачі та радіус при вершині, а й форму вставки.

Ключові слова: *профіль поверхні; точіння; форма вставки; подача; шорсткість поверхні; графік основного ефекту.*

UDC UDC 621.9.08:681.5.08 **doi: 10.20998/2078-7405.2026.104.08**

AUTOMATED SYSTEM FOR CONTROLLING SURFACE ROUGHNESS PARAMETERS USING LASER TRIANGULATION

Vadim **Shevchenko** [0009-0002-6485-4825], Mykola **Polushko** [0009-0001-2539-8938],

National Technical University of Ukraine "Igor Sikorsky Kyiv Polytechnic Institute", Kyiv, Ukraine
polushkomykola@gmail.com

Received: 10 April 2026/ Revised: 19 April 2026/ Accepted: 29 April 2026 / Published: 15 May 2026

Abstract. *The article discusses the development of an automated system for controlling the surface roughness parameters of parts, integrated directly into the machining process on CNC machines. The relevance of the study is due to the increasing requirements for the quality of surfaces that determine the operational characteristics of products, in particular wear resistance, tightness and strength of joints. The object of the study is the process of non-contact measurement of the surface microprofile by the laser triangulation method. The paper proposes a method for determining the microrelief parameters based on the analysis of the laser spot displacement on the CMOS matrix. To increase the accuracy, an algorithm for subpixel determination of the signal energy center and digital filtering using a Butterworth filter are used, which allows minimizing the impact of noise, vibrations and production interference. The results obtained confirm the effectiveness of the proposed approach and allow reducing the percentage of defects by 12–15%. The proposed system corresponds to the concept of Industry 4.0 and contributes to increasing the level of production automation.*

Keywords: *roughness parameter control; laser triangulation; non-contact measurements; production automation; CMOS matrix; signal filtering.*

1. Introduction

The modern development of mechanical engineering and instrument-making is characterized by a transition to a high level of automation of production processes, which involves minimizing operator participation and ensuring stable product quality. In these conditions, control of surface roughness parameters of parts becomes of particular importance [1].

Surface microgeometry directly affects the operational properties of products, including wear resistance, joint strength, friction and durability. Ensuring specified roughness parameters is an important component of the technological process of processing.

At the same time, traditional approaches to surface quality control do not fully meet the requirements of modern production. This necessitates the development of new methods and measuring tools that can be integrated directly into the processing

process.

The paper considers an approach to automated control of roughness parameters based on laser triangulation, which allows for non-contact measurement of the microprofile in real time.

2. Problem statement

Ensuring stable parameters of the surface roughness of parts during mechanical processing remains a difficult scientific and technical task, especially in automated production. The main requirement is the ability to carry out control directly during processing without stopping the technological process [2].

Existing contact methods are characterized by limited speed and are not suitable for use in real time. Non-contact optical systems, although they provide high accuracy, often turn out to be insufficiently resistant to the influence of production factors, such as vibrations, noise and pollution.

In this regard, the task of developing a control method that combines high speed, sufficient accuracy and the ability to integrate into automated control systems is relevant. Of particular importance is increasing the reliability of determining microprofile parameters by improving signal processing algorithms and reducing the impact of measurement errors.

3. Literature review

Methods for controlling surface roughness parameters are conventionally divided into contact and non-contact. Contact methods, in particular profilometry, provide high measurement accuracy, but their application is limited by low productivity and complexity of use in automated production [3].

Among non-contact approaches, confocal and interferometric methods have become widely used. They allow achieving high resolution, but are characterized by complexity of implementation and increased sensitivity to external influences [4].

The laser triangulation method is considered an effective alternative, since it provides a compromise between accuracy and speed. Its application in industrial conditions is promising due to the relative simplicity of implementation and the possibility of integration into automated systems [5].

At the same time, an analysis of literary sources shows that the issue of increasing measurement accuracy and noise immunity of such systems in real production conditions remains insufficiently studied.

4. Materials and Methods

The functioning of the developed automated system is based on the principle of active optical triangulation, which is based on solving the geometric parameters of the triangle formed by the radiation source, the investigated surface and the receiving optical system. Unlike passive methods, this technology involves active probing of the microprofile with a narrowly focused laser beam. The laser diode projects a light spot onto the surface of the part, and the scattered (diffuse) radiation is collected by a lens and focused on a photosensitive CMOS matrix located at a certain angle to the radiation axis. The optical diagram of the measuring module based on laser triangulation is presented in fig. 1.

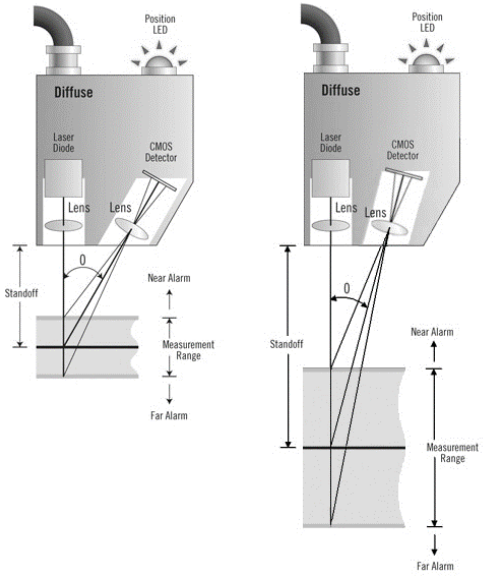

Figure 1 – Optical scheme and geometric model of the laser triangulation method

The fundamental task of the mathematical apparatus of the system is to convert the displacement of the light spot on the plane of the photodetector into a real change in the height of the microrelief. When the surface of the part has a protrusion or a depression, the point of incidence of the laser beam is shifted along its axis, which leads to a corresponding shift of the image of this point on the matrix. The mathematical dependence describing this process is derived from the trigonometric ratios of the optical scheme:

$$\Delta z = \frac{\Delta x \cdot L}{f \cdot \sin\theta + \Delta x \cdot \cos\theta}, \quad (1)$$

Where Δz – the desired change in the height of the microprofile (vertical deviation), which determines the amplitude parameters of the roughness, mm; Δx – the physical displacement of the energy center of the light spot on the CMOS sensor plane relative to the base point, mm; L – the working distance from the main optical plane of the lens to the zero measurement line, which determines the range of the sensor operation, mm; f – is the effective focal length of the receiving lens system, which affects the magnification factor of the scheme, mm; θ – the triangulation angle, i.e. the angle between the optical axis of the laser emitter and the axis of the receiver, degrees.

Since the image of a laser spot on the matrix usually covers an area of several pixels, there is a problem of discretization, which limits the measurement accuracy to the physical size of the pixel. To overcome this barrier and achieve the nanometer resolution necessary for the analysis of finished surfaces, the system implements an algorithm for calculating the centroid (energy center) of the spot. This allows determining the position x_c with an accuracy that is 10–20 times greater than the physical pixel pitch:

$$x_c = \frac{\sum_{i=k}^{m} i \cdot I_i}{\sum_{i=k}^{m} I_i}, \quad (2)$$

Where x_c – the calculated coordinate of the spot center; i – the pixel index; I_i – the signal amplitude (light intensity) recorded by the pixel; k and m – the boundaries of the reading area. This approach minimizes the influence of digital noise and provides high linearity of measurements.

The minimum step of roughness change, which is able to record the optical path, determines the sensitivity threshold of the system. It directly depends on the geometric configuration of the sensor:

$$S_z = \frac{p \cdot L}{f \cdot \sin\theta}, \quad (3)$$

Where S_z – the theoretical limit of vertical resolution, μm; p – the physical size of the matrix pixel. From the analysis of the formula it follows that to increase the accuracy it is necessary to increase the triangulation angle θ or reduce the working distance L, which is taken into account when designing the measuring head for different types of machines.

Since the measurements are carried out "in-situ", the received signal contains components of low-frequency vibrations and waviness. To isolate the roughness parameters, a Butterworth filter is used, the transfer function of which has the form:

$$H(s) = \frac{1}{1 + \left(\frac{s}{\omega_c}\right)^n}, \tag{4}$$

After filtering the array of z_i values, the system calculates the arithmetic mean deviation Ra, which is the basic indicator of processing quality:

$$Ra = \frac{1}{n}\sum_{i=1}^{n} |z_i - \bar{z}|, \tag{5}$$

Where n – the number of measurement points; z_i – the current deviation; $\bar{z}$ – the average profile line. Additionally, to assess the metrological reliability in conditions of shop noise, the total error σ_z is calculated, which takes into account the instability of the beam incidence angle due to microvibrations of the machine tool (σ_θ):

$$\sigma_z = \sqrt{\left(\frac{\delta z}{\delta x}\right)^2 \cdot \sigma_x^2 + \left(\frac{\delta z}{\delta \theta}\right)^2 \cdot \sigma_\theta^2}. \tag{6}$$

This set of mathematical models allows the system not only to measure microgeometry with high accuracy, but also to adapt to the dynamic conditions of the industrial environment, ensuring the reliability of data for further control of the technological process.

The developed automated roughness control system is integrated into the overall control structure of the metal-cutting machine as an intelligent feedback node. The interaction between its components and information flows is presented in the structural and functional diagram in fig. 2, and the algorithm of its operation is presented in fig. 3.

The main source of primary information about the surface microprofile is the measuring head, which contains a laser emitter (pos. 1, fig. 2) and focusing optics. The optical signal reflected from the part is recorded by a high-speed CMOS matrix (pos. 2), where light energy is converted into an array of electric charges. The received primary signal passes through the pre-processing block (pos. 3), which includes an amplifier and a hardware module for subpixel localization of the spot centroid to increase the accuracy of reading coordinates.

Next, the digital data is fed to the central computing module (pos. 4), the key element of which is the digital Butterworth filter (pos. 5). In this block, signal separation is carried out: separation of the high-frequency component (actually roughness) from low-frequency vibrations and waviness. Further analysis of the parameters is performed in the statistical evaluation block (pos. 6), where the Ra and Rz indicators are calculated based on mathematical models.

In the comparison block (pos. 7), continuous quality monitoring is carried out based on data on the regulatory tolerance limits (pos. 8), which are set by the technological map. In case of detection of critical deviation of parameters, the system through the logical decision-making module (pos. 10) sends an emergency stop signal to the machine tool actuators (pos. 13), in particular to the feed and main motion drives.

In addition, the system provides an adaptive control loop. Information about the current processing modes (speed, feed) comes from the CNC block (pos. 11) according to the control program (pos. 12). This data, together with the calculated roughness, is processed in the tool condition prediction block (pos. 9).

After determining the level of wear of the cutting edge, the data is transmitted to the correction formation block (pos. 10), where commands are generated for the CNC (pos. 11) to change the processing parameters in real time. If the correction does not allow the roughness indicators to return to normal, the system initiates a tool replacement cycle. The CNC, receiving the appropriate signals, makes changes to the control commands that are sent to the actuators (pos. 13) to safely complete or interrupt the operation.

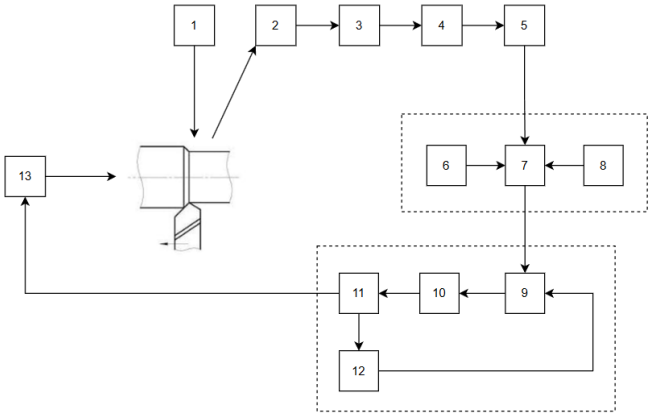

Figure 2 – Block diagram of an automated system for controlling surface roughness parameters of parts

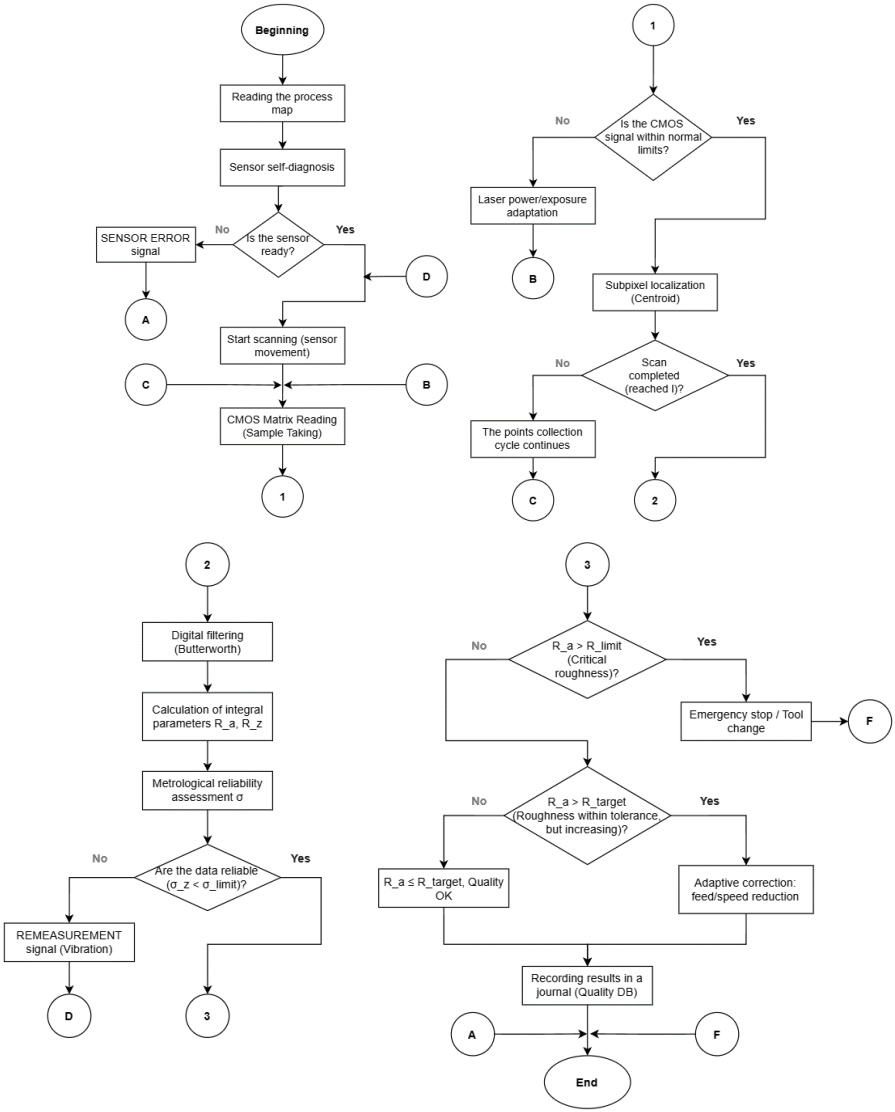

Figure 3 – Algorithm of functioning of the automated system for controlling the surface quality of parts

5. Experiments

The following parameters of the laser triangulation scheme were selected for the numerical experiment: $L = 100\ mm, f = 50\ mm, \theta = 45°$ ($\sin\theta = 0{,}7071;\ \cos\theta = 0{,}7071$); $\sigma_x = 0{,}00036\ mm$; $\sigma_\theta = 0{,}0001745$ rad

Partial derivative formulas:

1. By displacement: $\frac{\delta z}{\delta x} = \frac{L}{f \cdot \sin\theta} = \frac{100}{50 \cdot 0{,}7071} = 2{,}82843$
2. Around the corner: $\frac{\delta z}{\delta \theta} = \frac{\Delta x \cdot L \cdot \cos\theta}{f \cdot \sin^2\theta} = \frac{\Delta x \cdot 100 \cdot 0{,}7071}{50 \cdot 0{,}5} = \Delta x \cdot 2{,}8284$

Let $\Delta x_1 = 0{,}005\ mm$, then:

1. Height: $\Delta z_1 = \frac{0{,}005 \cdot 100}{50 \cdot 0{,}7071 + 0{,}005 \cdot 0{,}7071} = \frac{0{,}5}{35{,}3553 + 0{,}0035} = 0{,}01413\ mm$
2. Error according to the formula (6):

$$\sigma_{z_1} = \sqrt{(2{,}82843)^2 \cdot (0{,}00036)^2 + (0.005 \cdot 2{,}82843)^2 \cdot (0{,}0001745)^2}$$

$$\sigma_{z_1} = \sqrt{0{,}00000103675 + 0{,}00000000000607} \approx 1{,}0182\ \mu m$$

Let $\Delta x_2 = 0{,}015\ mm$, then:

1. Height: $\Delta z_2 = \frac{1{,}5}{35{,}3553 + 0{,}0106} = \frac{1{,}5}{35{,}3659} = 0{,}04241\ mm$
2. Error according to the formula (6):

$$\sigma_{z_2} = \sqrt{0{,}00000103675 + (0{,}015 \cdot 2{,}82843)^2 \cdot (0{,}0001745)^2}$$

$$\sigma_{z_2} = \sqrt{0{,}00000103675 + 0{,}0000000000546} \approx 1{,}0183\ \mu m$$

Let $\Delta x_3 = 0{,}040\ mm$, then:

1. Height: $\Delta z_3 = \frac{4}{35{,}3553 + 0{,}0282} = \frac{4}{35{,}3835} = 0{,}11305\ mm$
2. Error according to the formula (6):

$$\sigma_{z_3} = \sqrt{0{,}00000103675 + (0{,}040 \cdot 2{,}82843)^2 \cdot (0{,}0001745)^2}$$

$$\sigma_{z_3} = \sqrt{0{,}00000103675 + 0{,}0000000003886} \approx 1{,}0184\ \mu m$$

Let $\Delta x_4 = 0{,}085\ mm$, then:

1. Height: $\Delta z_4 = \frac{8,5}{35,3553+ 0,0601} = \frac{8,5}{35,4154} = 0,24001\ mm$
2. Error according to the formula (6):

$$\sigma_{z_4} = \sqrt{0,00000103675 + (0,085 \cdot 2,82843)^2 \cdot (0,0001745)^2}$$

$$\sigma_{z_4} = \sqrt{0,00000103675 + 0,0000000017551} \approx 1,0191\ \mu m$$

Based on the calculations, a data set was formed that reflects the dynamics of changes in the metrological characteristics of the system within the specified measurement range. The generalized results of the calculations of the microprofile height and the corresponding values of the mean square error are given below in table 1.

Table 1 – Simulation results

№	Δx, mm	Δz, mm	σ_z, μm	Recommended control system action
1	0,005	0,0141	1,0182	Continuation of processing
2	0,015	0,0424	1,0183	Continuation of processing
3	0,040	0,1131	1,0184	Feed reduction
4	0,085	0,2400	1,0191	Stop / Tool Correction

6. Results

Analysis of the simulation results allows us to formulate the logic of the automated system. At Δz values from 0,014 to 0,042 mm, the surface condition meets the requirements of finishing, and the measurement error remains stable, which allows us to continue the process without correction.

When the microprofile height increases to 0,113 mm, the system records the beginning of process destabilization: despite the fact that the total error increases only by fractions of a nanometer, a threefold increase in the measured value indicates initial tool wear or increased vibrations. In this case, the system initiates a feed reduction to stabilize quality. Reaching the critical mark of 0,240 mm by the Δz parameter indicates significant wear or breakage of the cutting edge, which is accompanied by the highest rate of error growth. In such a state, further processing will inevitably lead to a defect, so the intelligent algorithm issues a command to completely stop the equipment to replace the tool or introduce technical correction.

7. Discussion

The results of the study indicate the feasibility of using the laser triangulation method to implement non-contact control of surface roughness parameters in automated production.

The main advantage of the approach is the ability to combine sufficient measurement accuracy with high speed, which makes it suitable for use as part of process control systems. This opens up the possibility of transitioning from periodic to continuous control of the surface condition.

At the same time, the efficiency of the system is largely determined by the choice of optical circuit parameters and signal processing algorithms. In real production conditions, equipment vibrations and lighting instability can have an additional impact, which requires further improvement of filtering methods and error compensation.

Conclusions

Automation of non-contact control of surface microgeometry in real time is a key stage in the development of modern intelligent production. The introduction of "in-situ" laser diagnostics systems allows to radically increase the stability of technological processes and ensure guaranteed product quality in finishing operations. The use of progressive methods of digital filtering and subpixel processing of optical signals provides high metrological reliability of control of roughness parameters even under conditions of intense vibrations and dynamic interference inherent in the operation of metal-cutting equipment.

The integration of active control tools with the CNC architecture allows the system not only to record deviations, but also to promptly adjust processing parameters, minimizing the impact of tool wear and the human factor. This approach contributes to a significant reduction in production costs, optimization of equipment service life and increase in the overall energy efficiency of industrial complexes.

References: **1.** *Shevchenko, V. (2024).* Details Processing Control System at the Automated Manufacturing. In*: Bezuglyi, M., Bouraou, N., Mykytenko, V., Tymchyk, G., Zaporozhets, A. (eds)* Advanced System Development Technologies I. Studies in Systems, Decision and Control, vol 511. Springer, Cham. doi: 10.1007/978-3-031-44347-3. **2.** *Bohachov Y., Korobtsov Y., Shevchenko V.* Method for Increasing the Reliability of Cutting Tool Condition Diagnostics in Automated Machining // Bulletin of the Kyiv Polytechnic Institute. Series: Instrument Making. – 2018. – No. 55(1). – pp. 72–76. – doi: 10.20535/1970.55(1).2018.135899. **3.** *Dhiren R. P., Kiran M. B.* A non-contact approach for surface roughness prediction in CNC turning using a linear regression model // Materials Today: Proceedings. – 2020. – Vol. 26. – pp. 350–355. – doi: 10.1016/j.matpr.2019.12.029. **4.** *Lishchenko N., O'Donnell G.E., Culleton M.* Contactless Method for Measurement of Surface Roughness Based on a Chromatic Confocal Sensor // Machines. – 2023. – Vol. 11, No. 8. – Art. 836. – doi: 10.3390/machines11080836. **5.** *Dong Z., Sun X., Liu W., Yang H.* Measurement of Free-Form Curved Surfaces Using Laser Triangulation // Sensors. – 2018. – Vol. 18, No. 10. – Art. 3527. – doi: 10.3390/s18103527.

Вадим Шевченко, Микола Полушко, Київ, Україна

АВТОМАТИЗОВАНА СИСТЕМА КОНТРОЛЮ ПАРАМЕТРІВ ШОРСТКОСТІ ПОВЕРХНІ ДЕТАЛЕЙ ЗА ДОПОМОГОЮ МЕТОДУ ЛАЗЕРНОЇ ТРІАНГУЛЯЦІЇ

Анотація. *У статті представлено розробку автоматизованої системи контролю параметрів шорсткості поверхні деталей, інтегрованої безпосередньо у виробничий цикл механічної обробки. Актуальність дослідження зумовлена зростанням вимог сучасної промисловості до експлуатаційних характеристик виробів, оскільки мікрогеометрія поверхні суттєво впливає на зносостійкість, герметичність і втомну міцність з'єднань. Показано, що традиційні методи контролю, зокрема контактне профілювання та використання хроматичних зондів, мають обмежену ефективність у виробничих умовах через чутливість до вібрацій, забруднення та значні витрати часу на вимірювання і повторне базування деталей. Об'єктом дослідження є процес безконтактного вимірювання мікропрофілю поверхні із застосуванням методу лазерної тріангуляції. Розкрито фізичні принципи формування тріангуляційної схеми та наведено аналітичні залежності між зміщенням лазерної плями на CMOS-матриці й реальними параметрами висоти нерівностей поверхні. Запропонована структура системи охоплює повний цикл обробки даних: від первинної фільтрації оптичного шуму та компенсації похибок, спричинених розсіюванням світла, до обчислення стандартизованих параметрів шорсткості. Додатково обґрунтовано вибір параметрів оптичної схеми та чутливих елементів системи з урахуванням умов реального виробництва. Особливу увагу приділено алгоритмічному забезпеченню, реалізованому за принципом зворотного зв'язку. Розроблений алгоритм забезпечує не лише оцінювання відповідності параметрів шорсткості заданим вимогам, а й формування керуючих впливів для промислових контролерів з метою оперативної корекції режимів різання при зносі інструменту. Практичне значення роботи полягає у можливості створення замкнутих інтелектуальних систем контролю якості типу in-situ, що сприяє зниженню рівня браку на 12–15% і підвищенню рівня автоматизації машинобудівних та приладобудівних виробництв у межах концепції Індустрії 4.0.*

Ключові слова: *контроль параметрів шорсткості; безконтактні вимірювання; лазерна тріангуляція; CMOS-матриця; обробка сигналів; автоматизація виробництва.*

UDC 621.91.01 **doi: 10.20998/2078-7405.2026.104.09**

EVALUATION OF MACHINABILITY BASED ON CUTTING FORCE AND SURFACE QUALITY CHARACTERISTICS USING THE TOPSIS METHOD

Béla **Mészáros** [0009-0000-4928-8445], Balázs **Mikó** [0000-0003-3609-0290]

Óbuda University, Budapest, Hungary
meszaros.bela@uni-obuda.hu

Received: 16 April 2026/ Revised: 21 April 2026/ Accepted: 30 April 2026 / Published: 15 May 2026

Abstract. *The study proposes a multi-criteria machinability evaluation based on cutting forces, surface quality, and productivity characteristics obtained from CNC milling experiments. Three tool steels (1.2379, 1.2842, and ES Aktuell 1200) and four long-reach milling cutters were tested under controlled machining conditions. The experimental data set, including force components and surface roughness parameters, was analysed using the TOPSIS (Technique for Order Preference by Similarity to Ideal Solution) method to integrate multiple performance indicators into a single metric, referred to as the Cutting Ability Index (CAI). The results show that the proposed approach enables the ranking of material-tool combinations and provides a more comprehensive interpretation of machinability compared to single-parameter evaluations. However, the resulting rankings are sensitive to the selection and balance of input criteria and, in certain cases, deviate from expected physical behaviour. This highlights the limitations of equally weighted multi-criteria approaches and underscores the importance of appropriate parameter selection and weighting. The study confirms that while TOPSIS can serve as an effective decision-support tool in machining analysis, its application requires careful methodological consideration.*

Keywords: *machinability; CNC milling; TOPSIS; multi-criteria decision making; surface roughness.*

1. Introduction

In machining technology, process parameters and circumstances such as cutting speed, feed rate, and depth of cut, tool and material properties also significantly influence surface quality, tool wear, energy consumption, and productivity. However, these performance measures often conflict with each other. Therefore, parameter selection cannot be treated as a single-objective optimization problem [1].

Traditional optimization approaches typically focus on a single objective function, which cannot adequately handle the multivariate and complex nature of machining processes. As a result, increasing attention is being paid to Multi-Criteria Decision Making (MCDM) methods, which enable the simultaneous consideration of multiple conflicting criteria [2].

In machining applications, performance evaluation often requires the joint

consideration of quality, economy, and process stability. Such problems can be addressed using MCDM methods, which provide a structured and mathematically based ranking of alternatives by evaluating multiple criteria simultaneously [3]. MCDM approaches typically rely on a decision matrix, followed by normalization, weighting, and aggregation steps. Several methods have been developed, including AHP, ELECTRE, VIKOR, and TOPSIS, all aiming to compare alternatives across multiple, often conflicting criteria [4].

TOPSIS (Technique for Order Preference by Similarity to Ideal Solution) was introduced by Hwang and Yoon as a multi-attribute decision-making method based on the principle that the optimal alternative has the shortest distance from the ideal solution and the greatest distance from the anti-ideal solution [5]. The method is particularly suitable for processing engineering and experimental data due to its simple mathematical structure and clear ranking procedure.

The application of TOPSIS has been reported in machining research. Previous studies have investigated the multi-criteria optimization of CNC turning parameters, where surface roughness and material removal rate were evaluated simultaneously [6]. Other studies have combined TOPSIS with statistical and optimization techniques to achieve a more comprehensive evaluation of machining responses [7].

The aim of this study is to develop a multi-criteria framework for assessment of machinability, integrating cutting force and surface quality into a unified performance indicator. The approach enables the interpretation of machinability as a composite, data-driven property. The TOPSIS method is applied to construct a Cutting Ability Index (CAI), supporting the ranking of technological alternatives. The aim of this article is to examine the applicability and sensitivity of the method. The novelty of this study lies in modelling machinability as a unified and interpretable performance measure.

2. Material and methods

The study is based on an end-milling experiment, which varies the cutting parameters, tool geometries and workpiece materials. The test ensures different types of comparisons. The cutting experiments were performed on a Mazak Nexus 410A-II CNC machining centre. During the experiments, long-reach milling tools were used, which represent particularly critical, vibration-sensitive machining conditions in manufacturing technology. The experiments were designed to evaluate different material–tool–parameter combinations under identical machining conditions, considering multiple performance criteria simultaneously.

Four different long-reach milling tool types (F1–F4) were used for the test, which differed in the number of teeth, edge geometry and tool rake angle. Figure 1 shows the main tool characteristics. Every tool contains partially polished blade for cutting corner reinforcement. The F1 and F3 tools have special protective chamfer, which allows higher feed; and they have variable helix angle, which ensures higher

material removal rate and tool life by minimizing the vibration and oscillation. The F3 and F4 tools contain special edge conditioning, which increases the edge stability and tool life. The F2, F3 and F4 tools contain chip breakers, which are advantageous for large depth of cut. Finally the F2 tool has variable tool pitch to reduce vibration and noise, and ensures better surface quality; further, the increased core diameter improves the tool rigidity.

		z	D	R	λ	γ							
F1	P46210 450	4	10	0.2	43	6	X	X		X			
F2	P45280 450	4	10	0.2	43	3	X				X	X	X
F3	P8315 450	5	10	0.2	45	10	X	X	X	X		X	
F4	P8311 450	7	10	0.2	55	10	X		X			X	

Figure 1 - Applied tools and their properties.

The tests were carried out on three alloyed tool steel grades: 1.2842 (90MnCrV8), 1.2379 (X153CrMoV12), and ES Aktuell 1200. Their tensile strength (R_m) and chemical compositions are summarized in Table 1.

Table 1. - Chemical composition and mechanical properties of the investigated materials.

Material	**R_m [MPa]**	**C%**	**Cr%**	**Mn%**	**Mo%**	**Ni%**	**Si%**	**V%**
1.2842	1050	0.90	0.35	2.00	-	-	0.25	0.10
1.2379	1000	1.55	11.30	0.30	0.75	-	0.30	0.75
ES1200	1200	0.26	1.25	-	0.50	1.05	0.10	0.10

The materials differ significantly in carbon and alloying element content, resulting in distinct mechanical and machining properties. Steel 1.2842 provides a balanced combination of hardness and machinability. In contrast, 1.2379, with its high carbon and chromium content, exhibits high hardness and wear resistance but reduced machinability. The ES Aktuell 1200 is a non-standard grade. It has a lower carbon content and a more complex alloying system, leading to improved toughness and different cutting characteristics, particularly under dynamic loading conditions.

The cutting speed was constant (v_c = 50 m/min, n = 1590 1/min) throughout the entire series of experiments, in order to ensure that the effects examined were primarily due to changes in the feed parameters, tool geometry and material properties. The feed per tooth (f_z) was varied at four levels: 0.03; 0.05; 0.07 and 0.09 mm. The axial depth of cut was fixed at a_p = 35 mm throughout the entire series of experiments, while the radial depth of cut was fixed at a_e = 0.2 mm. Table 2 shows

the cutting parameters. The feed rate (v_f) is determined by feed per tooth (f_z), spindle speed (n) and number of teeth (z). The feed rates (v_f) for the different tool and feed combinations were determined based on the number of teeth and the feed per tooth. These values are detailed in Table 2.

Based on the cutting parameters the material removal rate (MRR, mm³/min) was calculated, as the indicator of the productivity.

$$MRR = V_f \cdot a_e \cdot a_p \quad (1)$$

Table 2. - Cutting parameters.

Tool	f_z **[mm/tooth]**	v_f **[mm/min]**	v_c **[m/min]**
F1	0.03	190.8	50
	0.05	318.0	
	0.07	445.2	
	0.09	572.4	
F2	0.03	190.8	
	0.05	318.0	
	0.07	445.2	
	0.09	572.4	
F3	0.03	238.5	
	0.05	397.5	
	0.07	556.5	
	0.09	715.5	
F4	0.03	333.9	
	0.05	556.5	
	0.07	779.1	
	0.09	1001.7	

The cutting performance was characterised by cutting force components and surface roughness parameters. The cutting force components were measured by a Kistler 9257B piezoelectric dynamometer during the cutting process. The measuring system recorded the three orthogonal cutting force components, namely the axial force (F_z), the feed force (F_f) and the passive force (F_p). The force data were evaluated using the Kistler DynoWare software, which enabled the processing of time-dependent force signals and the determination of statistical characteristics.

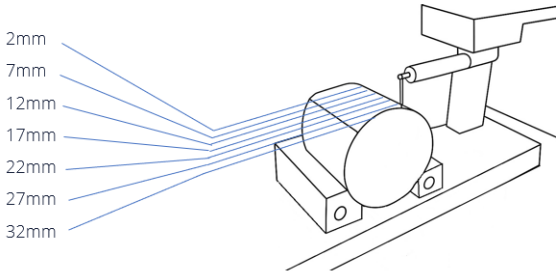

Figure 2 - Surface roughness measurement.

To characterize the quality of the machined surfaces, surface roughness measurements were performed by a Mahr-Perthen GD120 roughness measuring device. For each parameter setting, the roughness parameters were measured at seven different positions on the machined surface (Figure 2). During the roughness evaluation, the parameters R_a, R_z and R_{Sm} were examined, and the mean value and the standard deviation were calculated in each case.

The cutting force components, surface roughness characteristics and material removal rate together formed an extensive database, which served as the basis for the subsequent multi-criteria decision support analysis. Using the collected data, the different material-tool-technology alternatives were objectively compared and ranked using the TOPSIS method.

3. Multi-criteria decision and the TOPSIS method

The TOPSIS (Technique for Order Preference by Similarity to Ideal Solution) method used in this research is one of the best-known and most widely used MCDM methods. The basic idea of the method is that the optimal alternative is the one that is as close as possible to the ideal solution, while being the farthest from the anti-ideal solution. The ideal solution is a theoretical reference state that contains the most favourable values for each criterion, while the anti-ideal solution consists of the most unfavourable values [8].

The first step in applying the TOPSIS method is to establish a decision matrix that contains the criterion values for the alternatives:

$$X = \begin{bmatrix} x_{11} & x_{12} & \dots & x_{1n} \\ x_{21} & x_{22} & \dots & x_{2n} \\ . & . & . & . \\ . & . & . & . \\ x_{m1} & x_{m2} & \dots & x_{mn} \end{bmatrix} \quad (2)$$

Due to the different units of measurement, the elements of the decision matrix cannot be directly compared, so normalization is necessary. The most common method used in TOPSIS is vector normalization, which can be described by the following equation:

$$r_{ij} = \frac{x_{ij}}{\sqrt{\sum_{i-1}^{m} x_{ij}^2}} \quad (3)$$

The elements of the normalized decision matrix were then multiplied by weight factors expressing the relative importance of the criteria, resulting in the weighted normalized decision matrix. In the present study, all criteria in the decision matrix were assigned the same weight values, i. e. each characteristic contributed equally to the evaluation of the alternatives. This approach was used to avoid prior preference for a single cutting characteristic and to ensure a balanced consideration of cutting force and surface quality parameters. The weighting thus created does not result in an absolute machinability index, but expresses a compromise performance interpreted based on the criteria involved.

Based on these, the so-called ideal and anti-ideal solutions can be determined. The ideal solution represents a theoretical reference state that contains the most favourable values possible for the criteria under study, while the anti-ideal solution is built up of the most unfavourable values. Based on the nature of the criteria, the ideal solution is determined by selecting the maximum values for benefit-type criteria, while the minimum values for cost-type criteria; the anti-ideal solution accordingly contains the opposite extreme values.

Subsequently, the distance from the ideal and anti-ideal solutions is determined for each alternative examined. These distances express the extent to which the given alternative approaches the optimal state and how far it is from the most unfavourable solution. This step of the method allows for an objective comparison of alternatives in the multidimensional criterion space and establishes the basis for the subsequent ranking, which takes into account the proximity to the good solution and the distance from the bad solution together (Figure 3).

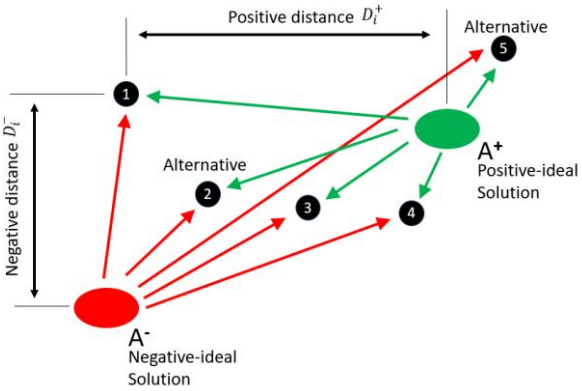

Figure 3 - Interpretation of the distance measured from each alternative in the TOPSIS system.

During the ranking, the evaluation of each alternative is done by taking into account the distances measured from the ideal and anti-ideal solutions together. To quantify this, the TOPSIS method uses the relative proximity coefficient, which expresses how close the given alternative is to the ideal solution compared to the most unfavorable state. The basis for the final ranking is the relative proximity coefficient:

$$c_i = \frac{D_i^-}{D_i^+ + D_i^-} \tag{4}$$

The value of C_i ranges between 0 and 1; the higher its value, the more favorable the given alternative is, since it is closer to the ideal solution and further away from the anti-ideal state. The advantage of the TOPSIS method is that it has a simple and understandable mathematical structure, provides a complete ranking of alternatives, and can be effectively applied to multi-criteria evaluation of engineering experimental data, especially when the examined criteria can be measured numerically [5][9].

4. Results and Discussion

Because of the interdependence of the evaluated parameters, the results and their interpretation are presented together in this section.

Table 3 summarises the type of parameters used in the TOPSIS analysis and their roles. The selected variables represent the key aspects of machining performance, including cutting forces, surface quality, and productivity. Only the most representative parameters were considered in order to ensure a balanced and transparent evaluation while avoiding redundancy in the dataset.

Table 3. - Criteria used in the TOPSIS analysis

Parameter	Description	Role in analysis	Type
F_i	Radial cutting force	Load	Cost
R_i	Surface roughness	Surface quality	Cost
MRR	Material removal rate	Productivity	Benefit

Cutting force and surface roughness parameters were treated as cost-type criteria (lower values are preferable), while material removal rate was considered a benefit-type criterion. During the analyses the following parameters were considered: F_{f_mean}, F_{f_max}, F_{p_mean}, F_{p_max}, F_{z_mean}, F_{z_max}, R_{a_mean}, R_{a_SD}, R_{z_mean}, R_{z_SD}, R_{Sm}/f_z, R_{Sm_SD} and *MRR* (SD means standard deviation).

The presentation of all data is not possible because of the amount and variation of measured parameters, but some examples are presented in order to demonstrate the problem of the assessment. Figure 4 shows the measured surface roughness (R_a) and axial cutting force (F_z) data as a function of material grade. The mean value of R_a is the smallest in case of ES1200, but the mean of F_z is the largest.

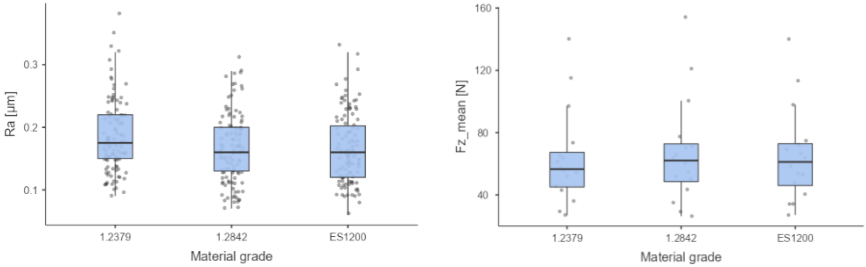

Figure 4. Distribution of surface roughness (R_a) and axial cutting force (F_z) values for different material grades.

Figure 5 shows the measured surface roughness (R_a) and axial cutting force (F_z) values as a function of cutting tool. The results indicate that the applied tool geometry has a noticeable influence on both surface quality and cutting forces. Tool F2 performs the highest R_a values and the greatest variation, while tool F4 results in lower R_a values with reduced variability. In contrast, the axial cutting force shows an increasing trend from F1 to F4, with tool F4 producing the highest force levels, because of the 7 teeth.

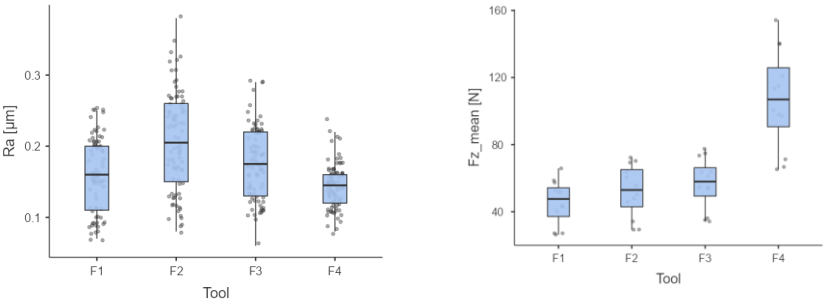

Figure 5. Distribution of surface roughness (R_a) and axial cutting force (F_z) values for different cutting tools.

Figure 6 presents box plots of the average passive cutting force (F_{p_mean}) values as a function of both material grade and cutting tool. The results indicate that ES1200 exhibits the highest average passive force, while materials 1.2379 and 1.2842 show lower and comparable values. A clear increasing trend can also be observed across the cutting tools, with tool F4 producing the highest and tool F1 the lowest force levels, while tools F2 and F3 form an intermediate group.

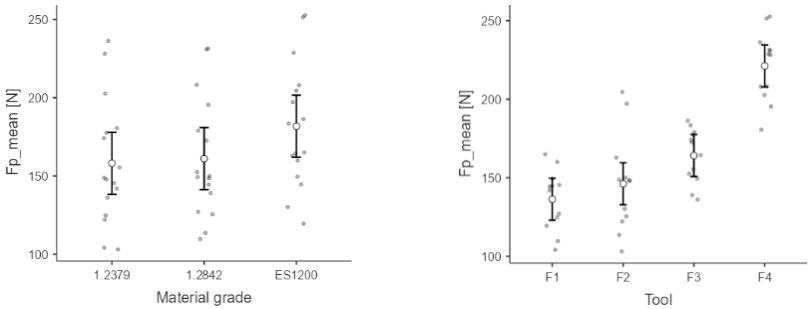

Figure 6 - Average passive cutting force (F_{p_mean}) values for different material grades and cutting tools.

The elevated force levels observed for tool F4 may be attributed to its higher number of cutting edges (z = 7). Under identical feed conditions, a larger number of teeth are engaged simultaneously in the cutting process, which can increase the contact area and, consequently, the passive cutting force. In addition, reduced flute space may hinder chip evacuation, further contributing to higher force levels.

The difference between tools F1 and F2, despite having the same number of teeth, may be related to their different rake angles. Tool F1, with a higher rake angle ($\gamma = 6°$), promotes more favourable chip formation, resulting in lower cutting forces, whereas the lower rake angle of tool F2 ($\gamma = 3°$) may increase cutting resistance.

Figure 7 shows the material removal rate (*MRR*) values as a function of cutting tool. The results indicate a clear increasing trend from tool F1 to F4, with tool F4 achieving the highest *MRR* values, while tool F1 presents the lowest productivity. This trend is directly related to the number of cutting edges, as a higher tooth count increases the feed rate under identical feed per tooth conditions, resulting in a higher material removal rate.

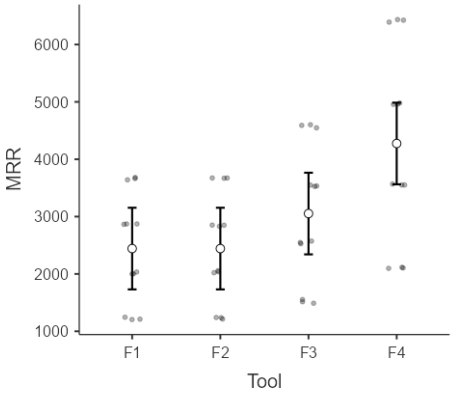

Figure 7. Material removal rate (*MRR*) values for different cutting tools

The larger deviation observed for tool F4 may be attributed to the wider range of applicable cutting conditions, as well as increased sensitivity to process parameters such as feed rate. In addition, the higher number of engaged cutting edges may lead to more complex chip formation and evacuation conditions, which can contribute to increased variability in the calculated *MRR* values.

The presented particular parameters cannot be used to evaluate the performance of the cutting tools, or machinability of the materials. Therefore, an overall assessment is required. Now the application of the TOPSIS method is presented.

The TOPSIS method enables the reduction of a large set of measured data into a single performance indicator, allowing the ranking of materials, tools, and process parameters. In this study, a Cutting Ability Index (CAI) was introduced to quantify machinability by integrating multiple performance criteria into a unified metric.

Figure 8 presents the TOPSIS-based ranking of the investigated materials and cutting tools expressed by the CAI values. Among the materials, 1.2379 achieved the highest relative proximity coefficient (Ci = 0.75), followed by 1.2842 (Ci = 0.48), while ES1200 exhibited the lowest value (Ci = 0.31). According to the CAI, material 1.2379 shows the most favourable overall machinability under the investigated conditions. This result is somewhat unexpected, considering that its higher alloying

content and mechanical strength are generally associated with less favourable machinability. However, the CAI reflects the combined effect of cutting forces, surface quality, and productivity, indicating a more balanced overall performance.

Figure 8. TOPSIS-based ranking of the investigated materials and cutting tools expressed by the Cutting Ability Index (CAI).

For the cutting tools, tool F1 achieved the highest ranking (Ci = 0.70), followed by F3 (Ci = 0.55) and F2 (Ci = 0.52), while tool F4 exhibited the lowest value (Ci = 0.45). This result highlights that the best overall performance is not determined by a single parameter, but by the balance between competing criteria. Although certain tools may provide advantages in specific aspects, the CAI identifies tool F1 as the most favourable option due to its balanced machining performance.

Figure 9 presents the TOPSIS-based ranking of the investigated cutting tools for each material separately. The results show that tool F1 consistently achieves the highest CAI values across all materials, while tool F4 generally exhibits the lowest performance.

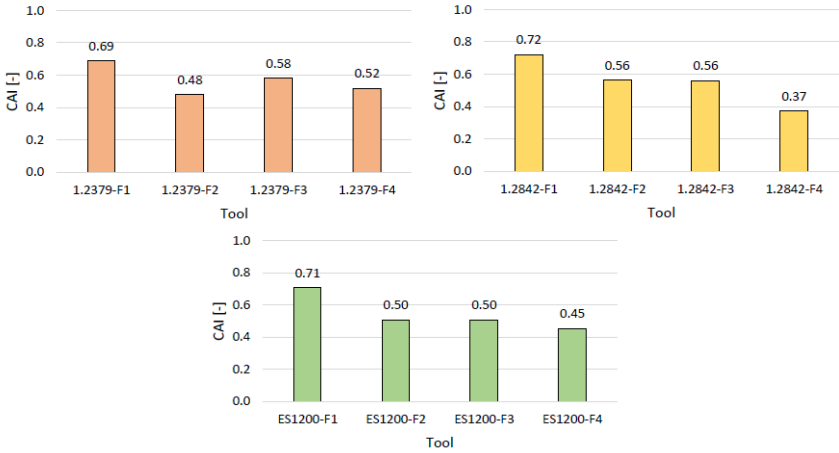

Figure 9. TOPSIS-based ranking of cutting tools for each material using the Cutting Ability Index (CAI).

These results highlight that the performance of cutting tools is strongly dependent on the material–tool combination, and that different evaluation perspectives can reveal additional relationships within the dataset. While global rankings provide an overall comparison, the material-specific analysis allows a more detailed interpretation of machining performance.

Figure 10 presents the TOPSIS-based ranking of the investigated materials for each cutting tool. The results indicate that the relative performance of the materials varies depending on the applied tool, confirming that machinability cannot be described independently of the tool geometry. While material 1.2842 achieves the highest CAI values for tools F1, F2, and F3, tool F4 shows a different trend, where ES1200 exhibits the most favourable performance.

This variation highlights the interaction between tool geometry and material properties, suggesting that the optimal material–tool combination depends on the specific cutting conditions. The results further demonstrate that the proposed CAI-based approach enables multi-perspective evaluation, providing deeper insight into machining behaviour beyond conventional single-factor analyses.

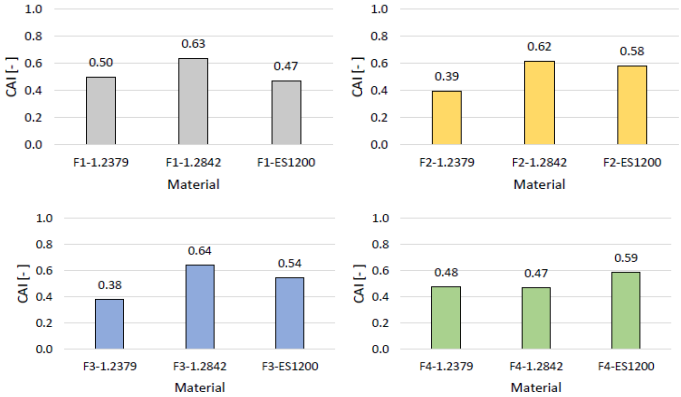

Figure 10. TOPSIS-based ranking of materials for each cutting tool using the Cutting Ability Index (CAI).

5. Summary

This study presented a multi-criteria evaluation for machinability based on cutting force, surface quality, and productivity characteristics, using the TOPSIS method. The proposed approach integrates multiple, often conflicting performance

indicators into a single comparative index, defined as the Cutting Ability Index (CAI), enabling the ranking of materials and cutting tools under identical machining conditions.

The results confirmed that machinability strongly depends on the material–tool combination. However, the obtained rankings revealed several inconsistencies with expected physical behaviour. Material 1.2379 achieved the highest CAI value despite its unfavourable composition and mechanical properties, while tool F4, although providing the highest material removal rate, exhibited one of the lowest overall rankings. These findings clearly demonstrate that the results are highly sensitive to the selection and interaction of input parameters.

This observation highlights a fundamental limitation of the TOPSIS-based approach: the resulting ranking does not necessarily represent the actual machinability behaviour. Favourable values in certain criteria (e.g., cutting force or surface quality) may not compensate for disadvantages in others (e.g., productivity), which may lead to misleading conclusions. The inconsistencies observed do not indicate limitations of the TOPSIS method itself, but rather reflect the sensitivity of multi-criteria evaluation to the definition of input parameters.

Therefore, the appropriate selection, weighting and number of input parameters are critical for obtaining reliable results. The selected parameter set in this study does not fully capture the complexity of the machining process. Additional factors such as tool wear, vibration, temperature, or energy consumption may also significantly influence machinability and should be considered in future studies. Furthermore, the applied cutting conditions, particularly the cutting speed, may alter the relative performance of the tools, indicating that different parameter ranges could lead to different rankings.

The proposed CAI represents a step toward a data-driven and quantitative characterization of machinability as a measurable and comparable property. However, its effectiveness strongly depends on the appropriate definition of the evaluation model; therefore, it should be interpreted as part of a broader analytical framework rather than as a standalone indicator.

Overall, the study demonstrates that while TOPSIS provides an effective framework for integrating multiple machinability-related criteria into a single performance index, the validity of the resulting rankings critically depends on careful model definition. When appropriately applied, the method can support advanced, data-driven approaches for machining process evaluation and optimization.

References: 1. *Debnath, S., Reddy, M. M., & Yi, Q. S.* (2016). Influence of cutting parameters on surface roughness and tool wear in turning process. Materials Today: Proceedings, 3(6):1810–1819. https://doi.org/10.1016/j.matpr.2016.04. **2.** *Chakraborty, S., & Zavadskas, E. K.* (2014). Applications of WASPAS method in manufacturing decision making. Informatica, 25(1):1–20. https://doi.org/10.15388/Informatica.2014. **3.** *Bhardwaj, V., Gaur, M. K., Chaturvedi, V., & Agrawal, S.*

(2018). Optimization of machining parameters for Nylon-6 composite in CNC turning using PCA-based TOPSIS. International Journal of Manufacturing and Materials Processing. PDF: https://scispace.com/pdf/optimization-of-machining-parameters-for-nylon-6-composite-bvrc9tzr12.pdf **4.** *Doumpos, M., & Zopounidis, C.* (2002). Multicriteria decision aid classification methods. Kluwer Academic Publishers, New York. **5.** *Chakraborty, S., & Chakraborty, S.* (2022). A scoping review on the applications of MCDM techniques for parametric optimization of machining processes. Archives of Computational Methods in Engineering, 29: 4165–4186. https://doi.org/10.1007/s11831-022-09731-w **6.** *Hwang, C. L., & Yoon, K.* (1981). Multiple Attribute Decision Making: Methods and Applications. Springer-Verlag, Berlin. https://link.springer.com/book/10.1007/978-3-642-48318-9 **7.** *Reddy, V. V.* (2020). Turning process parameters optimization of AL7075 hybrid MMC's composite using TOPSIS method. Sigma Journal of Engineering and Natural Sciences, 38(4):1905–1914. PDF: https://sigma.yildiz.edu.tr/storage/upload/pdfs/1635421562-en.pdf **8.** *Chen, C. T.* (2000). Extensions of the TOPSIS for group decision-making under fuzzy environment. Fuzzy Sets and Systems, 114(1):1–9. https://doi.org/10.1016/S0165-0114(97)00377-1 **9.** *Opricovic, S., & Tzeng, G. H.* (2004). Compromise solution by MCDM methods: A comparative analysis of VIKOR and TOPSIS. European Journal of Operational Research, 156(2):445–455. https://doi.org/10.1016/S0377-2217(03)00020-1

Бела Месароš, Балаш Міко, Будапешт, Угорщина

ОЦІНКА ОБРОБЛЮВАНОСТІ МАТЕРІАЛУ ВИРОБУ НА ОСНОВІ СИЛИ РІЗАННЯ ТА ХАРАКТЕРИСТИК ЯКОСТІ ПОВЕРХНІ З ВИКОРИСТАННЯМ МЕТОДУ TOPSIS.

Анотація. *Дослідження пропонує багатокритерійну оцінку обробності на основі сил різання, якості поверхні та продуктивних характеристик, отриманих у експериментах з фрезеруванням на верстаті з ЧПУ. Три інструментальні стали (1.2379, 1.2842 та ES Aktuell 1200) та чотири циліндричні фрези збільшеної довжини тестувалися в умовах контрольованої обробки. Експериментальний набір даних, включно з компонентами сили та параметрами шорсткості поверхні, був проаналізований за методом TOPSIS (Technique for Order Preference by Similarity to Ideal Solution) для інтеграції кількох показників ефективності в одну метрику, відому як Індекс Cutting Ability (CAI). Результати показують, що запропонований підхід дозволяє ранжувати комбінації матеріалів і інструментів і забезпечує більш комплексне тлумачення обробності порівняно з однопараметричними оцінками. Однак отримані рейтинги чутливі до вибору та балансу критеріїв вхідних даних і в певних випадках відхиляються від очікуваної фізичної поведінки. Тому відповідний вибір, зважування та кількість вхідних параметрів є критично важливими для отримання надійних результатів. Вибраний набір параметрів у цьому дослідженні не повністю відображає складність процесу обробки. Додаткові фактори, такі як знос інструменту, вібрації, температура або енергоспоживання, також можуть суттєво впливати на оброблюваність і слід враховувати в майбутніх дослідженнях. Крім того, прикладені умови різання, особливо швидкість різання, можуть впливати на відносну продуктивність інструментів, що свідчить про те, що різні діапазони параметрів можуть призводити до різних рівнів. Це підкреслює обмеження рівноважних багатокритерійних підходів і підкреслює важливість відповідного вибору та зважування параметрів. Дослідження підтверджує, що хоча TOPSIS може слугувати ефективним інструментом підтримки прийняття рішень у аналізі машинної обробки, його застосування потребує ретельного методологічного розгляду.*

Ключові слова: *оброблюваність; фрезерування з ЧПУ; TOPSIS; багатокритеріальне прийняття рішень; поверхнева шорсткість.*

UDC 621.924.9 **doi: 10.20998/2078-7405.2026.104.10**

INVESTIGATION OF ENERGY INPUT AND MACHINING EFFICIENCY AT ABRASIVE WATER JET CUTTING

Zsolt **Maros** [0000-0001-5029-3559], Krisztina **Kun-Bodnár** [0000-0003-1904-4479]

University of Miskolc, 3515, Miskolc - Egyetemváros, Hungary
zsolt.maros@uni-miskolc.hu

Received: 08 April 2026 / Revised:12 April 2026 / Accepted: 26 April 2026 / Published: 15 May 2026

Abstract. *Abrasive waterjet machining is a widely used technology for cutting metal, ceramic and polymer sheets. Nowadays, it is becoming important that the applied technological parameters are efficient and economical. This requires the appropriate selection of the most important technological parameters. In this paper, we report on research in which the combined effect of technological parameters, i.e. the relationship between the input energy and the efficiency, was examined when machining three material qualities (metal, ceramic, polymer). The article examines the relationship between the depth of kerf and the amount of energy input by the jet and formulates conclusions regarding the machinability of different materials.*
Keywords: *abrasive waterjet machining; technological parameters; cutting energy; input energy.*

1. Introduction

The efficiency of abrasive waterjet cutting is most often characterized by researchers [1] with the so-called kerfing depth. When making kerfs, the material is not cut across its entire cross-section, but a certain depth of kerf is made in the material. This type of investigation is referred to as a kerfing test. The depth of kerf depends on the set technological parameters and other conditions of waterjet cutting. The interpretation and measurement of the depth of kerf is illustrated in Figure 1. Abrasive waterjet cutting can machine a wide range of materials, including difficult-to-cut metals like ceramics and polymers. The literature extensively studies the depth of kerf achievable as a function of process parameters [2,3,4]. The depth of kerf of abrasive waterjet cutting is influenced by various parameters, such as water pressure, abrasive flow rate, feed speed, nozzle height, and nozzle geometry [5,6,7]. Researchers primarily investigate the efficiency and accuracy of cutting in relation to these parameters when machining different materials [8,9,10,11].

The effect of the energy input by the jet on the cutting efficiency has been studied by few researchers, mostly through theoretical studies [12]. The aim of this

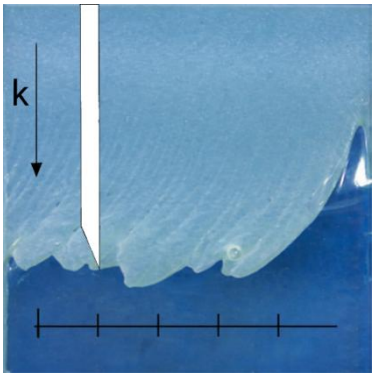

Figure 1 – Interpretation and measurement of kerf depth

research is to determine how the amount of energy input by the jet into the material during abrasive waterjet cutting affects the depth of kerf, i.e. the efficiency, when cutting different materials.

2. Theoretical energy of the jet

The combined effect of the technological parameters can be examined by determining the theoretical energy of the beam during the various parameter settings. For this, we need to write down the theoretical kinetic energy represented by the beam and introduced into a given point on the entry side of the workpiece, which can be determined in the simplest way as follows:

$$E_m = \frac{m_a \cdot v^2}{2} \tag{1}$$

where m_a: mass of abrasive added to the during the contact time, kg
v: velocity of the flowing particles, m/s

The actual energy of the beam is of course not exactly this value, because it is influenced by a lot of factors - the beam does not consist only of abrasive particles, the speed and size of the particles are not the same, etc. - but this value is proportional to the real energy of the beam.

According to the simplified Bernoulli equation, the velocity of the water flowing out of the nozzle is:

$$v = \sqrt{\frac{2p}{\rho}} \tag{2}$$

where p: applied pressure, Pa
ρ: density of the water (1000 kg/m3)

Mass of the abrasive powder:

$$m_a = \dot{m} \cdot t_a \quad (3)$$

where $\dot{m}$: extent of abrasive flow rate, kg/s
t_a: the time of impact, s (the time the jet is in contact with a given point)

Considering that the exposure time:

$$t_a = \frac{d_m}{v_f} \quad (4)$$

where d_m: diameter of the abrasive nozzle, m
v_f: feed speed of the cutting head, m/s

Combining equations (1)-(4) yields that

$$E_m = \frac{\dot{m} \cdot d_m \cdot p}{\rho \cdot v_f} \quad (5)$$

Using equation (5), we determined the theoretical energy of the abrasive water jet for each technological parameter setting during the experiments.

3. Experimental conditions

3.1 Machined materials

Our tests were conducted on materials with significantly different properties:
- White marble (Carrara marble).
- General purpose structural steel S235JR.
- PVC (polyvinyl chloride).

White marble is a chemically metamorphosed rock from sedimentary limestone. Pure marble contains more than 95% calcite. Its structure is dense and granular. The typical compressive strength of white marble is 90–150 MPa, its modulus of

elasticity is 50–70 GPa, and its hardness on the Mohs scale is 3.5, which corresponds to a hardness of approximately 229 HV. A 50 mm thick piece of white marble was used for the experiment.

S235JR general purpose unalloyed structural steel is an unalloyed structural steel with excellent weldability, machinability and cold forming properties. Its chemical composition is shown in Table 1.

Table 1 –Chemical composition of unalloyed structural steel S235JR

Material	**C, %**	**Si, %**	**Mn, %**	**P, %**	**S, %**	**Cu, %**	**N, %**
S235JR	0.17–0.2	≤ 0.3	≤ 1.4	≤ 0,045	≤ 0,045	≤ 0,4	≤ 0,012

The typical tensile strength of S235JR steel is R_m=340–510 MPa, yield strength R_{eh}=225–235 MPa, and specific elongation at break is 21–26%. The test piece was a 40 mm thick rolled plate.

PVC (polyvinyl chloride) is a thermoplastic, flammable, chemically resistant, hard, amorphous plastic. It is the third most mass-produced synthetic polymer. The typical tensile strength of soft PVC is 15 MPa, the density is 1.2 g/cm3, and the melting point is 140 °C. The workpiece used was 40 mm thick PVC.

3.2 Technological parameters

Among the technological parameters influencing the efficiency, the effect of the feed speed (v_f), the pressure (p) and the abrasive flow (m_a) – the mass of abrasive powder added to the water jet per unit time – was investigated. The values of these parameters were changed within predetermined ranges based on the conducted preliminary experiments. The other parameters, such as the type of abrasive material, the height of the nozzle, the diameter of the abrasive and primary nozzles, were kept unchanged throughout. The values of the changed technological data (Table 2) were determined based on literature and empirical data [13].

Table 2 – S235JR Technological parameters changed during the cutting experiments

White marble	
Water pressure, p [bar]	**1380 – 2500 – 3590**
Feed speed, v_f [mm/min]	**650 – 750 – 850 – 950 - 1050**
Abrasive flow, m_a [g/min]	**320 - 550**
S235JR	
Water pressure, p [bar]	**1380 – 2500 – 3590**

Feed speed, v_f [mm/min]	**100 – 120 – 140 – 160 – 180 – 200**
Abrasive flow, m_a [g/min]	**320 - 550**
PVC	
Water pressure, p [bar]	**1380 – 2500 – 3590**
Feed speed, v_f [mm/min]	**1000 – 1400 – 1800 – 2200 - 2600**
Abrasive flow, m_a [g/min]	**320 - 550**

The diameter of the primary nozzle was 0.41 mm, the diameter of the abrasive nozzle was 1.07 mm, and the height of the nozzle was 2 mm. Garnet #80 abrasive powder was used. In industrial practice, this is the most commonly used abrasive type in abrasive waterjet cutting.

Figure 2 shows the kerfs made in the S235JR structural steel material during the experiments.

Figure 2 – Results of kerf tests on S235JR structural steel

4. Experimental results

After performing the cutting experiments on marble, steel and PVC materials, we measured the cutting depth corresponding to the given parameter combinations and illustrated the change in the cutting depth as a function of the different combinations of the changed parameters. Figure 3 shows the change in the depth of kerf as a function of the feed speed and pressure with two types of applied abrasive flows, on white marble material.

It can be seen from Fig. 3 that increasing the feed speed reduces, and increasing the pressure and abrasive flow increases, the depth of kerf.

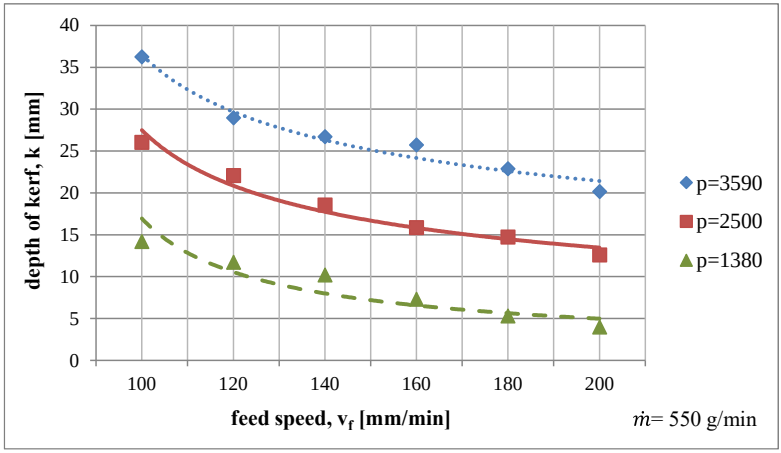

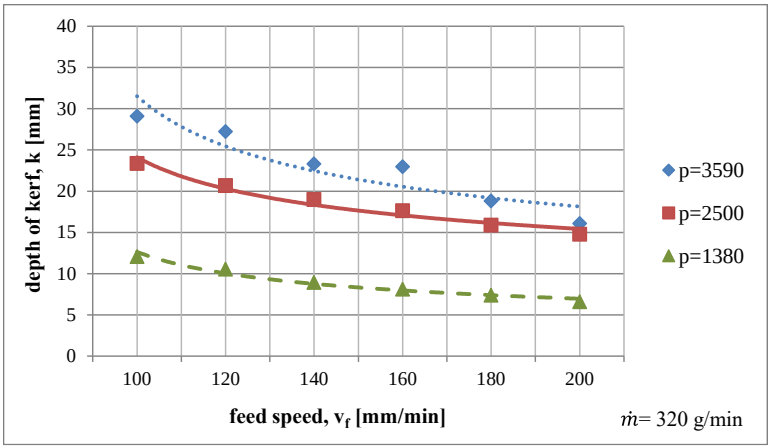

Figure 3 – Variation of depth of kerf as a function of feed speed at different pressures and abrasive flow on S235JR structural steel

Figure 4 illustrates the machinability of the three tested material qualities at a given pressure and abrasive flow.

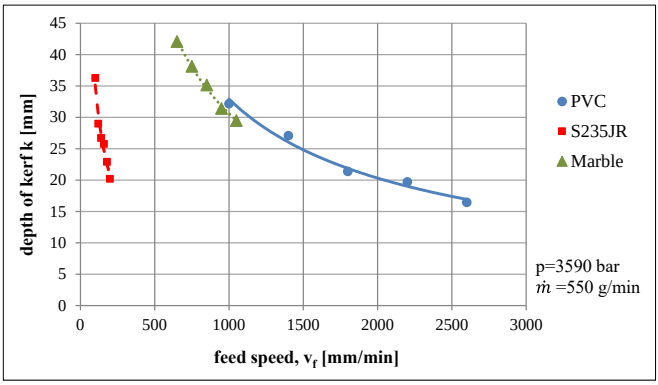

Figure 4 – Effect of feed rate on depth of kerf for different materials

Based on Figure 4, it can be concluded that of the three materials, structural steel is the most difficult to cut and polymer is the easiest. Polymer can be cut at about ten times and marble five times the speed of steel. This can be explained by the appearance of different erosion mechanisms in addition to physical mechanical properties.

However, the combined effect of the technological parameters cannot be read from Figures 3 and 4. The combined effect of the parameters was examined using the input energy. As described in chapter 2, we determined the theoretical input energy for each technological experiment and examined the change in the depth of kerf as a function of this. The change in the depth of kerf as a function of the input energy is shown in Figures 5. and 6. for marble and PVC materials.

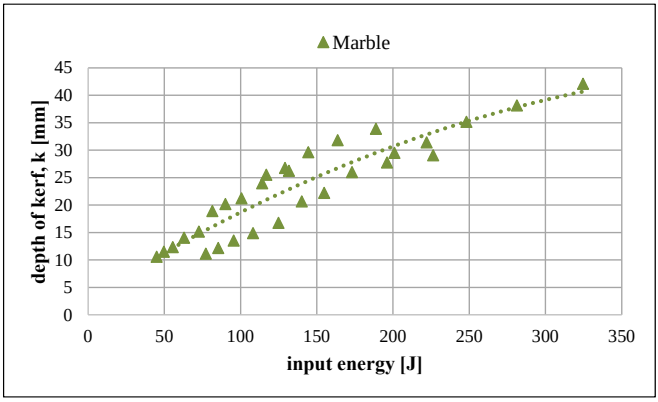

Figure 5 – Variation of the depth of kerf as a function of the input energy on white marble material

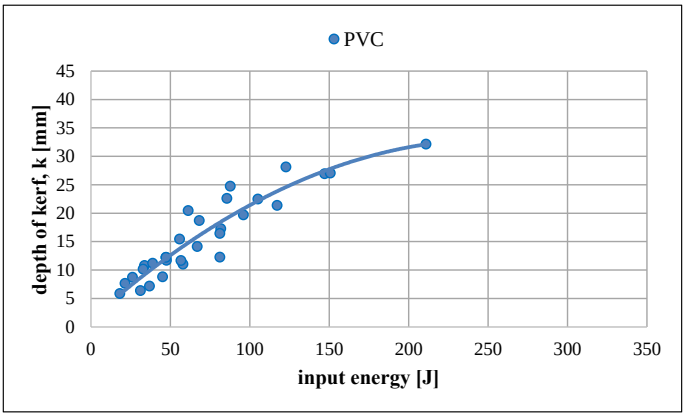

Figure 6 – Variation of the depth of kerf as a function of the input energy on PVC material

It can be seen from Figures 5 and 6 that the energy input clearly increases the depth of kerf, i.e. the efficiency of the cut. The change is not linear, for larger depths, the application of higher energy increases the efficiency of cutting less.

Comparing the Figures 5 and 6 also shows that the machinability of marble and PVC materials is very similar, both can be cut with a low energy input.

Figure 7 shows the change in the depth of kerf of all three materials as a function of the energy input.

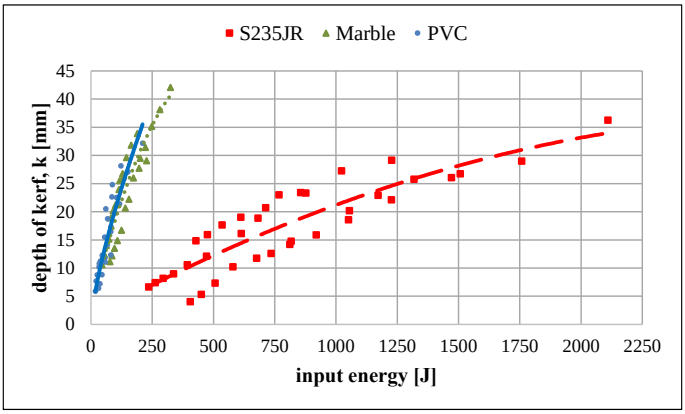

Figure 7 – Variation of cutting depth as a function of energy input on marble, PVC and structural steel materials

Based on Figure 7 it can be said that cutting S235JR structural steel requires the highest energy input of the three materials. The energy required can be up to ten times greater than when cutting PVC or marble. Increasing the energy increases the cutting efficiency for all the three materials.

5. Conclusions

Based on the evaluation of the experimental results, the following conclusions can be drawn regarding the kerf tests of the three types of machined materials:

- Increasing the feed speed reduces the depth of kerf, i.e. the efficiency of the cut, while increasing the pressure and abrasive flow increases it.
- Comparing the machining of different materials, it can be concluded that cutting steel is the least efficient and cutting PVC is the most productive.
- When using low feed speeds, marble - despite its relatively higher hardness - can be cut with a productivity similar to PVC. This can be explained by the so-called brittle erosion that occurs in marble.
- By examining the combined effect of the technological parameters using the theoretical energy input, it can be stated that the depth of kerf clearly increases with increasing cutting energy. This increase is not linear; the slope of the change is smaller for higher energy inputs.
- Cutting structural steel is much more difficult than cutting marble or PVC, requiring up to ten times more energy.

The results obtained show that in abrasive waterjet cutting, the cutting efficiency can be changed by controlling the input energy, which allows us to choose the feed-pressure-abrasive flow combination that provides the energy required to reach a given depth, according to the possibilities. In other words, we can ensure the same cutting efficiency for a given task at different pressures, abrasive flows and feed speeds.

References. **1.** H. *Wang, R. Yuan, X. Zhang, P. Zai, J. Deng.* Research Progress in Abrasive Water Jet Processing Technology. Micromachines, 14(8), 1526, (2023). DOI: 10.3390/mi14081526 **2.** *A. W. Momber, R. Kovacević.* Test-parameter analysis in abrasive water jet cutting of rock-like materials. International Journal of Rock Mechanics and Mining Sciences, 34(1), 17-25, (1997). DOI: 10.1016/S1365-1609(97)80030-5 **3.** *L. M. Hlaváč*: Revised model of abrasive water jet cutting for industrial applications. Materials, 2021, 14(14), 4032. DOI: 10.3390/ma14144032 **4.** *J.M. Llanto, M. Tolouei-Rad, A. Vafadar, M. Aamir.* Impacts of Traverse Speed and Material Thickness on Abrasive Waterjet Contour Cutting of Austenitic Stainless Steel AISI 304L. Applied Sciences, 11(11), 4925. DOI: 10.3390/app11114925 **5.** *M. Llanto, M. Tolouei-Rad, A. Vafadar, M. Aamir.* Recent Progress Trend on Abrasive Waterjet Cutting of Metallic Materials, A Review, Applied Sciences, 2021, 11, 33–44. DOI: 10.3390/app11083344 **6.** *M.C.P. Selvan, R. Vandanapu, V. Chinnasamy.* Abrasive Waterjet Cutting of Stainless Steel - An Experimental Investigation, Advances in Science and Engineering Technology

International Conferences, ASET, 1–5. 2022, DOI: 10.1109/ASET53988.2022.9734923 **7.** *S. Sun, Y. Qian, W. Lu, S. Wu, Y. Kang, A. Tan, D. Li*. Improving the cutting quality of aluminium alloy machined by abrasive waterjet with a relatively low pressure, Journal of the Brazilian Society of Mechanical Sciences and Engineering, 2023, 45 (7)377 p10., DOI: 10.1007/s40430-023-04306-7 **8.** *M.C. Pon Selvan, S.R. Madara, S.S. Sampath, N.S.S. Raj*. Effects of process parameters on depth of cut in Abrasive Waterjet Cutting of phosphate glass, Advances in Science and Engineering Technology International Conferences, 2018 ASET, 1–6., DOI: 10.1109/ICASET.2018.8376868 **9.** *J. Chen, Y. Yuan, H. Gao, T. Zhou*. Analytical modelling of effective depth of cut for ductile materials via abrasive waterjet machining, International Journal of Advanced Manufacturing Technology, 2023, 124 (5–6), 1813–1826., DOI: 10.1007/s00170-022-10538-z **10.** *Y. Yu, T. Sun, Y. Yuan, H. Gao, X. Wang.* Experimental investigation into the effect of abrasive process parameters on the cutting performance for abrasive waterjet technology: a case study, International Journal of Advanced Manufacturing Technology, 2020, 107 (5-6), 2757–2765., DOI: 10.1007/s00170-020-05183-3 **11.** *J. Chen, Y. Yuan, H. Gao, T. Zhou*. Gaussian distribution-based modelling of cutting depth predictions of kerf profiles for ductile materials machined by abrasive waterjet, Materials and Design, 2023, 227, art. no. 111759., DOI: 10.1016/j.matdes.2023.111759 **12**. *Momber, A. W.* An energy balance of high-speed abrasive water jet erosion. Proceedings of the Institution of Mechanical Engineers, Part B: Journal of Engineering Manufacture, 1999, 213(9), 723–731, DOI: 10.1243/1350650991542811 **13.** *Zs. Maros*. Machining of different materials with abrasive waterjet cutting, IOP Conference Series: Materials Science and Engineering, 2018, vol 448 (1) paper 012009, p6, DOI 10.1088/1757-899X/448/1/012009

Жолт Марош, Крістіна Кун-Боднар, Мішкольц, Угорщина

ДОСЛІДЖЕННЯ ВЗАЄМОЗВ'ЯЗКУ ВХІДНОЇ ЕНЕРГІЇ ТА ЕФЕКТИВНОСТІ ОБРОБКИ ПРИ ГІДРОАБРАЗИВНОМУ РІЗАННІ

Анотація. *Абразивна водоструменна обробка — це широко використовувана технологія для різання металевих, керамічних та полімерних листів. Сьогодні стає все більш важливим, щоб застосовувані технологічні параметри були ефективними та економічними. Це вимагає правильного вибору найважливіших технологічних параметрів. У цій статті ми розповідаємо про дослідження, в яких сукупний вплив технологічних параметрів, тобто взаємозв'язок між вхідною енергією та ефективністю, розглядався при обробці трьох матеріалів (метал, кераміка, полімер). На основі оцінки експериментальних результатів були зроблені деякі висновки. Збільшення швидкості подачі зменшує глибину прорізу, тобто ефективність розрізу, а збільшення тиску та абразивного потоку збільшує його. Порівнюючи обробку різних матеріалів, можна зробити висновок, що різання сталі є найменш ефективним, а різання ПВХ — найпродуктивнішим. При низьких швидкостях подачі мармур — незважаючи на відносно вищу твердість — можна різати з продуктивністю, подібною до ПВХ. Це можна пояснити так званою крихкою ерозією, що відбувається в мармурі. Аналізуючи сумарний вплив технологічних параметрів за теоретичними енергетичними вхідними даними, можна стверджувати, що глибина прориву явно зростає зі збільшенням енергії різання. Це збільшення не є лінійним; Нахил зміни менший для вищих енергетичних витрат. Різати конструкційну сталь набагато складніше, ніж різати мармур або ПВХ, і це вимагає до десяти разів більше енергії. Отримані результати показують, що при абразивному водоструменному різанні ефективність різання можна змінити, контролюючи вхідну енергію, що дозволяє обрати комбінацію подачі-тиску-абразивного потоку, яка забезпечує енергію, необхідну для досягнення заданої глибини відповідно до можливостей.*

Ключові слова: *абразивна водоструменна обробка; технологічні параметри; енергія різання; вхідна енергія.*

UDC 621.91.01 **doi: 10.20998/2078-7405.2026.104.11**

COMPARATIVE STUDY OF SURFACE HEIGHT AND GRADIENT PARAMETERS IN TURNING OF 42CRMO4 AND X5CRNI18-10

István **Sztankovics** [0000-0002-1147-7475]

University of Miskolc, 3515 Miskolc-Egyetemváros, Hungary
istvan.sztankovics@uni-miskolc.hu

Received: 10 April 2026/ Revised: 19 April 2026/ Accepted: 29 April 2026 / Published: 15 May 2026

Abstract. *This study presents a comparative investigation of surface topography in turning of two engineering materials, 42CrMo4 alloy steel and X5CrNi18-10 austenitic stainless steel. A full factorial experimental design was applied to evaluate the effects of cutting speed, feed, depth of cut, and material type on selected areal surface roughness parameters. The analysis focused on S_q, S_p, S_v, and S_{dq}, representing surface height and gradient characteristics according to ISO 25178. The results show a strong dependence of surface topography on material properties. The 42CrMo4 steel exhibited significantly higher roughness and steeper surface features compared to the stainless steel under identical cutting conditions. Increasing cutting speed led to a consistent reduction in all evaluated parameters, while feed rate primarily influenced the amplitude-related characteristics. The S_{dq} parameter showed lower sensitivity to cutting conditions but highlighted clear differences in surface slopes between the materials. The findings demonstrate that the combined evaluation of height and gradient parameters provides an effective approach for characterizing machining-induced surface features and supports improved selection of cutting conditions.*

Keywords: *tangential turning; surface topography; roughness parameters; material comparison.*

1. Introduction

Surface quality is a critical aspect of machining performance, as it directly influences the functional behaviour, reliability, and service life of mechanical components [1,2]. In turning operations, the generated surface topography is controlled by a complex interaction between cutting parameters, tool geometry, and material properties [3]. While conventional surface characterization has long relied on profile-based parameters, the increasing availability of three-dimensional measurement techniques has led to a growing interest in areal surface roughness evaluation based on ISO 25178. These parameters provide a more comprehensive description of surface features, enabling improved interpretation of machining-induced surface characteristics.

Among the various groups of areal parameters, height-related metrics such as S_q, S_p, and S_v are widely used to quantify the amplitude of surface irregularities [4]. S_q represents the overall magnitude of surface deviations, while S_p and S_v describe

the extreme peak and valley features, respectively. In addition to amplitude, the functional performance of a surface is also influenced by its local slopes and gradients [5,6]. The S_{dq} parameter, defined as the root mean square gradient, provides insight into the steepness of surface features and complements the information obtained from height parameters. The combined evaluation of these parameters enables a more complete understanding of surface formation mechanisms during machining.

The generation of surface topography in turning is strongly affected by technological parameters such as cutting speed, feed, and depth of cut. Feed rate is typically considered the dominant factor influencing surface roughness, as it directly determines the theoretical surface profile [7,8]. Cutting speed can modify the cutting process through thermal and tribological effects, often leading to improved surface finish at higher values [9]. Depth of cut, although generally less influential than feed, can affect process stability and material deformation behaviour [10]. However, the extent to which these parameters influence areal surface characteristics may vary depending on the material being machined.

Material properties play a particularly important role in surface generation. Differences in hardness, ductility, strain hardening behaviour, and thermal conductivity can lead to distinct chip formation mechanisms and tool-workpiece interactions [11-13]. For example, high-strength alloy steels typically exhibit more stable cutting behaviour but may generate pronounced surface irregularities due to their resistance to plastic deformation [14,15]. In contrast, austenitic stainless steels are characterized by high ductility and significant strain hardening, which can result in smoother surfaces but may also introduce phenomena such as material smearing or adhesion.

Despite the numerous research on machining-induced surface roughness, comparative studies focusing on the combined analysis of amplitude and gradient parameters for different materials under identical cutting conditions remain limited. There is a need for systematic investigations that evaluate how material-dependent behaviour influences not only the magnitude but also the morphology of surface features [16]. Such studies are essential for improving the understanding of surface generation mechanisms and for supporting the selection of appropriate machining parameters in industrial applications.

In this context, the present study aims to perform a comparative analysis of surface height and gradient parameters in turning of two widely used engineering materials: 42CrMo4 alloy steel and X5CrNi18-10 austenitic stainless steel. These materials were selected due to their distinctly different mechanical and physical properties, which are expected to result in different surface formation characteristics. A full factorial experimental design was applied, considering cutting speed, feed, depth of cut, and material type as input factors. The surface topography was evaluated using selected ISO 25178 parameters, namely S_q, S_p, S_v, and S_{dq}. This

selection enables a focused yet comprehensive characterization of both amplitude and slope-related surface features. The study seeks to identify the dominant factors affecting these parameters and to quantify the differences between the two materials under identical machining conditions.

The results of this work contribute to a better understanding of material-dependent surface generation in tangential turning and provide practical insights for the optimization of cutting conditions when surface quality is of primary importance.

2. Experimental conditions and methods

Machining tests were performed using a CNC turning centre (EMAG VSC 400 DS) under stable operating conditions. A tangential turning approach was applied, where the cutting edge is oriented at an inclination angle relative to the workpiece surface (S117.0032.00 insert mounted in an H117.2530.4132 tool holder). This configuration alters the mechanics of material removal compared to conventional turning processes. Cutting was carried out under dry conditions using an uncoated cemented carbide insert. The tool geometry was kept constant throughout the experiments, and the cutting edge condition was controlled by regularly replacing inserts to avoid the influence of tool wear.

The experimental investigation was carried out on two metallic materials with significantly different mechanical behaviour in machining. The first material was 42CrMo4 alloy steel in quenched and tempered condition, exhibiting a hardness of approximately 410 HV10. The second material was X5CrNi18-10 austenitic stainless steel with a hardness of around 300 HV10. While the alloy steel represents a relatively stable cutting material, the stainless steel is characterized by higher ductility and strain hardening, which can affect chip formation and surface generation.

Surface characterization was conducted using a three-dimensional optical measurement system (AltiSurf 520). For each machined sample, a 4 mm × 4 mm area was analysed in the steady-state region of the cut, excluding entry and exit zones. The acquired topography data were evaluated in accordance with ISO 25178. To maintain a focused analysis, four areal surface parameters were selected:

- S_q - root mean square height, representing the overall surface height variation;
- S_p - maximum peak height, indicating the highest point above the mean plane;
- S_v - maximum pit depth, corresponding to the deepest valley below the mean plane;
- S_{dq} - root mean square gradient, describing the average slope of the surface.

These parameters jointly characterize both amplitude and gradient features of the machined surface.

The experimental plan was based on a full factorial design including cutting speed, feed, depth of cut, and material type. Each numerical factor was examined at two levels: cutting speed of 100 and 200 m/min, feed of 0.3 and 0.6 mm/rev, and depth of cut of 0.1 and 0.2 mm. Together with the two material types, this resulted in 16 distinct machining conditions, which are summarized in Table 1.

Table 1 – Experimental setups

Setup	1	2	3	4	5	6	7	8
v_c [m/min]	100	100	100	100	200	200	200	200
f [mm]	0.3	0.3	0.6	0.6	0.3	0.3	0.6	0.6
a [mm]	0.1	0.2	0.1	0.2	0.1	0.2	0.1	0.2

3. Experimental results

The measured surface topography parameters obtained from the full factorial experiments are summarized in Tables 2 and 3 for X5CrNi18-10 and 42CrMo4, respectively. The results clearly indicate substantial differences in both magnitude and variability of the evaluated parameters (S_q, S_p, S_v, S_{dq}) between the two materials, as well as notable dependencies on the applied cutting conditions.

Table 2 – Experimental results – X5CrNi18-10

Setup	1	2	3	4	5	6	7	8
S_q [µm]	0.50	0.40	0.53	0.61	0.29	0.30	0.49	0.58
S_p [µm]	3.29	5.45	3.97	5.43	3.03	1.81	1.94	2.40
S_v [µm]	3.44	5.81	3.20	5.50	1.59	1.76	1.95	2.50
S_{dq} [–]	0.14	0.16	0.13	0.15	0.16	0.13	0.16	0.13

For X5CrNi18-10, the S_q values range from 0.288 µm to 0.605 µm. The lowest S_q value is observed at the higher cutting speed (200 m/min) combined with low feed (0.3 mm/rev) and low depth of cut (0.1 mm), while the highest S_q occurs at lower cutting speed (100 m/min) and higher feed (0.6 mm/rev) with increased depth of cut. In general, S_q values remain within a relatively narrow band, indicating a stable

surface generation process across the investigated parameter space. The S_p parameter for X5CrNi18-10 varies between 1.805 µm and 5.453 µm. The highest peak values are associated with lower cutting speed and higher depth of cut, whereas increasing cutting speed tends to reduce peak height. A similar tendency is observed for S_v, where values range from 1.594 µm to 5.812 µm. The highest valley depths occur at lower cutting speed and higher depth of cut, while reduced values are observed at higher cutting speeds. The S_{dq} parameter for X5CrNi18-10 shows limited variation, with values between 0.127 and 0.163. No extreme deviations are observed, suggesting relatively uniform surface slopes across all cutting conditions.

Table 3 – Experimental results – 42CrMo4

Setup	1	2	3	4	5	6	7	8
S_q [µm]	2.91	1.90	1.27	3.56	0.58	0.36	0.54	0.51
S_p [µm]	9.39	7.07	8.50	12.31	3.77	3.16	4.18	3.20
S_v [µm]	14.29	8.81	7.00	13.32	4.13	4.23	2.30	2.15
S_{dq} [–]	0.40	0.32	0.25	0.40	0.23	0.21	0.24	0.25

In contrast, significantly higher values are observed for 42CrMo4. The S_q parameter ranges from 0.360 µm to 3.556 µm, with the highest values occurring at lower cutting speed and higher depth of cut. A pronounced reduction in S_q is observed when increasing cutting speed from 100 m/min to 200 m/min. The S_p values for 42CrMo4 range from 3.164 µm to 12.312 µm, while S_v varies between 2.145 µm and 14.29 µm. These values are substantially higher than those measured for X5CrNi18-10, indicating more pronounced peak and valley formation. The highest S_p and S_v values are consistently associated with low cutting speed and high depth of cut. The S_{dq} parameter for 42CrMo4 ranges from 0.209 to 0.404, showing considerably higher values compared to the stainless steel. This indicates steeper surface gradients and more irregular surface features.

Overall, the results demonstrate a strong material dependency of all investigated surface parameters, as well as consistent trends with respect to cutting speed, feed, and depth of cut.

4. Discussion

The experimental results reveal clear and systematic differences in surface topography between X5CrNi18-10 and 42CrMo4, which can be interpreted by considering both the machining parameters and the intrinsic material properties.

As shown in Figure 1, a comparison of S_q values indicates that the surfaces generated on 42CrMo4 exhibit significantly higher roughness levels than those on X5CrNi18-10. At a cutting speed of 100 m/min, S_q values for 42CrMo4 reach up to 3.556 µm, whereas the corresponding maximum for X5CrNi18-10 remains below 0.61 µm. This represents a difference of more than a factor of five. When the cutting speed is increased to 200 m/min, S_q values decrease markedly for both materials, but the relative difference remains substantial. This behaviour may be attributed to the higher hardness and lower ductility of 42CrMo4, which can promote more brittle-like material removal and the formation of irregular surface features. In contrast, the more ductile X5CrNi18-10 likely undergoes greater plastic deformation, leading to smoother surface profiles. Feed rate exhibits a strong influence on S_q for both materials. Increasing the feed from 0.3 mm/rev to 0.6 mm/rev generally leads to higher S_q values. This effect is particularly pronounced for 42CrMo4 at low cutting speed, where S_q increases from approximately 1.265 µm to 3.556 µm. This trend is consistent with the increased uncut chip thickness, which directly affects the resulting surface geometry.

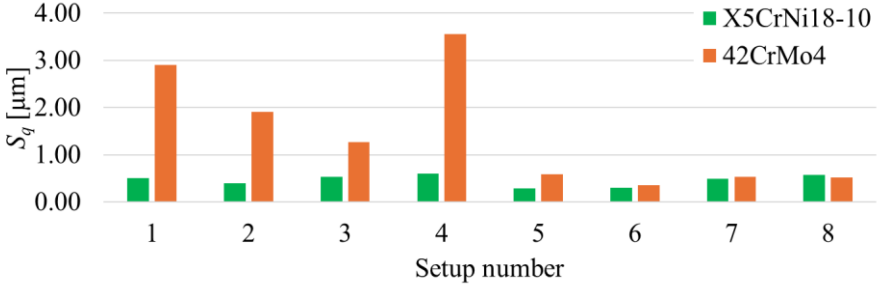

Figure 1 – Alteration of the S_q in the studied range

The analysis of S_p and S_v provides further insight into the asymmetry of surface features (Figure 2 and 3). For X5CrNi18-10, S_p and S_v values are relatively balanced, typically remaining within a similar range. In contrast, 42CrMo4 often exhibits higher S_v values than S_p, particularly at lower cutting speeds, where S_v reaches 14.29 µm compared to S_p of 9.39 µm. This indicates the presence of deeper valleys relative to peak heights. Such behaviour may be related to material fracture and localized material pull-out, which can generate deeper surface defects. For X5CrNi18-10, the more homogeneous deformation behaviour appears to limit the formation of extreme valleys. Cutting speed has a consistently beneficial effect on both S_p and S_v. Increasing the cutting speed from 100 m/min to 200 m/min results in a significant reduction in both peak and valley magnitudes for both materials. For example, in

42CrMo4, S_v decreases from 14.29 µm to approximately 4 µm or lower at higher cutting speed. This suggests improved surface formation stability at elevated speeds.

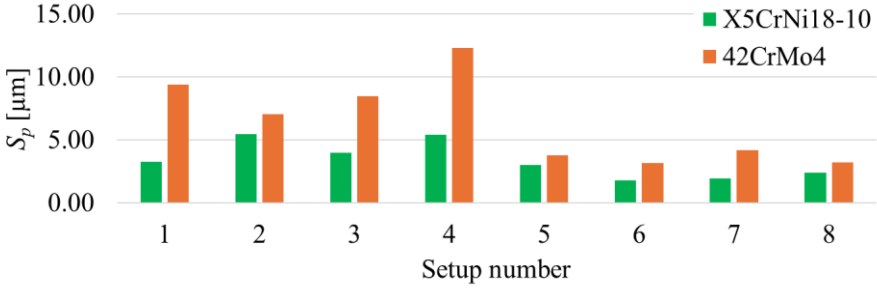

Figure 2 – Alteration of the S_p in the studied range

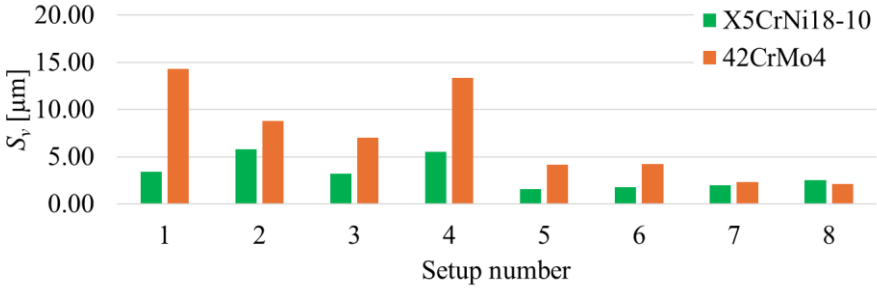

Figure 3 – Alteration of the S_v in the studied range

The S_{dq} parameter provides additional insight into surface slope characteristics (Figure 4). The results show that S_{dq} values for 42CrMo4 are approximately 1.5 to 3 times higher than those for X5CrNi18-10. For instance, maximum S_{dq} values reach 0.404 for 42CrMo4, compared to approximately 0.16 for the stainless steel. This indicates that surfaces produced on 42CrMo4 are not only rougher in terms of amplitude but also exhibit significantly steeper gradients. From a functional perspective, this may have implications for contact behaviour, friction, and wear performance. The influence of cutting parameters on S_{dq} is less pronounced than for S_q, S_p, and S_v, particularly in the case of X5CrNi18-10, where S_{dq} remains within a narrow range across all conditions. However, for 42CrMo4, higher S_{dq} values are observed at lower cutting speeds and higher feeds, indicating that aggressive cutting conditions promote sharper surface features.

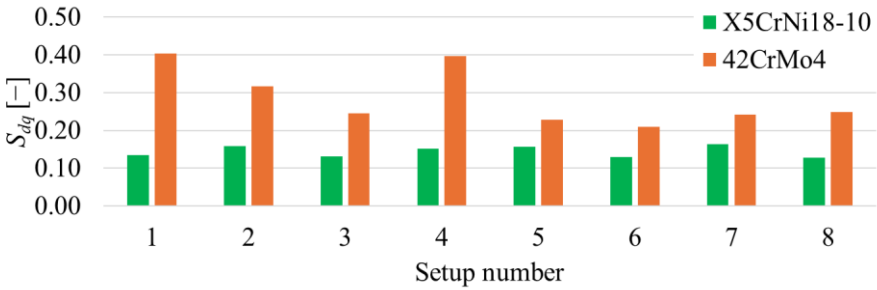

Figure 4 – Alteration of the S_{dq} in the studied range

A combined interpretation of S_q and S_{dq} highlights an important aspect of surface characterization. While S_q describes the overall magnitude of surface deviations, S_{dq} reflects the local steepness of these features. The results show that high S_q values are generally accompanied by high S_{dq} values for 42CrMo4, indicating that rougher surfaces are also steeper. In contrast, X5CrNi18-10 maintains relatively low S_{dq} values even when S_q increases, suggesting smoother transitions between peaks and valleys. From a practical standpoint, the results suggest that cutting speed is the most effective parameter for improving surface quality for both materials. Increasing cutting speed consistently reduces S_q, S_p, and S_v, and also contributes to lower S_{dq} values. Feed rate remains a dominant factor influencing surface amplitude, while depth of cut shows a secondary but still noticeable effect.

Finally, the observed differences between the two materials emphasize the importance of material-specific parameter selection in turning operations. Identical cutting conditions do not yield comparable surface characteristics, and the choice of parameters must consider the underlying material behaviour.

5. Conclusions

This study presented a comparative experimental investigation of surface topography generated during turning of 42CrMo4 and X5CrNi18-10, based on selected ISO 25178 areal parameters (S_q, S_p, S_v, S_{dq}). The applied full factorial design enabled a systematic evaluation of the effects of cutting speed, feed, depth of cut, and material type on both amplitude- and gradient-related surface characteristics. The results clearly demonstrate that both machining parameters and material properties play a decisive role in surface formation. Significant differences were observed not only in the magnitude of the measured parameters, but also in their

sensitivity to changes in cutting conditions. While similar trends were identified for certain parameters, the extent of these effects varied considerably between the two materials. The main findings of the study can be summarized as follows:

1. The material type has a dominant influence on surface topography. The 42CrMo4 alloy steel consistently exhibited higher values of the analysed parameters compared to X5CrNi18-10, indicating rougher and steeper surface profiles. In contrast, the austenitic stainless steel produced smoother and more uniform surfaces under identical cutting conditions.
2. Cutting speed proved to be an influential technological parameter in improving surface quality. Increasing the cutting speed from 100 m/min to 200 m/min resulted in a significant reduction in all evaluated parameters for both materials, particularly in the case of 42CrMo4, where substantial decreases in peak and valley magnitudes were observed.
3. Feed rate primarily affected the amplitude-related parameters (S_q, S_p, S_v), with higher feed values leading to increased surface roughness. The S_{dq} parameter showed lower sensitivity overall, but higher values were associated with more aggressive cutting conditions, especially for 42CrMo4.

In summary, the findings highlight that identical machining conditions can lead to markedly different surface characteristics depending on the workpiece material. The combined evaluation of height and gradient parameters proved to be an effective approach for capturing these differences. The results provide a useful basis for selecting appropriate cutting conditions in practical turning operations where surface quality is a critical requirement.

6. Acknowledgement

Supported by the University Research Scholarship Program of the Ministry for Culture and Innovation from the source of the National Research, Development and Innovation Fund. Contract identifier: TNI/1834-39/2025. Scholarship identifier: EKÖP-25-4-II/35.

References: 1. *Javidi, A., Rieger, U., & Eichlseder, W.* (2008). The effect of machining on the surface integrity and fatigue life. International Journal of Fatigue, 30(10–11), 2050–2055. https://doi.org/10.1016/j.ijfatigue.2008.01.005 **2.** *Lu, C.* (2007). Study on prediction of surface quality in machining process. Journal of Materials Processing Technology, 205(1–3), 439–450. https://doi.org/10.1016/j.jmatprotec.2007.11.270 **3.** *He, C., & Zong, W.* (2019). Influencing factors and theoretical models for the surface topography in diamond Turning Process: a review. Micromachines, 10(5), 288. https://doi.org/10.3390/mi10050288 **4.** *Alar, V., Razumić, A., Runje, B., Stojanović, I., Kurtela, M., & Štrbac, B*. (2025). Application of areal topography parameters in surface characterization. Applied

Sciences, 15(12), 6573. https://doi.org/10.3390/app15126573 **5.** *Pawlus, P., Reizer, R., & Wieczorowski, M.* (2021). Functional importance of surface texture parameters. Materials, 14(18), 5326. https://doi.org/10.3390/ma14185326 **6.** *Jiang, Z., He, P., Zhang, X., Zhang, G., & Liu, F.* (2023). Comprehensive evaluation of surface parameter correlation in running-in wear process. Journal of Physics Conference Series, 2591(1), 012003. https://doi.org/10.1088/1742-6596/2591/1/012003 **7.** *He, C., Zong, W., & Zhang, J.* (2018). Influencing factors and theoretical modeling methods of surface roughness in turning process: State-of-the-art. International Journal of Machine Tools and Manufacture, 129, 15–26. https://doi.org/10.1016/j.ijmachtools.2018.02.001 **8.** *Kundrák, J., Felhő, C., & Nagy, A.* (2022). Analysis and Prediction of Roughness of Face Milled Surfaces using CAD Model. MANUFACTURING TECHNOLOGY, 22(5), 558–572. https://doi.org/10.21062/mft.2022.061 **9.** *Zheng, G., Xu, R., Cheng, X., Zhao, G., Li, L., & Zhao, J.* (2018). Effect of cutting parameters on wear behavior of coated tool and surface roughness in high-speed turning of 300M. Measurement, 125, 99–108. https://doi.org/10.1016/j.measurement.2018.04.078 **10.** *Dahlman, P., Gunnberg, F., & Jacobson, M.* (2004). The influence of rake angle, cutting feed and cutting depth on residual stresses in hard turning. Journal of Materials Processing Technology, 147(2), 181–184. https://doi.org/10.1016/j.jmatprotec.2003.12.014 **11.** *Dogra, M., Sharma, V. S., Sachdeva, A., Suri, N. M., & Dureja, J. S.* (2010). Tool wear, chip formation and workpiece surface issues in CBN hard turning: A review. International Journal of Precision Engineering and Manufacturing, 11(2), 341–358. https://doi.org/10.1007/s12541-010-0040-1 **12.** *Pálmai, Z., Kundrák, J., Felhő, C., & Makkai, T.* (2024). Investigation of the transient change of the cutting force during the milling of C45 and X5CrNi18-10 steel taking into account the dynamics of the electro-mechanical measuring system. The International Journal of Advanced Manufacturing Technology, 133(1–2), 163–182. https://doi.org/10.1007/s00170-024-13640-6 **13.** *Kalafatova, L.* (2025). MODERN MATERIALS AND PROCESSING TECHNOLOGIES AS a FACTOR IN THE DEVELOPMENT OF THE AEROSPACE AND ROCKET INDUSTRIES. Cutting & Tools in Technological System, 103, 132–144. https://doi.org/10.20998/2078-7405.2025.103.10 **14.** *Jiang, H., Wang, C., Ren, Z., Yi, Y., He, L., & Zhao, X.* (2021). Influence of cutting velocity on gradient microstructure of machined surface during turning of high-strength alloy steel. Materials Science and Engineering A, 819, 141354. https://doi.org/10.1016/j.msea.2021.141354 **15.** *Kovalov, V., Klymenko, G., Vasylchenko, Y., Shapovalov, M., Boroday, R., & Zakharov, Y.* (2025). IMPROVING THE EFFICIENCY OF TOOLS FOR TURNING HIGH-STRENGTH MATERIALS. Cutting & Tools in Technological System, 103, 119–131. https://doi.org/10.20998/2078-7405.2025.103.09 **16.** *Alsoufi, M. S., & Bawazeer, S. A.* (2025). Mechanistic prediction of Machining-Induced deformation in metallic alloys using Property-Based regression and principal component analysis. Machines, 14(1), 37. https://doi.org/10.3390/machines14010037

Іштван Штанкович, Мішкольц, Угорщина

ПОРІВНЯЛЬНЕ ДОСЛІДЖЕННЯ ПОВЕРХНЕВОЇ ТОПОГРАФІЇ ТА ГРАДІЄНТА ПАРАМЕТРІВ ОБРОБКИ ПРИ ТОЧІННІ СТАЛЕЙ 42CRMO4 ТА X5CRNI18-10

Анотація. *У цьому дослідженні представлено порівняльне дослідження поверхневої топографії при токарній обробці двох інженерних матеріалів — легованої сталі 42CrMo4 та аустенітної нержавіючої сталі X5CrNi18-10. Було застосовано повний факторіальний експериментальний дизайн для оцінки впливу швидкості різання, подачі, глибини розрізу та типу матеріалу на вибрані параметри шорсткості поверхні. Аналіз був зосереджений на Sq, Sp, Sv та Sdq, що відображають висоту нерівностей поверхні та характеристики градієнта відповідно до ISO 25178. Результати показують сильну залежність топографії поверхні від властивостей матеріалу. Сталь 42CrMo4 демонструвала значно вищу шорсткість і крутішу поверхню порівняно з нержавіючою сталлю за однакових умов різання. Збільшення швидкості різання призводило до послідовного зниження всіх*

оцінюваних параметрів, тоді як величина подачі головним чином впливала на амплітудні характеристики. Параметр S_{dq} показав нижчу чутливість до умов різання, але чітко підкреслив відмінності у нахилах поверхні між матеріалами. Тип матеріалу має домінуючий вплив на поверхневий рельєф. Легована сталь 42CrMo4 стабільно демонструвала вищі значення аналізованих параметрів порівняно з X5CrNi18-10, що свідчить про більш шорсткі та крутіші поверхневі профілі. Натомість аустенітна нержавіюча сталь забезпечувала більш гладкі та однорідні поверхні за однакових умов різання. Швидкість різання виявилася важливим технологічним параметром для покращення якості поверхні. Збільшення швидкості різання з 100 м/хв до 200 м/хв призвело до значного зниження всіх оцінюваних параметрів для обох матеріалів, особливо у випадку 42CrMo4, де спостерігалося значне зниження пікових і долинних магнітуд. Результати показують, що комбінована оцінка параметрів висоти та градієнта забезпечує ефективний підхід до характеристики поверхонь, викликаних механічною обробкою, і сприяє кращому вибору умов різання.

Ключові слова: *тангенціальне обточування; топографія поверхні; параметри шорсткості; порівняння матеріалів.*

UDC 621.924.9 **doi: 10.20998/2078-7405.2026.104.12**

PROCESS PARAMETER OPTIMIZATION IN THE MACHINING OF FIBER-REINFORCED POLYMERS: A REVIEW OF METHODOLOGIES FROM TAGUCHI TO NEURAL NETWORKS

Mikayil **Valizada** [0009-0005-6649-1089], István **Sztankovics** [0000-0002-1147-7475]

University of Miskolc, 3515 Miskolc-Egyetemváros, Hungary
istvan.sztankovics@uni-miskolc.hu

Received: 08 April 2026/ Revised: 17 April 2026/ Accepted: 28 April 2026 / Published: 15 May 2026

Abstract. *The widespread adoption of Fiber Reinforced Polymers (FRPs), such as CFRP and GFRP, in weight-critical industries has necessitated highly precise secondary machining operations. However, the heterogeneous and anisotropic nature of these composites makes them susceptible to severe machining-induced defects, including delamination, matrix smearing, and rapid tool wear. To mitigate these issues, selecting and controlling optimal machining parameters (cutting speed, feed rate, and depth of cut) is critical. This paper comprehensively reviews the evolution of process optimization strategies in composite machining. It begins by examining established traditional statistical methods, including the Taguchi Method, Analysis of Variance (ANOVA), and Response Surface Methodology (RSM), which offer robust, data-efficient frameworks for linear process control. Subsequently, the paper explores the paradigm shift toward Artificial Intelligence (AI) and machine learning techniques, specifically Artificial Neural Networks (ANN), Genetic Algorithms (GA), and Fuzzy Logic systems. These data-driven approaches successfully overcome the limitations of traditional models by capturing complex, non-linear thermo-mechanical dynamics and resolving multi-objective conflicts. Ultimately, this review highlights that the future of zero-defect composite manufacturing lies in integrating these methodologies into intelligent hybrid models that bridge the gap between experimental efficiency and advanced predictive accuracy.*
Keywords: *composite machining; process parameter optimization; artificial intelligence.*

1. Introduction

Composite materials, particularly Fiber Reinforced Polymers (FRPs) such as Carbon Fiber (CFRP) and Glass Fiber Reinforced Plastics (GFRP), have revolutionized modern engineering. Characterized by their exceptional strength-to-weight ratios, high stiffness, and excellent corrosion resistance, these materials have become indispensable in weight-critical sectors such as the aerospace, automotive, and marine industries. While composite components are typically molded to near-net shapes, secondary machining operations such as drilling for fastener assembly or milling for precise edge trimming are inevitably required to achieve final dimensional tolerances.

However, the machining of composite materials presents profound challenges

compared to traditional homogeneous metals. Composites are inherently heterogeneous and anisotropic; their mechanical properties vary significantly depending on the fiber orientation. Furthermore, the highly abrasive nature of the reinforcing fibers leads to rapid tool wear. If the machining process parameters, primarily cutting speed, feed rate, and depth of cut, are not meticulously controlled, the resulting mechanical and thermal stresses can induce severe workpiece damage. These defects include matrix smearing, fiber pull-out, and most critically, delamination (the separation of adjacent composite layers), which drastically reduces the structural integrity and fatigue life of the final component.

Given the high material and manufacturing costs associated with aerospace- and automotive-grade composites, relying on trial-and-error to find the optimal machining parameters is economically unfeasible. Consequently, the manufacturing industry has historically relied on robust statistical optimization strategies. Techniques such as the Taguchi Method, Analysis of Variance (ANOVA), and Response Surface Methodology (RSM) have provided structured, highly data-efficient frameworks to minimize surface defects and maximize tool life.

As manufacturing demands stricter tolerances and composite structures become more complex, the limitations of linear, discrete statistical models have become apparent. This has prompted a paradigm shift toward data-driven Artificial Intelligence (AI) techniques, including Artificial Neural Networks (ANN), Genetic Algorithms (GA), and Fuzzy Logic systems. These intelligent systems excel at recognizing the complex, non-linear thermo-mechanical behaviors inherent in composite cutting. This paper comprehensively reviews both the traditional and AI-driven methodologies used to optimize composite machining. Furthermore, it explores how the future of process optimization lies not in choosing between traditional and AI methods, but in integrating them into intelligent hybrid models that pave the way for zero-defect, highly efficient manufacturing.

2. Review Methodology

To ensure transparency and reproducibility, a systematic approach was adopted to select, screen, and categorize the literature reviewed in this manuscript. Relevant studies were identified through comprehensive searches across major academic databases, primarily relying on Scopus, Web of Science, ScienceDirect, and Google Scholar. The search strategy utilized targeted combinations of keywords including "Composite machining," "Process parameter optimization," "Taguchi method," "Response Surface Methodology," "Artificial Neural Networks," "Genetic Algorithms," and "Fuzzy Logic."

The screening process focused strictly on peer-reviewed journal articles and conference proceedings published within the last two decades. Studies were selected based on their explicit focus on optimizing secondary machining parameters (cutting

speed, feed rate, depth of cut, tool geometry) for fiber-reinforced polymers (specifically CFRP and GFRP). Articles focusing purely on composite synthesis, primary forming processes, or non-machining applications were excluded to maintain focus. Once screened, the selected literature was logically categorized into two primary domains: traditional statistical optimization strategies (Section 3) and predictive modeling using artificial intelligence (Section 4), enabling a structured comparative discussion.

3. Traditional Optimization Strategies

In the machining of composite materials, selecting the correct process parameters, such as cutting speed, feed rate, and depth of cut, is critical. Unlike metals, composites are heterogeneous and anisotropic, meaning their properties vary with direction. This makes them prone to specific defects like delamination (separation of layers) and fiber pull-out. To address these challenges without wasting expensive materials on trial-and-error, researchers rely on statistical optimization strategies. The most established "traditional" methods are the Taguchi Method, Analysis of Variance (ANOVA), and Response Surface Methodology (RSM) [1].

3.1 The Taguchi Method

Developed by Dr. Genichi Taguchi, this method is widely regarded as a robust design strategy for quality engineering. Its primary goal is not just to maximize performance, but to make the manufacturing process insensitive to "noise," which represents uncontrollable variables such as machine vibrations or slight inconsistencies in the composite material. The methodology relies fundamentally on Orthogonal Arrays (OA), which are specialized standard tables that allow researchers to investigate a large number of variables with a minimum number of experiments. For instance, while a full study of three factors at three levels would typically require 27 separate experiments, a Taguchi L_9 array can derive statistically significant results in just 9 runs. This efficiency is particularly crucial in machining composites, where tool wear is rapid, and the workpieces are often prohibitively expensive to waste.

Another distinct feature of this approach is the use of the Signal-to-Noise (S/N) ratio to analyze data. Instead of simply evaluating the average result, the S/N ratio consolidates the mean and the variance into a single metric. The "Signal" represents the desirable value, such as a smooth surface finish, while the "Noise" represents the undesirable variability. In composite machining research, the "Smaller-the-Better" category is typically selected for minimizing defects like surface roughness (R_a) or delamination factor (F_d), where a higher S/N ratio indicates a more robust and stable process. Research by Palanikumar demonstrates the effectiveness of this method in turning Glass Fiber Reinforced Plastics (GFRP) [2]. Using an L_{27}

orthogonal array, the study optimized cutting parameters to minimize surface roughness. The analysis revealed that the Taguchi method successfully identified a robust operating window, highlighting that low feed rates and high cutting speeds are generally preferred to minimize the brittle fracture of fibers.

Similarly, Erkan et al. applied the Taguchi method to optimize the end milling process for Glass Fiber Reinforced Polymer (GFRP) composites [3]. By employing an L27 orthogonal array, they systematically evaluated the effects of cutting speed, feed rate, and depth of cut, along with tools with varying numbers of flutes, on the resulting surface roughness. Through the analysis of S/N ratios, the study corroborated that higher cutting speeds paired with low feed rates produced the optimal, smoothest surface finish, successfully minimizing surface roughness down to 1.626 μm.

3.2 Analysis of Variance (ANOVA)

While the Taguchi method is excellent for identifying the best levels for parameters (e.g., determining that Speed Level 2 is superior to Level 1), it does not explicitly quantify the magnitude of influence each parameter has on the final outcome. To bridge this gap, researchers employ Analysis of Variance (ANOVA). This statistical tool calculates the percentage contribution of each machining parameter to the total variation in the result, effectively separating the variation caused by control factors from that caused by experimental error. By establishing a hierarchy of influence, ANOVA allows engineers to prioritize which settings must be strictly controlled and which can be adjusted with less risk.

The utility of ANOVA is evident in studies such as those by Davim et al., which analyzed the milling of GFRP composites [4]. Their statistical analysis of machining forces and surface roughness provided a clear breakdown of parameter influence, revealing that the feed rate was the dominant factor, contributing over 70% to the variation in machining force, while cutting speed had a much smaller impact. Similarly, a simplified version of this technique, known as Pareto ANOVA, based on the Pareto principle (80/20 rule), is often utilized in industrial settings. This method allows engineers to quickly identify the "vital few" parameters, typically, feed rate in composite machining, that drive the majority of quality issues, ensuring that optimization efforts are focused where they will yield the most significant reduction in defects.

Further highlighting the necessity of ANOVA in varying contexts, Rao et al. applied this statistical method to a different machining operation: the drilling of GFRP composite laminates using High Speed Steel (HSS) twist drills. Using a Full Factorial Design, they measured the resulting surface roughness and applied ANOVA to evaluate the exact percentage contribution of drill diameter, feed rate, and spindle speed [5]. They found that the drill diameter was the most critical factor, contributing a massive 75.76% to the total variance in surface roughness, while feed

rate and spindle speed had marginal impacts of 8.34% and 7.57%, respectively. This specific quantification allowed the researchers to confidently conclude that selecting a smaller drill size (such as the 6 mm diameter in their optimized setup) is the most decisive parameter for achieving high surface quality and dimensional accuracy in composite hole-making.

3.3 Response Surface Methodology (RSM)

Response Surface Methodology (RSM) represents a more advanced statistical technique used for modeling and analyzing problems where a response of interest is influenced by several variables. Unlike the Taguchi method, which identifies the best point from discrete, pre-defined levels, RSM fits a mathematical equation (usually a second-order polynomial) to the experimental data. This creates a continuous "map" of the entire experimental region, allowing for the prediction of results at any point within the design space, even those that were not experimentally tested. The output is often visualized through 3D surface plots or 2D contour graphs, which are instrumental in visualizing the interaction between parameters—for instance, demonstrating how a high cutting speed might improve finish only if the depth of cut remains low.

The precision of RSM was demonstrated in a study by Nor Khairusshima et al., which utilized a Central Composite Design (CCD) to optimize the milling of Carbon Fiber Reinforced Plastics (CFRP) [6]. The developed mathematical model allowed the researchers to pinpoint a precise global optimum, specifically, a spindle speed of 3061 rpm and a depth of cut of 0.72 mm, rather than settling for a general level. The study confirmed that RSM is particularly superior when the interaction effects between variables are significant and need to be understood to prevent complex failure modes like delamination.

In another compelling application, Parida et al. utilized RSM to develop a second-order mathematical model for predicting surface roughness during the drilling of GFRP composites with High-Speed Steel (HSS) tools [7]. While many studies isolate the effects of individual parameters, the RSM approach successfully mapped the continuous, interacting relationships among spindle speed, feed rate, and drill bit diameter. The resulting response surface models and ANOVA validation (at a 95% confidence level) showed that spindle speed was the overwhelmingly dominant factor driving surface roughness, while feed rate had a statistically insignificant effect. By visualizing these mathematical relationships on a plotted response surface, the researchers were able to pinpoint a highly specific optimal operating window, using a low spindle speed, a medium feed rate, and a medium drill bit diameter that minimized surface defects, proving RSM's efficacy in generating highly reliable predictive equations for composite machining.

4. Artificial Intelligence and Predictive Modelling in Composite Machining

While traditional statistical methods like Taguchi and RSM are effective for defining linear relationships and robust operating windows, they often struggle to capture the complex, non-linear, and stochastic nature of composite machining. To overcome these limitations, researchers have increasingly adopted Artificial Intelligence (AI) techniques. These data-driven approaches require less domain-specific physical knowledge and can uncover intricate patterns within experimental data, enabling highly accurate predictions of process characteristics such as cutting force, temperature, and surface defects [8]. This section explores the application of Artificial Neural Networks (ANN), Genetic Algorithms (GA), and Fuzzy Logic systems in the optimization of composite machining.

4.1 Artificial Neural Networks (ANN)

Artificial Neural Networks (ANN) are computational models inspired by the human brain, consisting of interconnected neurons arranged in layers. They are particularly powerful in machining research for their ability to model non-linear relationships between input parameters (such as speed and feed) and outputs (such as delamination or tool wear) without needing a pre-defined mathematical equation [8].

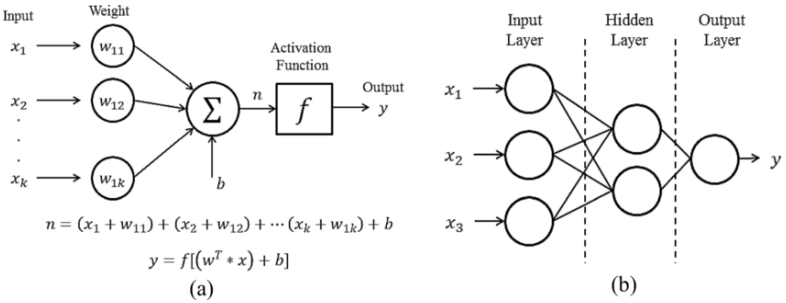

Figure 1 - a) ANN structure with one neuron. b) ANN scheme [9]

A significant application of ANN in composite machining is the prediction and prevention of delamination, a critical failure mode where layers separate. Research by Karnik et al. utilized ANN to model high-speed drilling of Carbon Fiber Reinforced Polymers (CFRP) [10]. Their study processed experimental data to predict the delamination factor based on spindle speed, feed rate, and point angle. A key finding from their ANN model was the counterintuitive benefit of high-speed machining; the model correctly predicted that higher spindle speeds generated

frictional heat, which softened the polymer matrix (matrix softening), thereby reducing the thrust force and subsequent delamination damage.

Similarly, Popan et al. developed a feed-forward ANN model trained with backpropagation to optimize the piercing phase of Abrasive Water Jet (AWJ) machining of CFRP [11]. This phase is notorious for causing delamination due to the high initial impact pressure. The ANN analyzed inputs including water pressure (100–400 MPa), standoff distance (0.5–10 mm), and abrasive start synchronization (On/Off). The model predicted that reducing the water pressure to 100 MPa and maintaining a low standoff distance of 0.5 mm, combined with abrasive start synchronization ON, would eliminate delamination for the piercing process. Validation experiments confirmed the ANN's predictions, producing defect-free holes and preventing the rejection of expensive aerospace components.

Furthermore, researchers like Stone and Krishnamurthy implemented ANN for real-time process control [12]. They developed a neural network controller that monitored thrust force during drilling. The system could predict the onset of delamination and dynamically adjust the feed rate in real-time, effectively maintaining forces within a safe envelope and preventing damage at the hole exit.

4.2 Genetic Algorithms (GA)

Genetic Algorithms (GA) are optimization techniques based on the principles of natural selection and genetics. Unlike ANN, which is primarily a predictive tool, GA is an optimization search tool used to find the "global optimum" in a vast solution space. It operates by evolving a population of potential solutions through operations like selection, crossover, and mutation to find the best possible combination of machining parameters [8].

Kumar and Sait applied GA to optimize the turning parameters of composite pipes [14]. Their objective was to optimize the machining parameters to yield a minimum cutting force. The GA processed the experimental data and converged on a specific optimal set of parameters. From this analysis, the following conclusions are drawn: Force acting on the cutting tool is found to be minimum at a cutting speed of 75 m/min, a feed rate of 0.2 mm/rev, and a depth of cut of 0.5 mm.

To further enhance accuracy, researchers often combine GA with Neural Networks. Cao et al. utilized a hybrid GA-BPNN (Genetic Algorithm optimized Back-Propagation Neural Network) to model the high-speed milling of Carbon Fiber/Polyetheretherketone (CF/PEEK) laminates [15]. In this hybrid approach, the GA was used to optimize the initial weights and thresholds of the neural network, preventing it from getting stuck in local optima. This improved model was used to predict surface roughness (S_q) and fractal dimension (D_s). The results showed that the GA-BPNN model achieved a prediction accuracy exceeding 90%, significantly outperforming standard regression models in predicting the complex surface topography of machined thermoplastic composites.

These advanced optimization techniques are essential not only in the machining phase but also in the broader structural design of composites. Demonstrating this, Al-Hamzawi and Kovács developed a novel multi-objective optimization methodology to simultaneously minimize the weight and improve the structural responses of corrugated composite sandwich structures [16]. In their study, they utilized a hybrid framework that integrated Finite Element Analysis (FEA) for data generation with Artificial Neural Networks (ANN) to create highly accurate predictive models for structural behaviors such as deflection and stress. A Genetic Algorithm (GA) was then applied to these models to systematically identify optimal design variables, including ply orientations and core geometric dimensions. The approach successfully yielded a set of Pareto-optimal solutions that achieved significant weight reduction while maintaining and even improving the structural integrity of the composites. By leveraging these advanced algorithmic approaches, their research proves the effectiveness of navigating complex, multi-objective composite design problems, which share the same underlying mathematical complexities found in multi-objective machining parameter optimization.

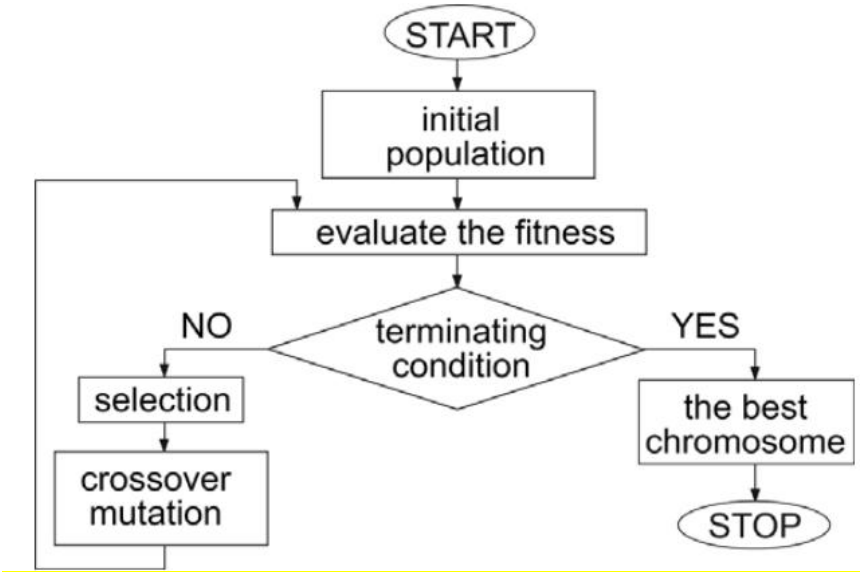

Figure 2 - Genetic algorithm scheme [13]

In the context of composite machining, GA is often used to find optimal parameters that lie between the discrete levels tested in standard experiments.

4.3 Fuzzy Logic and Adaptive Neuro-Fuzzy Inference Systems (ANFIS)

Fuzzy Logic is a computing approach based on "degrees of truth" rather than the usual "true or false" (1 or 0) Boolean logic. It uses linguistic variables (e.g., "High," "Medium," "Low") and rule-based inference (IF-THEN rules) to model uncertainty. When combined with the learning capabilities of neural networks, it forms an Adaptive Neuro-Fuzzy Inference System (ANFIS), which is highly effective for modelling complex, ambiguous systems [8].

Fuzzy logic is particularly useful for multi-objective optimization, where manufacturers must balance conflicting goals, such as minimizing force while maximizing speed. Hari Babu et al. employed a Fuzzy Inference System (FIS) to optimize the drilling of hybrid Glass-Carbon Fiber Reinforced (GCFR) epoxy composites [17]. The study aimed to simultaneously minimize four distinct responses: Thrust Force, Torque, Delamination Factor, and Surface Roughness. The FIS combined these four values into a single metric called the Multi-Response Performance Index (MPI).

The experiments involved varying spindle speed (1000–3000 RPM), drill diameter (5–7 mm), and feed rate (50–150 mm/min). The FIS analysis identified that the optimal parameter combination for the best overall quality was a spindle speed of 3000 RPM, a drill diameter of 5 mm, and a feed rate of 50 mm/min. Furthermore, Analysis of Variance (ANOVA) on the MPI revealed that drill diameter was the most significant factor influencing the overall drilling quality of the hybrid composite, followed by feed rate.

In another application involving biocomposites, Tran et al. used ANFIS to predict surface roughness and thrust force [18]. Biocomposites often exhibit high material variability, which makes standard regression difficult. The ANFIS model, by adjusting its internal membership functions, was able to map the non-linear relationships between cutting parameters and surface quality more accurately than linear regression models, providing reliable predictions despite the "noise" inherent in natural fiber materials.

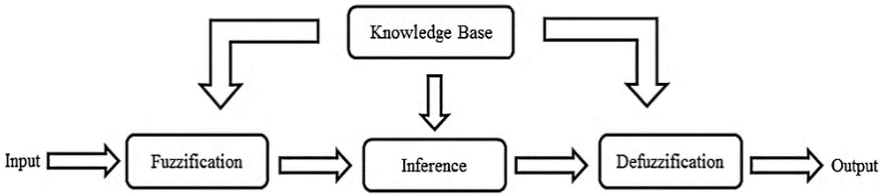

Figure 3 - Fuzzy logic scheme [9]

5. Comparative Discussion

The evolution of process optimization in composite machining, from statistical designs (Taguchi, RSM) to data-driven intelligence (ANN, GA, Fuzzy Logic), represents a shift from "robust design" to "intelligent manufacturing." While both approaches share the ultimate goal of improving quality and efficiency, their underlying mechanisms, capabilities, and applications differ significantly. This section compares these methodologies and highlights the emergence of hybrid models that leverage the strengths of both.

5.1 Linear Approximations vs Non-Linear Dynamics

Traditional methods, particularly RSM and Taguchi, are founded on the assumption that the relationship between machining inputs (e.g., speed, feed) and outputs (e.g., delamination, thrust force, surface roughness) can be approximated by smooth, continuous functions. Typically, linear or quadratic polynomials. This assumption holds well for homogeneous metals but often falls short for composites like CFRP and GFRP. As noted in the study by Karnik et al. [10], effects such as "matrix softening" introduce sharp non-linearities where an increase in speed suddenly reduces damage due to thermal softening. Traditional regression models might average this effect out, whereas AI models like ANN can capture the specific inflection point, providing a more accurate representation of the thermo-mechanical reality.

Furthermore, traditional methods generally require rigid experimental designs (e.g., Orthogonal Arrays) that test parameters at discrete levels (Level 1, 2, 3). If the true optimum lies between Level 2 and Level 3, the Taguchi method may miss it. In contrast, Genetic Algorithms (GA) operate as global search heuristics. As demonstrated by Kumar and Sait [14], GA can search the continuous space between discrete experimental levels, identifying a precise global optimum (e.g., 75 m/min) that was not explicitly tested in the initial design.

5.2 Multi-Objective Conflicts

A significant limitation of traditional methods is their struggle with multi-objective optimization. In composite machining, higher feed rates typically increase productivity (a positive outcome) but also increase thrust force and surface roughness (negative outcomes). Standard Taguchi analysis optimizes each response individually, often leading to conflicting optimal parameter sets. Researchers must then rely on engineering judgment to find a compromise.

AI methods, particularly Fuzzy Logic, offer a mathematical solution to this ambiguity. By converting disparate responses into linguistic variables and fusing them into a single index (such as the MPI used by Hari Babu et al. [17]), fuzzy

systems provide a structured way to balance competing goals. This allows for the identification of a single "best compromise" setup that satisfies multiple quality criteria simultaneously, a capability that is less intuitive in standard ANOVA or Taguchi analysis.

Table 1 - Comparison of Traditional and AI Optimization Methods

Feature	**Traditional Methods (Taguchi, RSM, ANOVA)**	**AI Methods (ANN, GA, Fuzzy Logic/ANFIS)**
Primary Mechanism	Statistical inference, linear/quadratic regression, signal-to-noise ratios.	Pattern recognition, non-linear mapping, evolutionary search, linguistic reasoning.
Relationship Modelling	Best for linear or simple non-linear relationships. Assumes continuity.	Excellent for complex, highly non-linear, and discontinuous relationships.
Optimization Scope	Discrete (local). Limited to specific levels tested in the experiment.	Continuous (global). Can find optimal points between tested levels (GA).
Data Requirement	Low. Efficient designs (e.g., L9, L27) require fewer experiments.	High. Generally, requires larger training datasets to avoid overfitting.
Multi-Objective Capability	Limited. Optimizes responses individually; requires manual trade-offs.	High. Fuzzy logic and neural networks can fuse multiple outputs into a single index.
Interpretability	High. ANOVA explicitly quantifies the % contribution of each factor.	Low/Medium. ANNs are often "black boxes"; Fuzzy Logic provides interpretable rules.

5.3 Data Efficiency and Prediction Accuracy

The primary advantage of traditional methods remains their efficiency. A Taguchi L_9 array can yield statistically valid conclusions with only 9 experiments, making it highly cost-effective for industrial screening. In contrast, AI models, especially Deep Learning and complex ANNs, typically require large datasets to train effectively without overfitting. The "data scarcity" problem in composite machining—where experimental data is expensive to generate—is a key hurdle for AI. However, methods like ANFIS (used by Tran et al. [18]) and GPR (Gaussian Process Regression) are gaining popularity precisely because they can provide accurate non-linear predictions even with smaller datasets, bridging the gap between data hunger and experimental constraints.

6. Conclusions

The optimization of machining parameters for composite materials has undergone a significant evolution, transitioning from traditional statistical designs to advanced, data-driven artificial intelligence. The inherent heterogeneity and anisotropy of composites like GFRP and CFRP make machining a complex process, highly susceptible to defects such as delamination, fiber pull-out, and poor surface finish. As this review highlights, traditional methodologies (such as the Taguchi method, ANOVA, and RSM) have long provided robust, cost-effective frameworks for identifying critical parameters and establishing stable operating windows. They remain highly valuable for initial process screening and quantifying the linear impacts of factors like feed rate, cutting speed, and tool geometry.

However, the non-linear, stochastic nature of composite machining often exceeds the capabilities of standard regression models. AI techniques, including Artificial Neural Networks (ANN), Genetic Algorithms (GA), and Fuzzy Logic systems, have emerged as powerful alternatives that require less domain-specific physical pre-definitions. These intelligent systems offer superior predictive accuracy by mapping complex thermo-mechanical behaviors, such as matrix softening, and by enabling continuous global optimization beyond discrete experimental levels. Furthermore, tools like Fuzzy Logic provide structured mathematical solutions to multi-objective conflicts, allowing manufacturers to simultaneously optimize competing goals like productivity and surface quality.

Ultimately, the future of composite machining optimization lies not in choosing between traditional and AI methods, but in integrating them. Hybrid approaches (e.g, using GA to optimize neural network weights (GA-BPNN) or combining fuzzy logic with adaptive learning (ANFIS)) demonstrate the highest potential.

Despite these advancements, several concrete research gaps remain to be addressed in future studies. First, the industrial implementation of AI-driven real-time adaptive control is heavily restricted by computational latency and a lack of robust, sensor-integrated edge computing solutions on the shop floor. Second, the training of highly accurate predictive models is frequently hampered by a scarcity of standardized, publicly available machining datasets. Finally, the inherent "black-box" nature of many deep learning algorithms limits their interpretability and hinders trust among manufacturing engineers. Future research must prioritize the development of Explainable AI (XAI) frameworks to clarify how these models reach their predictions. Furthermore, bridging these hybrid algorithms with Digital Twin technology could enable dynamic, real-time optimization and autonomous error correction, propelling the industry closer to the ultimate goal of zero-defect composite machining.

References: 1. *Srinivasan, S., et al.* A review of optimization techniques in machining of composite materials. Materials Today: Proceedings, 47, 6811–6814. (2021). https://doi.org/10.1016/j.matpr.2021.05.136 **2.** *Palanikumar, K.* Cutting parameters optimization for surface roughness in machining of GFRP composites using Taguchi's method. Journal of Reinforced Plastics and Composites, 25(16), 1739–1751. (2006). https://doi.org/10.1177/0731684406068445 **3.** *Erkan, Ö., et al.* Selection of optimal machining conditions for the composite materials by using Taguchi and GONNs. Measurement, 48, 306–313. (2014). https://doi.org/10.1016/j.measurement.2013.11.011 **4.** *Davim, J. P., et al.* A study on milling of glass fiber reinforced plastics manufactured by hand-lay up using statistical analysis (ANOVA). Composite Structures, 64(3–4), 493–500. (2004). https://doi.org/10.1016/j.compstruct.2003.09.054 **5.** *Rao, U. S.* Controlling process factors to optimize surface quality in drilling of GFRP composites by integrating DoE, ANOVA and RSM techniques. Indian Journal of Science and Technology, 8(1), 1–9. (2015). https://doi.org/10.17485/ijst/2015/v8i29/70728 **6.** *Khairusshima, M. K. N., et al.* Optimization of milling carbon fibre reinforced plastic using RSM. Procedia Engineering, 184, 518–528. (2017). https://doi.org/10.1016/j.proeng.2017.04.122 **7.** *Parida, A. K., et al.* Surface roughness model and parametric optimization in machining of GFRP composite: Taguchi and response surface methodology approach. Materials Today: Proceedings, 2(4–5), 3065–3074. (2015). https://doi.org/10.1016/j.matpr.2015.07.247 **8.** *Ge, J., et al.* Intelligent machining of CFRP composites via data-driven prediction and optimization: Advances, challenges and future prospects. ResearchGate. (2025). https://doi.org/10.26434/chemrxiv-2025-b1jjg **9.** *Leyva-Bravo, J., et al.* Electrochemical discharge machining modeling through different soft computing approaches. The International Journal of Advanced Manufacturing Technology, 106(7–8), 3587–3596. (2020). https://doi.org/10.1007/s00170-019-04766-z **10.** *Karnik, S. R., et al.* Delamination analysis in high speed drilling of carbon fiber reinforced plastics (CFRP) using artificial neural network model. Materials & Design, 29(9), 1768–1776. (2008). https://doi.org/10.1016/j.matdes.2008.03.014 **11.** *Popan, I. A., et al.* Artificial intelligence model used for optimizing abrasive water jet machining parameters to minimize delamination in carbon fiber-reinforced polymer. Applied Sciences, 14(18), 8512. (2024). https://doi.org/10.3390/app14188512 **12.** *Stone, R., & Krishnamurthy, K.* A neural network thrust force controller to minimize delamination during drilling of graphite-epoxy laminates. International Journal of Machine Tools & Manufacture, 36(9), 985–1003. (1996). https://doi.org/10.1016/0890-6955(96)00013-2 **13.** *Jopek, H., & Strek,* T. Optimization of the effective thermal conductivity of a composite. InTech eBooks. (2011). https://doi.org/10.5772/24531 **14.** *Kumar, K. V., & Sait, A. N.* Modelling and optimisation of machining parameters for composite pipes using artificial neural network and genetic algorithm. International Journal on Interactive Design and Manufacturing (IJIDeM), 11(2), 435–443.

(2014). https://doi.org/10.1007/s12008-014-0253-0 **15.** *Cao, H., et al.* Process optimization of high-speed dry milling UD-CF/PEEK laminates using GA-BP neural network. Composites Part B: Engineering, 221, 109034. (2021). https://doi.org/10.1016/j.compositesb.2021.109034 **16.** *Sahib, M. M., & Kovács, G.* Multi-objective optimization of composite sandwich structures using artificial neural networks and genetic algorithm. Results in Engineering, 21, 101937. (2024). https://doi.org/10.1016/j.rineng.2024.101937 **17.** *Babu, U. H., et al.* Artificial intelligence system approach for optimization of drilling parameters of glass-carbon fiber/polymer composites. Silicon, 13(9), 2943–2957. (2020). https://doi.org/10.1007/s12633-020-00637-5 **18.** *Tran, D. S., et al.* Regression and ANFIS-based models for predicting surface roughness and thrust force during drilling of biocomposites. Neural Computing and Applications, 33(18), 11721–11738. (2021). https://doi.org/10.1007/s00521-021-05869-z

Мікаїл Валізада, Іштван Штанкович, Мішкольц, Угорщина

ОПТИМІЗАЦІЯ ПАРАМЕТРІВ ПРОЦЕСУ ОБРОБКИ ВОЛОКОННО-АРМОВАНИХ ПОЛІМЕРІВ: ОГЛЯД МЕТОДОЛОГІЙ ВІД ТАГУЧІ ДО НЕЙРОННИХ МЕРЕЖ

Анотація. *Широке впровадження волокно-армованих полімерів (FRP), таких як CFRP та GFRP, у критично важливих галузях, вимагало високоточних вторинних операцій з обробки. Однак гетерогенний і анізотропний характер цих композитів робить їх вразливими до серйозних дефектів, спричинених обробкою, включно з розшаруванням, розмазуванням матриці та швидким зношенням інструментів. Для вирішення цих проблем критично важливо вибрати та контролювати оптимальні параметри обробки (швидкість різання, швидкість подачі та глибину різу). У цій статті ґрунтовно розглядається еволюція стратегій оптимізації процесів у композитній обробці. Він починається з вивчення усталених традиційних статистичних методів, зокрема методу Тагучі, аналізу дисперсії (ANOVA) та методології поверхні відгуку (RSM), які пропонують надійні, ефективні для даних рамки для лінійного керування процесами. Далі у статті розглядається зсув парадигми на користь штучного інтелекту (AI) та методів машинного навчання, зокрема штучних нейронних мереж (ANN), генетичних алгоритмів (GA) та систем нечіткої логіки. Ці підходи, засновані на даних, успішно долають обмеження традиційних моделей, фіксуючи складну, нелінійну термомеханічну динаміку та вирішуючи багатооб'єктні конфлікти. Незважаючи на ці досягнення, ще кілька конкретних дослідницьких прогалин залишаються для усунення в майбутніх дослідженнях. По-перше, промислове впровадження адаптивного керування в реальному часі на основі ШІ суттєво обмежене обчислювальною затримкою та відсутністю надійних рішень з інтеграцією сенсорів на периферії на виробництві. По-друге, навчання високоточних прогностичних моделей часто ускладнюється через нестачу стандартизованих, публічно доступних наборів даних для обробки. Нарешті, притаманна «чорна скринька» багатьох алгоритмів глибокого навчання обмежує їхню інтерпретацію та зменшує довіру серед інженерів-виробників. Зрештою, цей огляд підкреслює, що майбутнє виробництва композитів з нульовими дефектами полягає в інтеграції цих методологій у інтелектуальні гібридні моделі, які поєднують експериментальну ефективність і передову прогнозну точність.*
Ключові слова: *обробка композитів; оптимізація параметрів процесу; штучний інтелект.*

UDC 621.9.048 **doi: 10.20998/2078-7405.2026.104.13**

ANALYSIS OF FUNCTION-DEFINING 3D SURFACE PARAMETERS IN DIAMOND BURNISHING

Viktoria **Ferencsik** [0000-0002-8673-1095]

University of Miskolc, 3515 Miskolc-Egyetemváros, Hungary
ferencsik.viktoria@uni-miskolc.hu

Received: 22 April 2026 / Revised: 26 April 2026 / Accepted: 28 April 2026 / Published: 15 May 2026

Abstract. *The tribological effects of diamond burnishing are investigated on EN AW-2011 aluminium alloy cylindrical surfaces. In engineering practice, the tribological behaviour of machined parts is often characterized using functional surface roughness parameters such as the S_k (core roughness depth), S_{pk} (reduced peak height), and S_{vk} (reduced valley depth) 3D roughness parameters. In the present study, the influence of various burnishing parameter settings is evaluated comprehensively through both their quantitative roughness values and the corresponding Abbott-Firestone material ratio curves. This combined approach enables a deeper understanding of how the burnishing process modifies the surface topography and, consequently, the tribological performance of the material under operational conditions.*
Keywords: *diamond burnishing; surface roughness; functional parameters, Abbott-Firestone.*

1. Introduction

Surface burnishing is a cold plastic finishing technique in which a hard (typically PCD) tool plastically deforms the surface layer of a workpiece to improve its overall surface integrity. During the process, the applied force, in combination with the selected burnishing parameters, induces material flow in the near-surface region, resulting in enhanced smoothness and improved functional properties [1–3]. In contrast to conventional abrasive methods such as grinding or honing, burnishing does not involve material removal; instead, it generates beneficial compressive residual stresses, increases surface hardness, and significantly reduces surface roughness. The appropriate selection of burnishing parameters is therefore essential to achieve optimal performance characteristics in the final component [4].

Due to various disturbances inherent in machining processes, the resulting surface profile often contains irregular features whose geometry may deviate significantly from idealized forms. Consequently, surfaces produced by manufacturing operations typically exhibit highly complex topographies and textures. In such cases, three-dimensional surface roughness analysis provides a more comprehensive

characterization of surface features compared to conventional two-dimensional evaluation methods [5]. Therefore, Sztankovics [6], in order to ensure a comprehensive evaluation of surface topography, selected six S-parameters for tangential turning analysis. A general parameter was chosen to describe the overall surface texture. In addition, three parameters derived from the Abbott-Firestone curve were included to characterize the material ratio curve and to provide insight into the load-bearing properties of the surface. Furthermore, two functional parameters were also considered in the surface description, as they are critical for evaluating surface functionality in machining applications.

Nagy [7] examined the functional parameters in the case of face milling, while Kebede et al. [1] also examined them in the case of surface burnishing because slide burnishing plays a significant role in improving surface quality, but there is a noticeable lack of studies addressing the efficiency of the process.

The current paper aims to contribute to a deeper understanding of burnishing process and its role in enhancing the functional performance of critical mechanical components with particular emphasis on the tribological significance of functional surface parameters governing friction, wear, and lubrication behaviour on low alloyed aluminium workpieces.

2. Experimental conditions

For the investigation, burnishing experiments were carried out on an E400 universal lathe (the surface of the workpiece was pre-machined by finishing turning set at $f_1 = 0.2$ than $f_2 = 0.15$ mm/rev) using PCD (polycrystalline diamond) tool with 3.5 mm radius (r). During cylindrical surface burnishing, the workpiece rotates at a defined speed (ω_w) while a deforming tool passes over its surface under burnishing force (F_b) with defined feed rate (f), causing elastic-plastic deformation in the near-surface layer [8], as shown in Figure 1.

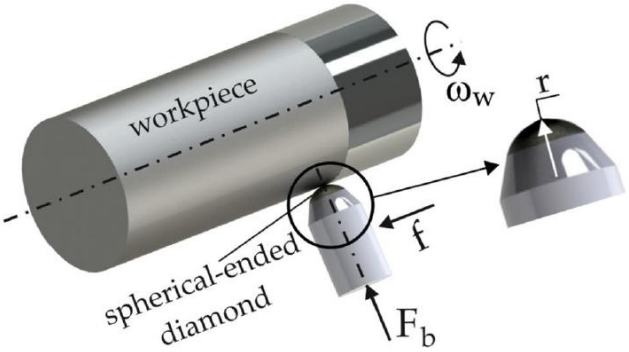

Figure 1 – Scheme of burnishing process on external cylindrical surface [8]

The application of this finishing process aims to improve surface quality and prolong component lifetime by inducing compressive residual stresses and increasing the hardness of the near-surface layer [9, 10].

Table 1 summarizes the adjusted burnishing parameters (F – burnishing force, f – feed, v – burnishing speed, i – number of passes) derived from preliminary experimental work, with due consideration given to the mechanical properties of the workpiece material (EN AW-2011) subjected to burnishing.

Table 1 – Numerical value of the analysed burnishing parameters

No	F [N]	f [mm/rev]	v [m/min]	i [-]
1	15	0.05	50.54	2
2	25	0.05	50.54	2
3	35	0.05	50.54	2
4	25	0.01	50.54	2
5	25	0.1	50.54	2
6	25	0.05	35.71	2
7	25	0.05	71.43	2
8	25	0.05	50.54	1
9	25	0.05	50.54	3

3. Evaluation of 3D surface roughness

The 3D surface roughness of turned and burnished surfaces was measured in three 2 × 2 mm regions, separated by a 120° rotational angle. Measurements were performed using an Altisurf 520 surface profiler with a CL2 confocal chromatic sensor and MG140 magnification. Data evaluation was carried out using Altimap Premium software.

To evaluate the surface topography, three S-parameters were selected for the analysis: S_k – core roughness depth, S_{vk} – reduced valley depth, S_{pk} – reduced peak height. These parameters, derived from the Abbott-Firestone curve, are used to characterize the material ratio curve and to determine the load-bearing properties of the surface [9]. Their selection is further justified by the fact that burnishing improves the bearing area ratio by effectively flattening surface asperity peaks, thereby modifying the functional surface profile. Using this approach, the aim of the study was to define a practical and effective evaluation range that provides reliable S-parameter values.

4. Results

The surface topographies obtained from the measurements were analysed together with their corresponding Abbott-Firestone material ratio curves in order to evaluate the functional characteristics of the machined surfaces. Representative examples of the measured 3D surface topographies and material ratio curves are presented in the paper for specimens No. 1 and No. 9 to illustrate the effects of the applied processing conditions.

The evaluated 3D surface topographies reveal a clear modification of the surface structure induced by the burnishing process. Compared to the turned surfaces, the burnished specimens exhibit a more uniform height distribution, reduced peak prominence, and smoother surface features aligned with the processing direction. These changes indicate effective plastic deformation of surface asperities, consistent with the observed improvements in functional roughness characteristics and the corresponding behaviour of the Abbott-Firestone material ratio curve.

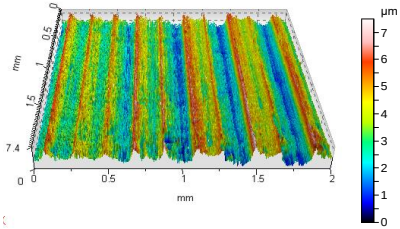

No. 1.1 Turned

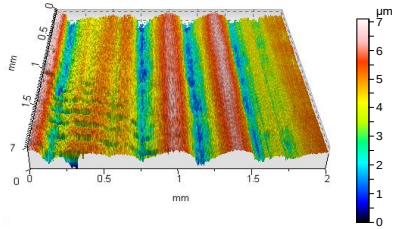

No. 1.1. Burnished

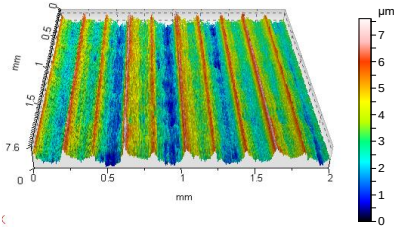

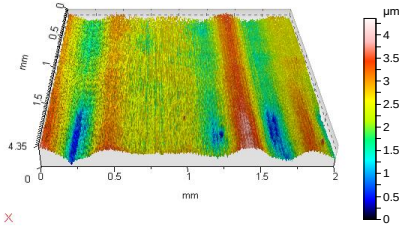

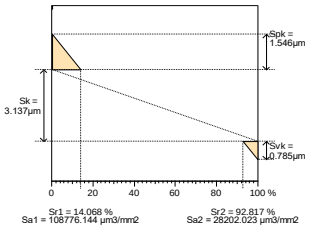

No. 9.1 Turned

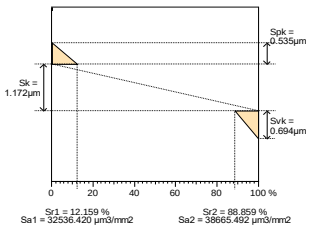

No. 9.1. Burnished

Figure 2 – Measured 3D surface morphology illustrating the effect of burnishing

Table 2 presents the averaged values of the measured roughness parameters and includes dimensionless ratios introduced to facilitate a clearer interpretation of the observed changes. The calculations were performed in accordance with the methodology proposed by El-Taweel and El-Axir [10].

$$\Delta\rho_{S_x}\% = \left(\frac{S_{x\text{before}} - S_{x\text{after}}}{S_{x\text{before}}}\right) \cdot 100\%, \quad (1)$$

where:

$S_{x\ before}$ Surface roughness parameter measured after turning,
$S_{x\ after}$ Surface roughness parameter measured after burnishing,
$\Delta\rho S_x\%$ Percentage value of the calculated ratio.

Table 1 – The results of S_k, S_{vk} and S_{pk} with the calculated ratios of the experiment

No.	S_k [µm]		$\Delta\rho_{S_k}$ [%]
	before	after	
1	3.232	2.251	30.359
2	2.982	0.878	70.557
3	0.809	0.904	-11.743
4	0.839	0.917	-9.297
5	0.845	1.063	-25.799
6	3.285	0.933	71.598
7	3.042	1.063	65.056
8	3.643	1.341	63.189
9	3.351	1.038	69.024
No.	**S_{vk} [µm]**		**$\Delta\rho_{S_{vk}}$ [%]**
	before	**after**	
1	0.601	1.141	-89.850
2	0.733	0.509	30.559
3	0.674	0.371	44.955
4	0.422	0.375	11.137
5	0.413	0.466	-12.833

6	0.711	0.344	51.617
7	0.593	0.394	33.558
8	0.654	0.700	-7.034
9	0.829	0.528	36.309

No.	S_{pk} [µm]		$\Delta\rho_{S_{pk}}$ [%]
	before	after	
1	1.311	0.479	63.463
2	1.255	0.297	76.335
3	0.402	0.419	-4.229
4	0.325	0.292	10.154
5	0.351	0.770	-119.373
6	1.761	0.321	81.771
7	1.603	0.436	72.801
8	1.153	0.424	63.226
9	1.443	0.483	66.528

The evaluated improvement ratios indicate that the surface labelled No. 6 was produced under the most favourable set of process parameters. The optimal surface roughness characteristics were achieved with a burnishing force of F = 25 N, a feed rate of f = 0.05 mm/rev, burnishing speed of v = 35.71 m/min, and two burnishing passes (i = 2). Furthermore, the influence of the investigated burnishing parameters, presented along the horizontal axis, on the corresponding improvement ratios shown on the vertical axis is illustrated in Diagrams 1-4.

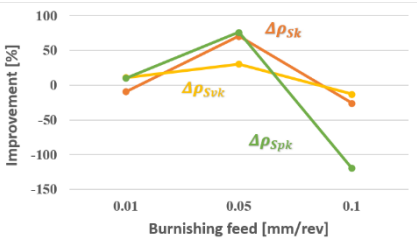

Diagram 1 – Effect of feed rate

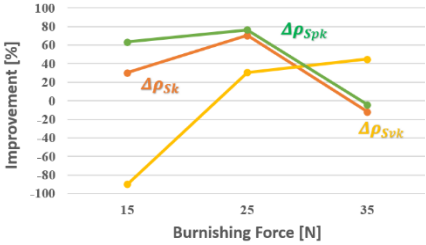

Diagram 2 – Effect of force

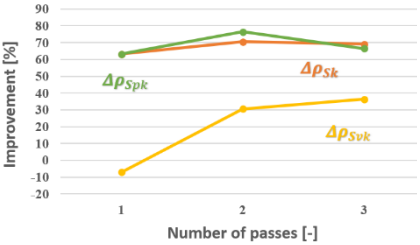

Diagram 3 – Effect of number of passes

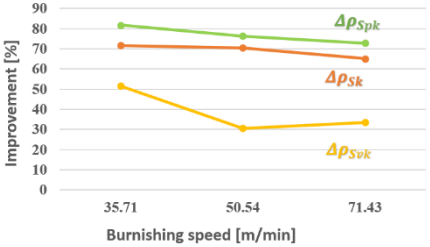

Diagram 4 – Effect of speed

The presented diagrams provide a comparative overview of the influence of the investigated burnishing parameters on surface roughness improvement ratios. In general, higher improvement values correspond to a more pronounced enhancement of surface condition as a result of the burnishing process. The observed trends clearly demonstrate that the applied technological parameters have a significant impact on the achievable surface quality, thereby underlining the importance of parameter optimization in burnishing operations.

5. Conclusions

The paper presents an experimental investigation of slide burnishing applied to low-alloyed aluminium workpieces, focusing on the effects of burnishing force, feed rate, burnishing speed and number of passes on selected functional 3D surface roughness parameters. The surface integrity was evaluated using the S_k (core roughness depth), S_{pk} (reduced peak height), and S_{vk} (reduced valley depth) parameters, which are closely related to load-bearing capacity, initial wear behaviour, and lubricant retention.

Based on the measured values before and after burnishing, the calculated improvement ratios, and their graphical representation, the following main conclusions can be drawn:

- The most favourable overall modification of the functional surface characteristics was observed for the specimen marked No. 6. In this case, S_k decreased from 3.285 μm to 0.933 μm (71.6% improvement), S_{pk} was reduced from 1.761 μm to 0.321 μm (81.8% improvement), while S_{vk} decreased from 0.711 μm to 0.344 μm (51.6% improvement). These results indicate a significantly smoother surface with reduced asperity peaks and a stabilized core structure as a result of the burnishing process.
- The numerical results clearly show that unfavourable parameter combinations can lead to a deterioration of functional roughness properties. This phenomenon is evident for example in specimen No. 5, where increases in S_k (+25.8%), S_{pk} (+119.4%), and S_{vk} (+12.8%) were observed, confirming that higher feed rate and burnishing speed settings adversely affect the surface modification efficiency.
- The tendencies observed in the improvement ratio diagrams suggest that the burnishing parameters should not be considered independently but rather in a combined manner; an increased burnishing force is particularly effective at moderate feed rates, where longer tool-surface contact time enhances the redistribution of material from peaks toward valleys, leading to reduced S_{pk} values and a more stable S_k core structure. Overall, the results indicate that optimal burnishing performance is obtained through a well-balanced combination of process parameters, in which a moderate feed rate, adequately

high burnishing forces, and modest speeds act synergistically to improve the functional surface roughness parameters.

- The simultaneous reduction of S_{pk} and S_k, together with a controlled modification of S_{vk}, indicates that slide burnishing leads to a more favourable functional surface topography. These changes result in improved load-bearing capacity, reduced initial wear tendency, and a more balanced lubricant retention behaviour. Consequently, the optimized burnishing conditions enhance the overall tribological performance of the machined surface.

Future research will focus on the investigation of additional functional and spatial 3D surface parameters, as well as on further optimization of burnishing parameters, in order to gain a more comprehensive understanding of the surface transformation mechanisms governing tribological performance.

References: 1. *Kebede, F. T., Felhő, C, Sztankovics, I.,* Improving surface roughness of 42CrMo4 low alloy steel shafts by applying varying feed in the multi-pass slide burnishing process. Applied Sciences. 2025. vol. 15. pp. 1–22 **2.** *Smolnicki, S., Varga, G.,* Analysis of surface roughness of diamond-burnished surfaces using Kraljic Matrices and experimental design. Applied Sciences-Basel. 2025. vol. 15. pp. 1–24. **3.** *Kovács, Z. F., Viharos, Z. J., Kodácsy, J.,* Improvements of surface tribological properties by magnetic assisted ball burnishing. Surface & Coatings Technology. 2022. vol. 437. pp. 1–12 **4.** *Ferencsik, V., Varga, G.,* The influence of diamond burnishing process parameters on surface roughness of low-alloyed aluminium workpieces. Machines. 2022. vol. 10. pp. 1–11 **5.** *Grzesik, W., Zak, K.,* Modification of surface finish produced by hard turning using superfinishing and burnishing operations. Journal of Materials Processing Technology. 2012. vol. 212. pp. 315–322. **6.** *Sztankovics, I.,* Optimization of measurement area selection for accurate 3D surface topography characterization in high-feed tangential turning of 42CrMo4 alloy steel. Metrology. 2025. vol. 5. pp. 1–22. **7.** *Nagy, A.,* Functional roughness parameter characterization of a plane surface face-milled with an octagonal insert. Fiatalok a Tudományért 2024. 2024. (in Hungarian) pp. 51–56. **8.** *Maximov, J., Duncheva, G.,* Effect of diamond burnishing process on surface integrity, fatigue, wear, and corrosion of metal components – review and perspectives. The International Journal of Advanced Manufacturing Technology. 2025. vol. 139. pp. 4233–4267. **9.** ISO 22081:2021, Geometrical product specifications (GPS) — Geometrical tolerancing — General geometrical specifications and general size specifications, (2021), https://www.iso.org/standard/72514.html (Viewed: 14/09/24) **10.** *El-Taweel, T.A., El-Axir M.H.,* Analysis and optimization of the ball burnishing process through the Taguchi technique. International Journal of Advanced Manufacturing Technologies. 2009. vol. 41. pp. 301–310.

Вікторія Ференчик, Мішкольц, Угорщина

АНАЛІЗ ФУНКЦІЙНО-ВИЗНАЧЕНИХ ПАРАМЕТРІВ 3D-ПОВЕРХНІ, ПРИ АЛМАЗНОМУ ПОЛІРУВАННІ

Анотація. *Трибологічні ефекти алмазного вигладжування досліджуються на циліндричних поверхнях алюмінієвого сплаву EN AW2011. В інженерній практиці трибологічну поведінку оброблених деталей часто характеризують за допомогою параметрів шорсткості функціональної поверхні, таких як S_k (глибина шорсткості ядра), S_{pk} (зменшена пікова висота) та S_{vk} (зменшена глибина западини) 3D шорсткості. У цьому дослідженні комплексно оцінюється вплив різних параметрів полірування через їхні кількісні значення шорсткості та відповідні криві*

співвідношення матеріалів Ебботта-Файрстоуна. Такий комбінований підхід дозволяє глибше зрозуміти, як процес полірування змінює топографію поверхні і, відповідно, трибологічні характеристики матеріалу в експлуатаційних умовах. Виходячи з виміряних значень до і після полірування, розрахованих коефіцієнтів покращення та їх графічного представлення, можна зробити деякі основні висновки. Найбільш сприятлива загальна модифікація функціональних характеристик поверхні була зафіксована для зразка, позначеного No6. У цьому випадку S_k зменшився з 3,285 мкм до 0,933 мкм (покращення на 71,6%), S_{pk} зменшився з 1,761 мкм до 0,321 мкм (покращення на 81,8%), а S vk зменшився з 0,711 мкм до 0,344 мкм (покращення на 51,6%). Ці результати свідчать про значно гладкішу поверхню з зменшеними піками асперності та стабілізовану структуру ядра внаслідок процесу полірування. Чисельні результати чітко показують, що несприятливі комбінації параметрів можуть призводити до погіршення функціональних властивостей шорсткості. Це явище помітне, наприклад, у зразку No5, де спостерігалося збільшення S_k (+25,8%), S pk (+119,4%) та S_{vk} (+12,8%), що підтверджує, що вища швидкість подачі та швидкість полірування негативно впливають на ефективність модифікації поверхні. Тенденції, виявлені на діаграмах коефіцієнтів покращення, свідчать, що параметри полірування слід розглядати не окремо, а в комбінованому вигляді; збільшена сила полірування особливо ефективна при помірних швидкостях подачі, де є довший час контакту з поверхнею інструменту, покращує перерозподіл матеріалу від піків до западин, що призводить до зниження значень S_{pk} і більш стабільної структури ядра S k. Загалом результати свідчать, що оптимальна ефективність полірування досягається завдяки добре збалансованому поєднанню параметрів процесу, де помірна швидкість подачі, достатньо високі сили полірування та помірні швидкості взаємодіють синергічно для покращення функціональних параметрів шорсткості поверхні. Одночасне зменшення S_{pk} і S_k, разом із контрольованою модифікацією S_{vk}, свідчить про те, що полірування зразка призводить до більш сприятливого функціонального рельєфу поверхні. Ці зміни призводять до покращення несучої здатності, зниження початкової схильності до зношування та більш збалансованої поведінки утримання мастила. Відповідно, оптимізовані умови полірування покращують загальні трибологічні характеристики обробленої поверхні. Майбутні дослідження будуть зосереджені на вивченні додаткових функціональних і просторових 3D-параметрів поверхні, а також на подальшій оптимізації параметрів полірування, щоб отримати більш повне розуміння механізмів трансформації поверхні, що регулюють трибологічну продуктивність.

Ключові слова: *алмазне полірування; шорсткість поверхні; функціональні параметри Abbott-Firestone.*

UDC 621.914.22 **doi: 10.20998/2078-7405.2026.104.14**

QUALITY OF MACHINED SURFACES OF THIN-WALLED ELEMENTS OF PARTS UNDER THE ACTION OF REGENERATIVE VIBRATIONS DURING MILLING WITH END MILLS

Sergei **Dyadya** [0000-0002-7457-7772], Olena **Kozlova** [0000-0002-3478-5913], Pavlo **Tryshyn** [0000-0002-3301-5124], Eduard **Kondratiuk** [0000-0002-2672-7174], Oleksii **Kramarenko** [0009-0003-4628-853X]

National University «Zaporizhzhya Polytechnic», Zaporizhzhya, Ukraine
kozlova@zntu.edu.ua

Received: 30 April 2026 / Revised: 05 May 2026 / Accepted: 12 May 2026 / Published: 15 May 2026

Abstract. *Monowheels, in which the disk and working blades constitute a single structure without detachable connections, are critically important components of new generation gas turbine engines for aviation and power engineering. The use of such structures allows to reduce the weight and increase the reliability of the units. However, errors in the shape of the functional surfaces of the blades that arise during mechanical processing lead to a decrease in the engine efficiency and an increase in fuel consumption. To ensure the accuracy of manufacturing the functional surfaces of the blades during the technological process, it is necessary to know the conditions under which cutting occurs. The work uses an approach based on the distribution of the entire range of cutting speeds into five speed oscillation zones. It was established that the third speed zone is the most unfavorable during milling of blades on multi-coordinate CNC machines. It is characterized by high-intensity vibrations, which worsens the quality of the machined surface and reduces the stability of the cutter. Their cause is regenerative oscillations, which are excited during machining by the trace left on the cutting surface by the accompanying free oscillation. The purpose of the study is to determine the influence of the axial depth of cut on the quality of the machined surface during milling in the third speed zone of vibrations. The results of the experiments showed that due to the peculiarities of up-milling with an axial depth of cut of a_p = 1 mm, waviness on the machined surface is not formed, even in the presence of regenerative oscillations. The obtained data allow us to develop recommendations for the selection of cutting modes that minimize the amplitude of oscillations and ensure that the monowheel blades meet high operational requirements.*

Keywords: *milling; end-mill; cutting surface; waviness; regenerative oscillation; forced vibrations; accompanying free oscillation.*

1. Introduction

Ensuring the accuracy of high-tech products, such as gas turbine engines and power plants, and the productivity of their production are urgent tasks in the aerospace and energy industries. A characteristic feature of new generation gas turbine engines is the use of monowheels in compressors and turbines. The monowheel is a single design of the disk and blades without detachable connections. The error in the shape of the complex-profile functional surfaces of the blades

reduces the efficiency of the engine and increases fuel consumption. Because of this, much attention is paid to the conditions in which they are processed. Thin-walled elements of the blades, which are located on a massive hub, are very sensitive to vibrations that arise during surface milling and affect the accuracy of its shape and roughness [1, 2]. Vibration-free milling conditions are achieved by selecting spindle speeds and cutting depths using stability lobe diagrams [3–5] or by suppressing vibrations with tools with special geometry [6].

Analysis of the influence of vibrations on the quality of the machined surface shows that the greatest contribution is made by regenerative vibrations [7, 8], which arise due to the phase difference between the waves on the cutting surface on the current and previous rotation of the part or tool pass. It should be noted that regenerative vibrations do not always act, but only in cases where there is waviness on the cutting surface. To determine such conditions during milling with end mills, the division of the cutting speed range into five speed vibration zones is used [9]. In the first, fourth and fifth speed vibration zones, only forced vibrations act. There is no waviness on the cutting surface, so there is no reason for the occurrence of regenerative vibrations. It is for these speed zones that stability lobe diagrams are suitable, when the assigned cutting speed is coordinated according to the ratio of the frequency of free oscillations of the part to the frequency of forced oscillations [6]. During milling in the second and third speed oscillation zones, when the cutter is cut into the part, forced oscillations are excited, which are superimposed by accompanying free oscillations (AFO) [10], which act for a short time [11]. However, during milling of thin-walled elements of the part (TWE) with end mills, which include monowheel blades, this time is enough to form waviness on the cutting surface [12]. It contributes to the excitation of regenerative oscillations. At the same time, their greatest intensity falls on the third speed zone. To ensure stable milling in the second speed oscillation zone, a concomitant feed direction is used. Milling under this condition has a damping property at the beginning of cutting due to the greatest thickness of the cut layer, which suppresses the occurrence of accompanying free vibrations and the formation of waviness on the cutting surface. Therefore, the current task remains to ensure the accuracy of manufacturing parts during milling in the third speed zone of oscillations. One of the directions of its solution is to determine the optimal cutting modes. This article shows how the axial depth of cut affects the intensity of regenerative vibrations and the formation of the machined surface during up- and down-milling of the TWE by an end mill in the third speed zone of oscillations.

2. Research methodology

The research was conducted on a special stand [13], where the oscillator is an elastic plate with a processed sample, which models a thin-walled element of a part

with one degree of freedom. This simplification allows us to study the most unfavorable conditions during the action of the first mode of oscillations, which are bending in shape, have the highest intensity of action and the lowest frequency of natural oscillations. To record oscillations, the sensor (proximeter XS1M18AB120) was fixed in the stand and located in the middle of the elastic plate. The signal from its oscillations during cutting was digitized using an analog-to-digital converter and recorded on a computer. The processing of samples from St3, was performed with a carbide milling cutter from VK8 according to the initial data given in Table 1. The cutting speed was chosen such that milling took place in the third speed zone of oscillations, when regenerative oscillations act. The reliability of the obtained results was checked by variance analysis with an assessment according to the Fisher criterion [14].

Table 1 - Input data for studying the influence of axial depth of cut on the laws of motion of the TWE during up- and down-milling

Frequency/period of free oscillations of the elastic element with the sample in the feed directions, *f/T*, Hz/s	$415/2.4\cdot10^{-3}$ – up-milling $415/2.4\cdot10^{-3}$ – down-milling
Milling cutter stiffness, *j*, N/m	21805555
Frequency/period of free oscillations of the milling cutter, *f/T*, Hz/s	$833/1.2\cdot10^{-3}$
Milling cutter diameter, *d*, mm	50
Number of milling cutter-teeth, z	1
Rake angle of the milling cutter tooth, deg	0
Flank angle of the milling cutter tooth, deg	10
Angle of inclination of the milling cutter teeth, ω, deg	0
Feed per tooth, S_z, mm	0.1
Spindle speed, *n*, rpm	280
Radial cutting depth, a_e, mm	0.5
Axial cutting depth, a_p, mm	1; 2; 3; 4

3. Experiments and discussion of results

After milling, profilograms were recorded (Fig. 1), which determined the pitch – *S*w and the waviness height – *W*z of the machined surfaces, the values of which are given in Table 2.

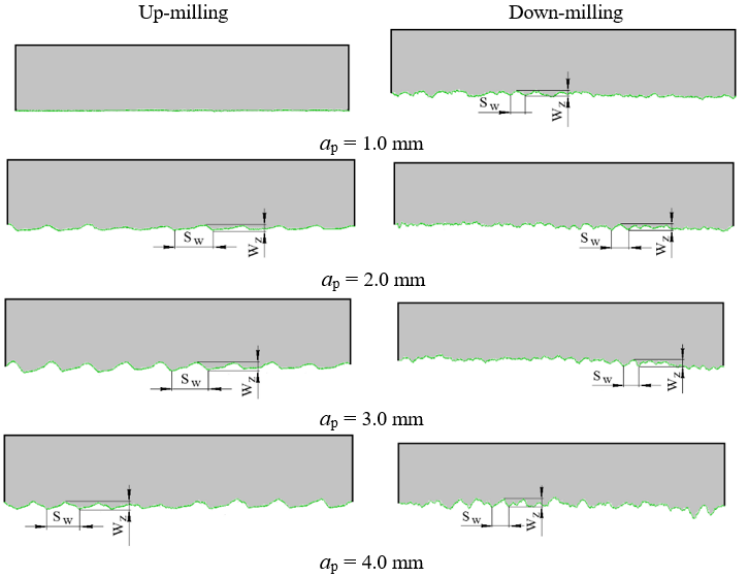

Sw, *Wz* – pitch and height of waviness on the machined surface of the TWE

Figure 1 – Profiles of machined surfaces after up- and down-milling of the TWE with different axial cutting depths

Table 2 – Pitch and height of waviness on machined surfaces after up- and down-milling of TWE with different axial depths of cut

Axial depth of cut a_p, mm	Waviness pitch, S_w, mm		Waviness height, W_z, mm	
	Up- milling	Down-milling	Up- milling	Down-milling
1.0	-	1.14	-	0.054
2.0	2.78	1.09	0.055	0.060
3.0	2.72	1.05	0.086	0.065
4.0	2.68	1.23	0.096	0.105

On the profilegraphs obtained after milling, waviness is observed on all machined surfaces, except for the surface after up-milling with an axial cutting depth of 1 mm. To determine the influence of the axial cutting depth on the pitch and height of waviness on the machined surfaces, an analysis of variance was performed with an assessment using the Fisher criterion. The calculation results are given in Tables 3-6. The Fisher criterion determined by the results of measuring the waviness pitch

is less than the critical value. This indicates that the axial cutting depth does not affect the waviness step during up- and down milling.

Table 3 – One-way analysis of variance of the influence of axial depth of cut on the waviness pitch of machined TWE surfaces during up-milling

Sum of squares		Number of degrees of freedom		Variance		Fisher's exact test	
Q_A	Q_W	f_A	f_W	S_A^2	S_W^2	F	F_{cr}
0.050	1.405	2	27	0.025	0.052	2.08	3.354

Table 4 – One-factor analysis of variance of the influence of axial depth of cut on the waviness height of machined TWE surfaces during up-milling

Sum of squares		Number of degrees of freedom		Variance		Fisher's exact test	
Q_A	Q_W	f_A	f_W	S_A^2	S_W^2	F	F_{cr}
0,010	0,007	2	30	0,005	0,00023	21,74	3,316

Table 5 – One-way analysis of variance of the influence of axial depth of cut on the waviness pitch of machined TWE surfaces during down-cutting

Sum of squares		Number of degrees of freedom		Variance		Fisher's exact test	
Q_A	Q_W	f_A	f_W	S_A^2	S_W^2	F	F_{cr}
0.128	0.734	3	23	0.0427	0.0319	1.338	3.028

Table 6 – One-way analysis of variance of the influence of axial depth of cut on the waviness height of machined TWE surfaces during down-cutting

Sum of squares		Number of degrees of freedom		Variance		Fisher's exact test	
Q_A	Q_W	f_A	f_W	S_A^2	S_W^2	F	F_{cr}
0.019	0.008	3	40	0.00633	0.0002	31.65	2.827

The Fisher criterion determined by the results of measuring the waviness height is greater than the critical value. This indicates that the axial depth of cut affects the waviness height during up- and down milling. The results shown in Table 2 confirm these conclusions.

To study the waviness on the cutting surfaces, which causes regenerative vibrations, fragments of oscillograms were considered, on which the vibrations of the part during cutting were recorded (Fig. 2).

Up-milling Down-milling

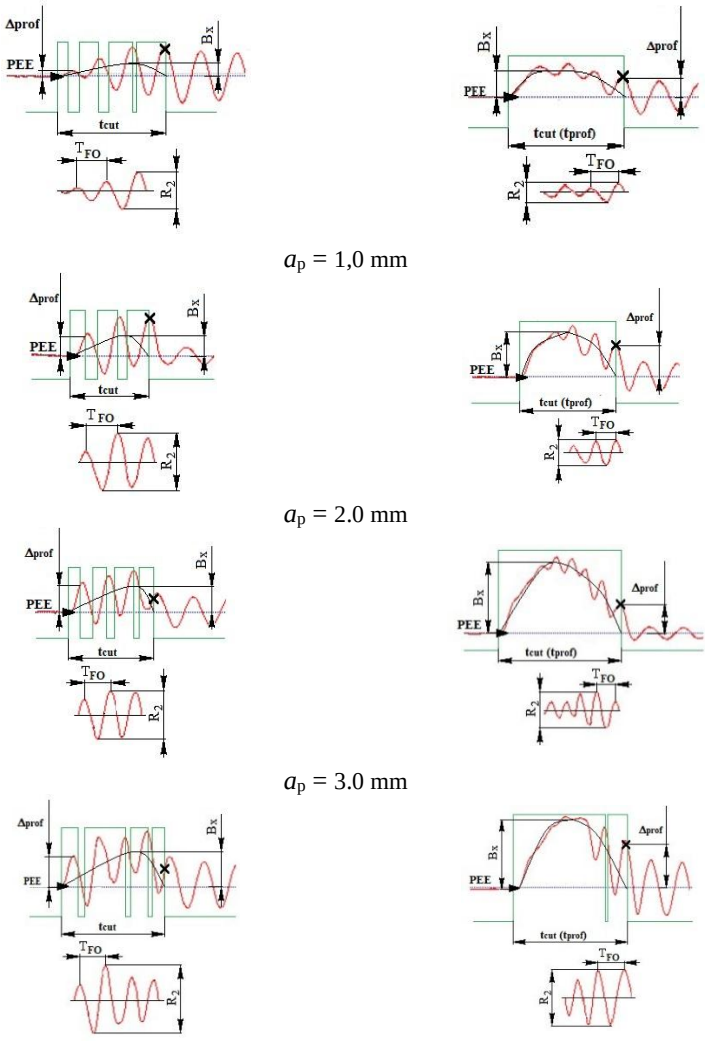

a_p = 1,0 mm

a_p = 2.0 mm

a_p = 3.0 mm

a_p = 4.0 mm

PEE – position of elastic equilibrium; T_{FO} – period of the AFO; R_2 – AFO range; t_{cut} – cutting time; B_x – maximum static displacement of the TWE from PEE; Δ_{prof} –deflection from PEE

of the first wave of the TWE during up-milling and the last wave of the TWE during down-milling

Figure 2 – Fragments of oscillograms of the oscillations of TWE obtained during up- and down-milling with different axial depths of cut

The recorded oscillation oscillograms of the thin-walled element of the part during cutting are identical in shape to the cutting surfaces [15]. Based on this, it can be said that the waviness on the cutting surfaces is present at all axial depths of cutting, which contributes to the excitation of regenerative oscillations. To determine their influence on the machined surface, graphs of changes in the ~~deviation~~ deflection from the initial equilibrium position (PEE) Δ_{prof} of the first wave of the AFO during up-milling and the last wave of the AFO during down- milling were plotted (Fig. 3).

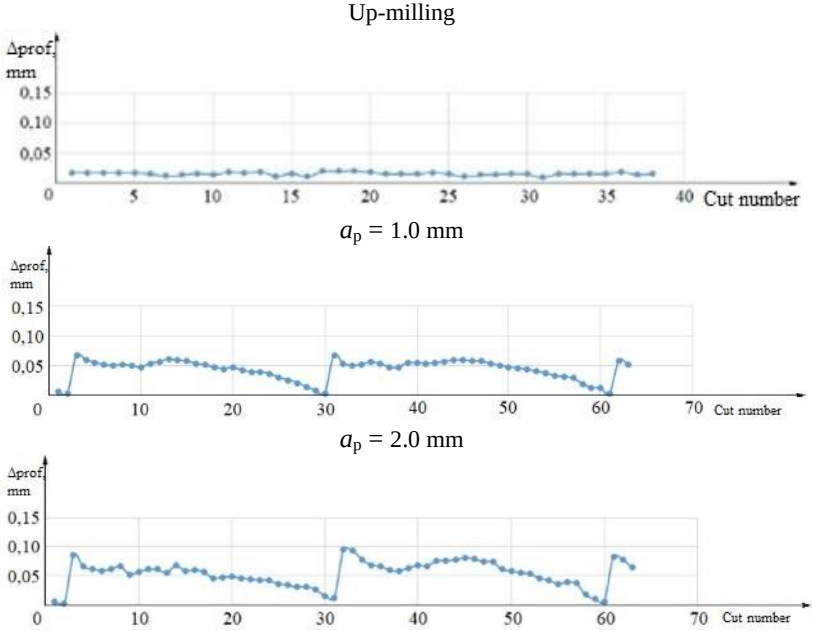

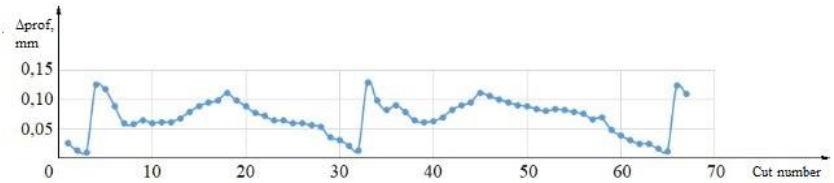

a_p = 4.0 mm
Down-milling

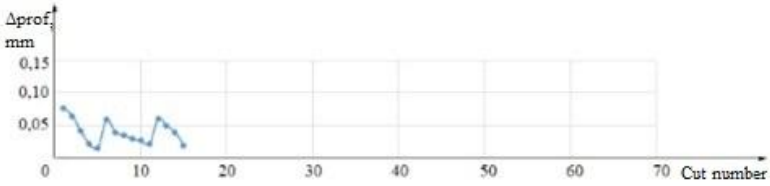

a_p = 1.0 mm

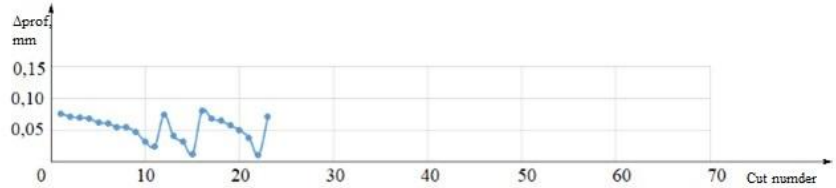

a_p = 2.0 mm

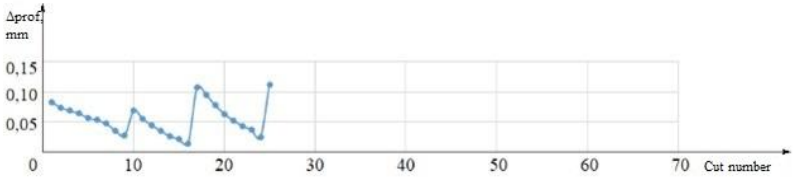

a_p = 3.0 mm

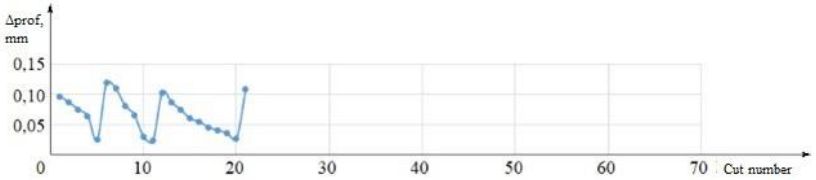

a_p = 4.0 mm

Figure 3 –Deflection from the PEE of the first wave of the AFO - Δ_{prof} during up-milling and the last wave of the AFO - Δ_{prof} during down-milling of the TWE with different axial cutting depths

These deflection characterize the marks on the machined surface after moving the sample by the feed rate per tooth. The graphs show that the deflection from the PEE of the first wave of the AFO during up-milling and the last wave of the AFO during down-milling have a periodicity of changes and increase with increasing axial depth of cut, except for the values obtained during up- milling with an axial depth of cut of 1 mm. This is facilitated by the peculiarities of up- and down-milling, which determine the influence of regenerative oscillations on the formation. During up-milling, it occurs at the beginning of cutting, when regenerative oscillations have not yet arisen. It is precisely because of the identical conditions for cutting the allowance during cutting with an axial depth of 1 mm that marks of the same depth remain on the machined surface and waviness is absent. With an axial cutting depth of more than a_p = 1 mm during up-milling, the height of the waviness at the beginning of the cutting surface increases from the AFO, which affects the change in the depth of the marks that remain on the machined surface and form waviness on it. Its height increases with increasing axial depth. During up-milling, surface generation occurs at the end of cutting, when the regenerative vibrations are already excited during the movement of the cutter along the wave trace and the conditions change during cutting the allowance, due to which the marks that remain have different depths and form waviness on the machined surface at all axial cutting depths. Such features of the formation of the machined TWE surface must be taken into account when choosing the feed direction and assigning the axial cutting depth to ensure the accuracy of manufacturing complex-profile functional surfaces of the blades of monowheels during milling with end mills in the third high-speed oscillation zone.

4. Conclusions

Milling of thin-walled elements of parts by an end mill in the third speed zone of oscillations occurs with regenerative oscillations, which are excited when moving along a wavy trace formed on the cutting surface from accompanying free oscillations, and affect the stability of the tool and the quality of the machined surface. When assigning the axial cutting depth under such conditions, it should be taken into account that during up-milling, regenerative oscillations are excited after the tool passes through the surface generation zone, and during down-milling, their effect covers the area. Therefore, preference is given to down-milling. In this case, the axial cutting depth is assigned to the minimum so that during cutting the allowance, the conditions for surface generation the machined surface are the same, in which depressions of the same depth remain on it and there is no shape error in the form of waviness.

The results obtained can be used to substantiate rational cutting modes to ensure the accuracy of the functional surfaces of complex-profile thin-walled

monowheel blades under the action of regenerative vibrations during milling with an end mill.

References: **1**. *Erhan Budak* An analytical design method for milling cutters with nonconstant pitch to increase stability – Part I: Theory; Part II: Application, Trans., ASME Journal of Manufacturing Science and Engineering, vol. 125, pp. 29–38, 2003. DOI:10.1016/j.ijmachtools.2005.09.009. **2**. *Zhou-Long Li, Oguzhan Tuysuz, Li-Min Zhu, Yusuf Altintas* Surface form error prediction in five-axis flank milling of thin-walled parts, International Journal of Machine Tools and Manufacture. Vol. 128, pp. 21–32, 2018. https://doi.org/10.1016/j.ijmachtools.2018.01.005. **3**. *Muhittin Caner Eksioglu, Z. Murat Kilic, Yusuf Altintas* Discrete-time prediction of chatter stability, cutting forces, and surface location errors in flexible milling systems, J. Manuf. Sci. Eng. Vol. 134, 61006, 2012. https://doi.org/10.1115/1.4007622. **4**. *Oguzhan Tuysuz, Yusuf Altintas* Frequency domain prediction of varying thin-walled workpiece dynamics in machining, J. Manuf. Sci. Eng. Vol. 139, 71013, 2017. https://doi.org/10.1115/1.4036124. **5**. *Oguzhan Tuysuz, Yusuf Altintas* Time domain modeling of varying dynamic characteristics in thin-wall machining using perturbation and reduced order substructuring methods., J. Manuf. Sci. Eng. Vol. 140, 11015, 2018. https://doi.org/10.1115/1.4038000. **6**. *Jokin Munoa, Xavier Beudaert, Kaan Erkorkmaz, Alex Iglesias, Asier Barrios, Mikel Zatarain* Active suppression of structural chatter vibrations using machine drives and accelerometers, CIRP Annals, vol. 64(1), pp. 385–388, 2015. https://doi.org/10.1016/j.cirp.2015.04.106. **7**. *Iñigo Bediaga, Igor Egana, Jokin Munoa* Time and Frequency Domain Models for Chatter Prediction in Milling, Chapter 04 in DAAAM International Scientific Book, pp. 033-048, 2005. **8**. *Jiawei Mei, Ming Luo, Jianglong Guo, Haonan Li, Dinghua Zhang* Analytical modelling, design and performance evaluation of chatter-free milling cutter with alternating pitch variations, IEEE Access, vol. 6, pp. 32367 – 32375, 2018. https://doi.org/10.1109/access.2018.2841000. **9**. *Sergey Dyadya, Mykhaylo Frolov, Serhiy Tanchenko Vasyl Solokha* Attendant Free Vibrations and Assessment of Their Influence on the Machined Surface Macrogeometry While End Milling, Lecture Notes in Mechanical Engineering, P.327–337, 2025. DOI:10.1007/978-3-031-95211-1_27. **10.** *Vnukov Yuriy, Dyadya Serhiy., Kozlova Olena., Trishyn Pavlo ., Zubarev Andriy* Influence of cutting time on types of oscillations during blade processing, Ukrainian Journal of Mechanical Engineering and Materials Science, Vol. 9, Number 1, pp. 53-66, 2023. https://doi.org/10.23939/ujmems2023.01.053. **11.** *Yusuf Altintas* Manufacturing automation: metal cutting mechanics, machine tool vibrations, and CNC design.. 2nd ed. Cambridge University Press, 2012. 380 p. https://doi.org/10.1017/CBO9780511843723. 12. *Dyadya Serhiy., Vnukov Yuriy., Kozlova Olena., Trishyn Pavlo* Regularities of Oscillations During Turning and End Milling, Lecture Notes in Mechanical Engineering, pp. 136–144, 2024. https://doi.org/10.1007/978-3-031-42778-7_13. **13.** *Dyadya Sergei, Kozlova Olena, Tryshyn Pavlo, Brukhno Eduard, Yakhno Denys* Influence of radial depth of cut on initial conditions of oscillations during end–milling of thin -walled parts, Cutting & Tools in Technological System, Vol. 99, pp. 153–164, 2023. https://doi.org/10.20998/2078-7405.2023.99.14. **14.** *Vnukov Yuriy, Dyadya Sergei, Kozlova Olena et al.* Self-oscillations during milling of thin-walled elements of parts: monograph. Zaporizhzhia: ZNTU, 2017. 208 p. **15.** *Mozgovoy Volodymyr, Dyadya Sergei, Kozlova Olena et al*. Formation of the machined surface profile during cylindrical end milling under self-oscillation conditions, Engineering Bulletin, No. 1. pp. 92–100, 2018.

Сергій Дядя, Олена Козлова, Павло Тришин, Едуард Кондратюк,
Олексій Крамаренко, Запоріжжя, Україна

ЯКІСТЬ ОБРОБЛЕНИХ ПОВЕРХОНЬ ТОНКОСТІННИХ ЕЛЕМЕНТІВ ДЕТАЛЕЙ В УМОВАХ ДІЇ РЕГЕНЕРАТИВНИХ КОЛИВАНЬ ПРИ ФРЕЗУВАННІ КІНЦЕВИМИ ФРЕЗАМИ

Анотація. *Моноколеса, у яких диск та робочі лопатки становлять єдину конструкцію без рознімних з'єднань, є критично важливими компонентами газотурбінних двигунів нового покоління для авіації та енергетики. Використання таких конструкцій дозволяє знизити вагу та підвищити надійність агрегатів. Однак похибки форми функціональних поверхонь лопаток, що виникають під час механічного оброблення, призводять до зниження коефіцієнта корисної дії двигуна та зростання витрат пального. Для забезпечення точності виготовлення функціональних поверхонь лопаток впродовж технологічного процесу необхідно знати умови, за яких відбувається різання. У роботі використано підхід, що базується на розподілі всього діапазону швидкостей різання на п'ять швидкісних зон коливань. Встановлено, що найбільш несприятливою під час фрезерування лопаток на багатокоординатних верстатах з ЧПК є третя швидкісна зона. Вона характеризується вібраціями високої інтенсивності, що погіршує якість обробленої поверхні та знижує стійкість фрези. Їх причиною є регенеративні коливання, які збуджуються при обробленні по сліду, що залишається на поверхні різання від супроводжуючих вільних коливань. Метою дослідження є визначення впливу осьової глибини різання на якість обробленої поверхні під час фрезування у третій швидкісній зоні коливань. Результати експериментів показали, що завдяки особливостям зустрічного фрезування з осьовою глибиною різання a_p = 1 мм хвилястість на обробленій поверхні не утворюється, навіть за наявності регенеративних коливань. Отримані дані дозволяють розробити рекомендації щодо вибору режимів різання, які мінімізують амплітуду коливань та забезпечують відповідність лопаток моноколіс високим експлуатаційним вимогам.*

Ключові слова: *фрезування; кінцева фреза; поверхня різання; хвилястість; регенеративні коливання; вимушені коливання; супроводжуючі вільні коливання*.

CONTENT

Scientific edition

CUTTING AND TOOLS
in technological systems

Collection of scientific papers

Issue No 104

Compiled by *Doctor of Technical Sciences, Prof. I.M. Pyzhov*
Original-model *by A.M. Borzenko*
Responsible for the graduation *of Candidate of Technical Sciences, Prof. Y.V. Ostroverkh*

In the author's edition

Materials reproduced from the author's originals

Subpara. to print 10.12.2025.Format 60x84 1/16. PaperSoruRareg.
Printing - risography. The Times Typeface. Conditions.print.p. 10,93. Accounting.vid.ark. 11.0.
Circulation 30 copies.
1st Plant 1-100. Deputy. № 1149. The price is negotiable.

Publishing Center of NTU "KhPI"
Certificate of state registration DK No. 116 dated 10.07.2000
61002, Kharkiv, st. Kirpichova, 2